

Hybrid Lead Halide Perovskite Thin Films and Solar Cells by Chemical Vapour Deposition

Siphelo Ngqoloda



**A thesis submitted in fulfilment of the requirements for the degree
of Doctor Philosophiae in the Department of Physics and Astronomy,
University of the Western Cape**

Supervisor : Prof CJ Arendse, University of the Western Cape

Co-Supervisors : Dr TFG Muller, University of the Western Cape

**: Dr CJ Oliphant, National Metrology Institute of South
Africa**

August 2021

<http://etd.uwc.ac.za/>

KEY WORDS

‘Hybrid Lead Halide Perovskite Thin Films and Solar Cells by Chemical Vapour Deposition’

Siphelo Ngqoloda

Organic-inorganic hybrid perovskites

Low-pressure chemical vapour deposition

Sequential method

Lead Iodide

Lead chloride

Lead chloride iodide

Methyl ammonium lead iodide perovskites

Mixed halide perovskites

Planar perovskites solar cells

Thin films

Photovoltaics

Large grains

Air stable

Intercalation reaction

Crystallinity



ABSTRACT

‘Hybrid Lead Halide Perovskite Thin Films and Solar Cells by Chemical Vapour Deposition’

S. Ngqoloda

PhD. Thesis, Department of Physics and Astronomy, University of the Western Cape

The organic-inorganic hybrid perovskites such as methyl ammonium lead iodide (MAPbI₃) or mixed halide MAPbI_{3-x}Cl_x (x is usually very small) have emerged as an interesting class of semiconductor materials for their application in photovoltaic (PV) and other semiconducting devices. A fast rise in PCE of this material observed in just under a decade from 3.8% in 2009 to over 25.2% recently is highly unique compared to other established PV technologies such as c-Si, GaAs, and CdTe. The high efficiency of perovskites solar cells has been attributed to its excellent optical and electronic properties. Perovskites thin film solar cells are usually deposited via spin coating, vacuum thermal evaporation, and chemical vapour deposition (CVD). The spin-coating methods have some challenges, which include incomplete surface coverage, use of solvents which promotes film instability, and lack of reproducibility. Thermal evaporation on the other hand requires the use of dedicated ultrahigh vacuum systems and is not easily scalable.

Here a sequential low-pressure CVD method was developed to prepare perovskites thin films starting by optimising the deposition of lead halide (PbX₂) thin films in the first step and subsequently converting these to perovskite phase in the last step. The optimisation study was carried out by investigating the effect of substrate temperature during the deposition of these PbX₂ films, namely: lead iodide (PbI₂) and lead chloride (PbCl₂), independently. Highly

crystalline films were realised for both lead halide compounds with PbI_2 films showing high texture compared to reduced texture of the PbCl_2 films based on the X-ray diffraction results. Large lateral grain sizes were observed for the PbI_2 films with flat platelets grain morphology compared to smaller columnar grain shapes of PbCl_2 films.

The PbI_2 films were then converted to perovskite phase during their exposure to methyl-ammonium iodide (MAI) vapour using the same reactor forming a methyl-ammonium lead iodide (MAPbI_3) perovskite films in second step of the process. Different exposure times were investigated with complete conversion realized after 90 minutes of exposure forming a perovskite with large grains. The coverage and quality of the perovskite thin films is controlled by that of the pre-deposited PbI_2 film. The absorbance measurements confirmed air stability of the fully converted perovskite for 21 days, ascribed to its superior morphology and grain size and a planar perovskite solar cell had a best power conversion efficiency of 11.7%. The solar cell device maintains 85% of its performance up to 13 days in open-air with relative humidity up to 80%.

Further, Cl-doped perovskite ($\text{MAPbI}_{3-x}\text{Cl}_x$) film solar cells were prepared by this facile sequential chemical vapour deposition method where chlorine containing lead halides were employed, i.e., lead chloride and lead chloride iodide (PbICl). The lead chloride iodide films were prepared by depositing PbCl_2 and then PbI_2 on top and these films reacted together forming this new phase (PbICl). A complete substitution of Cl ions by iodine ions was realised during the conversion of the PbCl_2 and PbICl films to perovskite phase. Cl doped perovskite solar cell showed improved device efficiency of 10.87% compared to un-doped perovskite solar cell which had PCE of 8.76% attributed to improved open circuit voltage of the Cl-doped perovskites.

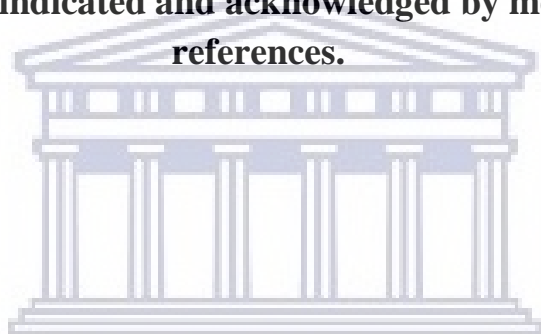
August 2021

DECLARATION

I declare that


Hybrid Lead Halide Perovskite Thin Films and Solar Cells by Chemical Vapour Deposition

is my own work, that it has not been submitted for any degree or examination in any other university, and that all the sources I have used or quoted have been indicated and acknowledged by means of complete references.



UNIVERSITY of the
WESTERN CAPE

Siphelo Ngqoloda

Signature: 

August 2021

Dedicated to my immediate and extended family.



UNIVERSITY *of the*
WESTERN CAPE

ACKNOWLEDGEMENT

I am grateful to the following people and organisation without whose assistance, advice, and guidance the completion of this thesis would not be possible.

Prof Christopher Arendse (Department of Physics & Astronomy, UWC) for the excellent supervision of this thesis, his guidance, encouragement, friendship and for many stimulating discussions

Dr Theo Muller (Department of Physics & Astronomy, UWC), who acted as co-supervisor, for his constant encouragement and interest in my progress.

Dr Clive Oliphant (NMISA), who also acted as co-supervisor, for his guidance, friendship, and many fruitful discussions.

Prof Suchi Guha (Department of Physics & Astronomy, University of Missouri-Columbia, USA) for her much-valued input into this thesis and the optical measurements.

Dr Francious Cummings (Department of Physics, UWC), for his constant encouragement and interest in my progress and assisted me with electron microscopy together with Earl.

The staff of the Physics and Astronomy department, UWC, for their support; Mrs. A. Adams, and Mrs. N. Kenseley for all the administration on my behalf.

To my immediate family: my mother and all my siblings, and not to forget my extended families and friends, for their encouragement and support.

To a special friend Olwethu for her support, encouragement, love, and keeping me sane.

My colleagues and friends at UWC for their support and encouragement, Sihle, Sfiso, Stephen, Mohamad Bello, Natasha, Lionel, Amy, Floyd, Norman, and Siyambonga (Siya)

Prof E. Iwuoha and C. Linder for arranging my two visits to research labs in Europe.

The National Research Foundation (NRF) and University of the Western Cape for the financial support during this study. The National Metrology Institute of South Africa for the use of their instruments.

CONTENTS

| | |
|--|------------|
| TITLE PAGE | i |
| KEY WORDS | ii |
| ABSTRACT | iii |
| DECLARATION | v |
| ACKNOWLEDGEMENT | vii |
| CHAPTER ONE | 1 |
| Background: Energy Mix and Photovoltaics Solar cells..... | 1 |
| 1.1 Introduction | 1 |
| 1.2 First Generation Solar Cells | 4 |
| 1.3 Second Generation Solar Cells | 5 |
| 1.4 Third Generation Solar Cells..... | 7 |
| 1.5 Perovskites Solar Cells..... | 9 |
| 1.5.1 Introduction..... | 9 |
| 1.5.2 Crystal Structure of Perovskites..... | 12 |
| 1.5.3 Optical Properties of Perovskites..... | 18 |
| 1.5.4 Deposition Methods of Perovskites Solar Cells..... | 22 |
| 1.5.4.1 Introduction..... | 22 |
| 1.5.4.2 Spin Coating Deposition | 24 |
| 1.5.4.3 Vapour-Assisted Solution Deposition..... | 29 |
| 1.5.4.4 Vacuum Thermal Evaporation | 32 |
| 1.5.4.5 Chemical Vapour Deposition Method | 36 |
| 1.5.5 Challenges and Conclusions of Perovskites Solar Cells | 43 |
| 1.6 Aims and Outlines | 44 |
| 1.7 References | 48 |
| CHAPTER TWO | 55 |
| Experimental Procedure: Deposition Optimization and Characterization | 55 |
| 2.1 Introduction | 55 |
| 2.2 Introduction to Chemical Vapour Deposition | 55 |
| 2.3 Thermal Chemical Vapour Deposition..... | 57 |
| 2.4 Thermal CVD System Setup | 58 |

| | | |
|---|---|------------|
| 2.5 | Optimizing Deposition Conditions..... | 59 |
| 2.5.1 | Lead Halide Deposition | 60 |
| 2.5.2 | Pb Halide Conversion to Perovskites..... | 65 |
| 2.6 | Perovskites Solar Cell Fabrication | 67 |
| 2.7 | Characterisation of Perovskites Thin Films..... | 71 |
| 2.8 | Perovskite Solar Cell Performance Measurements..... | 73 |
| 2.8.1 | Basic Solar Cell Parameters | 73 |
| 2.8.2 | Perovskite Solar Cell Measurements | 75 |
| 2.9 | References | 77 |
| CHAPTER THREE..... | | 79 |
| Controlled Deposition of Lead Iodide and Lead Chloride Thin Films by Low-Pressure Chemical Vapor Deposition | | 79 |
| 3.1 | Introduction | 80 |
| 3.2 | Experimental Procedure and Characterisation..... | 82 |
| 3.2.1 | Lead Halide Film Deposition | 82 |
| 3.2.2 | Characterisation | 84 |
| 3.3 | Results and Discussion | 85 |
| 3.3.1 | Structural Properties of Lead Iodide Films | 85 |
| 3.3.2 | Morphology of Lead Iodide Films | 88 |
| 3.3.3 | Structural Properties of Lead Chloride Films | 93 |
| 3.3.4 | Morphology of Lead Chloride Films | 96 |
| 3.3.5 | Optical Properties of the Lead Halide Films..... | 99 |
| 3.4 | Conclusion..... | 101 |
| 3.5 | References | 102 |
| CHAPTER FOUR..... | | 105 |
| Air-stable Hybrid Perovskite Solar Cell by Sequential Vapor Deposition in a Single Reactor..... | | 105 |
| 4.1 | Introduction | 106 |
| 4.2 | Experimental Methods..... | 109 |
| 4.2.1 | Perovskite Film Fabrication | 109 |
| 4.2.2 | Perovskite Solar Cell Fabrication | 111 |
| 4.2.3 | Characterization | 112 |
| 4.3 | Results and Discussion | 113 |
| 4.3.1 | Thin Film Deposition | 113 |

| | | |
|---|--|------------|
| 4.3.2 | Film Optical Properties and Stability | 126 |
| 4.3.3 | Device Performance and Stability..... | 129 |
| 4.4 | Conclusion..... | 133 |
| 4.5 | References | 134 |
| CHAPTER FIVE | | 138 |
| Mixed-Halide Perovskites Solar Cells Through PbI ₂ and PbCl ₂ Precursor Films by Sequential Chemical Vapor Deposition..... | | 138 |
| 5.1 | Introduction | 139 |
| 5.2 | Experimental Section..... | 142 |
| 5.2.1 | Fabrication of Perovskite Solar Cells..... | 142 |
| 5.2.2 | Characterization | 145 |
| 5.3 | Results and Discussion | 146 |
| 5.3.1 | Structural and Morphological Properties | 146 |
| 5.3.2 | Optical Properties and Device Characterization | 158 |
| 5.4 | Conclusion..... | 164 |
| 5.5 | References | 164 |
| SUMMARY | | 170 |
| APPENDIX A | | 174 |
| PUBLICATIONS | | 175 |



CHAPTER ONE

Background: Energy Mix and Photovoltaics

Solar cells

1.1 Introduction

Humanity's survival, sustainability, and development requires electricity as a basic need for cooking, lights, heat, transportation of goods, agriculture, communication, industrial evolution, and any other survival necessities. Unfortunately, a vast amount of energy is required to meet these basic human needs and that comes with great impact on the environment, such as the emission of greenhouse gases to the atmosphere causing global climate change [1.1 – 1.5].

The major source of electricity generation globally is based on combustion of fossil fuels such as coal, oil, and natural gas as shown in Figure 1.1. The combustion of fossil fuels results in emission of carbon dioxide (CO₂), which rises to the atmosphere and in turn causes a rise in earth's surface temperature – a process known as global warming. Fossil fuels are a result from plant and animal remains buried underground millions of years ago and as such they are depleting and soon the world will be out of electricity generating sources. This depletion of fossil fuels has resulted in high global sale competition causing a rise in their prices, with developing countries bearing the brunt. Due to the depletion of fossil fuels and their global warming effects, new sources of energy are required and must be environmentally benign, sustainable, renewable, and have low CO₂ emission [1.1 – 1.5].

Clean and renewable energy generating technologies exist around the globe, but their contribution to the global energy mix is still very low compared to energy generated from fossil fuels, even in the well-developed regions such as the North America, Europe and East Asia

(see Figure 1.1). With more research and development, the goal of using renewable energy across the world will be achieved, depending on the economic stabilities of the respective regions or countries. Indeed, a steady rise on the use of renewable energy have been observed over the years as shown in Figure 1.1, even though this rise is in accordance with the increase in fossil fuel uses and that is due to increasing global energy demand [1.1 – 1.5].

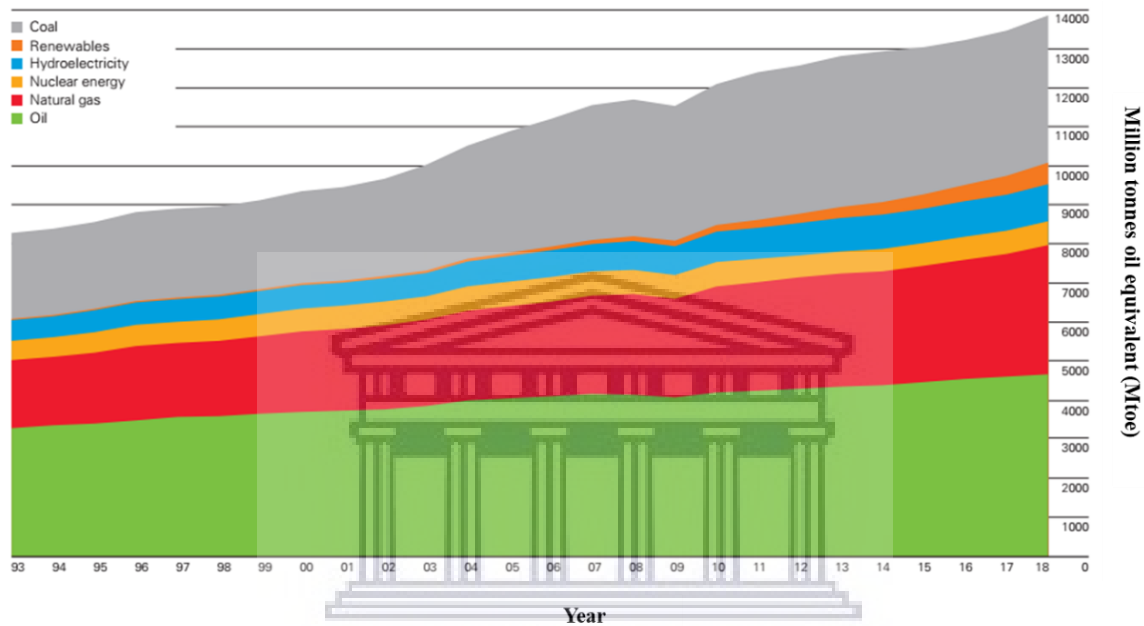


Figure 1.1: Global energy consumption by fuel taken between 1993 and 2018 [1.3].

Renewable energy sources are naturally occurring sources that can be continuously replenished in a short time scale and include biomass or bioenergy, geothermal energy, wind energy, hydropower, solar energy, and oceanic energy. The application of these renewable energy sources depends mainly on the suitability of the region or country. For example, wind energy needs to be implemented in a region where the average wind speed per year is high enough or solar energy implemented in a region with high solar radiation per year. The economic stability and land availability are some of the major factors that need to be considered when choosing an appropriate source of renewable energy. Solar energy is by far the cheapest

and most available source of renewable energy. As such, the conversion of solar energy to electricity is the leading research topic in renewable energy sources in the world [1.1 – 1.5].

A country like South Africa is the major electricity generating and consuming country in Africa and depends mainly on coal generated electricity as shown in Figure 1.2. Therefore, South Africa can utilise some of the renewable energy sources [1.3]. Alternative clean source like hydroelectricity will not be suitable for South Africa due to the lack of water. Wind energy, on the other hand, would require displacing humans as more land is required for this type of renewable energy. This leaves solar energy as the most suitable source that should be implemented and explored in South Africa, as this region receives high solar radiation per year and solar power plants can be situated in desert lands.

The rate at which solar energy reach earth is about 10 000 times more than the rate at which the world (humanity) consumes primary energy. If solar energy is converted to electricity efficiently it could satisfy every human being in the entire world. Solar energy can be directly converted to electricity using photovoltaic (PV) technology or indirectly using concentrated solar power (CSP) systems. CSP systems concentrate the direct radiant energy towards a fluid which is then used to generate electricity by means of turbines, like combustion of fossil fuels. Photovoltaic technology on the other hand converts radiant energy directly to electricity by means of photovoltaic effect, using solar panels (made up of solar cells). This converted energy can be stored in batteries for later use when the sunlight is unavailable. Both technologies are highly effective for clean energy generation suitable for developing countries like South Africa. However, the cost of CSP surpass that of PV technology, making it undesirable [1.5].

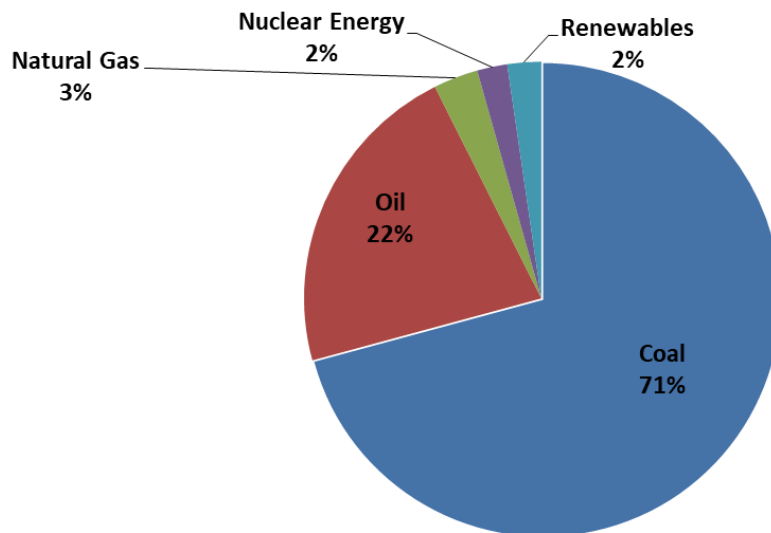


Figure 1.2: Energy consumption in South Africa as in 2018, dominated by use of fossil fuel (coal and oil) [1.3].

1.2 First Generation Solar Cells

The earth receives an abundant amount of solar energy per year and therefore it is sensible to harvest this solar energy by converting it into electricity through photovoltaic technology. Harvesting solar energy using photovoltaic technology will reduce the levels of CO₂ emission to the atmosphere and hence reduce global warming effect.

Photovoltaic (PV) technology is based on the photovoltaic effect, which was first observed by A.E. Becquerel in 1839. A deeper understanding of this phenomenon was only realised after the development of quantum mechanics theory between 1900 and 1930 [1.6]. However, it was only until 1954 that the first crystalline silicon (c-Si) based solar cell was reported with a power conversion efficiency (PCE) of 6% [1.6]. Crystalline silicon has since been developed over the years reaching a PCE above 24%; and now makes up over 90% of commercially available solar cells and panels [1.6, 1.7].

Crystalline Si includes mono-crystalline and polycrystalline silicon (Figure 1.3) and their drawback is the indirect band gap of the material (band gap of ~ 1.1 eV), resulting in poor light absorption in the near infrared [1.6 – 1.8]. Solar panels based on c-Si are called first generation solar cells and have a high cost. This high cost is due to the expensive purification process to produce single-crystal c-Si (through Czochralski process) and to the required thick wafers (~ 500 μm thick) to achieve better light absorption [1.8]. Despite the high-cost, these c-Si based solar cells/panels have seen great achievements in terms of PCE, mainly due to improve light trapping methods and optimised doping with boron or phosphorus to form extrinsic silicon [1.6 – 1.8]. Since the global aim is to reduce the cost of photovoltaic technology, while maintaining a high PCE, other generations of solar cells have been developed over the years that includes thin films (second generation solar cells) and third generation solar cell technologies.

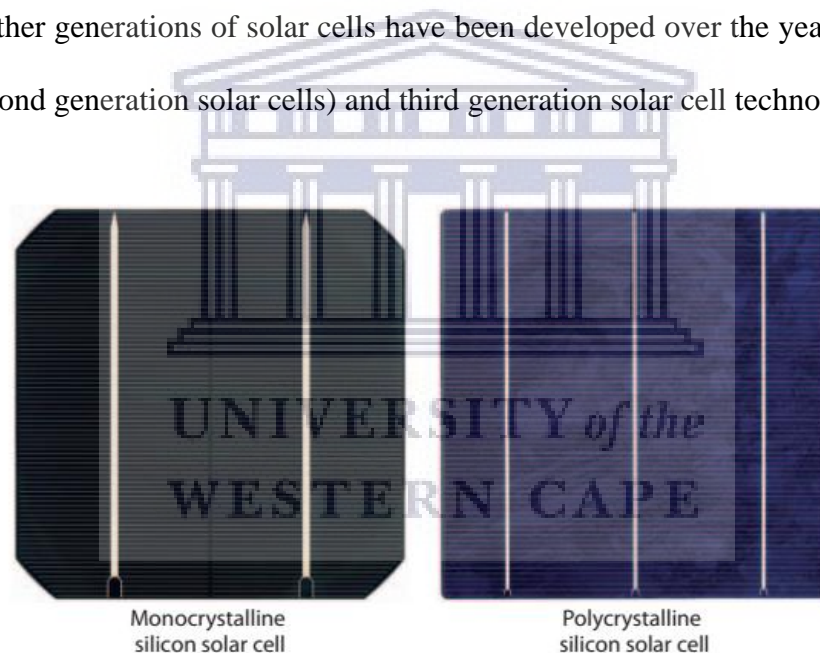


Figure 1.3: Photographs of Monocrystalline and polycrystalline silicon solar modules [1.8].

1.3 Second Generation Solar Cells

Thin film PV technologies are based on thin film semiconductors of few micrometres in thickness compared to hundreds of micrometres of crystalline silicon. This technology was developed as means to reduce the production cost of solar panels based on c-Si. Hydrogenated

amorphous silicon (a -Si:H), cadmium telluride (CdTe), and copper indium gallium selenide (CIGS) are the most studied thin film-based technologies and are available in the market [1.7, 1.9, 1.10]. Among these thin film semiconductors, a -Si offers better advantages such as thinner optimum film thickness of about 1 μm with an improved absorption coefficient. CdTe requires between 3-5 μm of film thickness and contains toxic cadmium and rare tellurium, whereas CIGS require between 1-2 μm film thickness with rare earth indium and gallium metals, making this semiconductor expensive to produce and commercialise [1.7].

The other interesting property of these thin films is their direct band gap, implying that they can absorb sufficient light while using a thin layer. The band gap of a -Si:H is tunable in the region 1.2 - 1.8 eV depending on the hydrogen concentration. CdTe has a band gap of 1.4 eV and CIGS has a tunable band gap ranging between 1.0 eV and 1.6 eV with varying chemical composition [1.7]. Research in a -Si:H solar cells began in 1976 with an initial power conversion efficiency (PCE) of 2.4%, which has risen to 13.6% for a triple junction solar cell and a stabilised PCE of 14% [1.7, 1.11]. A typical solar cell structure of a -Si:H composes of a transparent conductive oxide (TCO) layer, such as indium tin oxide (ITO), deposited on a glass substrate. This is followed by the consecutive deposition of a p-type a -Si:H layer, an intrinsic a -Si:H layer, and an n-type a -Si:H, forming a p-i-n junction cell, which is finally coated with a Ag metal electrode [1.7].

CIGS on the other hand has a device structure composed of Mo layer deposited on glass substrate followed by p-type CIGS (CuInGaSe_2), n-type CdS serving as a buffer layer, intrinsic ZnO layer followed by aluminium doped ZnO layer as a transparent electrode. CIGS research also dates to the same year as a -Si (1976) with first reported PCE of 4.5% which has reached 23.4% recently after further optimisation of the absorber layer including doping with alkali elements [1.7, 1.11]. CdTe research started four years earlier than the two technologies in 1972

where a PCE of 6% was first reported and now has reached 22.1% for lab scale cells [1.7, 1.11]. Different device structures of CdTe solar cells have been investigated over the years but a typical structure is made of glass substrates coated with tin oxide layer, followed by CdS layer, then a CdTe absorber and finally a metal back contact.

Even though these technologies are available in the market, they still face major problems such as electronic issues with *a*-Si due to its structural short-range order and dangling bonds which reduces minority charge carrier diffusion lengths resulting in poor device performances. As noted before, CdTe solar cells poses treats due to toxicity of Cd in both the producers and consumers of the final device, and tellurium is rare. Indium and gallium are both rare, toxic, and expensive; making CIGS another undesired PV based technology. Other thin film-based technologies are gallium arsenide (GaAs) and copper zinc tin sulphide/ selenide (CZTS/Se), with the later derived from CIGS technology [1.7, 1.9].

1.4 Third Generation Solar Cells

In contrast to the thin film solar cells, third generation solar cells involve solution processed semiconductors at lower temperatures and at low cost. These includes organic or polymers, inorganic, hybrid, and some nanostructured solar cells [1.6, 1.12, 1.13]. Organic solar cells are based on semiconducting polymer/fullerene blends as the photoactive layer of the device. The first device efficiency of an organic solar cell was reported in 1986 with 1% PCE from a semiconductor bilayer where PCE depended on the interface properties of the two materials [1.7, 1.9, 1.12, 1.13].

The widely studied polymer/fullerene is poly(3-hexylthiophene):phenyl C61-butyric acid methylester (P3HT:PCBM) as an absorber often deposited on a hole transport layer and has achieved PCE of more than 7% [1.7, 1.9, 1.12, 1.13]. Here, P3HT is a p-type polymer material

and acts as donor material, whereas PCBM is an n-type fullerene acting as an acceptor [1.7, 1.12, 1.13]. The conduction band of the organic semiconductor is referred to as the lowest unoccupied molecular orbital (LUMO) and the valence band as the highest occupied molecular orbital (HOMO). During operation of the organic solar cell, light is absorbed by the photoactive blend and an electron-hole pair called exciton is generated within the donor material (P3HT). The photo-excited electron (after the generation) hops from the LUMO of the donor material (P3HT) to the LUMO of the acceptor material (PCBM). This electron will then be collected on the back metal contact usually aluminium and the hole is transferred to the transparent electrode such as ITO through a hole transport layer [1.7, 1.12, 1.13].

The conventional architecture of organic solar cells can be fabricated at low temperatures when employing solution processed charge transport layers. Metal oxides are also employed as charge transport layers for the inverted structure of organic solar cells such as titanium dioxide (TiO₂), zinc oxide (ZnO), and tin oxide (SnO), but this architecture is undesirable due to high temperatures required to prepare these metal oxides. Other different polymers and fullerene derivatives have been tested in organic solar cells to improve on the device efficiency, yielding the highest PCE of an organic solar cell at 16.5% [1.7, 1.9, 1.12, 1.13]. Even though organic based cells can be deposited through solution methods at low temperatures and are environmentally friendly; they produce low efficiencies and both commonly used P3HT and PCBM fullerene are expensive due to their lengthy and complicated purification process.

Another interesting third generation based solar cell technology is the dye sensitised solar cells (DSSC) or Gratzel cell named after its inventor Michael Gratzel [1.6, 1.12, 1.13]. DSSC were developed in the early 1990's as means of reducing photovoltaic technology cost based on c-Si with initial PCE of around 7% [1.12, 1.13]. The solar cell usually composed of a transparent conductive oxide substrate coated with a wide band gap semiconductor

nanomaterial such as n-type TiO₂ or ZnO, or a p-type nickel oxide. A sensitising dye e.g., iodine is coated on the semiconductor nanoparticles and acting as the photo absorber layer. An electrolyte containing redox mediator is also required and the device is completed with a counter electrode such as carbon or platinum [1.7, 1.12, 1.13].

During operation incident photons are absorbed by a dye sensitizer thereby photo exciting electrons from the ground state to the excited state of the dye. The excited electrons are then injected to the conduction band of the semiconductor nanomaterial in which this conduction band lie below the excited state of the dye. These generated electrons are collected by the electrode before they recombine with holes. Due to extensive research in DSSC with optimisation of the dye around the nanomaterials highest device PCE of about 11.9% has been achieved [1.12, 1.13]. The research in DSSC have further led to the discovery of organic-inorganic hybrid perovskite solar cells, which have seen fast increase in record PCE since 2009 [1.12, 1.13].

1.5 Perovskites Solar Cells

1.5.1 Introduction

Organic-inorganic hybrid perovskite thin films are an emerging thin film based semiconducting material competing for the next generation solar cell technologies. These perovskite thin films have been widely investigated in the past few years for applications in solar cells, lasing, light-emitting diodes, and photodetectors [1.14 – 1.16]. Perovskite, which was named after Russian mineralogist L. A. Perovski, was at first referred to a calcium titanium oxide mineral (CaTiO₃) adopting a chemical formula of ABX₃ format as shown in Figure 1.4(a) [1.17, 1.18]. In hybrid organic-inorganic perovskites the structure is slightly altered with ‘A’ position commonly occupied by methyl-ammonium, MA (CH₃NH₃⁺) or formamidinium, FA

($\text{CH}[\text{NH}_2]_2^+$), both organic; or inorganic caesium (Cs^+) monovalent cations. This monovalent cation is enclosed by an octahedral cage of metal cations such as lead (Pb^{2+}) or tin (Sn^{2+}) at ‘B’ position bonded to halide anions, iodine (I^-), chlorine (Cl^-), bromine (Br^-) or their mixtures, occupying position ‘X’ as shown in Figure 1.4(b) [1.17, 1.18]. The common perovskite thin films composition is methyl-ammonium lead iodide, MAPbI_3 ($\text{CH}_3\text{NH}_3\text{PbI}_3$), or mixed halide perovskites such as $\text{MAPbI}_{3-x}\text{Cl}_x$ and $\text{MAPbI}_{3-x}\text{Br}_x$ ($x = 1-2$) [1.14 – 1.18].

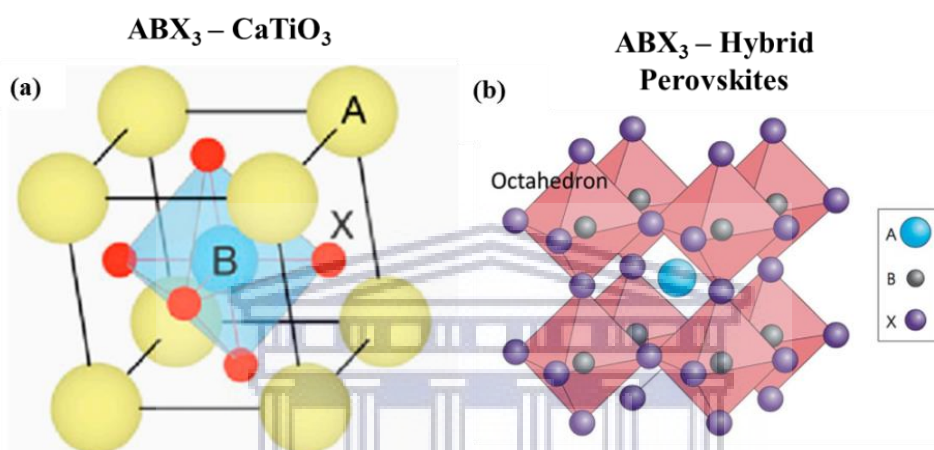


Figure 1.4: (a) Schematic of the oxide-based perovskite (CaTiO_3), (b) the hybrid organic-inorganic perovskite showing the octahedral cage surrounding the A site ion, e.g., MA^+ [1.17, 1.18].

The extensive interest in hybrid perovskites in these recent years, especially for their application in PV technologies, is motivated by their high-absorption coefficients (i.e., high absorption over visible spectrum), long-range balanced charge (electron and hole) transport, low cost, and simple deposition techniques [1.14 – 1.18]. Other impressive properties of these perovskites are their suitable direct band gap that is tunable between 1.5 eV and 2.2 eV, high carrier mobility, and long-range carrier diffusion lengths [1.17]. Single crystalline hybrid perovskite in particular MAPbI_3 and mixed halides counterparts possess a remarkably low trap-

state density and low recombination rates, which is comparable to high quality single crystalline silicon solar cells [1.19].

The research in hybrid perovskite began in 2009 from a report by A. Kojima and co-workers [1.20] where the perovskite compounds $\text{CH}_3\text{NH}_3\text{PbBr}_3$ and $\text{CH}_3\text{NH}_3\text{PbI}_3$ were used as visible-light sensitizers in photo-electrochemical cells, achieving a PCE of 3.8%. Three years later, the efficiency of perovskite based solar cell significantly increased to about 10.9%, as reported by Snaith *et al.* [1.21]. Since then, the research has intensively progressed together with great improvements in lab scale solar cell efficiencies with PCE surpassing 25% based on the data provided by National Renewable Energy Laboratory (NREL) [1.11] as shown in Figure 1.5. This clearly shows that perovskite films have opened doors for a new generation of solar cells, and with further studies and an improved understanding of this material, the drawbacks related to its operational stability will be rectified, allowing cheap and efficient solar cells.

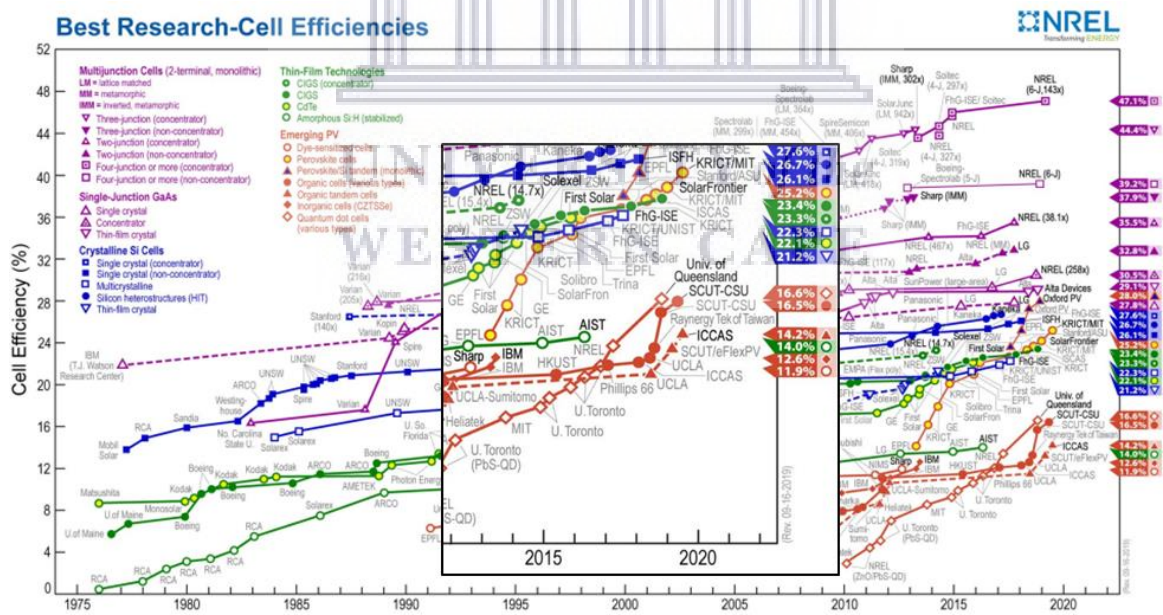


Figure 1.5: National Renewable Energy Laboratory record efficiency chart of all the PV technologies, insert shows a closer view to the recent efficiency records of perovskites [1.11].

1.5.2 Crystal Structure of Perovskites

Organic-inorganic hybrid perovskites are not new material but new in the photovoltaic field [1.22, 1.23]. The structural properties are very important for thin films to assess their crystal quality and X-ray diffraction (XRD) is one of the techniques that can be used for such investigations [1.24, 1.25] Crystal structure properties of this material need thorough investigation as there may be impurities on the deposited films inhibiting device performances.

As showed in Figure 1.4(b) an ideal perovskite such as MAPbI_3 in cubic symmetry the Pb^{2+} is coordinated with six halide anions (I^-) forming eight corner sharing PbI_6 octahedra. Each octahedron is positioned in the corner of a unit cell at position $(h\ k\ l) = (0\ 0\ 0)$ and in this arrangement one Pb^{2+} ion is coordinated with four I^- ions on the equatorial direction (in the same horizontal plane) and two I^- ions on the apical direction (vertical plane) with Pb^{2+} occupying the centre of the octahedron. Further from this arrangement I^- ions are sitting on the face centres of this ideal unit cell occupying the position $(\frac{1}{4}\ \frac{1}{4}\ \frac{1}{4})$. The octahedra cage encloses the MA^+ (CH_3NH_3^+) ion, sitting at the centre of the unit cell at position $(\frac{1}{2}\ \frac{1}{2}\ \frac{1}{2})$ and further coordinated with twelve I^- ions through hydrogen bonding thus forming a cuboctahedron [1.26, 1.27, 1.28].

Discussed above is the ionic coordination in MAPbI_3 perovskite structure according to the cubic symmetry. There are criteria used to estimate the formation of perovskite materials and those are Goldschmidt tolerance factor (t) and the octahedral factor (μ) [1.27, 1.28]. These factors are related to the bond lengths (r) between the MA^+ (at site 'A') and the I^- ions (at site 'X') given by r_{AX} and between Pb^{2+} (as 'B') and 'X' denoted by r_{BX} . The ions are assumed to be touching each other and thus the bond lengths are the sum of the effective ionic radii, where $r_{AX} = r_A + r_X$ and $r_{BX} = r_B + r_X$ [1.27, 1.28].

The Goldschmidt tolerance factor is thus given by:

$$t = \frac{r_{AX}}{\sqrt{2} \times r_{BX}} = \frac{r_A + r_X}{\sqrt{2} \times (r_B + r_X)} \quad \text{eq. (1.1)}$$

And the octahedral factor is:

$$\mu = \frac{r_B}{r_X} \quad \text{eq. (1.2)}$$

Cubic symmetry perovskites are estimated to exist if the Goldschmidt tolerance factor lies between 0.76 and 1.13 but the stability is not guaranteed and thus the range have been lowered to a more probable range between 0.8 and 0.9 based on the effective ionic radii of some of the known perovskite material. Kim *et al.* [1.28] calculated the tolerance factor for the MAPbX₃, where X again is I, Cl, or Br using 180 pm ionic radii for the MA⁺, 119 pm for Pb²⁺ and ionic radii for I⁻, Cl⁻, Br⁻ being 220, 181, and 196 pm, respectively, (1 pm = 1 × 10⁻¹² m). The group obtained tolerance factors of 0.83, 0.85, and 0.84 for X = I, Cl, and Br, respectively, which lies within a good estimation range for perovskites structures [1.28]. To further verify whether the perovskite will form, the octahedral factor must lie between 0.442 and 0.895. Based on the ionic radii given for the previous halides the octahedral factors of I⁻, Cl⁻, and Br⁻ based perovskites would be 0.54, 0.66, and 0.61, respectively, when using equation 1.2 which also lies within the accepted range of possible perovskite formation. With good estimate of the ionic radii of all the specific perovskite ionic composition, the perovskite formation may be estimated from those two equations (eq. 1.1 and 1.2).

Organic-inorganic halide perovskite are known to crystallise in cubic symmetry (space group *Pm3m*) which is the highest and most predictable form via the tolerance and octahedral factor criterions. However, all the MAPbI₃ perovskites tend to transform the crystal phase upon changes in temperature. Cubic which is the highest symmetry phase forms at high temperatures

(above 330 K), transforming into lower tetragonal phase (space group $I4/mcm$) which is stable between 330 K and 161 K, and then lower symmetrical orthorhombic phase (space group $Pbnm$) is stable at very low temperatures (below 161 K) [1.24, 1.26, 1.29, 1.30]. These phase transformations suggest that MAPbI_3 perovskites at room temperature exist in tetragonal phase and may transform into cubic phase during normal operational conditions of the solar cell. The phase transformation was found to influence the calculated band gaps, increasing from ≈ 1.3 eV in cubic phase to ≈ 1.43 eV in tetragonal and ≈ 1.61 eV for the orthorhombic phase [1.24]. During synthesis, the organic-inorganic halide perovskite requires annealing at higher temperature ca. 100 °C and that means the perovskite will crystallise into cubic then transform into lower symmetrical tetragonal phase during cooling. The cubic MAPbI_3 perovskite have lattice constant (a) ≈ 6.3 Å, tetragonal phase has $a = b \approx 8.80$ Å and $c \approx 12.68$ Å, with orthorhombic having $a \approx 8.84$ Å, $b \approx 8.56$ Å, and $c \approx 12.58$ Å [1.24, 1.25].

It is known that during phase transition of MAPbI_3 perovskite from cubic to lower symmetries the octahedral is distorted and tilted by an angle causing the structural changes due to reduction in temperatures [1.29, 1.30]. The lattice parameters show that there is a much stretching of the c -axis during cubic-to-tetragonal phase transformation followed by a slight reduction in this axis during tetragonal-to-orthorhombic phase. In the cubic phase there is a disorder in the MA^+ cation and a slight disorder in the Γ^- halide in which the MA^+ has a free rotation about the C–N (from CH_3NH_3) axis giving it a pseudo-spherical symmetry [1.29, 1.30]. Upon transformation, the Γ^- becomes ordered in tetragonal phase but the MA^+ ion is still disordered, with perfect order allowed in orthorhombic phase and the rotation of MA^+ restricted. It is hence believed that the cause of the phase transformation in perovskites is due to the disorder-to-order changes of the MA^+ cation and that of the Γ^- halide [1.24, 1.26, 1.30]. The ordering of the MA^+ cation and its C-N dipole alignment has also resulted into the

orthorhombic phase being the only stable phase of the MAPbI₃ perovskites and inducing some ferroelectric properties [1.26].

The cause of more structural stability in the orthorhombic phase has also been attributed to the strong bond interaction between the MA⁺ cation and the inorganic matrix more specifically the halide. There are 12 H–I bonds (hydrogen from MA⁺ cation and iodide in the octahedra) for the orthorhombic phase compared to 6 H–I bonds in the tetragonal phase [1.30]. Similarly, the weak interaction between the hydrogen and the iodide in the PbI₆ octahedral may be the trigger of the disorder and thus structural instability in the higher symmetrical MAPbI₃ phases. The reason for this weak interaction is that hydrogen bonds more strongly on the more electronegative nitrogen and carbon and weaker on the less electronegative iodine. These conditions are relaxed in the orthorhombic phase which may be due to the reorientation and distortion on the structure.

Quarti *et al.* [1.29] however observed no major effects on the properties of MAPbI₃ and MAPbI_{3-x}Cl_x upon phase transition from cubic to tetragonal and visa-versa. They carried through their investigations by means of UV-Vis absorption measurements and based on the external quantum efficiency measurements. No major differences were observed on the absorption spectra of the cubic as compared to that of tetragonal. They observed a slight gradual change in band gap from about 1.62 to 1.65 eV over the change in temperature from 290 to 400 K which is the range of the tetragonal-to-cubic phase transformation. The results were based on their calculation and experimental results [1.29]. It was mentioned somewhere [1.24] though that the structural changes should influence the band gap of this material leading to an influence on its photovoltaic performance. It is in essence important to investigate these structural phase transformations especially for the iodide-based perovskite as its tetragonal to cubic phase transformation temperature is within the operating temperatures of the PV devices.

Crystal structure evolution and organic-metal halide perovskite conversion during synthesis are mainly investigated by means of XRD technique without any distractions to the thin films. In most reports the XRD diffraction peaks of the MAPbI₃ films are assigned to the tetragonal (*I4/mcm*) structure which exist at room temperature [1.20, 1.31 – 1.33] even though others indexed their XRD patterns to the orthorhombic (*Pbnm*) phase [1.21, 1.34 – 1.36]. Mixed halide perovskite (MAPbI_{3-x}Cl_x) also crystallises with either tetragonal or orthorhombic with similar XRD diffraction patterns as the MAPbI₃ [1.37–1.39]. Bhachu and co-workers [1.40] reported on the existence of cubic MAPbI₃ with XRD measurements taken after deposition and cooling to room temperature of the thin film, but the tetragonal phase was realised after several days of storage in a dry box as shown in Figure 1.6(a).

Baike *et al.* [1.25] also reported on calculated XRD patterns emphasising more on the difference between cubic and tetragonal phases, Figure 1.6(b). The group elaborated that the (211) XRD peak at about 23° 2θ is inconsistent with cubic symmetry and thus shows the existence of a tetragonal phase similar to XRD results reported by Bhachu *et al.* [1.40]. XRD is also used to assess the perovskite conversion level during deposition by tracking the presence of impurities on the final film such as lead iodide (PbI₂) or the existence of excessive methylammonium iodide (MAI) and MAPbCl₃ on mixed halide perovskites [1.41, 1.42].

The absence of these impurities usually inferred to a good quality of the deposited perovskite films; similarly, their presence either demonstrates incomplete conversion or poor film quality [1.41]. The presence of these impurities in their respects has bad impact on solar cell device performance even though presence of PbI₂ has been demonstrated to be helpful in passivating perovskites grain boundaries [1.35]. These impurity-based peaks especially PbI₂ peak has also been used to investigate the stability of the perovskite films where the appearance of this peak on XRD data after storage of the films shows that the perovskite is degrading [1.43].

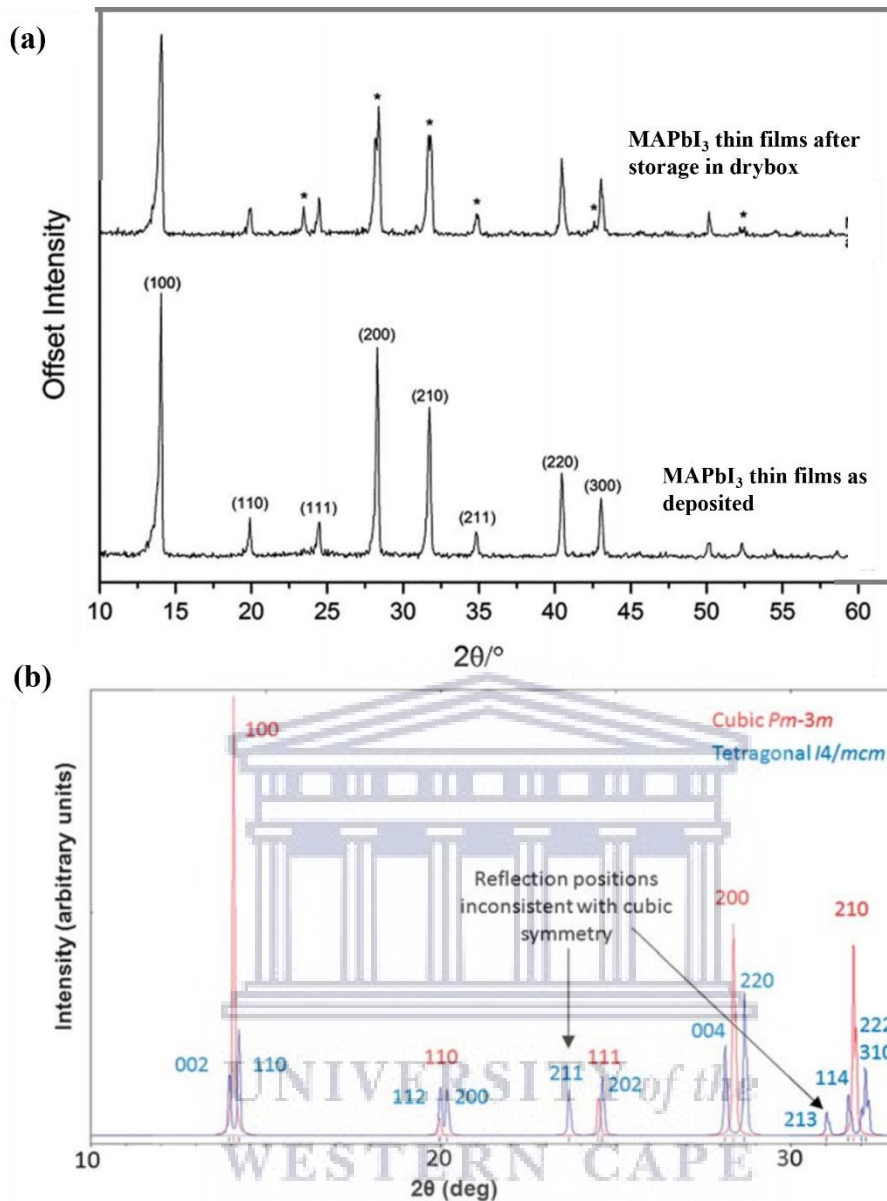


Figure 1.6: (a) Measured X-ray diffraction of as-deposited MAPbI₃ perovskite film in cubic phase (bottom pattern) and after transformation to tetragonal phase during storage (top pattern) [1.40], (b) calculated XRD pattern showing existence of tetragonal peaks, inconsistent with cubic symmetry [1.25].

Level of crystallinity and the size of crystal grains are usually investigated by means of XRD where sharper peaks suggest increased grain size and higher intensities showing good crystallinity with excellent orientation of grains [1.44]. These changes are usually traced on the

full width at half maximum of the most intense peak in which for tetragonal MAPbI₃ would be the (110) peak and the changes may be investigated upon change in annealing temperature or during storage of thin film samples [1.44].

There are few publications in literature reporting on the use of transmission electron microscopy (TEM) to investigate these organo-metal halide perovskite absorbers by means of high resolution-TEM (HR-TEM). The limitations on the use of HR-TEM are due to the difficulties in avoiding sample damages by an electron beam due to fragile and instability nature of hybrid perovskites [1.45 – 1.50]. Extra attention is required when preparing samples for TEM characterisation of MAPbI₃ as the long-time exposure to high voltage electron beam may destroy the thin film leading to its decomposition into PbI₂ and MAI. Focused ion beam milling employing gallium source has been used to obtain the cross sections of the thin films which are also used to probe atomic scales of these thin films and the studies have been carried through successfully without major damages on the thin films [1.45 – 1.50].

1.5.3 Optical Properties of Perovskites

Optical characteristics of semiconductors for photovoltaic application are of most importance to investigate as optical properties describes the material interaction with light. High light absorbance of a thin film can have a positive impact on the final device performance. Optical band gap of the semiconductor may be estimated from the measured optical response (absorbance, transmittance, or reflectance). Measurements of optical behaviour of hybrid perovskites are as well important as they can be linked to the device performances. Optical absorption measurements are usually conducted through UV-Vis spectroscopy, spectroscopic ellispometry, and photo-thermal deflection spectroscopy. Light absorbance per film thickness i.e., absorption coefficient is a proper optical parameter that can be used to quantify the absorbance of the film. Other important optical measurement for hybrid perovskites is the light

induced charge carrier emission and transfer, measured through photoluminescence (PL) spectroscopy.

Organic-inorganic hybrid perovskites thin films have broad band absorption over the entire visible range of the spectrum. This wide absorption range is accompanied by high absorption coefficient as shown in Figure 1.7(a) with values ranging between 2.5 and 9 μm^{-1} at about 2 eV varying according to different reports as compiled by Green *et al.* [1.51]. The absorption coefficient increases significantly at higher energies (about 3.5 eV) with values around 40 to 50 μm^{-1} .

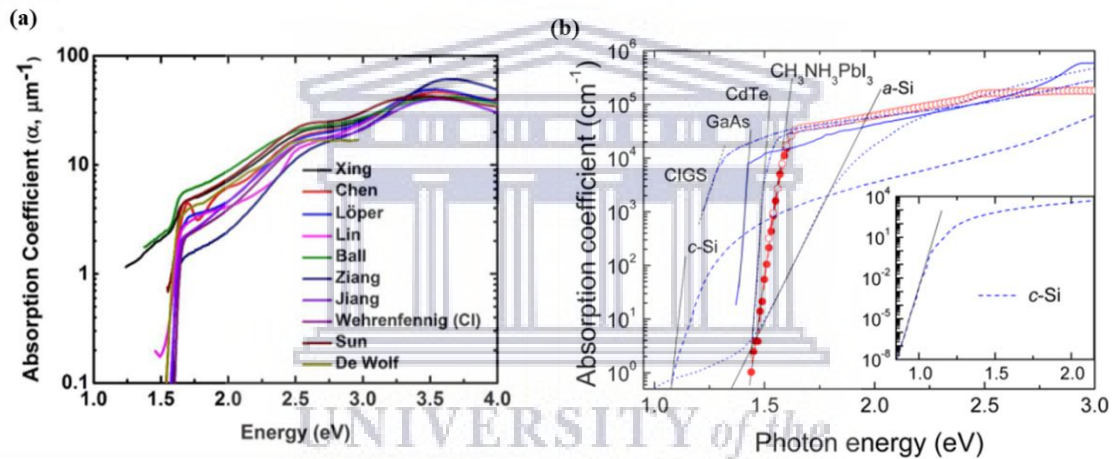


Figure 1.7: (a) A comparison of MAPbI_3 perovskite film absorption coefficients as measured by different groups [1.51], and (b) perovskite absorption coefficient compared to other market related semiconductors materials [1.52].

These absorption coefficients spectrums (Figure 1.7(a)) show a common absorption band edge of about 1.6 eV which is a common optical band gap of MAPbI_3 perovskites [1.51]. Interestingly, MAPbI_3 perovskite thin films are highly comparable to the high quality and mature CIGS and CdTe thin films and possess higher absorption coefficient than GaAs, a-Si, and c-Si for energies less than 2.25 eV as shown in Figure 1.7(b) [1.52]. The high absorption

coefficient of perovskite thin films and the direct band gap nature shown by the sharp absorption edge as seen in Figure 1.7(a) and (b) are some of the excellent properties that have led to the high device performances reported for this class of material.

Even though MAPbI₃ perovskite is formed through the incorporation of the CH₃NH₃⁺ (MA⁺) ion within the PbI₂ network, the band structure composes of the contributions from lead and iodine electronic states [1.51 – 1.56]. The perovskite valence band maximum (VBM) is associated with the in-plane 5p orbitals of iodine anti-bonded (out-of-phase) with Pb 6s orbitals, whereas the conduction band minimum (CBM) is associated with Pb 6p orbitals forming antibonding states with I 5p orbitals as shown schematically in Figure 1.8 [1.51, 1.54]. For clarity, valence band (VB) is the lowest occupied energy band level of a semiconductor and conduction band (CB) is the highest partially occupied energy band level.

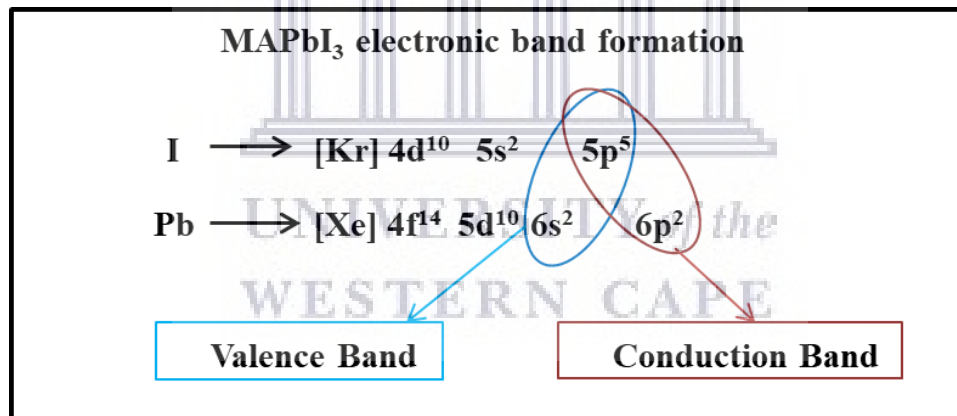


Figure 1.8: Schematic representation of the antibonding contributions between the iodine and lead forming the MAPbI₃ perovskite band gap [1.51, 1.54].

It has been shown via theoretical calculations that the VBM is dominated by I 5p states with a small contribution from the Pb 6s states; similarly, the CBM is dominated by Pb 6p states with small contribution from I 5p states [1.53, 1.54]. The contribution of Pb 6s states (with angular momentum quantum number $l = 0$ for s orbital) in the VBM and Pb 6p states ($l = 1$) in

the CBM shows a possibility of a strong optical transition between VBM and CBM with change in $l = 1$, which may also be related to the strong optical absorption by this material [1.53]. These orbital contributions to the VBM and CBM also shows that an electron will be excited from the I 5p orbital to the Pb 6p orbital during low energy transitions [1.51].

The organic cation (MA^+) does not contribute directly to the electronic or optical properties of MAPbI_3 perovskite semiconductors but influence the size of the band gap [1.55]. This is because the MA^+ electronic states are located far outside of the band gap (about 4 eV away from the Fermi level, both below VB and above CB) hence no contribution [1.54, 1.55]. The influence it provides towards band gap is distorting the octahedral network in result modifying the Pb–I–Pb bond angles and lengths in which that alters the band gap [1.54]. It has been reported that cations of different sizes can be used to tune the band gap as various cation sizes will distort the lead halide octahedron differently [1.54]. For instance, the use of a bigger cation FA^+ instead of MA^+ resulted into a reduced band gap, similarly the substitution with a smaller cation Cs^+ lead to a wider band gap [1.56].

It has been shown via measurements that these organic-inorganic perovskites have a direct band gap with a very sharp band edge [1.51]. The CBM and the VBM occur at the centre of the Brillion zone, Γ -point (0, 0, 0) for the room temperature stable tetragonal MAPbI_3 . For the higher temperature cubic MAPbI_3 phase the direct band gap is situated at the R-point ($\frac{1}{2}$, $\frac{1}{2}$, $\frac{1}{2}$) away from the Brillion zone centre [1.51, 1.53]. The knowledge and understanding of the optical band gap and electronic structure can help in optimising perovskite composition for different applications especially the metal and the halide composition.

1.5.4 Deposition Methods of Perovskites Solar Cells

1.5.4.1 Introduction

Deposition technique for every material plays a huge role on the final properties of the material. It is the same for perovskite thin films as the deposition conditions determine the film quality and properties. Thus, it is highly important to gain in-depth understanding of these deposition approaches to control film quality and properties. There are several deposition techniques that have been developed and tested over the past few years for the preparation of perovskite thin films dominated by spin coating from a precursor solution and vapour deposition [1.14 – 1.18]. These deposition methods are employed as one-step deposition for its ease or two-step sequential deposition for better control of film properties. In this section, spin coating from a solution during one-step and two-step will be briefly discussed, followed by a combined spin coating and vapour deposition, then thermal evaporation at high vacuum and the use of chemical vapour deposition (CVD) systems will be discussed in detail.

The different perovskite solar cell device architectures and energy band alignment are shown in Figure 1.9. In brief a hybrid perovskite solar cell is composed of a transparent conducting oxide (TCO) electrode on glass followed by a charge (electron or hole) transport layer, a perovskite absorbing layer, another charge transport layer, and finally a metal electrode as back contact (Au, Ag, or Al). Similar to organic solar cells, hybrid perovskites have two device structures, namely: n-i-p structure, Figure 1.9(a) and (b), and its inverted structure counterpart, p-i-n, Figure 1.9(c). In this terminology, ‘n-i-p or p-i-n’, ‘n’ stands for n-type layer (ETL), ‘i’ for intrinsic layer (absorber layer), ‘p’ for p-type layer (HTL). The n-i-p architecture has a fluorine doped tin oxide (FTO) on glass, followed by an electron transport layer (ETL), perovskite layer, hole transport layer (HTL), and finally metal contact. For the p-i-n, indium tin oxide (ITO) is usually preferred followed by a HTL, then perovskite, ETL, and finally metal back contact [1.14 – 1.18]. The name n-i-p is used when the light passes through the ETL

before being absorbed by the perovskite; same for the p-i-n where light passes through the HTL before absorption.

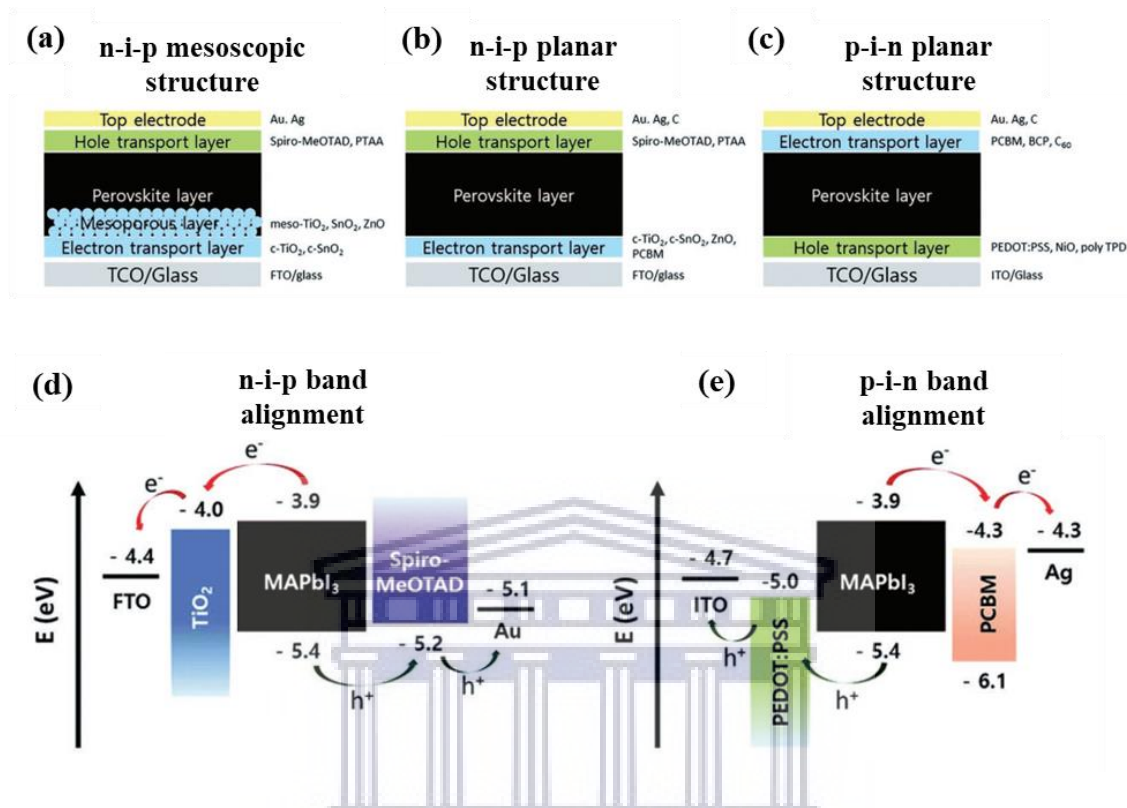


Figure 1.9: (a)–(c) Different hybrid perovskite solar cells architectures including (a) mesoscopic; (b) primary planar structure; (c) inverted planar structure. (d) and (e) Energy band alignment of the n-i-p and p-i-n architectures, respectively [1.14 – 1.18].

High device performances have mainly been achieved from the use of mesoscopic electron transport layer due to the enhancement of the perovskite/ETL interface area as shown in Figure 1.9(a) [1.16, 1.17]. Frequently used charge transport layers are also provided in Figure 1.9(a) – (c) even though the use of titanium dioxide (TiO₂) layer has dominated the research as both a compact layer and a mesoscopic layer for n-i-p architectures [1.14 – 1.18, 1.57]. The mostly used HTL for this structure is a small organic material called 2,2,7,7-tetrakis (N,N-di-methoxy-phenyl amine)-9, 9-spiro-bifluorene (Spiro-MeOTAD). Likewise, for p-i-n frequently used

ETL and HTL are organic materials such as [6,6]-phenyl-C61-butyric acid methyl ester (PCBM) and poly(3,4-ethylene dioxythiophene):polystyrene sulfonic acid (PEDOT:PSS) [1.14 – 1.18, 1.58, 1.59].

Figure 1.9(c) and (d) depicts the device energy band alignment and how the generated charge carriers (electrons and holes) move towards the two electrodes (FTO/ITO and Au/Ag) passing through the transport layers. These two figures summarise the perovskite device physics where electrons (e^-) and holes (h^+), called electron-hole pairs, are generated on the absorber layer during its exposure to light. These electron-hole pairs get separated and the electron will be injected to the ETL (e.g. TiO_2 or PCBM) due to the energy gradient between this layer and the absorber layer as shown on the left hand side of Figure 1.9(d) or right hand side of Figure 1.9(e) and collected by the electrodes (FTO or Ag). Similarly, generated holes are injected to the HTL (such as Spiro-MeOTAD or PEDOT:PSS) and eventually collected by the electrodes (ITO or Au). For efficient charge transport properties an excellent ETL needs to be a good hole blocking layer and an excellent HTL is similarly required to be a good electron blocking layer. Furthermore, an intimate contact between these transport layers and the perovskite absorber is required to reduce charge accumulation at the interfaces [1.14 – 1.18, 1.57 – 1.59].

1.5.4.2 Spin Coating Deposition

Spin-coating from a solution deposition method is a primary and the most studied technique for perovskite film deposition and most of the perovskite record device efficiencies have been achieved through this method. The method has gained an increasing interest because of its easiness to process at low cost allowing fast optimisation of the film and the final device. Perovskite films can be prepared by one-step spin coating from a solution of metal halide e.g., PbI_2 and organic halide, MAI for example, both dissolved from a common solvent. For better

control of film properties two-step sequential deposition method of PbI_2 followed by MAI to form MAPbI_3 perovskite is used [1.16 – 1.20, 1.31, 1.57 – 1.63].

Figure 1.10(a) illustrates a typical one-step spin coating method of the perovskite precursor solution [1.61, 1.64]. The metal halide powder (PbI_2) and organic halide salts (MAI) are different compounds and as a result dissolve differently. To obtain high quality films (continuous) these compounds need to be thoroughly dissolved in a solvent. Commonly used solvents for perovskites includes but not limited to, are N,N-dimethylformamide (DMF), dimethyl sulfoxide (DMSO), and γ -butyrolactone (GBL) amongst others [1.60, 1.65]. The perovskite precursor compounds may be dissolved in one of these solvents or in their mixtures for the desired film control. The precursor solution is usually spin-coated on FTO coated with either mesoporous or compact planar metal oxide layer (TiO_2) substrates [1.60].

Mesoporous scaffolds are commonly employed in conjunction with compact ETL allowing easy infiltration of the precursor solution, forming a continuous film with no pin-holes compared to using a compact ETL alone. After spin coating, the semi-wet films are dried on a hot plate at a temperatures range of 100–150 °C and standard room pressure for a varied time. This annealing step is used to crystallise the film forming a dense and pin-hole free perovskite phase. It was reported by Kojima *et al.* [1.20] that the spin-coated mixed precursor on the substrate changed colour upon annealing becoming black which indicated a formation of a perovskite thin film in a solid state. It is a standard procedure to use an equimolar ratio of PbI_2 :MAI i.e. (1:1) during one-step spin coating from a solution [1.65]. Due to high crystallization rate of MAPbI_3 during annealing the film usually results to poor surface coverage and high roughness thus leading to limited device performances.

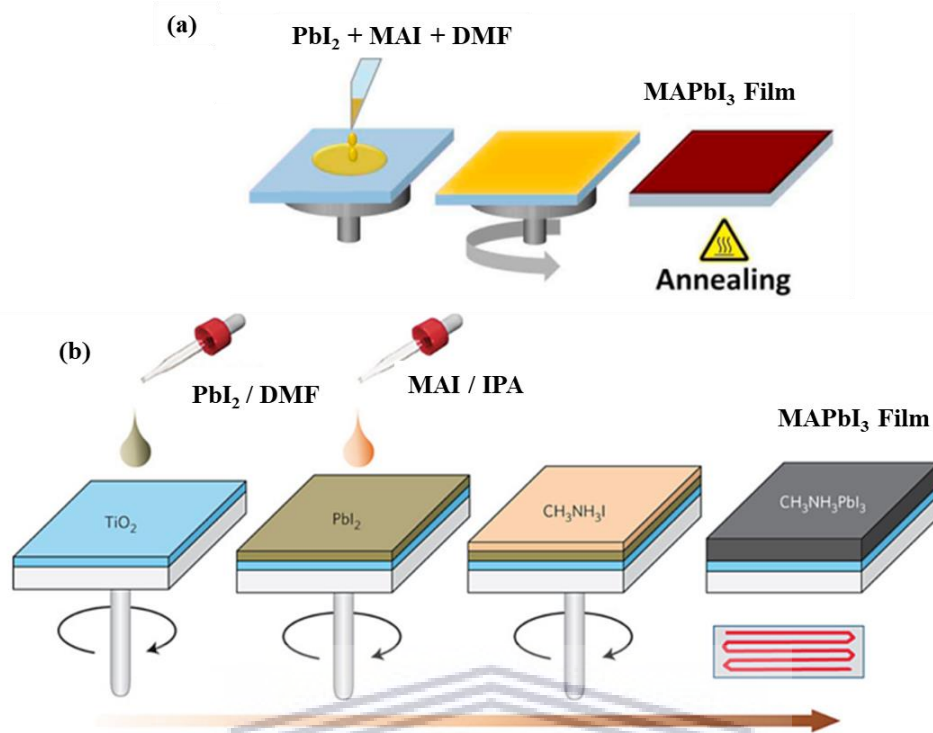


Figure 1.10: (a) Schematic representation of one-step and (b) two-step sequential spin-coating deposition from a solution of perovskite precursors [1.61, 1.64].

Different strategies have been proposed to solve the issue of poor coverage such as anti-solvent annealing and deposition of mixed halide perovskites such as $\text{MAPbI}_{3-x}\text{Cl}_x$. The mixed halide perovskite is usually prepared from a PbCl_2 precursor dissolved with an excess of MAI in molar ratio of 1:3 for PbCl_2/MAI [1.65]. Mixed halide perovskite has been reported to improve surface coverage and enhanced the device performances even though it is difficult to quantify the composition of Cl dopant [1.61, 1.65]. Anti-solvent annealing does not only improve on surface coverage but also increases grain size significantly compared to a standard annealing procedure. Anti-solvent annealing is usually carried out by placing a solvent such as DMF next to the perovskite thin films while heating on a hot plate, with the source of the solvent and the samples covered by a petri-dish. This allows the precursor ions to diffuse further into the film and hence increase grain size and crystallisation [1.61].

The choice of solvent also plays a major role in perovskite film morphology. Heo *et al.* [1.63] compared DMSO and DMF solubility in MAPbI₃ and found that DMF has less solubility as compared to DMSO unless an additive was used. They mixed DMF with hydroiodic acid (HI) to reduce pinholes in the perovskite film. The group further observed that a film prepared using DMSO solvent had bigger crystalline domains compared to a film prepared from a mixed DMF and HI which had no domains at all but continuous. This showed that an additive of HI improved the film uniformity. It was also reported by this group that the spin-coated solution spread out on the substrate due to centrifugal force and the perovskite crystallised from the outer edges and towards the centre of the substrate due to evaporation of the solvent during annealing [1.63].

To further gain control over the perovskite film morphology a two-step spin coating method was initiated by Burschka *et al.* [1.66]. Morphological variations found in perovskite deposited by one-step synthesis which limited cell efficiency forced researchers to look for an alternative way of deposition. This is mainly because it is much easier to gain morphological control when lead halide layer is pre-deposited. Further, morphology and crystal structure of this layer has decisive impact on the final perovskite properties. In general, the PbX₂ (X = I, Cl, or Br) dissolved in a solvent is first spin-coated on a substrate forming a thin layer of PbX₂ as shown in Figure 1.10(b) [1.61, 1.66, 1.67]. Second step is to spin-coat or a dip the PbX₂ coated substrate in MAI dissolved in isopropanol (IPA) for conversion to perovskite. Tang *et al.* [1.67] spin coating PbI₂ at 3000 rpm and 6000 rpm both for 5 sec and carried a two-step annealing at 70 °C and 100 °C both for 5 minutes. They then deposited MAI via spin-coating at 4000 rpm for 25 secs and annealed at 100 °C for 5 minutes for a complete conversion to perovskite phase. The conversion to perovskite happens as soon as the two components (PbX₂ and MAI) come into contact during their reaction. Crystal structure together with morphology evolves during

annealing, and that make annealing one of the crucial post-deposition step for spin coating method [1.61].

Type of solvent and additives again also plays an important role on improving the quality of the pre-deposited lead halide layer and the final device performance. For example, PbI_2 dissolved from DMSO resulted into an amorphous layer with uniform crystal grains but the resulting perovskite performed poorly as compared to when the DMF was employed [1.67]. A small amount of H_2O (2% wt.) with DMF was used to dissolve PbI_2 resulting on a dense and pin-hole free, smooth PbI_2 layer with high surface coverage (Figure 1.11(a)) leading to a dense and homogeneous perovskite film with large grains as shown in Figure 1.11(b) [1.68]. This was attributed to the fact that H_2O mixed with DMF had a better solubility parameter allowing a complete dissolution of PbI_2 and hence improving perovskite crystallisation.

The PCE was improved from less than 1% without additive to about 18% with additive as shown in Figure 1.11(c) demonstrating the importance of perovskite film morphology [1.68]. High external quantum efficiency was also measured showing efficient use of photo-generated charge carriers as shown in Figure 1.11(d) [1.68]. Two-step sequential solution deposition has been used to improve on the one-step deposition as it allows better film quality and uniformity. However, this method requires a use of mesoporous or nanostructured metal oxide layers such as TiO_2 , Al_2O_3 , or ZrO_2 and there are few successes of this method on planar heterojunction perovskite cells [1.34]. Due to these constraints in one-step and sequential deposition processes further methods for the deposition of perovskite thin films need to be explored.

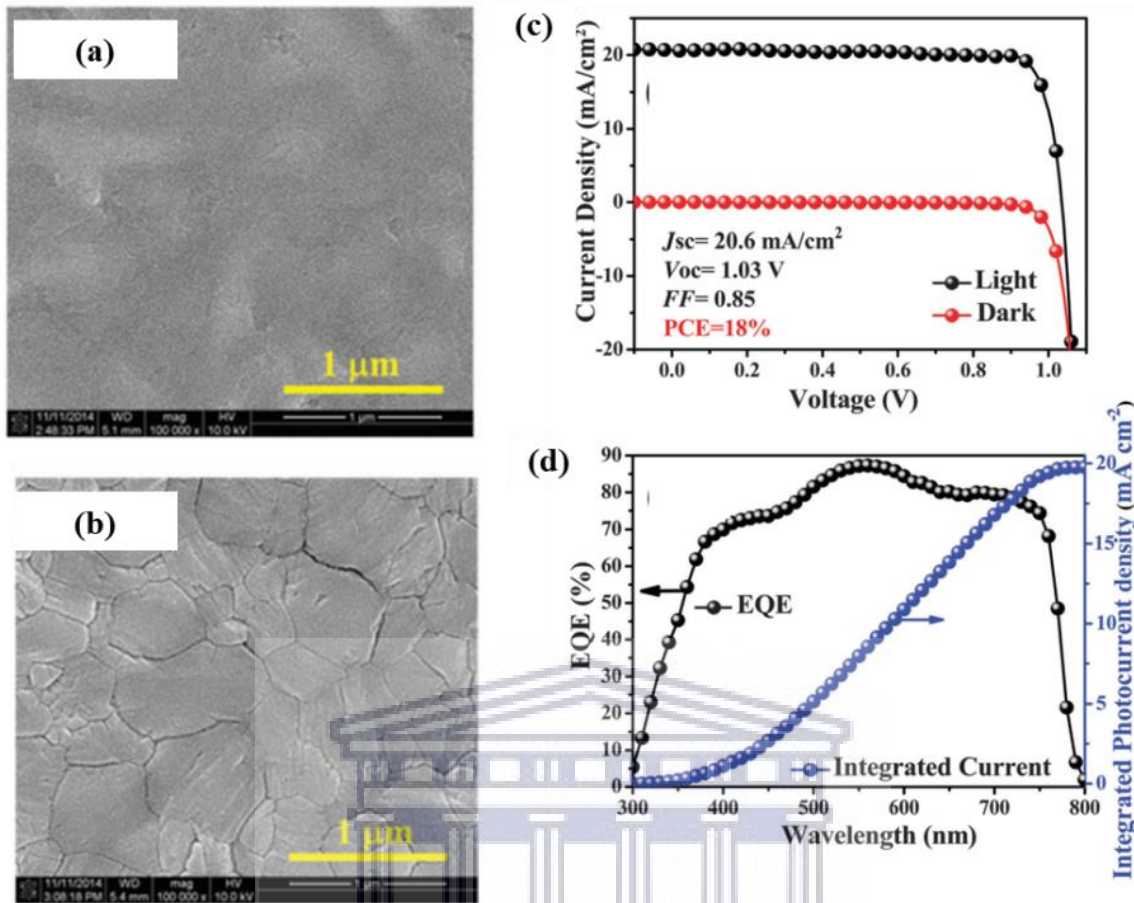


Figure 1.11: SEM planar micrographs of (a) PbI₂ film and (b) perovskite layer through modified two-step spin coating; (c) corresponding current density-voltage curve of the best device, and (d) its external quantum efficiency and integrated current density [1.68].

1.5.4.3 Vapour-Assisted Solution Deposition

Vapour-assisted solution process (VASP) is a modified two-step spin coating method but with the second step (conversion) performed through vaporised organic halide (MAI) [1.18, 1.34, 1.69 – 1.72]. This deposition method was developed by Chen *et al.* [1.34] where PbI₂ layers were deposited via spin coating on a compact TiO₂ layer followed by a conversion to perovskite through MAI vapour in a glove box for the preparation of planar perovskite solar cell devices as shown in Figure 1.12(a). Even though large grains (with micron size) of

perovskites were obtained with full coverage and free of voids and pin holes, the conversion required longer time (over 2 hours) to complete, compared to one-step and two-step spin coating.

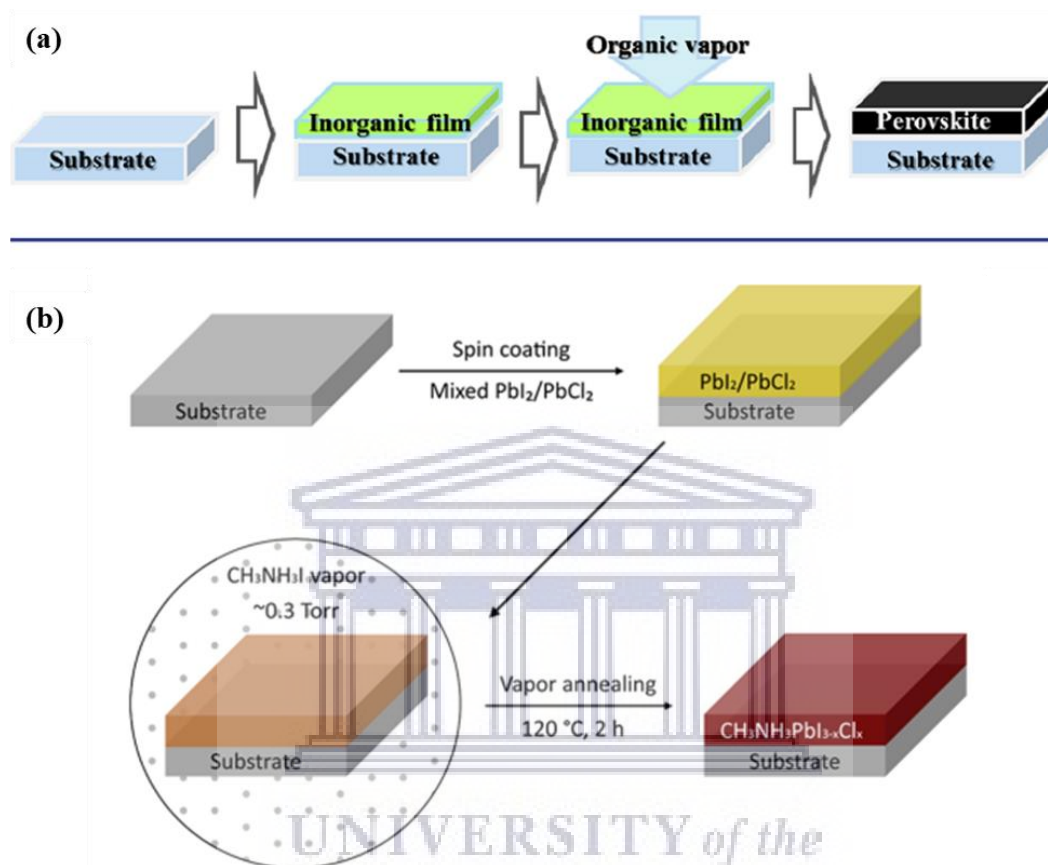


Figure 1.12: (a) Schematic of the first vapour assisted solution process (VASP) [1.34] and (b) low pressure derivative of VASP [1.70].

During this VASP process MAI powder was spread on the surface of the spin coated PbI_2 films and covered the samples with a glass petri dish and heated the sample at $150\text{ }^\circ\text{C}$ in N_2 atmosphere for different times (0 to 4 hours) for in-situ reaction [1.34]. No traces of PbI_2 impurities were observed confirming the full conversion of the layers to perovskite. Large grain sizes up to a micron as shown in Figure 1.13(a) were realised and attributed to volume expansion of the perovskite phase during transformation from pre-deposited PbI_2 . The group

achieved the best performance of a planar perovskite cell with PCE up to 12.1% [1.34]. Later, Sheng and others [1.69] reported on their deposition of MAPbBr₃ perovskite via vapour assisted method but they employed mesoporous TiO₂. They argued that even though it was possible to effectively deposit perovskite without the use of these meso-structures they are beneficial on the performance of the perovskite-based cells as they enhance surface coverage.

The VASP method has also been adopted for the preparation of mixed halide perovskite (MAPbI_{3-x}Cl_x) but at relatively low pressure [1.70] compared to the first use which was done at atmosphere [1.34]. Y. Li and co-workers [1.70] spin coated a mixture of PbI₂ (0.8 M) and PbCl₂ (0.2 M) in DMF solution and converted the films under MAI vapour at 120 °C for 2 hours at a pressure of ~0.3 Torr [1.69] as shown in Figure 1.12(b). Again, longer conversion time duration was required for the complete formation of perovskite. Nevertheless, improved device performance was achieved with PCE of 16.8% attributed mainly to the incorporation of chlorine on the film [1.70]. More recent advances on VASP method have seen record efficiencies of 18-19%, Figure 1.13(b), for small device areas due to modification of the PbI₂ spin coated layer [1.71, 1.72].

Even though Chen and co-workers [1.34] managed to deposit perovskite without the use of mesoporous metal oxides and achieved higher performances, this technique still faces some problems. The problem is on the spin coated PbX₂ layer which require absolute dissolution of the powder and spin coating method is not repeatable and that hinders upscaling and commercialisation. The process time for VASP shows to be another obstacle as it requires more than two hours of annealing for the formation of pure phase perovskites and that is another problem that needs to be solved. So, it is vital to look for other ways that may avoid the use of solution deposition but keep the growth price effective and allows for the up scaling.

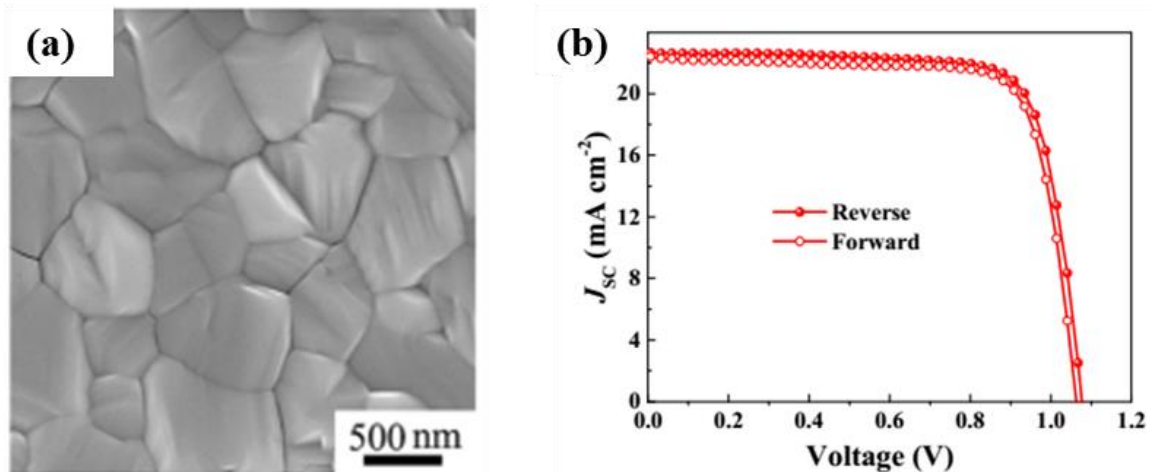


Figure 1.13: (a) Planar SEM of the first ever perovskite film by VASP [1.34], (b) current density-voltage (J-V) curve of one of the best reported solar cell device performance by VASP [1.71].

1.5.4.4 Vacuum Thermal Evaporation

Vacuum thermal evaporation is a type of physical vapour deposition referring to a thermal evaporation of precursor powders under vacuum pressures i.e., below 10^{-5} mbar (10^{-3} Pa). The generated vapour during evaporation moves away from the heated source boat and condenses on cooler substrates and chamber walls. The low pressure elongates mean free path of the evaporated source molecules allowing a continuous and uniform deposition on the substrates. Thermal evaporation systems are usually equipped with film thickness monitors situated close to the substrates, advantageous for film reproducibility. Vacuum deposition method has been employed more in thin film depositions and has shown its throughput in perovskite thin film depositions [1.16, 1.17]. There are two main methods that have been developed for perovskites deposition, namely: co-evaporation and two-step sequential evaporation.

Liu *et al.* [1.37] deposited thin films of mixed halide perovskite for the first time using a dual-source vapour deposition method obtaining a PCE of 15.4% as shown in Figure 1.14.

They co-evaporated PbCl_2 and MAI from two different sources under ultrahigh vacuum of about 10^{-5} mbar, Figure 1.14(a). The group elucidated that this method offer control over film thickness as this is one of the prerequisites of high performing perovskite solar cells. Inside the vacuum chamber they placed two crucibles with PbCl_2 and MAI heated to above the sources sublimation temperatures of $325\text{ }^\circ\text{C}$ and $120\text{ }^\circ\text{C}$, respectively, as to remove residual impurities before deposition. FTO glass substrate coated with a thin compact layer of TiO_2 was position a distance away from the sources and kept at room temperature, rotated for 5 minutes to form a uniform film thickness. The group deposited flat, dense, and uniform perovskites with complete surface coverage, shown in Figure 1.14(b) and compared that to a film deposited by spin-coating method which was non-uniform with incomplete coverage as shown in planar SEM micrograph of Figure 1.14(c) [1.37].

A group led by Graetzel [1.73] deposited MAPbI_3 via the same method through an evaporation of PbI_2 and MAI sources for the preparation of an inverted perovskite solar cell with the use of organic transport layers. This group employed relatively low source temperatures compared to Liu *et al.* [1.37] and they also scaled up the device to 0.98 cm^2 with an efficiency of about 8%. In both reports there was no post deposition annealing performed to crystallise the perovskites films even though the substrates were kept at room temperature during deposition. This means during vacuum evaporation; intercalation reaction takes place when the vapours condense on the substrate surface forming a perovskite phase. These non-annealed films are usually smooth with low surface roughness, advantageous for the deposition of charge transport layer on top of the perovskite layer. There have been many studies on the co-evaporation of perovskite precursors and after many optimisations the PCE has reached 20% comparable to some of the spin-coated device performance [1.16, 1.17, 1.74].

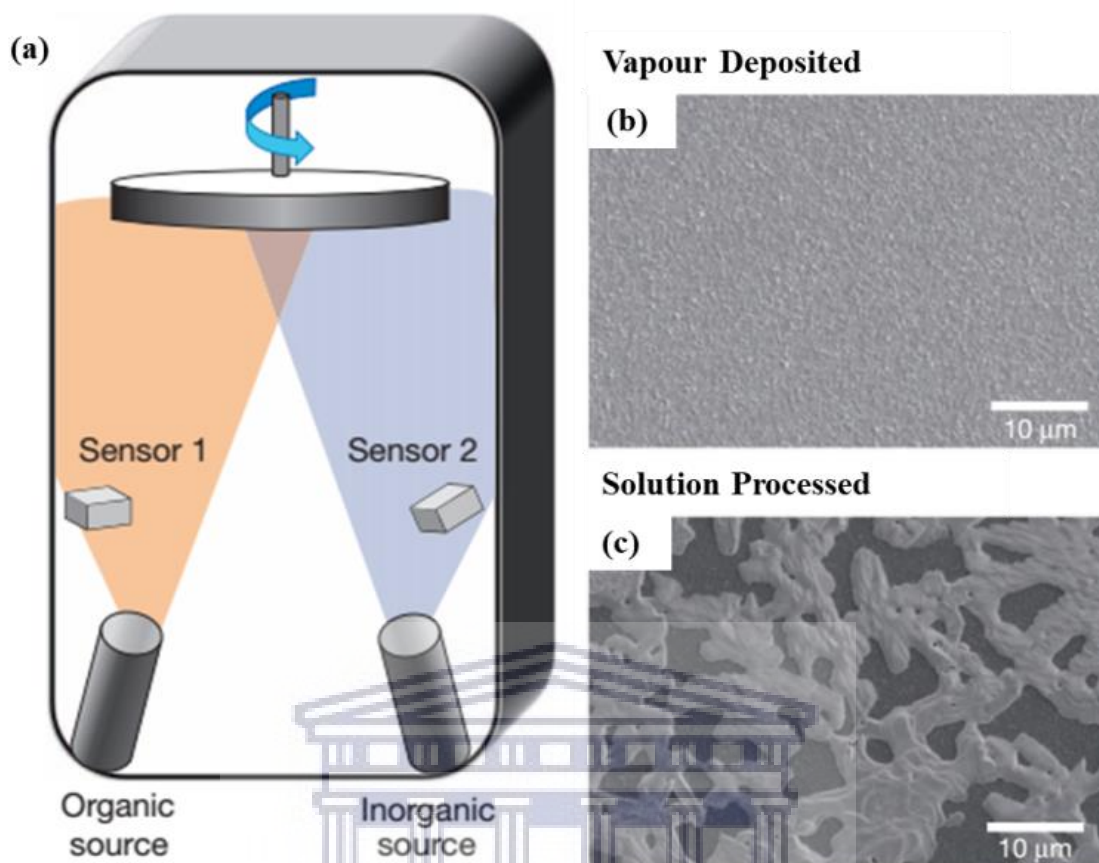


Figure 1.14: (a) Schematic representation of a vacuum thermal co-evaporation from Pb halide and MAI sources; (b) and (c) are the low magnification SEM micrographs of thermally evaporated perovskite film and spin coated one, respectively [1.37].

The problem in co-evaporation of PbX_2 and MAI lies in the difficulty to control the quality of the lead halide which affects the final quality of the perovskite. This difficulty arises from the requirement to simultaneous and careful control of source evaporation rates to achieve uniform and stoichiometric composition of the film. Two-step sequential evaporation of the precursors is one way of avoiding such complications during vacuum evaporation. Chen *et al.* [1.38] reported for the first time on the sequential deposition of perovskite via thermal evaporation.

This group evaporated PbCl_2 on a mesoporous free substrate followed by evaporation of MAI source in the second step to prepare $\text{MAPbI}_{3-x}\text{Cl}_x$ perovskite films as shown in Figure 1.15(a) [1.38]. They deposited extremely smooth and uniform films of PbCl_2 with full coverage and sublimated MAI on top which in-situ reacted with the pre-deposited metal halide forming a uniform and dense perovskite film over large area, Figure 1.15(b). The substrate temperature during PbCl_2 deposition was kept at room temperature but raised to 65, 75, and 85 °C during MAI sublimation with post annealing performed at 100 °C under vacuum. Films deposited at room substrate temperature had poor conversion and that resulted to poor device performance. A best 15.4% device performance was realised for the substrate temperature of 75 °C [1.38].

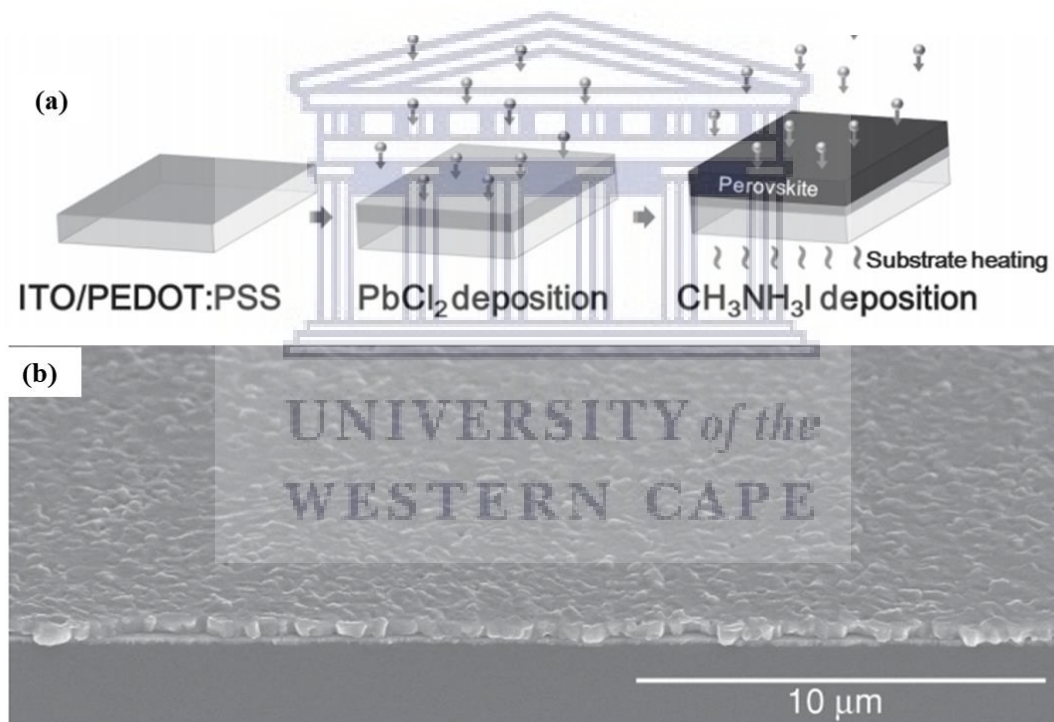


Figure 1.15: (a) Schematic diagram of the sequential thermal evaporation (vacuum deposition) method, (b) SEM micrograph of the resulting perovskite film over large scale [1.38].

This sequential deposition method has also been used to prepare MAPbI_3 perovskite solar cells with sequential sublimation of PbI_2 and MAI sources. Ng *et al.* [1.75] deposited seven

alternating stacks of PbI_2 (50 nm) and MAI (50 nm) achieving a final perovskite thickness of ~470 nm with surface roughness of ~20 nm. Post deposition annealing was also performed by this group at 90 °C for an hour under nitrogen ambient and achieved best device performance of 11.4% [1.75]. Even though the vacuum deposition technique offers good quality perovskites with good uniformity and high surface coverage only few groups have reported on this method compared to solution methods. The major drawback on this technique is the requirement of ultrahigh vacuum systems which hinders large scale production of perovskite based solar cells at low cost. Another drawback on this technique is the difficulty in controlling the diffusion of MAI molecules inside the vacuum chamber due to their low molecular weight. This requires a long-time optimization of the deposition parameters to obtain appropriate film thickness and quality. Furthermore, co-evaporation of precursor sources during thermal evaporation makes it difficult to control the stoichiometry of the inorganic-organic composition. Due to these drawbacks, further search on different techniques is still widely required, to look for methods that will allow cost effective deposition and upscaling of the photovoltaic cells.

1.5.4.5 Chemical Vapour Deposition Method

Chemical vapour deposition (CVD) is one of the mature and scalable deposition methods suitable for industrial use and allowing a wide variety of different materials. CVD is a vapour deposition method which employs a tube furnace surrounded by heating elements. This system allows independent control of source and substrate temperature, deposition pressure, inert gas flow rates for vapour transport, and deposition times. CVD systems have been used in perovskite absorber preparation during one-step deposition [1.36] and two-step deposition from a pre-deposited Pb halide films either through spin coating [1.35, 1.43, 1.76 – 1.78], or vacuum thermal evaporation [1.79 – 1.81]. Only few reports were both Pb halide (PbI_2) layer and the subsequent conversion were done on a CVD furnace [1.82, 1.83]. One other CVD based

method researchers have not used the most is called aerosol assisted CVD [1.40, 1.84]. CVD deposition is similar to VASP method except in CVD deposition method inert gas (Ar or N₂) is employed for the transportation of sublimated vapours at low pressures circa (ca.) 0.001-200 mbar. These operating pressures are better in terms of cost than in vacuum thermal evaporation where expensive systems are required.

D. Lewis and P. O'Brien [1.84] were one of the first groups to report on the synthesis of perovskite thin films via the CVD technique started in 2014. The duo used an aerosol assisted CVD (AACVD) to deposit MAPbBr₃ based perovskites from a single precursor solution. They describe their method as good for scaling up due to the processing under ambient pressure conditions. The precursor solution of MAPbBr₃ was mixed in a DMF solvent, transported as an aerosol via inert gas towards a heated substrate to temperatures of ca. 250 °C and ran for 90 minutes. They observed a good uniformity of the perovskite thin film deposited on a glass substrate with uniform distribution of the metal and halide over the substrate. Later, Bhachu and co-workers [1.40] deposited MAPbI₃ perovskites via the same AACVD method in which they also observed uniform distribution over larger scales (3 cm by 3 cm). AACVD starts from the precursor solution, transported by inert gas inside the CVD chamber using a frequency generated aerosol and the vapour condenses and deposit on a heated substrate [1.40, 1.84]. Both groups reported no performing solar cells from their respective reports.

In the same year (2014) another group of researchers managed to synthesise two-dimensional perovskite nano-platelets at elevated pressures between 50 and 200 Torr (1 Torr = 1.33 mbar = 133.3 Pa) [1.82]. Ha and co-workers [1.82] employed the two-step CVD method in which they deposited lead halide nano-platelets on muscovite mica substrates in the first step utilising the van der Waals epitaxial growth of lead halide unto muscovite mica substrates. The second step was the conversion to perovskites during the exposure of PbX₂ platelets to MAI

vapour which reacted to form perovskites platelets. Lead halides (PbI_2 , PbBr_2 , and PbCl_2) platelets were deposited at higher temperatures (between 350 and 510 °C) and higher chamber pressures (between 75 and 200 Torr) compared to the conversion which was performed at temperatures of 120 °C and at about 50 Torr pressure. The single zone furnace was employed by this group with PbX_2 substrates placed about 5-6 cm downstream away from the centre of the furnace which had MAI source to allow temperature gradient. A thickness increases by a factor of 1.8 from pre-deposited PbI_2 to MAPbI_3 platelets was observed by this group suggesting an easy tuning of thickness by controlling the thickness of the pre-deposited PbI_2 .

Leyden *et al.* [1.79] were the first group to prepare perovskite solar cells through a two-step CVD method and named this method hybrid CVD a name that has been adopted by many. In this report, the group deposited PbCl_2 film by vacuum thermal evaporation on FTO coated with compact TiO_2 (c- TiO_2) layer. PbCl_2 film was preferred due to its uniformity when deposited through thermal evaporation compared to PbI_2 . The PbCl_2 coated substrates were subsequently loaded to a two-zone CVD furnace as shown in Figure 1.16(a) with MAI source sublimated at 185 °C under pressure of 1 mbar and left for 1 hour under continuous flow of N_2 gas; substrates were ramped to 130 °C.

The MAI vapour diffused through the lead chloride film as gas and reacting to form solid perovskite phase. An intermediate stage was observed where the PbCl_2 film converted to PbI_2 during exposure to MAI vapour and with prolonged time a stable perovskite phase was formed. A post deposition annealing was performed in air and under N_2 ambient with air annealed solar cells performing better with a best PCE of 11.8% compared to N_2 ambient annealed devices which produced a best PCE of 8.8% [1.79]. The solar cells showed an impressive stability when stored under N_2 environment showing unchanged PCE for up to 1100 hours of testing. The stability was attributed to higher temperature processing of the films [1.79]. This hybrid CVD

method depicts simplicity and does not require very low pressures, except during the pre-deposition of lead halide which was done at high vacuum.

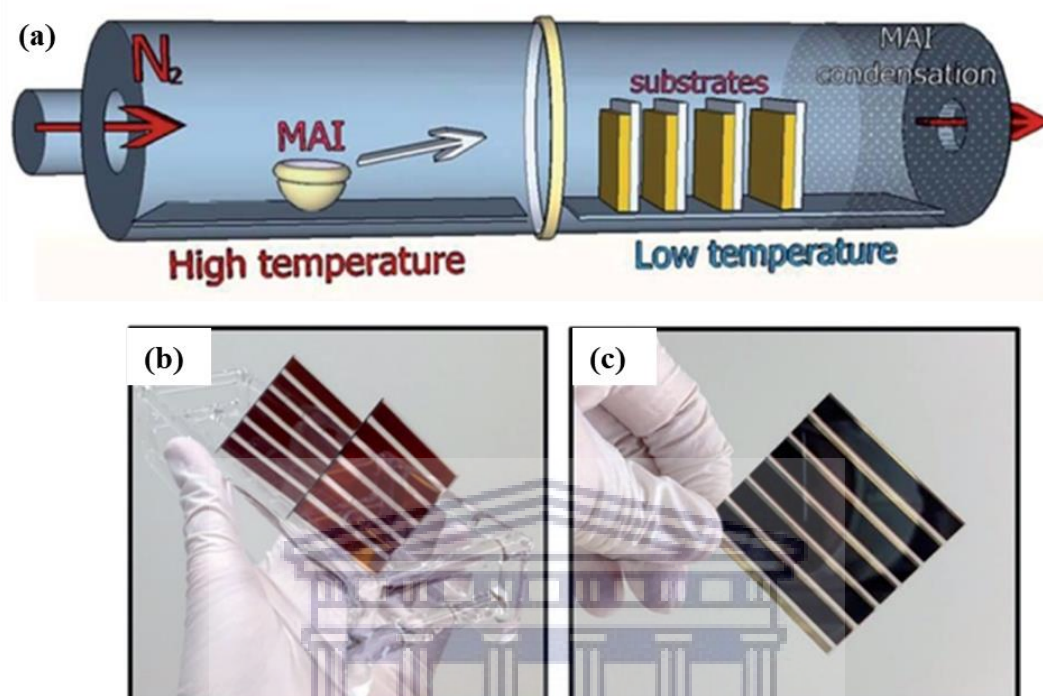


Figure 1.16: (a) Schematic illustration of a hybrid CVD method using a two-zone tube furnace [1.79], (b) and (c) photographs of small FAPbI₃ module devices fabricated by this method [1.80].

This group has also deposited pure iodine perovskite solar cells following the same procedure but more looking into the scaling up of CVD based perovskite cells [1.80]. In this case a PbI₂ was deposited through thermal evaporation and converted using a CVD furnace to form MAPbI₃ perovskite with a champion PCE of 15.6% for small device area (0.09 cm²). Larger solar modules with 12 cm² area were also prepared to investigate scaling up by CVD as shown in Figure 1.16(b) and (c). Formamidinium iodide (FAI) vapour was used during conversion to prepare formamidinium lead triiodide (FAPbI₃) modules similar to MAPbI₃

achieving module device performance of 9% compared to solar cell of 1 cm² having best PCE of 10.4%, for the same material (FAPbI₃).

Effect of PbI₂ deposition rate during thermal evaporation was investigated by Ioakeimidis *et al.* [1.81] on the performance of converted MAPbI₃ perovskite solar cells. Different deposition rates were tested with 3.5, 4.5, and 5.5 Å/s using the same substrate temperature of 55 °C. This group observed that slow deposition rates yielded larger grains of PbI₂ which resulted into insufficient conversion to perovskite during the exposure of these PbI₂ films to MAI vapour. These results showed the importance of optimisation in thermal evaporation process which might be one of the disadvantages of this process even though when fully optimised it yields good films.

Other hybrid CVD methods that have showed interest to researchers are the conversion of spin coated PbI₂ films using a CVD chamber. These methods are more similar to vapour assisted solution process except here the MAI vapour is sublimated in one zone of the CVD furnace at a higher temperature and transported towards cooler PbI₂ substrates at a different zone by inert gases. Large grain sizes, compact, and uniform films have been reported for the hybrid perovskites with best device efficiencies ranging between 12.73% and 15.37% for small devices [1.35, 1.43, 1.76 – 1.78]. Luo and co-workers [1.35] introduced this route and utilised a slow reaction between MAI vapour and spin coated PbI₂ films obtaining brownish perovskite film (Figure 1.17(b)) from a yellow PbI₂ film, shown in Figure 1.17(a). This group employed a two-zone CVD furnace where MAI powder precursor was sublimated at higher temperature of 180 °C and PbI₂ films kept at 140 °C and reaction allowed for 100 minutes achieving large grains (~500 nm average grain size) of perovskite as shown in a planar SEM micrograph in Figure 1.17(c).

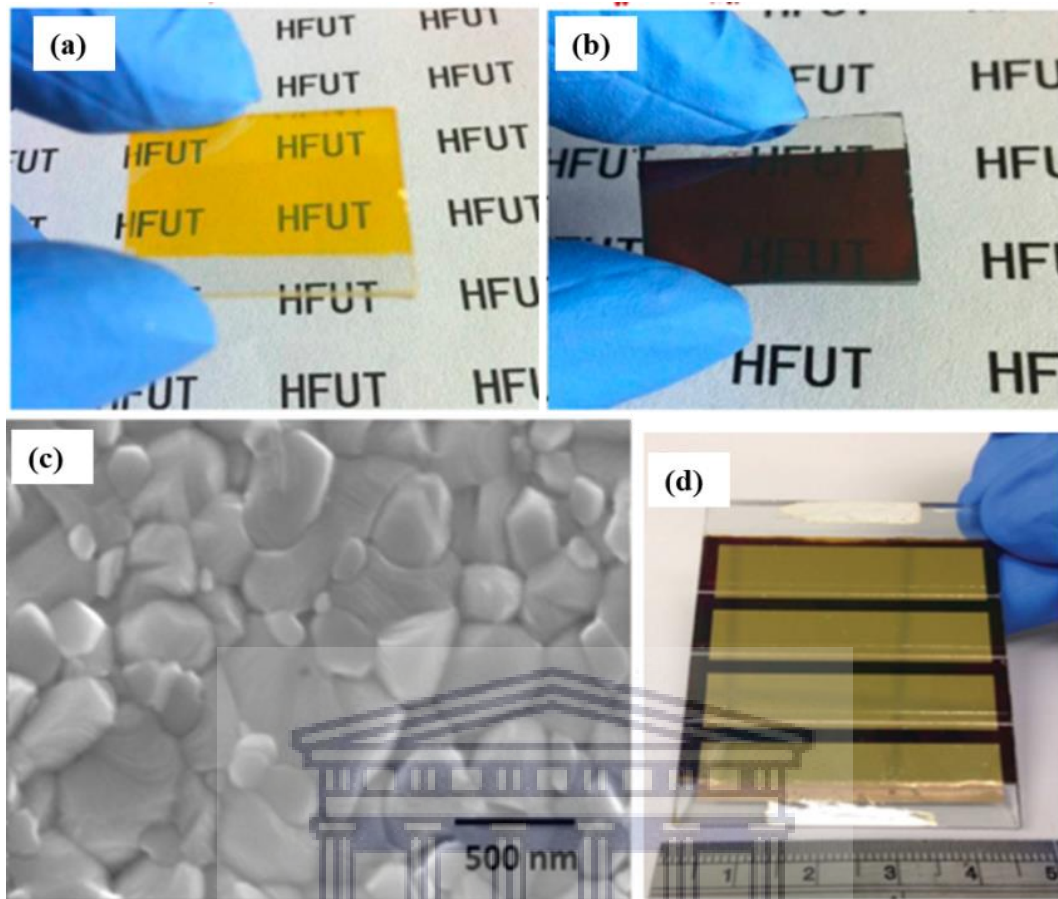


Figure 1.17: (a) and (b) Photographs of the solution spin coated PbI_2 film and the converted perovskite film, respectively, prepared by hybrid CVD and (c) planar SEM micrographs of the perovskite film [1.35]; (d) photographs of a small module device by a typical hybrid CVD method [1.76].

Shen *et al.* [1.76] also converted spin coated PbI_2 films to MAPbI_3 perovskite films on a CVD furnace where a graphite box was used to hold substrates and MAI source. The graphite box was used as a way of enhancing material yield, uniform heating environment, and up-scaling capability. Indeed, this group successfully fabricated a small perovskite module device with an area of 8.4 cm^2 as shown in Figure 1.17(d) and achieved 6.22% PCE compared to a 15.37% PCE for a smaller solar cell (0.24 cm^2) [1.76]. Stable perovskite solar cell fabricated through this solution-CVD hybrid method was demonstrated by B. Wang and T. Chen [1.43]

maintaining 90% of its starting efficiency for up to 100 days; the device was stored at 40% relative humidity between measurements. The highest PCE efficiency that have been achieved through hybrid CVD for planar devices is 18.9% after extensive optimisation of the pre-deposited PbI_2 layer demonstrating future promises of this method [1.85].

A simplified one-step CVD process was demonstrated by Tavakoli and others [1.36] where PbI_2 or PbCl_2 were co-evaporated with MAI to prepare MAPbI_3 or $\text{MAPbI}_{3-x}\text{Cl}_x$, respectively. During this facile method MAI source was placed at the start of the tube heated to 120 °C, followed by PbI_2 or PbCl_2 heated to 300 °C or 360 °C, respectively, placed at a distance away from the MAI source and the substrate placed downstream on the second zone and heated to 80 °C. The operating pressure was maintained at about 10^{-3} mbar with optimisation of different deposition parameters such as time, temperature, and post annealing undertaken to improve film quality. The $\text{MAPbI}_{3-x}\text{Cl}_x$ mixed halide perovskite performed better with PCE of 11.1% compared to MAPbI_3 perovskite with PCE of 9.2%. The high device performance of the mixed halide perovskite was attributed to its longer diffusion lengths of charge carriers (709 nm for electrons and 809 nm for holes) compared to MAPbI_3 counterpart (130 nm for electrons and 105 nm for holes) [1.36].

As far as literature goes there has only been one report on the use of two-step CVD process where lead halide films are deposited in the first step using CVD followed by their conversion during the second step [1.83]. The two-step CVD method offer unique advantages over these different derivatives of CVD process and these include better control of the pre-deposited Pb halide layers under relatively moderate pressures compared to vacuum thermal evaporation. This lack of use of the two-step CVD by researchers stems from a claimed difficulty on the deposition of Pb halide layer [1.17] which was proven to be easy by Tran *et al.* [1.83]. This group demonstrated perovskite films with large grains (up to 2 μm), free of pin holes, and high

surface coverage; PCE of 11.5% was obtained for a similar architecture as other discussed results above.

1.5.5 Challenges and Conclusions of Perovskites Solar Cells

The record perovskite solar cell efficiencies were all achieved through solution spin coating method and are usually on a small lab scale, about 0.09 cm² area as a standard. To commercialise perovskite based photovoltaic technology, the industrial upscaling challenge needs to be addressed. To achieve this, some of the perovskite major problems will need to be solved such as stability, high efficiency for large modules at low cost, and eradicate toxicity based on lead. Environmental instability of the perovskite solar cell device is still one of the major problems, where the hybrid perovskite solar cells devices are extrinsically unstable, degrading when exposed to high humidity, high temperature, and operated under ultraviolet light. The second issue is poor device performance for larger modules due to non-uniformity when perovskite is deposited over large areas especially for the primary spin coating method. And finally, the toxicity of lead (Pb²⁺) on these highly efficient devices is still a major drawback for commercialisation.

The moisture instability of the hybrid perovskite stems from the hygroscopic nature of the organic component, with MAPbI₃ absorber and its derivative decomposing to PbI₂ when exposed to high humidity levels (above 30%). One viable way of protecting the absorber layer from moisture without changing the structure or composition, is encapsulation with hydrophobic thin layers such as teflon, Al₂O₃ (aluminium oxide), poly (methyl methacrylate), polycarbonate (PC), SiN_x thin films. [1.15]. The toxicity of Pb will not be a problem if the metal is contained within the device during its operation and can be recycled at the end of the device lifetime. Substituting Pb with other metals such as tin (Sn²⁺) does not solve the problem because Sn²⁺ oxidises to Sn⁴⁺, which result to poorer device performance [1.17]. The film

uniformity problem can be improved by employing more mature industrial techniques such as the CVD method that has also showed highly stable small devices up to 155 days of tests for FAPbI₃ perovskite solar cells [1.86].

In conclusion, the vapour deposition methods are better for film control and do not require any use of mesoscopic electron transport layers. The CVD based technique is more cost effective than vacuum thermal evaporation and is suitable for industrial use as it does not depend on ultra-high vacuum systems. Hybrid CVD methods where Pb halide films are deposited by either spin coating or vacuum thermal evaporation are limited by the use of the aforementioned methods to prepare these Pb halide layers. A one-step CVD on the other side is facile but requires an exhausting optimisation of the co-evaporation conditions of the Pb halide and organic halide composition and hence making this technique challenging.

A two-step CVD method where Pb halide (PbI₂ or PbCl₂) layers are deposited in the first step and conversion to perovskite done during the second step offers more control of the perovskite film properties. The control of the pre-deposited Pb halide have been proven in both spin coating and thermal evaporation method to be effective for high quality, uniform over large scale, and large grain perovskite films. This thesis employs this two-step CVD method to prepare perovskite films for photovoltaic application.

1.6 Aims and Outlines

Organic metal halides hybrid perovskites have shown tremendous interest to researchers globally and the fabrication or deposition technique used has a direct effect on the properties of perovskite films. High quality perovskites films allow better solar cell device performances and better device stability. The overall aim of this study was to develop a novel and industrially scalable sequential low-pressure chemical vapour deposition (CVD) technique for stable

hybrid perovskites thin film preparation to be used in perovskites solar cells. To achieve this, the following research objectives were posed:

1. Optimising the deposition of lead iodide (PbI_2) and lead chloride (PbCl_2) thin films on glass during the first step of this sequential low-pressure CVD method.
2. Conversion of the PbI_2 thin films into hybrid perovskite films by exposing the as-deposited PbI_2 films to methyl ammonium iodide (MAI) vapour as the second step of the low-pressure CVD method forming MAPbI_3 perovskites.
3. Fabrication of planar perovskite solar cells using the optimum MAPbI_3 perovskite layer. This stage included (a) optimising the deposition of a compact titanium dioxide (c-TiO_2) as electron transport layer on fluorine doped tin oxide (FTO), and (b) optimising the deposition of a hole transport layer, namely, Spiro-MeOTAD. Both the c-TiO_2 and the Spiro-MeOTAD layer are fabricated by spin coating from a solution in open air. The perovskite is sandwiched between these two charge transport layers and the device is finalised by the deposition of silver (Ag) electrode layer.
4. Deposition of a lead chloride iodide (PbICl) and PbCl_2 on FTO/ c-TiO_2 to prepare Cl-doped perovskites thin film solar cells ($\text{MAPbI}_{3-x}\text{Cl}_x$) using the same sequential low-pressure CVD.

These objectives were successfully achieved, and the results are presented in this thesis.

The outline of this thesis is as follows:

- (i) **Chapter 1** introduces the global energy status and further focus more into the energy status of South Africa. The use of renewable energy sources as an alternative into the energy crisis and how photovoltaic technology can play a role. The concept of photovoltaic is briefly discussed leading into different solar cell generations such as c-Si solar cells, thin film solar cells, and third generation solar cells are discussed. Literature review on hybrid

organic-inorganic perovskite thin films focusing on the crystal structure, optical and electronic properties is discussed in detail. Different primary deposition methods are compared and briefly described, such as solution spin coating, vacuum thermal evaporation, and CVD based methods. Different CVD methods are reviewed and compared such as low-pressure CVD, hybrid CVD and one step CVD. This chapter is concluded by elaborating in brief the challenges and problems hindering the commercialisation of perovskite solar cell technology.

- (ii) **Chapter 2** provides a short background into CVD system, focusing more into thermal CVD method. Detailed experimental procedures for the deposition of perovskite films during the two-step low pressure CVD method used in this study starting with the optimisation of lead iodide deposition and the subsequent conversion to perovskite. Characterisation of the films and the solar cells is also discussed in detail in this chapter even though a brief experimental section is included in each results chapter.
- (iii) **Chapter 3** presents the results on the deposition of lead halide (PbI_2 and PbCl_2) thin films during the first step of the perovskite preparations. In this chapter the effect of substrate temperature on the deposition of these Pb halides films is compared, with two different substrate temperatures used for PbI_2 and for PbCl_2 .
- (iv) **Chapter 4** provide results on the preparation of perovskite thin films and solar cells starting with lead iodide thin films and discusses the conversion mechanism of these PbI_2 films to MAPbI_3 perovskite phase at different conversion times. Optical stability of CVD grown perovskites thin films on glass are discussed in this chapter. A solar cell performance based on the optimum converted perovskite condition is discussed here including the air stability of the solar cell.
- (v) **Chapter 5** presents results on mixed halide perovskite solar cells ($\text{MAPbI}_{3-x}\text{Cl}_x$), looking into the conversion of different lead halide films into perovskites phase including lead

chloride iodide, lead iodide, and lead chloride films. The performance of these perovskites planar solar cell devices are compared in this chapter investigating the effect of chlorine incorporation into the perovskite compared to without chlorine incorporation.

(vi) The final chapter gives an overall summary of the results chapters (chapter 3, 4, and 5)



1.7 References

- [1.1] O. Edenhofer, R. Madruga, Y. Sokona, K. Seyboth, P. Matschoss, S. Kadner, T. Zwickel, P. Eickemeier, G. Hansen, S. Schlömer, C. von Stechow, “Summary for Policymakers: In IPCC Special Report on Renewable Energy Sources and Climate Change Mitigation”, Cambridge University Press, Cambridge, United Kingdom and New York, USA (2011).
- [1.2] D. Y. Goswami, F. Kreith, “Energy Conversion”, CRC Press Taylor & Francis Group (2008).
- [1.3] BP Statistical Review of World Energy, (2019), 68th edition.
- [1.4] M. Kaltschmitt, W. Streicher, A. Wiese, “Renewable Energy–Technology, Economics and Environment”, Springer Berlin, Heidelberg and New York, USA (2007).
- [1.5] D. Arvizu, P. Balaya, L. Cabeza, T. Hollands, A. Jäger-Waldau, M. Kondo, C. Konseibo, V. Meleshko, W. Stein, Y. Tamaura, H. Xu, R. Zilles, “Direct Solar Energy: In IPCC Special Report on Renewable Energy Sources and Climate Change Mitigation”, Cambridge University Press, Cambridge, UK and New York, USA (2011).
- [1.6] L. El Chaar, L.A. Iamont, N. El Zein, *Renewable and Sustainable Energy Reviews* 15 (2011) 2165
- [1.7] T.D. Lee and A.U. Ebong, *Renewable and Sustainable Energy Reviews* 70 (2017) 1286
- [1.8] Tatsuo Saga, *NPG Asia Materials* 2 (2010) 96
- [1.9] B. Parida, S. Iniyan, R. Goic, *Renewable and Sustainable Energy Reviews* 15 (2011) 1625
- [1.10] Loucas Tsakalagos, *Materials Science and Engineering R* 62 (2008) 175
- [1.11] National Renewable Energy Laboratory (NREL) Best Research-Cell Efficiencies. (<https://www.nrel.gov/pv/assets/images/efficiency-chart.png>), Accessed on 9 June 2020

- [1.12] J. Yan and B.R. Saunders, *RSC Advances* 4 (2014) 43286
- [1.13] S. Sharma, K.K. Jain, A. Sharma, *Materials Sciences and Applications* 6 (2015) 1145
- [1.14] A. Kumar Jena, A. Kulkarni, and T. Miyasaka, *Chemical Reviews* 119 (2019) 3036
- [1.15] R. Wang, M. Mujahid, Y. Duan, Z.-K. Wang, J. Xue, and Y. Yang, *Advanced Functional Materials* (2019) 1808843
- [1.16] R. Swartwout, M.T. Hoerantner, and V. Bulovic, *Energy and Environmental Materials* 2 (2019) 119
- [1.17] L.K. Ono, M.R. Leyden, S. Wang and Y. Qi, *Journal of Materials Chemistry A* 4 (2016) 6693
- [1.18] Z. Shi and A.H. Jayatissa, *Materials* 11 (2018) 729
- [1.19] S. Stranks, G. Eperon, G. Grancini, L. Herz, A. Petrozza, H. Snaith, *Science* 342 (2013) 341
- [1.20] A. Kojima, K. Teshima, Y. Shirai, and T. Miyasaka, *Journal of American Chemical Society* 131 (2009) 6050
- [1.21] M. Lee, J. Teuscher, T. Miyasaka, T. Murakami, and H. Snaith, *Science* 338 (2012) 643
- [1.22] K. Liang, D. Mitzi, and M. Prikas, *Chemistry of Materials* 10 (1998) 403
- [1.23] I. Swainson, L. Chi, J.-H. Her, L. Cranswick, P. Stephens, B. Winkler, D. Wilsonc, and V. Milman, *Acta Crystallographica Section B* 66 (2010) 422
- [1.24] Takeo Oku, *Solar Cells - New Approaches and Reviews* (2015) 77
- [1.25] T. Baikie, Y. Fang, J.M. Kadro, M. Schreyer, F. Wei, S.G. Mhaisalkar, M. Graetzel, and T.J. White, *Journal of Materials Chemistry A* 1 (2013) 5628
- [1.26] S. Brittman, G. Adhyaksa, and E. Christian Garnett, *MRS Communications* 5 (2015) 7
- [1.27] W. Travis, E.N. Glover, H. Bronstein, D.O. Scanlon, and R.G. Palgrave, *Chemical Science* 7 (2016) 4548
- [1.28] H.-S. Kim, S. Im, and N.-G. Park, *Journal of Physical Chemistry C* 118 (2014) 5615

- [1.29] C. Quarti, E. Mosconi, J. Ball, V. D’Innocenzo, C. Tao, S. Pathak, H. Snaith, A. Petrozza, and F. De Angelis, *Energy and Environmental Science* 9 (2016) 155
- [1.30] W. Geng, L. Zhang, W.-M. Lau, and L.-M. Liu, *Journal of Physical Chemistry C* 118 (2014) 19565
- [1.31] D. Shi, V. Adinolfi, Y. Losovyj, X. Zhang, E. Sargent, and O. Bakr, *Science* 347 (2015) 519
- [1.32] F. Zhang, X. Yang, M. Cheng, W. Wang, L. Sun *Nano Energy* 20 (2016) 108
- [1.33] P. Fan, D. Gu, G.-X. Liang, J.-T. Luo, J.-L. Chen, Z.-H. Zheng, and D.-P. Zhang, *Scientific Reports* 6 (2016) 29910
- [1.34] Q. Chen, H. Zhou, S. Luo, Y. Liu, G. Li, and Y. Yang, *Journal of the American Chemical Society* 136 (2014) 622
- [1.35] P. Luo, Z. Liu, W. Xia, C. Yuan, J. Cheng, and Y. Lu, *ACS Applied Materials and Interfaces* 7 (2015) 2708
- [1.36] M. Tavakoli, L. Gu, Y. Gao, J. He, A. Rogach, Y. Yao, and Z. Fan, *Scientific Reports* 5 (2015) 14083
- [1.37] M. Liu, M. Johnston, and H. Snaith, *Nature* 501 (2013) 396
- [1.38] C.-W. Chen, H.-W. Kang, K.-M. Chiang, and H.-W. Lin, *Advanced Material* 26 (2014) 6647
- [1.39] Z. Liu, L. Qiu, E.J. Juarez-Perez, Z. Hawash, T. Kim, Y. Jiang, Z. Wu, S.R. Raga, L.K. Ono, S. Liu, and Y. Qi, *Nature Communication* 9 (2018) 3880
- [1.40] D. Bhachu, D. Scanlon, E. Saban, H. Bronstein, I. Parkin, C. Carmalt, and R. Palgrave, *Journal of Materials Chemistry A* 3 (2015) 9071
- [1.41] B. Wang, K.Y. Wong, X. Xiao, and T. Chen, *Scientific Reports* 5 (2015) 10557
- [1.42] Z. Song, S.C. Wathage, A.B. Phillips, B.L. Tompkins, R.J. Ellingson, and M.J. Heben, *Chemistry of Materials* 27 (2015) 4612

- [1.43] B. Wang and T. Chen, *Advanced Science* 3 (2016) 1500262
- [1.44] C. Bi, Y. Shao, Y. Yuan, Z. Xiao, C. Wang, Y. Gao and J. Huang, *Journal of Material Chemistry A* 2 (2014) 18508
- [1.45] Y. Zhou, O. Game, S. Pang, and N. Padture, *Journal of Physical Chemistry Letters* 6 (2015) 4827
- [1.46] M. Xiao, F. Huang, W. Huang, Y. Dkhissi, Y. Zhu, J. Etheridge, A. Gray-Weale, U. Bach, Y.-B. Cheng, and L. Spiccia, *Angewandte Chemical International Edition* 53 (2014) 9898
- [1.47] F. Huang, Y. Dkhissi, M. Xiao, S. Rubanov, Y. Zhu, X. Lin, L. Jiang, Y. Zhou, A. Gray-Weale, C. McNeill, R. Caruso, U. Bach, L. Spiccia, and Y.-B. Cheng, *Nano Energy* 10 (2014) 10
- [1.48] Y. Zhou, A. Vasiliev, W. Wu, M. Yang, S. Pang, K. Zhu, and N. Padture, *Journal of Physical Chemistry Letters* 6 (2015) 2292
- [1.49] Y. Zhou, M. Yang, W. Wu, A. Vasiliev, K. Zhu, and N. Padture, *Journal of Material Chemistry A* 3 (2015) 8178
- [1.50] Y. Zhou, M. Yang, A. Vasiliev, H. Garces, Y. Zhao, D. Wang, S. Pang, K. Zhu, and N. Padture, *Journal of Material Chemistry A* 3 (2015) 9249
- [1.51] M. Green, Y. Jiang, A. Soufiani, and A. Ho-Baillie, *Journal of Physical Chemistry Letters* 6 (2015) 4774
- [1.52] S. De Wolf, J. Holovsky, S.-J. Moon, P. Löper, B. Niesen, M. Ledinsky, F.-J. Haug, J.-H. Yum, and C. Ballif, *Journal of Physical Chemistry Letters* 5 (2014) 1035
- [1.53] R.A. Jishi, O.B. Ta, and A.A. Sharif, *Journal of Physical Chemistry C* 118 (2014) 28344
- [1.54] M.R. Filip, G.E. Eperon, H.J. Snaith, and F. Giustino, *Nature Communications* 5 (2014) 5757

- [1.55] F. El-Mellouhi, E.T. Bentría, S.N. Rashkeev, S. Kais, and F.H. Alharbi, *Scientific Repots* 6 (2016) 30305
- [1.56] A. Amat, E. Mosconi, E. Ronca, C. Quarti, P. Umari, M.K. Nazeeruddin, M. Gratzel, and F. De Angelis, *Nano Letters* 14 (2014) 3608
- [1.57] G. Yang, H. Tao, P. Qin, W. Ke, and G. Fang, *Journal of Materials Chemistry A*, 4 (2016) 3970
- [1.58] Z.H. Bakr, Q. Wali, A. Fakharuddin, L. Schmidt-Mende, T. M. Brown, and R. Jose, *Nano Energy* 34 (2017) 271
- [1.59] Z. Hawash, L.K. Ono, and Y. Qi, *Advanced Materials Interfaces* 5 (2018) 1700623
- [1.60] M. Saidaminov, A. Abdelhady, V. Burlakov, L. Wang, Y. He, A. Goriely, T. Wu, and O. Bakr, *Nature Communications* 6 (2015) 7586
- [1.61] Y. Chen, M. He, J. Peng, Y. Sun, and Z. Liang, *Advanced Science* 3 (2016) 1500392
- [1.62] H. Li, S. Li, Y. Wang, H. Sarvari, M. Wang, and Z. Chen, *Solar Energy* 126 (2016) 243
- [1.63] J. Heo, D. Song, J. Kim, H. Shin, C. Wolf, and S. Im, *Advanced Materials* 27 (2015) 3424
- [1.64] A.B. Djurisić, F.Z. Liu, H.W. Tam, M.K. Wong, A. Ng, C. Surya, W. Chen, and Z.B. He, *Progress in Quantum Electronics* 53 (2017) 1
- [1.65] L.K. Ono, E.J. Juarez-Perez, and Y. Qi, *ACS Applied Materials and Interfaces* 9 (2017) 30197
- [1.66] J. Burschka, N. Pellet, P. Gao, M. Nazeeruddin and M. Gratzel, *Nature* 499 (2013) 316
- [1.67] Z. Tanga, S. Tanakab, S. Ikedac, and T. Minemoto, *Nano Energy* 21 (2016) 51
- [1.68] C.-G. Wu, C.-H. Chiang, A. Hagfeldt, and M. Gratzel, *Energy and Environmental Science* 8 (2015) 2725
- [1.69] R. Sheng, A. Ho-Baillie, S. Huang, S. Chen, X. Wen, X. Hao, and M. Green, *Journal of Physical Chemistry C* 119 (2015) 3545

- [1.70] Y. Li, J.K. Cooper, R. Buonsanti, C. Giannini, Y. Liu, F.M. Toma, and I.D. Sharp, *Journal of Physical Chemistry letters* 6 (2015) 493
- [1.71] H. Chen, X. Ding, P. Xu, T. Hayat, A. Alsaedi, J. Yao, Y. Ding, and S. Dai, *ACS Applied Materials and Interfaces* 102 (2018) 1781
- [1.72] M.-H. Li, H.-H. Yeh, Y.-H. Chiang, U.-S. Jeng, C.-J. Su, H.-W. Shiu, Y.-J. Hsu, N. Kosugi, T. Ohigashi, Y.-A. Chen, P.-S. Shen, P. Chen, and T.-F. Guo, *Advanced Materials* (2018) 1801401
- [1.73] O. Malinkiewicz, A. Yella, M. Graetzel, and H. Bolink, *Nature Photonics* 8 (2014) 128
- [1.74] D. Perez-del-Rey, P.P. Boix, M. Sessolo, A. Hadipour, H.J. Bolink, *Journal of Physical Chemistry Letters* 9 (2018) 1041.
- [1.75] A. Ng, Z. Ren, Q. Shen, S.H. Cheung, H.C. Gokkaya, G. Bai, J. Wang, L. Yang, S.K. So, A.B. Djuricic, W.-F. Leung, J. Hao, W.K. Chan and, C. Surya, *Journal of Material Chemistry A* 3 (2015) 9223
- [1.76] P.-S. Shen, J.-S. Chen, Y.-H. Chiang, M.-H. Li, T.-F. Guo, and P. Chen, *Advanced Materials Interfaces* 3 (2016) 1500849
- [1.77] Y. Peng, G. Jing, and T. Cui, *RSC Advances* 5 (2015) 95847
- [1.78] Y. Peng, G. Jing, and T. Cui, *Journal of Material Chemistry A* 3 (2015) 12436
- [1.79] M. Leyden, L. Ono, S. Raga, Y. Kato, S. Wang, and Y. Qi, *Journal of Material Chemistry A* 2 (2014) 18742
- [1.80] M.R. Leyden, Y. Jiang, and Y. Qi, *Journal of Material Chemistry A* 4 (2016) 13125
- [1.81] A. Ioakeimidis, C. Christodoulou, M. Lux-Steiner, and K. Fostiropoulos, *Journal of Solid State Chemistry* 244 (2016) 20
- [1.82] S. Ha, X. Liu, Q. Zhang, D. Giovanni, T. Sum, and Q. Xiong, *Advanced Optical Material* 2 (2014) 838

- [1.83] V.-D. Tran, S.V.N. Pammi, V.-D. Dao, H.-S. Choi, S.-G. Yoon, *Journal of Alloys and Compounds* 747 (2018) 703
- [1.84] D. Lewis and P. O'Brien, *Chemical Communication* 50 (2014) 6319
- [1.85] J. Yin, H. Qu, J. Cao, H. Tai, J. Li, and N. Zheng, *Journal of Material Chemistry A* 4 (2016) 13203
- [1.86] M.R. Leyden, M.V. Lee, S.R. Raga, and Y. Qi, *Journal of Material Chemistry A* 3 (2015) 16097



CHAPTER TWO

Experimental Procedure: Deposition Optimization and Characterization

2.1 Introduction

This chapter provides the experimental procedures of this thesis, starting by introducing chemical vapour deposition (CVD) methods, with a detailed description of thermal CVD and its use for the preparation of organic-inorganic hybrid perovskite thin films. The focus will be on the two-step sequential CVD deposition of perovskites was used in this project. This will be followed by the fabrication of perovskite solar cells. Finally, a brief description of the main characterisation instruments will be introduced, which includes X-ray diffraction, scanning electron microscopy, UV-Vis measurements and the solar cell current density and voltage measurements.

2.2 Introduction to Chemical Vapour Deposition

Chemical Vapour Deposition (CVD) is a process whereby the dissociation and chemical reactions of activated (heat, light, plasma) gas species deposit on a substrate to form a solid material such as thin films or nanostructures at elevated temperatures [2.1, 2.2]. The application of the CVD technique for material deposition started in 1893 by de Lodyguine, who deposited tungsten on carbon lamp filaments during the reduction of WCl_6 by H_2 [2.2]. CVD was further exploited in the industry for other material productions such as Ti, Ni, Zr and Ta. This technique only advanced over the last 50 years where it has been used for the manufacturing of electronic semiconductor films and protective coatings such as C, B, Si, borides, carbides, nitrides, oxides, silicides, sulphides, and group III-V and II-VI materials [2.2].

There are different CVD systems aimed at achieving depositions of different materials depending on the temperature requirements of the reactants. The common aspect of these CVD systems is the requirement of the precursors, the CVD reactor and sometimes the pressure control system. The role of the precursor is to generate the necessary vapour that is directed towards the deposition substrates in the reactor. The role of the reactor is to complete the reaction of the precursors at the surface of the substrate and thus forming films or nanostructures. The final important component of a CVD system is a gas handling system, which may control the pressure in the reactor and handle the exhaust gasses [2.2, 2.3]. For film formation these steps are necessary: generation of gaseous (vapour) reactant species that are transported towards the substrate (in the reactor zone). These reactant species are absorbed on the surface of the substrate (which may be heated), forming deposit centres that crystallise and form a thin film [2.1, 2.2].

The reaction zone is what determines the type of CVD system and is based on the energy input of that CVD system. There is a plasma enhanced CVD (PECVD) system where the reactant species are generated through pre-created plasma (often argon plasma) by an electric discharge, and this plasma contains radicals, ions, and neutrals. Another system is hot filament (wire) CVD (HWCVD), which relies on a heated tungsten or tantalum wire, to temperatures above 1500 °C, to create reactive species. Then there is metal-organic CVD (MOCVD) to deposit metal organics and the most straightforward thermal CVD (TCVD) which uses heaters surrounding an enclosed tube where the substrates are allocated [2.1, 2.2]. In this thesis, we focus on thermal CVD, which is one of the advanced CVD systems for thin film deposition and has a wide variation of applications.

2.3 Thermal Chemical Vapour Deposition

The thermal chemical vapour deposition method is a conventional CVD process where chemical reactive species are initiated by thermal heating, often in a quartz or ceramic tube surrounded by resistive heaters. Precursors in the thermal CVD method are thermally decomposed in a gas phase or at the substrate surface thereby forming a thin film. These precursors are thermally sublimated, injected as liquid or gases into the heated tube and transported towards the heated substrates depending on the desired deposition [2.1, 2.2, 2.4 – 2.6].

The thermal CVD method is further divided into different methods depending on the deposition pressure employed. These methods include atmospheric pressure CVD (AP-CVD) where deposition occurs at atmospheric pressure ($\sim 10^3$ mbar); this is followed by low pressure CVD (LP-CVD), and then ultrahigh vacuum CVD (UHV-CVD). LP-CVD involves deposition pressure range of 0.1 - 500 mbar and deposition pressures for UHV-CVD are pressures below 0.001 mbar. AP-CVD is cheaper as no vacuum pumps are necessary, but the film quality is relatively poor compared to LP-CVD where film uniformity is usually superior, and UHV-CVD method has been developed to further improve film quality and uniformity [2.1, 2.2, 2.4 – 2.6].

Low pressure thermal CVD have been widely used in recent times mainly for the deposition of organic-inorganic halide hybrid perovskites for their application in photovoltaic [2.7 – 2.11]. During perovskite deposition, the thermal CVD furnace is used to sublime perovskite precursors such as metal halide or organic halides at moderate temperatures (120 – 500 °C) and low pressures (0.01 mbar – 1.5 mbar) [2.7 – 2.11]. The general idea is that the film of hybrid perovskite is formed during a reaction on the heated substrate surface and not during the gas phase. This has also been validated by exposing thin films of lead halide pre-deposited by other

means such as spin coating from solution or physical vapour deposition to a vapour of organic halide thermally evaporated in a CVD reactor [2.9]. The formation of the resultant perovskite film showed that the reaction happens at the substrate surface [2.11]. In this PhD project a horizontal tube furnace, low pressure thermal CVD system was used to deposit hybrid perovskite thin films following a two-step sequential method.

2.4 Thermal CVD System Setup

A home built low pressure thermal CVD system, used to deposit hybrid perovskite films during a two-step sequential method, is composed of a three-zone heating furnace (Brother XD 1600MT), where each zone is 20 cm in length. The schematic of this system is shown in Figure 2.1(a) and the actual photograph in Figure 2.1(b), showing the major components. These components include the actual horizontal furnace (CVD body), reactor tube (quartz or ceramic), gas cylinder, mass flow controller (MFC), pressure regulating valve and gauge, rough mechanical pump, and the exhaust. The gas used in this thesis is ultra-high purity nitrogen, which pass through an MKS mass flow controller (MFC) to control the gas flow rate. From the MFC, the gas is fed (purged) into the inlet of the CVD system as shown in the schematic (Figure 2.1(a)).

This CVD instrument has three heating zones shown in Figure 2.1(a), each zone is 20 cm wide and zones are separated by a 4 cm insulating material, and can reach a continuous working temperature of 1600 °C. The temperature of each heating zone is independently controlled, as shown by the temperature controllers in Figure 2.1(b).

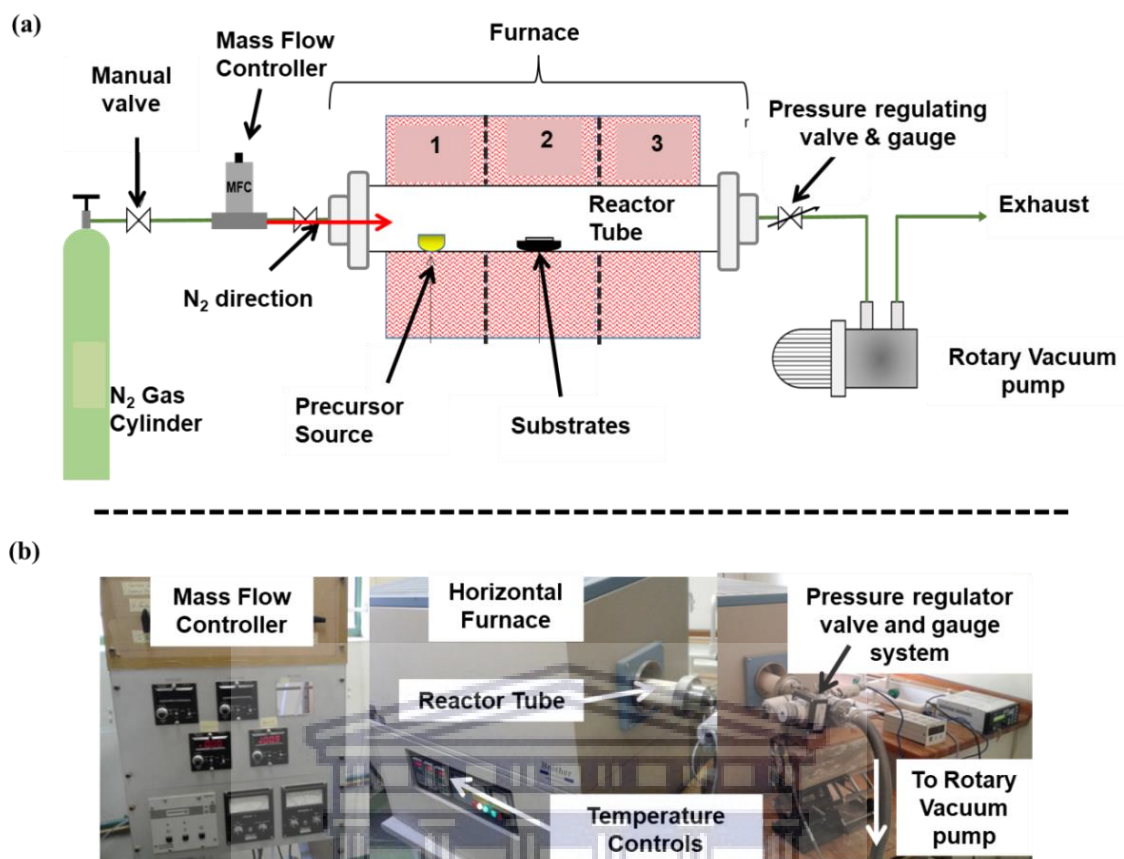


Figure 2.1: (a) Schematic representation of the home build thermal CVD setup used for the deposition of lead halides and their subsequent conversion to perovskites, (b) photographs of the different parts assembled to form the thermal CVD system.

2.5 Optimizing Deposition Conditions

In this PhD project the aim was to deposit and fabricate organic-inorganic hybrid perovskite solar cells where the perovskite thin films are prepared by a two-step sequential CVD method. This method begins with the deposition of a lead (Pb) halide layer such as lead iodide (PbI₂) or lead chloride (PbCl₂) thin films in the first step. This step is followed by an exposure of these Pb halide films into a vapour of methyl ammonium iodine (MAI) thus forming a methyl ammonium lead tri-halide (MAPbI₃ or MAPbI_{3-x}Cl_x in short, x is usually very small). It is

therefore important to optimise the Pb halide layer deposition as it acts as a seed layer for perovskite phase formation.

2.5.1 Lead Halide Deposition

Before any of the initial depositions, the ceramic and quartz tubes which are 120 cm in length with an inner diameter of 6 cm were cleaned thoroughly in soapy hot water and rinsed in hot clean water. The tubes were heated up in the CVD furnace where all the three zones were ramped up to 1000 °C to evaporate any contamination present. To prepare for deposition, corning glass substrates were cut into $1 \times 1 \text{ cm}^2$ in size and cleaned in acetone, then isopropanol, for 10 minutes each in ultrasonic bath. Thereafter the substrates were repeatedly rinsed in hot deionised water. The substrates were dried using dry nitrogen.

After the substrates were cleaned, about 150 mg of yellow lead (II) iodide powder (99%, Sigma) was measured using a mass balance with the source contained in a clean ceramic boat as shown in Figure 2.2(a). The ceramic source boat was placed at the centre of the first zone (zone 1 in Figure 2.1(a)) and the glass substrates placed on the downstream of the tube onto flat thick silicon wafer supports. The positioning of the sources and substrates is also illustrated in Figure 2.1(a).

After the source and substrates were loaded into their respective positions, the reactor ceramic tube was sealed with steel flanges in both the inlet and the outlet sides, then the rotary vacuum pump was switched on to start pumping. The base pressure in the reactor amounts about 10^{-2} mbar. The reactor was then purged with pure nitrogen gas (N_2) at flow rate of 150 sccm (standard cubic centimetre per minute) to purge the system of any contamination. The temperature profile of the thermal CVD system was then programmed to ramp up, dwell, and cools down automatically. For PbI_2 film deposition, the first zone with PbI_2 source was ramped

up to a nominal temperature of 380 °C, which is above the sublimation temperature of PbI₂ [2.7] at 10 °C/min ramping rate.

A temperature profile for PbI₂ deposition is shown in Figure 2.2(c) with three phases, ramping up, dwelling, and cooling. The substrate temperature profile is also shown in Figure 2.2(c), which follows that of the source temperature profile. It should be noted that only the first zone was heated during the deposition and therefore the substrate temperature is purely dependent on the distance away from the first zone. A temperature profile at different substrate positions from the source were measured with an external thermocouple inserted into the outlet side of the furnace and these distances were 14, 15, 16 cm away, downstream. These temperatures were 145 °C, 135 °C, and 125 °C for positions 14, 15, and 16 cm, away, respectively. Only the 135 °C substrate temperature profile is shown in Figure 2.2(c).

The N₂ gas flow of 100 sccm was initiated when the source temperature reached 380 °C and the deposition pressure was fixed using the automated pressure regulating system. The deposition was allowed to dwell for 40 minutes, after which the gas flow was shut and the throttle valve opened to allow the pressure to drop to 10⁻² mbar, while the furnace was cooling down to room temperature. After the cooling stage, the substrates and source boat were removed. Bright, yellow, and transparent or slightly opaque (depending on the film thickness) PbI₂ films on glass were successfully deposited as shown by a photograph in Figure 2.2(b); the source boat was empty confirming a full evaporation of the PbI₂ source powder. The initial experiments in this project showed that a temperature of 300 °C at 1 mbar pressure was not enough to evaporate or sublimate the PbI₂ source and hence it was increased to 380 °C.

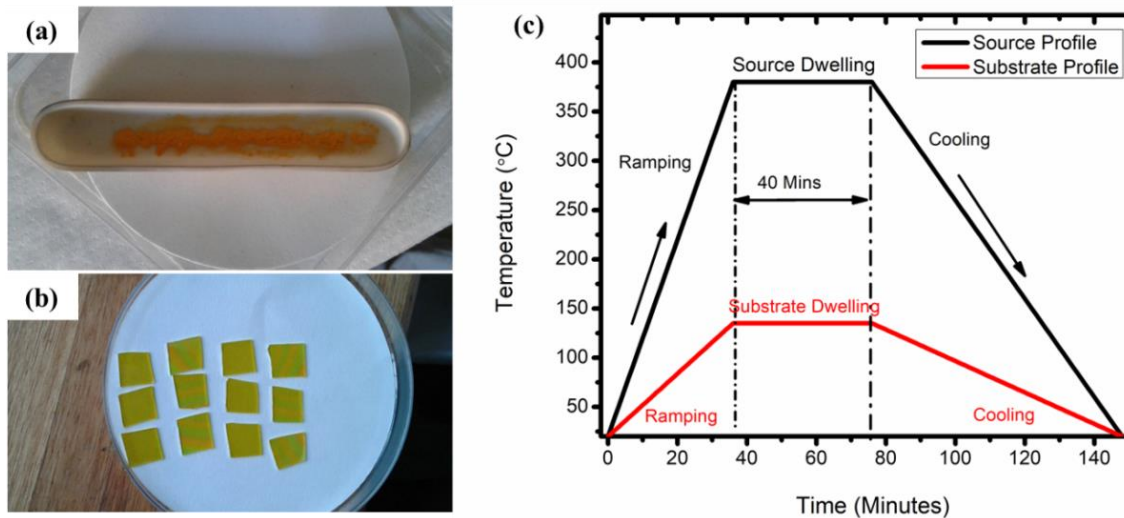


Figure 2.2: (a) Lead iodide source on a ceramic boat and (b) photographs of the PbI₂ films on glass substrates; (c) temperature profiles for the deposition of PbI₂ films.

Different deposition pressures of 1, 10, 100, 300, and 500 mbar were tested, and 300 mbar was selected as the best condition based on the quality of the film. This conclusion was drawn from the preliminary results showed by UV-Vis transmittance and X-ray diffraction (XRD) measurements. Overlaid transmittance spectra of PbI₂ films on corning glass obtained at different deposition pressures in Figure 2.3(a) showed that all films were of PbI₂ phase based on the transmittance edge [2.7, 2.12, 2.13]. In comparison to the glass transmittance spectrum, the films obtained at 10, 100, 300 mbar pressure showed higher transmittance compared to the 1 mbar and 500 mbar and this is linked to thinner film thickness of these samples.

The lead iodide film thickness is an important parameter that required monitoring during sequential CVD method because perovskites solar cells (MAPbI₃) have optimum required thickness [2.8]. Indeed, the PbI₂ films obtained under these conditions (10, 100, 300 mbar) had a relatively similar film thickness for samples deposited under the same substrate temperature; this film thickness was about 250 nm as measured from a Veeco Dektak 6M Stylus profilometer. A film deposited at 1 mbar was thick (about 700 nm) and rough, which assigned

to the fast evaporation of the source at this low pressure, thereby resulting in fast deposition. The 500 mbar sample also had a rough and opaque appearance with about 500 nm thickness, which is due to increased amount of source vapour in the reactor.

XRD patterns in Figure 2.3(b) verified that improved quality of the moderate pressure deposited samples (10, 100, 300 mbar) with the 300 mbar sample showing the most pronounced (001) XRD peak (Figure 2.3(c)), which is correlated to a higher degree crystallinity. The XRD results confirm the successful deposition of pure, highly crystalline PbI_2 films, as evident by the known PbI_2 (001), (002), (003), and (004) diffraction peaks [2.12, 2.13].

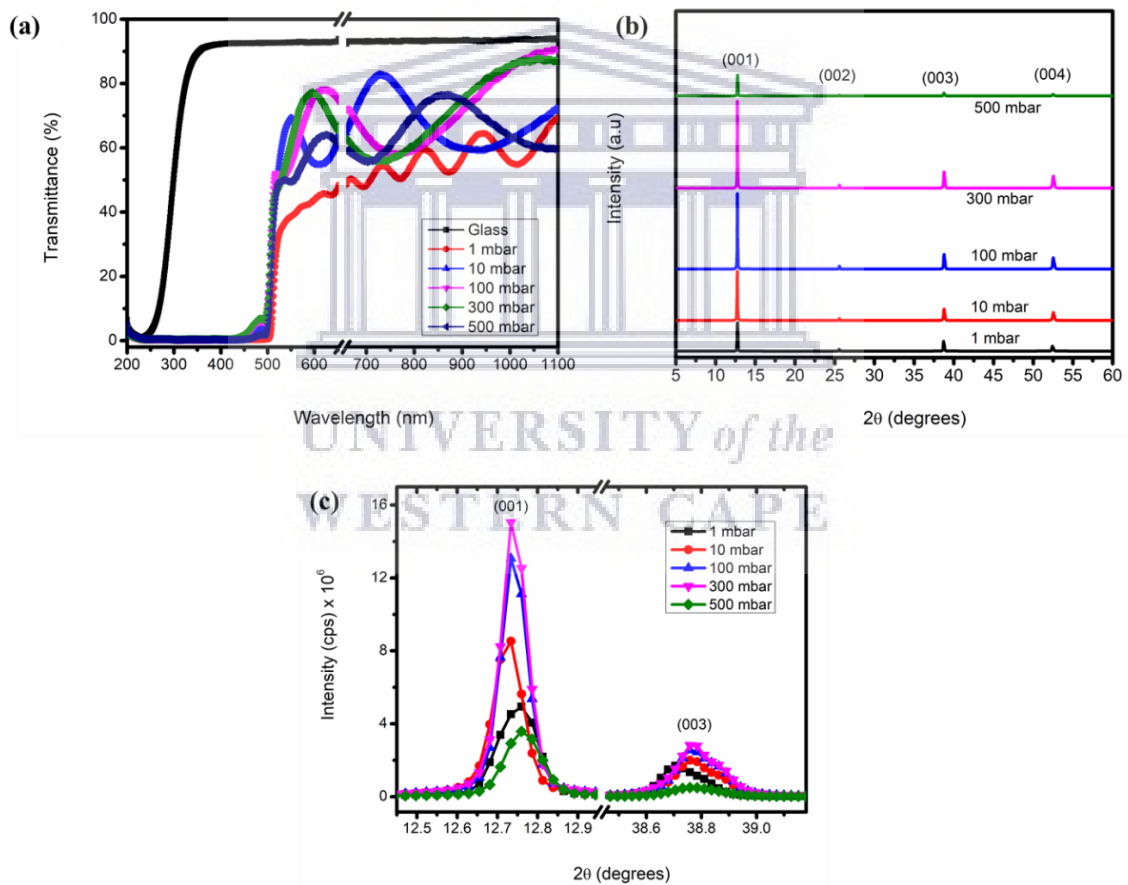


Figure 2.3: (a) Transmittance spectrums of PbI_2 films deposited at various pressures on glass substrates, (b) XRD patterns of the same PbI_2 samples, and (c) zoomed (001) and (003) XRD peaks of the PbI_2 films.

The final optimisation condition for the PbI_2 deposition was the substrate temperature, which depended on how far the substrates were placed with respect to the source zone centre set to a temperature of $380\text{ }^\circ\text{C}$. The results above were based on the initial position tested, which was 14 cm away from the source where the substrates were placed at $145\text{ }^\circ\text{C}$. It was shown that placing substrates at positions 14, 15, 16 cm correspond to substrate temperatures of 145, 135 and $125\text{ }^\circ\text{C}$, respectively, yielded different film thickness. These results are discussed in detail in Chapter 3 and 4.

The lead chloride (PbCl_2) film deposition is similar to that of the PbI_2 deposition, except for the source temperature was changed to $450\text{ }^\circ\text{C}$. The temperature profile of PbCl_2 film deposition in a thermal CVD system is shown in Figure 2.4(a), with a similar process as for PbI_2 deposition.

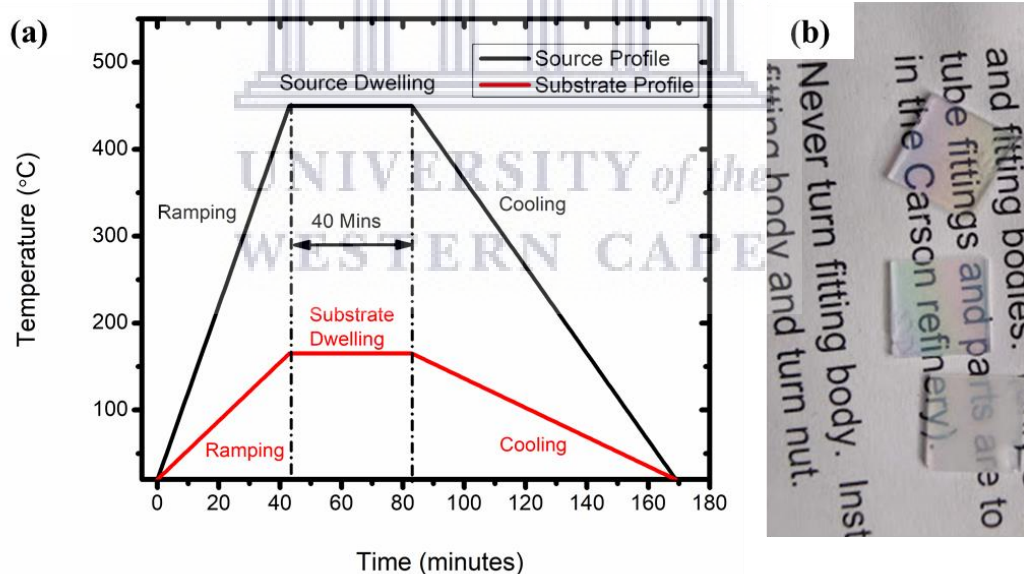


Figure 2.4: (a) Temperature profiles for the deposition of PbCl_2 films and (b) photographs of the PbCl_2 films on glass substrates.

About 150 mg of lead (II) chloride powder (98%, Sigma) was used and contained in a ceramic boat that was placed at the centre of zone 1. In this instance, the source temperature was ramped to 450 °C and the substrates were placed 16 cm and 17 cm away from the source at positions where temperature reached about 165 °C and 150 °C, respectively. The deposition pressure, flow rate, and dwelling time were kept the same as for the PbI₂ deposition. The result was white transparent PbCl₂ films, as indicated in Figure 2.4(b).

2.5.2 Pb Halide Conversion to Perovskites

After the deposition of lead halides (PbI₂ and PbCl₂) was optimised, these films were converted to perovskite phase as the second step of the two-step sequential low pressure CVD method. In this step the Pb halide films were exposed to methyl ammonium iodide (MAI) vapour in the same CVD reactor using a clean ceramic tube. Under favoured conditions the MAI molecules react with the Pb halide films the instant these species reach the surface of the films, thereby converting the Pb halide into a perovskite phase.

For the initial conversion experiments, pre-deposited PbI₂ films were used instead of PbCl₂ simply because of the simple structure of perovskite phase formed from the conversion of PbI₂ (i.e., MAPbI₃). During this conversion step, about 300 mg of MAI (Dyesol) salt was placed in a fresh ceramic boat (Figure 2.5(b)) and placed at the centre of the first zone. The PbI₂ thin films on corning glass substrates were placed downstream away from the source at distances 8, 12, and 16 cm. The purpose was to investigate the effect of substrate temperature on conversion, which depends on the distance away from zone 1 centre.

Once the MAI source and the PbI₂ films were loaded into the reactor tube, it was then sealed on both sides and was pumped down to a base pressure of 10⁻² mbar. This was followed by the N₂ purging at 150 sccm for 2 minutes (as for the Pb halides). The temperature of the MAI

source was then subsequently ramped up at 10 °C/min to a nominal temperature of 180 °C, as shown in Figure 2.5(a). The temperature of the PbI₂/glass substrate downstream at 8 cm away from the source amounted to 130 °C, shown in Figure 2.5(a). When the source temperature reached about 180 °C, N₂ was allowed to flow at 100 sccm and the pressure was increased and maintained at 50 mbar, using the pressure regulator. The exposure of the PbI₂ films to MAI vapour was allowed to dwell for different times of 15, 30, 60, 90 and 120 minutes. After the set dwelling time was complete, the system was allowed to cool down and the samples were removed for characterisation. These perovskite samples were stable for several days allowing all the necessary characterisation. This stability aspect is one advantage of the CVD method over solution processed perovskite films [2.7 – 2.11]. Only a maximum of about 140 mg MAI salt was consumed during the 120 minutes conversion and as low as 57 mg of MAI after 15 minutes conversion.

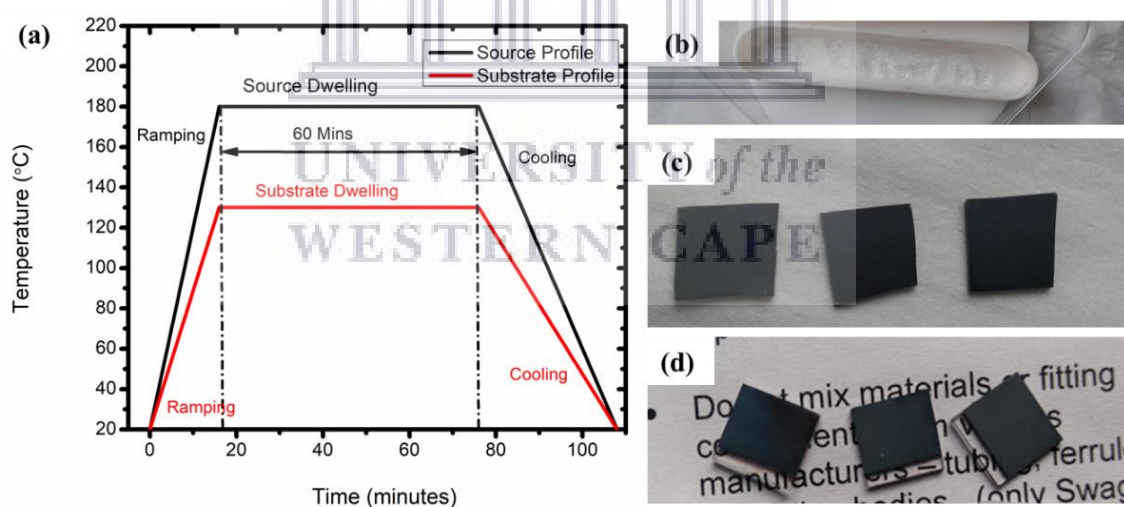


Figure 2.5: (a) Temperature profiles of the MAI sublimation during the conversion of Pb halides films to perovskite, (b) MAI source in a clean ceramic boat, (c) photographs MAPbI₃ perovskites films, and (d) MAPbI_{3-x}Cl_x perovskites films on glass substrates.

It is worth noting in this stage that poor conversion of PbI_2 to perovskite was realised at substrate distances of 12 and 16 cm. The films were under-converted and as a result were unstable due to low substrate temperatures of below 100 °C. Only samples that were placed at a distance of 8 cm away were fully converted depending on the conversion time. The conversion pressure was kept at 50 mbar. The results of the perovskite conversion from the pre-deposited Pb halides are discussed in Chapters 4 and 5. Typical photographs of perovskite films converted from PbI_2 are shown in Figure 2.5(c) and from PbCl_2 in Figure 2.5(d). A similar process was followed for the conversion of PbCl_2 to the perovskite phase. This was a first confirmation of a successful deposition of high-quality perovskite through a two-step sequential CVD method. These films are dark in colour showing a complete change in structure from a yellow PbI_2 and white transparent PbCl_2 films to dark perovskite phase MAPbI_3 and $\text{MAPbI}_{3-x}\text{Cl}_x$, respectively.

2.6 Perovskites Solar Cell Fabrication

With the perovskite absorber layer optimised from the deposition of Pb halides to the conversion stage, the project investigated the application of these CVD deposited perovskites in solar cell devices. There are two main configurations or architectures of perovskite solar cells, i.e., p-i-n and n-i-p, and here a planar n-i-p architecture was chosen with the n-type layer used being a compact titanium dioxide layer (c-TiO_2). The hole transport layer (HTL) or the p-type layer used was a small organic molecule material, Spiro-MeOTAD (short for 2,2',7,7'-tetrakis(N,N-di-p-methoxyphenylamine)-9,9-spirobifluorene), doped with 4-tert-butylpyridine (tBP) and lithium bis-(trifluoromethylsulfonyl)imide (LiTFSI). The n-type layer or electron transport layer (ETL) and the HTL sandwich the perovskite absorber layer. The solar cell fabrication steps are shown in Figure 2.6(a) and the complete device architecture is shown as the last step in Figure 2.6(a).

The solar cell device fabrications were done under ambient conditions (temperature and humidity) in air. All chemicals used here were purchased from Sigma-Aldrich and used as-bought. Fluorine-doped tin oxide (FTO) coated on glass substrates (Techinstro, 10 Ohms/sq.) were cut into $1.5 \times 2 \text{ cm}^2$ sections and etched with Zn powder and 2 M hydrochloric acid (HCl) patterned using a Kapton tape. These samples were sequentially cleaned with hellmanex detergent (2%), followed by isopropanol in an ultrasonic bath each for 10 minutes, and then followed by a thorough rinsing in hot deionized water and finally cleaned with UV ozone for 10 minutes.

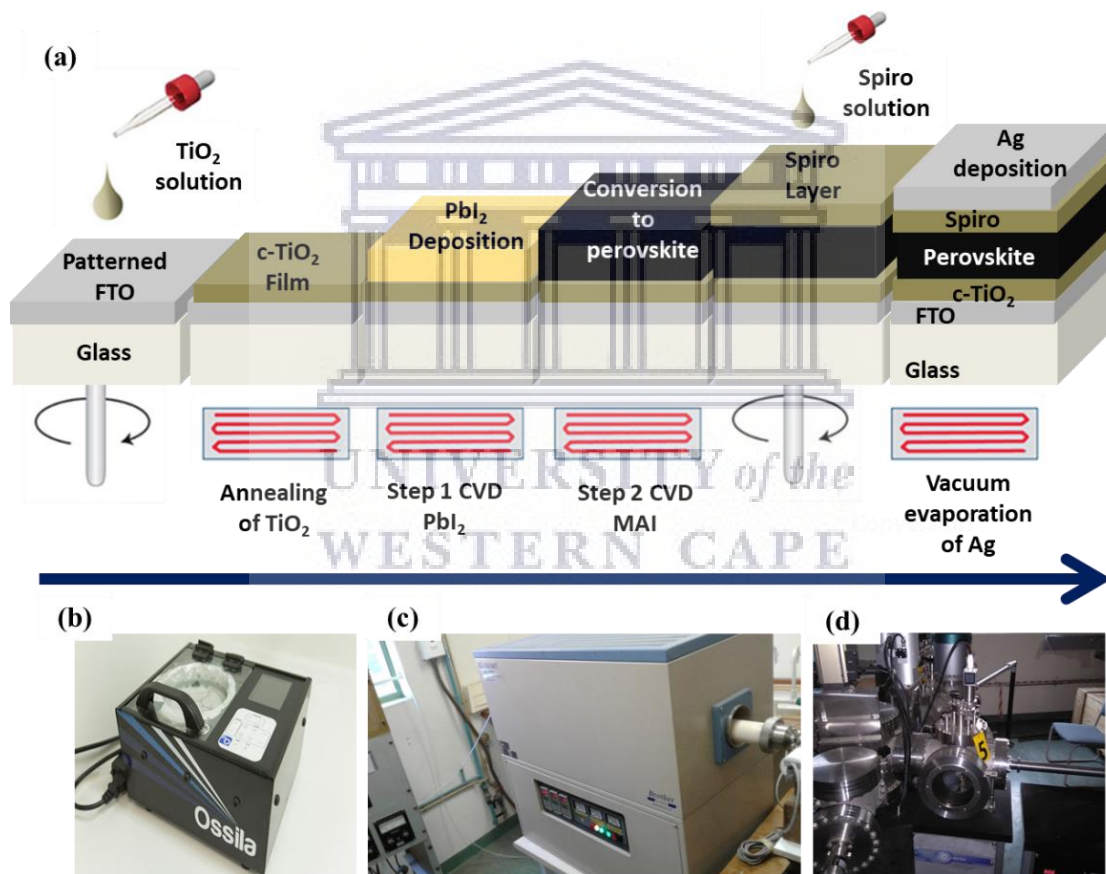


Figure 2.6: (a) Perovskites solar cell fabrication steps from the deposition of c-TiO_2 to Ag metal electrode, (b) Ossila spin coater used for c-TiO_2 and Spiro-MeOTAD layer, (c) CVD furnace used for annealing c-TiO_2 layer and perovskite deposition, and (d) vacuum thermal evaporator used for the deposition of the Ag metal electrode.

A 365 μL of titanium isopropoxide was added into 2.5 mL of ethanol, and 35 μL of HCl (2 M) also added into 2.5 mL of ethanol, mixed to form 5 mL solution, and stirred for an hour. The prepared solution was spin coated on the etched FTO substrates at 2000 rpm for 30 seconds to obtain a titanium containing film followed by 4000 rpm spin coating as a second coat, also for 30 sec, to fill any voids left during the first spin coating step. The edges of the patterned FTO substrate were covered with Kapton tape to leave them uncovered by the TiO_2 film and the spin coating was done using an Ossila spin coater showed in Figure 2.6(b) employing a static spin coating method (drop and spin). The samples were dried on a hot plate at 150 $^\circ\text{C}$ for 5 min and then annealed at 500 $^\circ\text{C}$ for 30 minutes using a tube furnace with a clean tube dedicated for annealing. The spin coated samples were annealed at atmosphere with both ends of the tube open for the formation of a compact TiO_2 film from the existing oxygen in the air.

The Glass/FTO/c- TiO_2 substrates were then placed in the CVD furnace for the deposition of PbI_2 films, which were then converted to perovskites as was discussed in section 2.5 using the CVD furnace in Figure 2.6(c). The photographs of the PbI_2 films (edges uncleaned) and the converted MAPbI_3 perovskite films (edges cleaned) on etched FTO are shown in Figure 2.7(a) and (b). To finalize the devices, the hole transport layer (HTL) was spin coated on top of the Glass/FTO/c- TiO_2 /perovskite film at spin speed of 2000 rpm for 30 s also using the Ossila spin coater. The HTL solution was prepared by dissolving 80 mg of Spiro-MeOTAD in 1 mL of chlorobenzene, to which 40 μL of 4-tert-butylpyridine (tBP) and 25 μL of lithium bis-(trifluoromethanesulfonyl) imide (LiTFSI) solution (52 mg of LiTFSI in 100 μL of acetonitrile) were added to dope Spiro-MeOTAD and stirred for 30 minutes before spin coating.

The edges of the Glass/FTO/c- TiO_2 /perovskite/Spiro-MeOTAD samples were cleaned with chlorobenzene and then dried on a hot plate at 100 $^\circ\text{C}$ for 2 minutes to evaporate any excess solvents. These samples are then left in an open desiccator overnight (12 hour or more) to

oxidise the Spiro-MeOTAD layer, thereby improving its conductivity. Finally, a 100 nm layer of silver (Ag) electrode was deposited by thermal evaporation shown in Figure 2.6(d) at a deposition pressure of about 10^{-5} mbar through a shadow mask with device active area of 0.08 cm^2 . After the deposition of the Ag layer (with no encapsulation), the devices were taken for measurements in open air and kept in a drawer between these measurements. The optimisation results of these solar cell devices are given in Reference [2.14]. The full device architecture is shown in Figure 2.7(c) including the method of measuring the device performance from the two contacts (FTO and Ag metal) using a source metre.

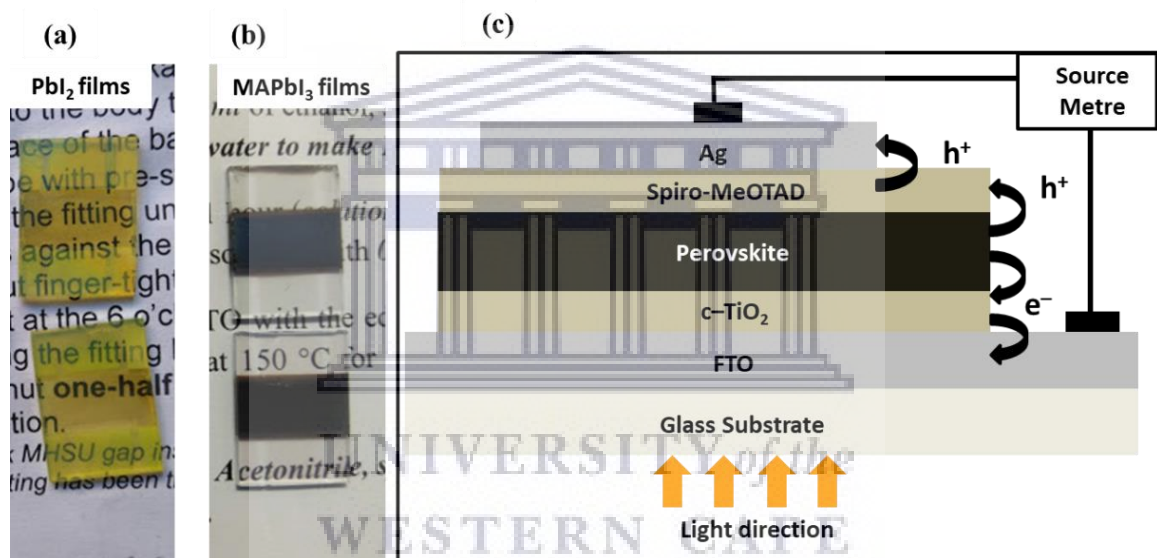


Figure 2.7: (a) Photographs of PbI_2 films on patterned FTO and (b) photographs of converted perovskite solar cells devices; (c) schematic of the n-i-p perovskite solar cell architecture.

2.7 Characterisation of Perovskites Thin Films

The phase composition and the crystal structure of the films were identified by X-ray diffraction (XRD) using a Panalytical Empyrean X-ray diffractometer. Copper (Cu X-ray source) was used with K-Alpha1 wavelength of 1.5406 Å and K-Alpha2 wavelength of 1.5444 Å and a K-Alpha2/K-Alpha1 ratio of 0.5. An acceleration voltage of 45 kV and a current of 40 mA were used and samples were scanned over the 2θ range of 5–99° with a scan step of 0.02626° employing a continuous scan type. The XRD data was collected from thin films on glass substrate without grinding the films into powder forms and a silicon standard was used for every measurement. It is also worth mentioning that these samples were not measured immediately after deposition as they had to be transferred over to the facility that hosts the XRD instrument.

The morphology of the thin films was investigated using a Zeiss Cross Beam 540 Focused Ion Beam Scanning Electron Microscope (FIB-SEM) operated at an acceleration voltage of 1–3 kV and equipped with energy dispersive X-ray spectroscopy (EDS) for elemental composition. A Zeiss Auriga field-emission gun SEM (FEG-SEM) operated at acceleration voltage of 1–5 kV also equipped with EDS facilities was also used. Samples were coated slightly with a carbon prior to loading into the FEG-SEM instrument and this was done to enhance the image quality and to reduce charging especially on the poorly conductive Pb halide films. The cross-section samples were prepared by making a deep scratch on the back side of the glass substrate with film protected. The glass substrate was then broken by applying a pressure at the edge of the scratch to break the glass and then get a fresh cut of the film without causing any film deformation.

X-ray photoelectron spectroscopy (XPS) was carried out on a Thermo Scientific ESCALAB 250 surface and depth analysis system equipped with a monochromatic Al K α X-ray (1486.7

eV) source. The data was collected for full XPS survey to detect all the chemical composition present on the film plus high resolution scan of the most prominent elements were taken. Atomic force microscopy (AFM) images of the surface of thin films were collected using a NANOSURF Flex AFM operated in contact mode at ambient conditions. Images were acquired with a size of 5×5 micron with 256 lines and 0.8 seconds per line.

Optical transmission spectra were measured from 250–1200 nm with a spectral resolution of 0.5 nm, using an Ocean Optics UV-Visible spectrophotometer. Before measurements, a black light absorbing (zero transmittance) reference sample was used and air was used to calibrate for 100% transmittance. The transmittance data was converted into absorbance using Beer–Lambert Law i.e. $A = -\log(T)$ ignoring the reflected light from the film surface; here A is absorbance and T is transmission [2.15, 2.16]. The transmittance spectra were analyzed with a SCOUT® simulation software (<https://wtheiss.com>), employing an iterative method using Bruggeman Effective Medium Approximation [2.17] to mix quantities of PbI₂ and MAPbI₃ perovskite optical functions, such as the refractive index and extinction coefficient [2.18, 2.19]. The experimental and modelled transmittance spectra of the PbI₂ and converted perovskite films are shown in Figure 2.8 with the fits depicting a good agreement between the experiments and simulations.

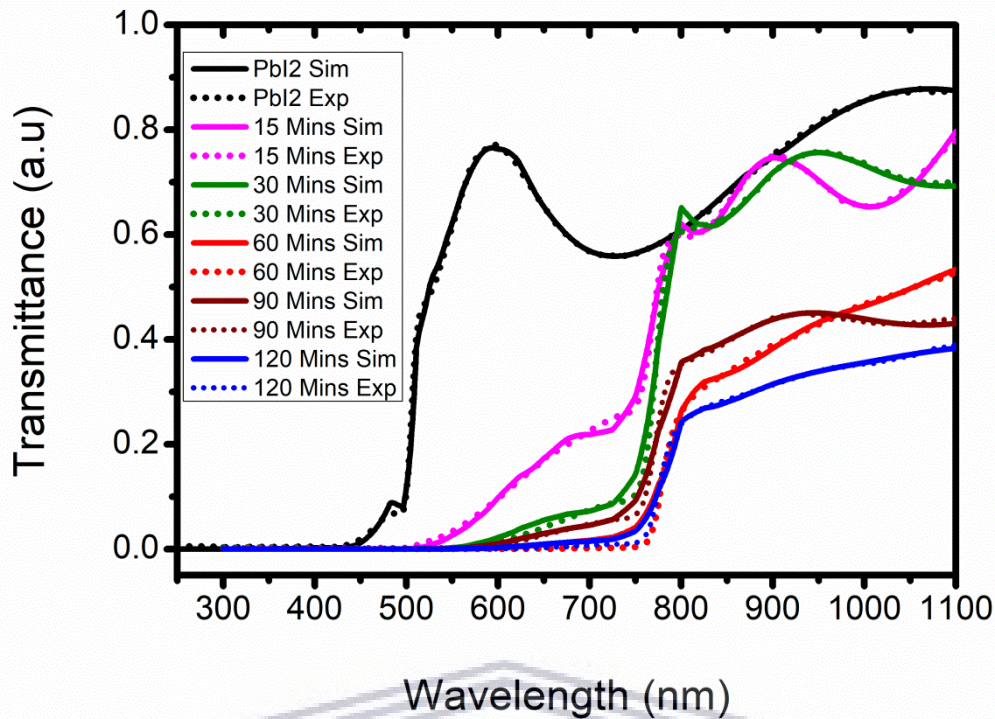


Figure 2.8: Experimental and simulated (modelled) transmittance spectrums of the PbI_2 film and the MAPbI_3 converted perovskites thin films on Corning glass for different conversion times.

2.8 Perovskite Solar Cell Performance Measurements

2.8.1 Basic Solar Cell Parameters

Solar cell performance testing is done by measuring current density (current per unit area) while sweeping voltage across the device. These measurements are referred to as current density (J)–voltage (V) measurements performed under light illumination and under dark as shown in Figure 2.9(a) and (b). Under illumination the solar cell develops a photo-voltage and when the terminals of the cell are isolated, i.e., infinite load resistance (no current is drawn), this photo-voltage is termed open circuit voltage (V_{oc}). When the terminals are connected under illumination (zero applied voltage) the photo induced current is called short circuit current density (J_{sc}). Under no illumination (dark) a very small or no current is generated across the

device and the shape of the curve follows that of a diode. When light is incident on the device the curve shifts down with an appropriate J_{sc} as shown in Figure 2.9(b) [2.20].

Under operational condition the device produce a certain maximum voltage (V_{max}) and current density (J_{max}) and their product giving maximum power output density (P_{max}) of the solar cell as shown in Figure 2.9(a). The ratio of the maximum power output density to the product of V_{oc} and J_{sc} gives another important parameter of the solar cell called the fill factor (FF), equation 2.1; defined to be a squareness of the J–V curve, Figure 2.9(a). The closer the V_{max} to V_{oc} and J_{max} to J_{sc} the better the FF; high FF is one of the requirements for high performing devices [2.20].

$$FF = \frac{V_{max} \times J_{max}}{V_{oc} \times J_{sc}} \quad (\text{eq. 2.1})$$

The power conversion efficiency (PCE) which is the main quantifying parameter for the solar cell performance is defined by a ratio of the maximum power output density to power input density (incident power). FF, V_{oc} , and J_{sc} are typically the parameters used to define the PCE as:

$$PCE = \frac{P_{max}}{P_{in}} = \frac{V_{max} \times J_{max}}{P_{in}} = \frac{FF \times V_{oc} \times J_{sc}}{P_{in}} \quad (\text{eq. 2.2})$$

The PCE is a ratio that is usually converted to percentages for comparison and the measurements of the J–V curve require to be collected under normal standard tests. These standard tests include solar (sun) simulated light intensity of 1000 W/m^2 (100 mW/cm^2) as power input density and measurements under room temperature conditions ($25 \text{ }^\circ\text{C}$) [2.20].

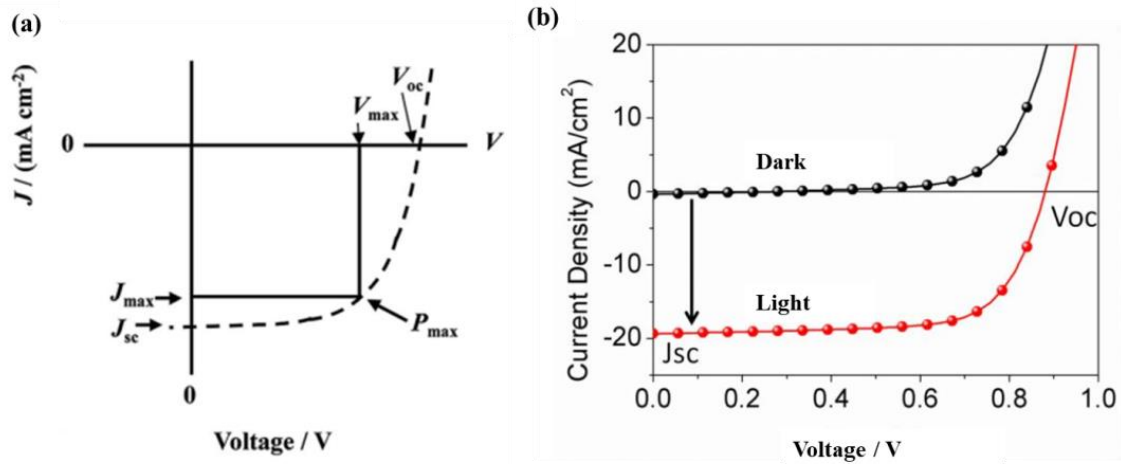


Figure 2.9: (a) Typical current density-voltage curves showing all the important solar cell parameters; (b) J–V curves of a working device under light illumination of 1000 W/m^2 (100 mW/cm^2) and under dark [2.20].

2.8.2 Perovskite Solar Cell Measurements

The solar cell performances were characterized by measuring the current density (J) and voltage (V) (J–V curves), recorded with a Keithley 2420 digital source meter where a bias voltage was applied and the generated current from the solar cell measured by the Keithley. The solar cells were measured under dark and with light illumination of 100 mW/cm^2 , AM1.5, generated by a solar simulator (Sciencetech Inc.) equipped with a xenon lamp. Figure 2.10(a) and (b) depicts the schematic and a photograph of the solar cell measurements setup, respectively. Illustrated components are a Sciencetech power supply, Sciencetech solar simulator with a xenon lamp, sample holder connected to a Keithley by a two-wire probe, and the Keithley which feeds the readings to a computer. The solar simulator has an optical filter to generate an AM1.5 spectrum and the lamp was adjusted to produce light intensity of 100 mW/cm^2 calibrated by a daystar light meter.

The solar cells were illuminated through a metal mask that defined an aperture area 0.05 cm^2 and the cells were illuminated from the glass side and through the FTO and c-TiO₂. The solar cells were illuminated for 15 seconds before measurements with J–V curves recorded in forward scan from -0.2 V to 1 V and reverse scan 1 V to -0.2 V with a fixed step voltage of 12 mV . Scanning from both forward and reverse scans was to take into consideration the effect of hysteresis in organic-inorganic hybrid perovskite solar cells [2.21, 2.22]. Some of the solar cell devices were stored in a drawer and measured at different days to study the stability of the devices.

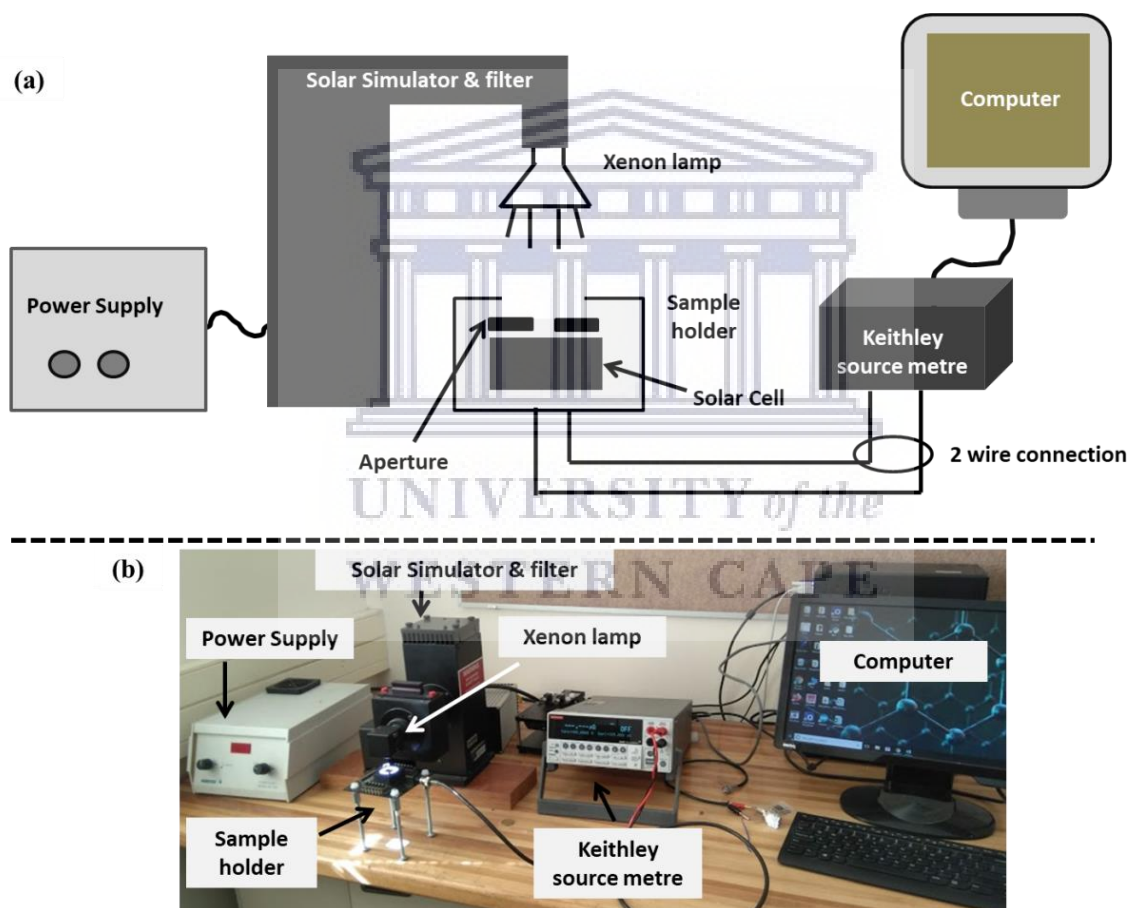


Figure 2.10: (a) Schematic of the J-V curve measurements in our lab showing all major components, (b) the photograph of the measurement setup.

2.9 References

- [2.1] Hugh O. Pierson, “Handbook of Chemical Vapor Deposition (CVD) – Principles, Technology, and Applications, (Second Edition)”, Noyes Publications/ William Andrew Publishing, LLC, Norwich, New York, U.S.A. (1999)
- [2.2] K.L. Choy, Progress in Materials Science 48 (2003) 57
- [2.3] P. O'Brien, N. L. Pickett, and D. J. Otway, Chemical Vapor Deposition, 8 (2002) 237
- [2.4] C.E. Morosanu, “Thin Films by Chemical Vapor Deposition”, Elsevier Publishing, Amsterdam, Netherlands (1990)
- [2.5] A. Sherman, “Chemical Vapor Deposition for Microelectronics” Noyes Publications, Park Ridge, New Jersey, USA (1987)
- [2.6] R.F. Bunshah, “Handbook of Deposition Technologies for Films and Coatings – Science, Technology, and Applications, (second edition)”, Noyes Publications, Park Ridge, New Jersey, USA (1994)
- [2.7] S. Ha, X. Liu, Q. Zhang, D. Giovanni, T. Sum, and Q. Xiong, Advanced Optical Material 2 (2014) 838
- [2.8] M. Tavakoli, L. Gu, Y. Gao, J. He, A. Rogach, Y. Yao, and Z. Fan, Scientific Reports 5 (2015) 14083
- [2.9] P. Luo, Z. Liu, W. Xia, C. Yuan, J. Cheng, and Y. Lu, ACS Applied Materials and Interfaces 7 (2015) 2708
- [2.10] V.-D. Tran, S.V.N. Pammi, V.-D. Dao, H.-S. Choi, and S.-G. Yoon, Journal of Alloys and Compounds 747 (2018) 703
- [2.11] S. Ngqoloda, C.J. Arendse, T.F. Muller, P.F. Miceli, S. Guha, L. Mostert, and C.J. Oliphant, ACS Applied Energy Materials 3 (2020) 2350
- [2.12] H. Sun, X. Zhu, D. Yang, J. Yang, X. Gao, and X. Li, Journal of Crystal Growth 405 (2014) 29

- [2.13] M. Schieber, N. Zamoshchik, O. Khakhan, and A. Zuck, *Journal of Crystal Growth* h 310 (2008) 3168
- [2.14] S. Ngqoloda, C.J. Arendse, T.F. Muller, F.R. Cummings, and C. Oliphant, *Materials Today: Proceedings* (2020)
- [2.15] M. Fox, “*Optical Properties of Solids*”, Oxford University Press Inc., New York, USA, (2001)
- [2.16] T.-B. Song, T. Yokoyama, S. Aramaki, and M.G. Kanatzidis, *ACS Energy Letters* 2 (2017) 897
- [2.17] D.A.G. Bruggeman, *Annals of Physics* 24 (1935) 636
- [2.18] R. Ahuja, H. Arwin, A. Ferreira da Silva, C. Persson, J.M. Osorio-Guillén, J. Souza de Almeida, C. Moyses Araujo, E. Veje, N. Veissid, C.Y. An, I. Pepe, and B. Johansson, *Journal of Applied Physics* 92 (2002) 7219
- [2.19] P. Löper, M. Stuckelberger, B. Niesen, J. Werner, M. Filipič, S. Moon, J. Yum, M. Topič, S. De Wolf, and C. Ballif, *Journal of Physical Chemistry Letters* 6 (2015) 66
- [2.20] J. Yan and B.R. Saunders, *RSC Advances* 4 (2014) 43286
- [2.21] A.K. Jena, H.-W. Chen, A. Kogo, Y. Sanehira, M. Ikegami, and T. Miyasaka, *ACS Applied Material Interfaces* 7 (2015) 9817
- [2.22] R.B. Dunbar, B.C. Duck, T. Moriarty, K.F. Anderson, N.W. Duffy, C.J. Fell, J. Kim, A. Ho-Baillie, D. Vak, T. Duong, Y. Wu, K. Weber, A. Pascoe, Y.-B. Cheng, Q. Lin, P.L. Burn, R. Bhattacharjee, H. Wang, and G.J. Wilson, *Journal of Materials Chemistry A*, 5 (2017) 22542

CHAPTER THREE

Controlled Deposition of Lead Iodide and Lead Chloride Thin Films by Low-Pressure Chemical Vapor Deposition

ABSTRACT:

Lead halide thin films, such as lead iodide (PbI_2) and lead chloride (PbCl_2), are used as precursor films for perovskites preparation that are frequently achieved by vacuum thermal evaporation, but rarely by the low-pressure chemical vapor deposition (CVD) method. Here we report on the deposition of PbI_2 and PbCl_2 thin films on glass substrates employing the low-pressure CVD method. The effect of the substrate temperature on the structure and morphology of the lead halide films is investigated. Crystalline films were realized for both lead halides with PbI_2 films showing high texture compared to the reduced texture of the PbCl_2 films. Large lateral grain sizes were observed for the PbI_2 films with flat platelets grain morphology and up to 734.2 ± 144.8 nm average grain size. PbCl_2 films have columnar grains with an average grain size up to 386.7 ± 119.5 nm. The PbI_2 films showed a band gap of about 2.4 eV confirming its semiconducting properties and the PbCl_2 had a wide band gap of 4.3 eV, which shows the insulating properties of this material.

The contents of this chapter were published in: MDPI Coatings 2020, 10, 1208. Modifications were made in this chapter to suit thesis presentation and published supporting information has been included with discussion.

3.1 Introduction

Lead halide (PbX_2) thin films have been studied extensively as precursors for the recently discovered organic-inorganic halide perovskite thin film absorbers for photovoltaic application [3.1 – 3.6]. The deposition of PbX_2 ($X =$ iodine, chlorine, or bromine halide anions) is usually performed in the first step of the sequential two-step deposition of the hybrid perovskite thin films [3.3 – 3.6]. A primary hybrid perovskite compound is methyl ammonium (MA) lead iodide (MAPbI_3), and the mixed halide perovskites are $\text{MAPbI}_{3-x}\text{Cl}_x$ and $\text{MAPbI}_{3-x}\text{Br}_x$ ($x = 1 - 3$) [3.3 – 3.6].

Lead iodide (PbI_2) is a semiconductor with a wide optical band gap ($E_g > 2.3$ eV) and a hexagonal structure with a layer-by-layer growth of grains where lead ions are sandwiched between two layers of iodine ions [3.7 – 3.9]. Due to the high atomic weight ($Z_{\text{Pb}} = 82$, $Z_{\text{I}} = 53$) of PbI_2 , it is also applied as a good absorber of X-rays [3.7 – 3.10]. It has also been used as a stable nuclear radiation detector that is able to detect X-rays and Gamma rays [3.9, 3.10]. When PbI_2 is used as a scintillation detector, electron-hole pairs are created and thermalized in the conduction and valence bands of this semiconductor, upon the absorption of either an X-ray or Gamma ray. PbI_2 can further be used for printing, lithography, and X-ray imaging, among other applications [3.9, 3.10].

There are various deposition methods that have been reported for the preparation of Pb halide thin films or single crystals, such as spray pyrolysis, sol-gel, Bridgman's method, vacuum thermal evaporation [3.6, 3.7, 3.9 – 3.17], and, recently, solution method through spin coating for perovskites thin film preparation [3.3 – 3.5]. Pb halides have poor solubility in water and hence require dedicated solvents during spin coating, which makes this method of deposition un-attractive for scaling up [3.3, 3.5]. In addition, spin coating from a solution often results in smaller grains of PbI_2 and non-uniform layers, which produces poor quality converted

perovskite films [3.3 – 3.5]. Although vacuum thermal evaporation offers high control of the PbX_2 film coverage and thickness; this method requires relatively expensive ultra-high vacuum systems, thereby making low-pressure CVD a low-cost alternative [3.6, 3.9, 3.18, 3.19].

The deposition of PbI_2 platelets through low-pressure CVD has been reported on muscovite mica substrates [3.1, 3.13, 3.14]. However, reports on the deposition of PbI_2 thin films by the aforementioned method on glass substrates are scarce. On the other hand, PbCl_2 deposition by low-pressure CVD method has not been reported, except through high vacuum thermal evaporation. Since the hybrid perovskite thin film solar cells require deposition on transparent conductive oxides (TCO) substrates, it is important to study the deposition of Pb halides precursor films on similar substrates as research is still lacking [3.20, 3.21].

Herein we report on the deposition PbI_2 and PbCl_2 thin films on glass substrates through the low-pressure CVD method. The novelty of this study is demonstrated by the successful deposition of these lead halide films on glass substrates, which has not been achieved before, especially in the case of PbCl_2 thin films. The effect of the substrate temperature, which was controlled by adjusting the position of the glass substrates with respect to the heated Pb halide source zone in the tube furnace, is investigated. Highly crystalline thin films were obtained for both lead halides, with the PbI_2 films showing a high texture compared to the reduced texture of the PbCl_2 films, as observed from the X-ray diffraction results. Large lateral grain sizes were observed for the PbI_2 films with up to 734.2 ± 144.8 nm average grain size. The PbCl_2 films on the other hand have columnar grain shape with an average grain size up to 386.7 ± 119.5 nm. The band gap of the PbI_2 film amounts to 2.4 eV, confirming its semiconducting properties, whereas the PbCl_2 film has a wide band gap of 4.3 eV that confirms the insulating property of this material.

3.2 Experimental Procedure and Characterisation

3.2.1 Lead Halide Film Deposition

Before deposition, small pieces (2 cm²) of corning glass substrates were cleaned in acetone and isopropanol in an ultrasonic bath for 10 minutes each and then rinsed repeatedly with warm deionized water. A three-zone chemical vapor deposition (CVD) system with a horizontal ceramic tube (Zhengzhou Brother XD-1600MT Furnace Co., LTD, Zhengzhou City, China; tube has 6 cm inner diameter, and each zone is 20 cm in length [3.22]) was used to deposit the lead halides [3.20, 3.21]. The outlet side of the ceramic tube is connected to a rotary vacuum pump, which achieves a base pressure of 0.05 mbar. An automated pressure regulator controls the deposition pressure. The inlet side of the ceramic tube is connected to a nitrogen gas (N₂) line, which passes through a mass flow controller (MFC) from the N₂ cylinder. The schematic representation of the CVD furnace system is shown in Figure 3.1(a), showing all the major components.

About 150 mg of lead (II) iodide (Cas No. 10101-63-0, yellow powder, purity, 99%, Sigma-Aldrich Co., Saint Louis, MO, USA) or lead (II) chloride (Cas No. 7758-95-4, white powder, purity, 98%, Sigma-Aldrich Co., Saint Louis, MO, USA) were used as vapor sources, separately. During deposition, PbI₂ or PbCl₂ powder source was contained in ceramic boats and positioned at the centre of the first zone with substrates placed at the downstream of the tube onto flat silicon wafer supports. The respective positions of the sources and substrates are also illustrated in Figure 3.1(a). For the PbI₂ film deposition, the first zone with PbI₂ source was ramped up to a nominal temperature of 380 °C for the source evaporation with a ramping rate of 10 °C/minute [3.20, 3.21]. Substrates were placed at optimized distances of 15 cm or 16 cm away from the source, downstream, in positions that reach nominal substrate

temperatures of 135 °C or 125 °C, respectively, as measured using an external thermocouple prior to the deposition.

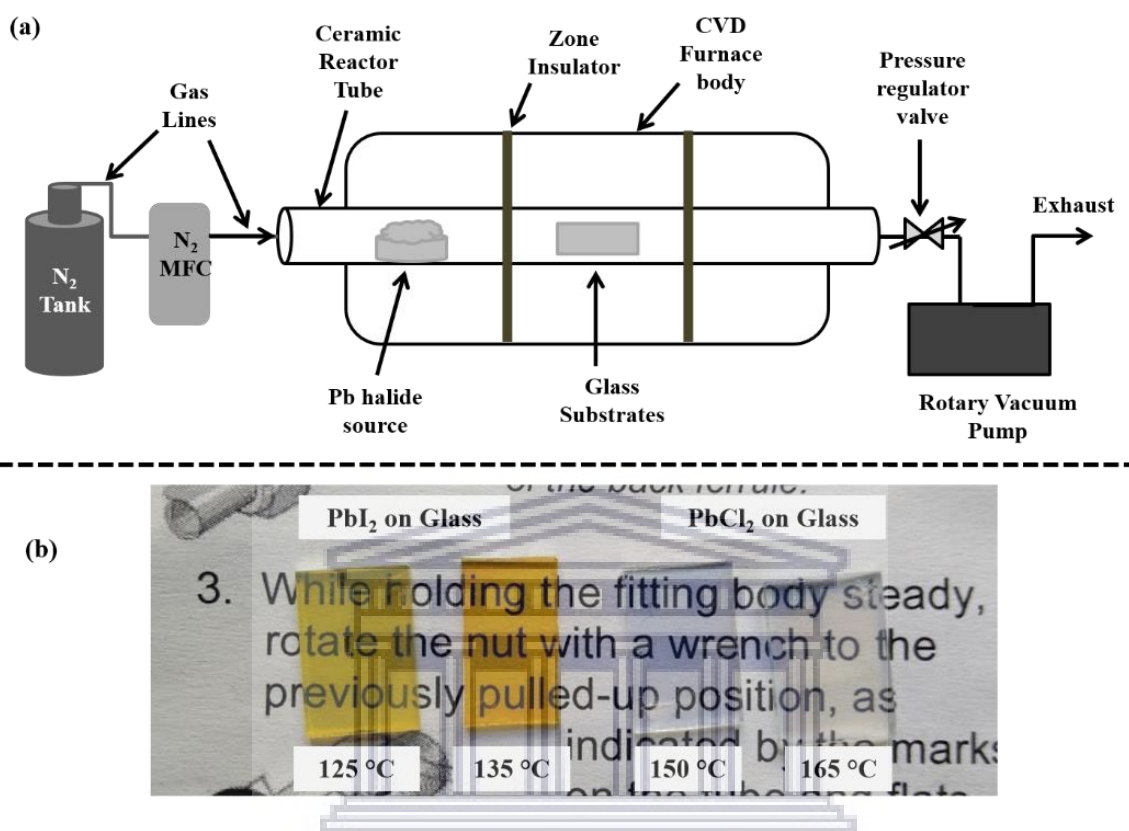


Figure 3.1: (a) CVD system schematic employed here showing all the important components; (b) Photographs of the as-deposited Pb halide films on glass at different deposition temperatures as shown (PbI₂ transparent yellow and PbCl₂ transparent white).

Similar conditions for PbCl₂ were followed except for the source sublimation temperature, which was 450 °C, and the substrates placed at optimized distances of 16 cm or 17 cm away from the source with nominal substrate temperatures of 165 °C or 150 °C, respectively. These substrate temperatures were selected based on preliminary experiments during the deposition optimization of Pb halide film thickness. Only the first zone was heated during these depositions and the different substrate temperatures were due the temperature gradient from the heated first zone towards the tube outlet. The depositions were allowed to dwell for 40

minutes with pressure controlled and maintained at 300 mbar during this deposition under continuous flow of N₂ at 100 standard cubic centimetres per minute (sccm). Transparent yellowish PbI₂ and whitish PbCl₂ thin films were obtained and no post-deposition treatments were performed on these thin films; the photographs of the films are shown in Figure 3.1(b). The observed difference in colour in the PbI₂ and PbCl₂ pairs is due to the thickness difference, where the thicker films are deposited at the higher substrate temperatures (135 °C for PbI₂ and 165 °C for PbCl₂).

3.2.2 Characterisation

To study phase composition and structure of these thin films, X-ray diffraction (XRD) was employed using a Panalytical Empyrean X-ray diffractometer (Malvern Panalytical Ltd. Malvern, Worcestershire, UK) with Cu K α 1 radiation (1.5406 Å) and operated at an acceleration voltage of 45 kV and 40 mA current. Samples were scanned over a 2 θ range of 5–99° with a scan step of 0.02626°. The morphology (surface and cross-sectional views) of the Pb halide layers was investigated using a Zeiss Auriga field-emission gun Scanning Electron Microscope (FEG-SEM, Jena, Germany) operated at acceleration voltages of 3–5 kV and equipped with energy dispersive X-ray spectroscopy (EDS) facilities to probe the elemental composition. The samples were lightly coated with carbon to enhance image quality. The cross-sectional samples were prepared by breaking the glass substrate after making a deep scratch on the back side of the glass to break it easily. A Tecnai F20 FEG transmission electron microscopy (FEG-TEM, Hillsboro, OR, USA) operated at 200 kV was used to examine the internal structure of the PbI₂ platelets and allows for electron diffraction measurements. The samples for the TEM were obtained by scratching the surface of the film and dispersing the flakes in an ethanol solution by sonication, followed by dropping it onto a Cu grid that was dried under a lamp. For optical transmission measurements, an Ocean Optics UV-visible

spectrophotometer (Ocean Insight, Orlando, FL, USA) was used with measurements taken from 250–1000 nm with a spectral resolution of 0.5 nm. Thin film thicknesses were measured using a Veeco Dektak 6M Stylus thickness profiler (Veeco Instruments, Inc. Tucson, Arizona, USA).

3.3 Results and Discussion

3.3.1 Structural Properties of Lead Iodide Films

The X-ray diffraction (XRD) patterns of the PbI₂ thin films on glass substrates deposited at substrate temperatures of 125 °C and 135 °C are shown in Figure 3.2(a). The observed peaks (2θ) at 12.7°, 25.6°, 38.8°, and 52.5° are assigned to the (001), (002), (003), and (004) diffraction planes, respectively, consistent with the results of previous reports [3.7, 3.8]. These XRD patterns are indexed to the 2H hexagonal ($P3\bar{m}1$) structure [3.7, 3.8] of crystalline PbI₂ phase. For both samples, the (001) peak is the most intense compared to other diffraction peaks, as shown in Figure 3.2(a) and (b), indicating a preferential growth orientation along the [001] direction that is parallel to the c-axis of the hexagonal PbI₂ unit cell [3.7, 3.8].

This highly intense (001) peak demonstrates that these PbI₂ films are highly textured as there appears no other family of planes in the XRD pattern such as the (110) [3.8]. The preferred growth orientation of PbI₂ thin films is related to its growth mechanism that follows a layer-by-layer growth through the Van der Waals bonding along the c-axis [3.1, 3.7]. Furthermore, the PbI₂ thin film deposited at the higher substrate temperature of 135 °C showed a slightly higher (001) peak intensity, as demonstrated in Figure 3.2(b). This may be due to improved crystallinity of the film due to higher substrate temperature deposition (135 °C), or it could be due to a thicker film thickness compared to its low-substrate-temperature (125 °C) counterpart.

The XRD patterns were fitted to obtain peak information on its peak position and peak width (full width at half maximum). The peak position in degrees was used to estimate the planar d-spacing via Bragg's diffraction equation: $2d_{hkl} \sin\theta = \lambda$, where d_{hkl} is the planar spacing, θ is half the XRD peak position and λ is the Cu K α 1 wavelength [3.23]. The planar d-spacing was in turn used to estimate the lattice constants of these films, summarized in Table 3.1. The lattice parameters are almost identical for the films and this is also indicated in Figure 3.2(b) where there is no distinct shift in the XRD peak positions of the (001) and (003) planes. The sample grown at the higher substrate temperature of 135 °C shows a slight lattice compression compared to the low substrate temperature sample (125 °C), which may be due to the compressive stress induced by the higher substrate temperature.

Table 3.1: Summary of X-ray diffraction information including lattice parameters (constants), crystallite sizes and strain of the two PbI₂ films deposited at different substrate temperatures.

| Sample Conditions | Lattice Parameter 'c' (nm) | Lattice Parameter 'a' (nm) | Crystallite Size (nm) | Strain ($\times 10^{-3}$) |
|-------------------|----------------------------|----------------------------|-----------------------|-----------------------------|
| 125 °C | 0.6959 | 0.4548 | 154.3 | 1.32 |
| 135 °C | 0.6956 | 0.4547 | 172.4 | 0.581 |

The vertical crystallite sizes of the films were also estimated using the Williamson-Hall (W-H) method, which takes into consideration the effect of strain. The W-H equation relates the peak broadening to the crystallites size via this relation: $\beta_d \cos\theta = 4\varepsilon \sin\theta + (k\lambda/D)$, where D is the crystallite size, k is a constant (0.94), λ is the Cu K α 1 wavelength, β_d is the full-width at half-maximum in radians (as discussed in [3.23]), θ is the peak position and ε is the strain parameter [3.23]. The W-H equation is explained and derived in [3.23] and the crystallite size

and strain are obtained through a linear plot of $\beta d \cos \theta$ vs. $4 \sin \theta$ as shown in Figure 3.2(c) and (d). The crystallite sizes were calculated by equating the y-intercepts to $k\lambda/D$ and strain (ϵ) is the slope of the linear fit, shown in Figure 3.2(c) and (d).

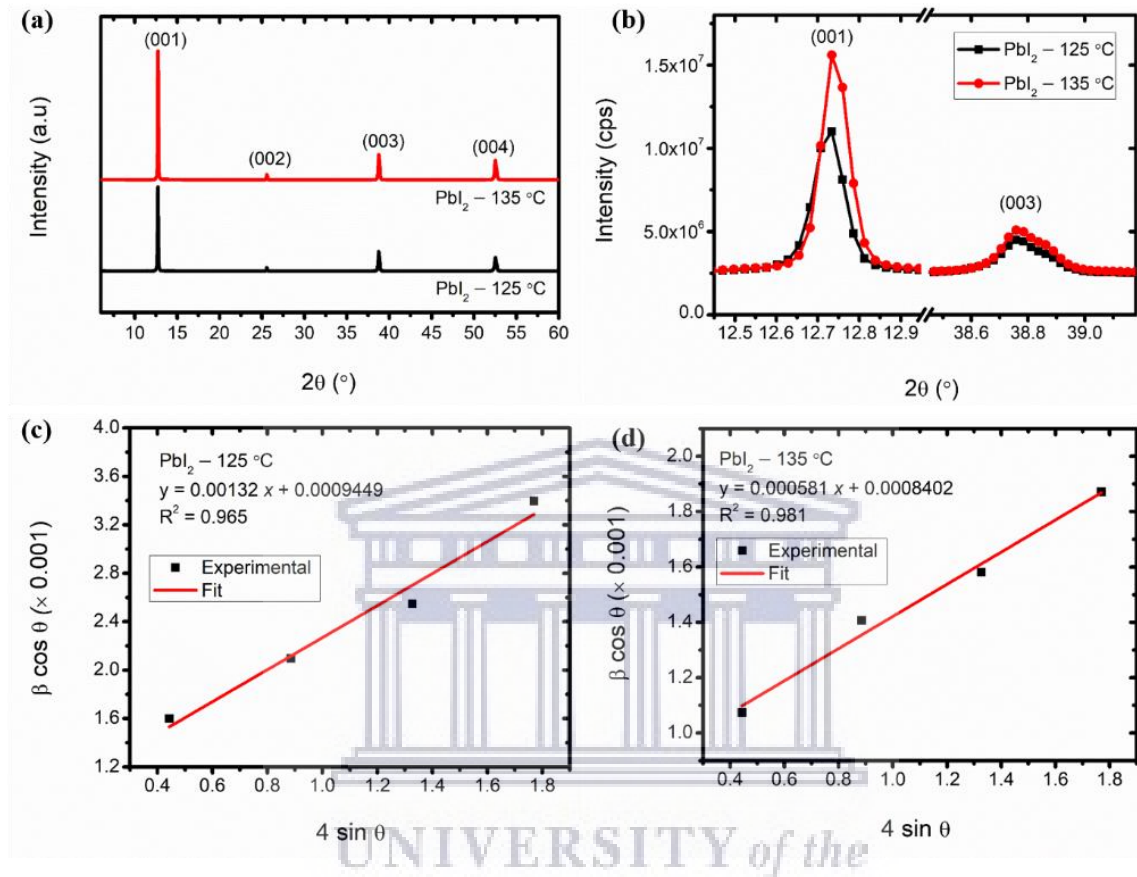


Figure 3.2: (a) Full XRD patterns of PbI_2 thin films on glass deposited at different substrate temperatures; (b) zoomed XRD patterns showing the two intense (001) and (003) peaks of the PbI_2 films; (c, d) Williamson-Hall plots for crystallite size and strain estimation of the two PbI_2 films.

The estimated crystallite sizes of these samples are also included in Table 3.1. The sample deposited at 125 °C substrate temperature had smaller crystallites size of about 154.3 nm compared to the sample deposited at higher substrate temperature of 135 °C, which amounted to about 172.4 nm. The increased crystallite size of the 135 °C sample is evident in the higher XRD peak intensity (Figure 3.2(b)), indicating the superior crystallinity of this sample. The

XRD data proves that the substrate temperature influences the crystallinity of the resulting PbI_2 films and therefore reiterates the importance of investigating the crystal structure of films deposited at different substrate temperatures, which in this case is also position-dependent that also has an effect on the film thickness, as will be discussed in the next section.

3.3.2 Morphology of Lead Iodide Films

The scanning electron microscopy (SEM) micrographs of the as-deposited PbI_2 films deposited at different substrate temperatures are provided in Figure 3.3(a) and (b). The film morphology is similar for both deposition conditions and is characterized by flat and compact grains, as shown by the higher magnification SEM micrographs in Figure 3.3(a) and (b). These flat grains are formed from coalesced hexagonal platelet grains and this is a common morphology of vapor deposited PbI_2 films [3.1, 3.7, 3.8, 3.11]. Some of these hexagonal platelet grains grow at angles with respect to the film surface with some lying perpendicular to the film surface as shown by the selected area in Figure 3.3(a) and (b).

The concentration of these surface platelets was higher for the sample grown at a higher substrate temperature, which is clearer in the lower magnification micrograph in Figure 3.3(d). These films are uniform over large areas, as evident from the lower magnification SEM micrographs in Figure 3.3(c) and (d). This is an indication of the suitability of the low-pressure CVD method for the deposition of PbI_2 films with tailored morphology at different substrate temperatures.

The compactness of the grains is also evinced by the fact that there are no clear observable grain boundaries between the grains. The histograms showing the distribution of the measured lateral grain sizes are given in Figure 3.4(a) and (b). The PbI_2 film deposited at 125 and 135 °C has an average lateral grain size of 588.7 ± 117.6 nm and 734.2 ± 144.8 nm, respectively. The

lateral grain sizes are larger than the vertical crystallite sizes estimated from the XRD results. This implies that these grains are composed of smaller crystallites. The flatness of the PbI_2 film morphology was also depicted in the cross-sectional SEM micrographs shown in Figure 3.4(c) and (d).

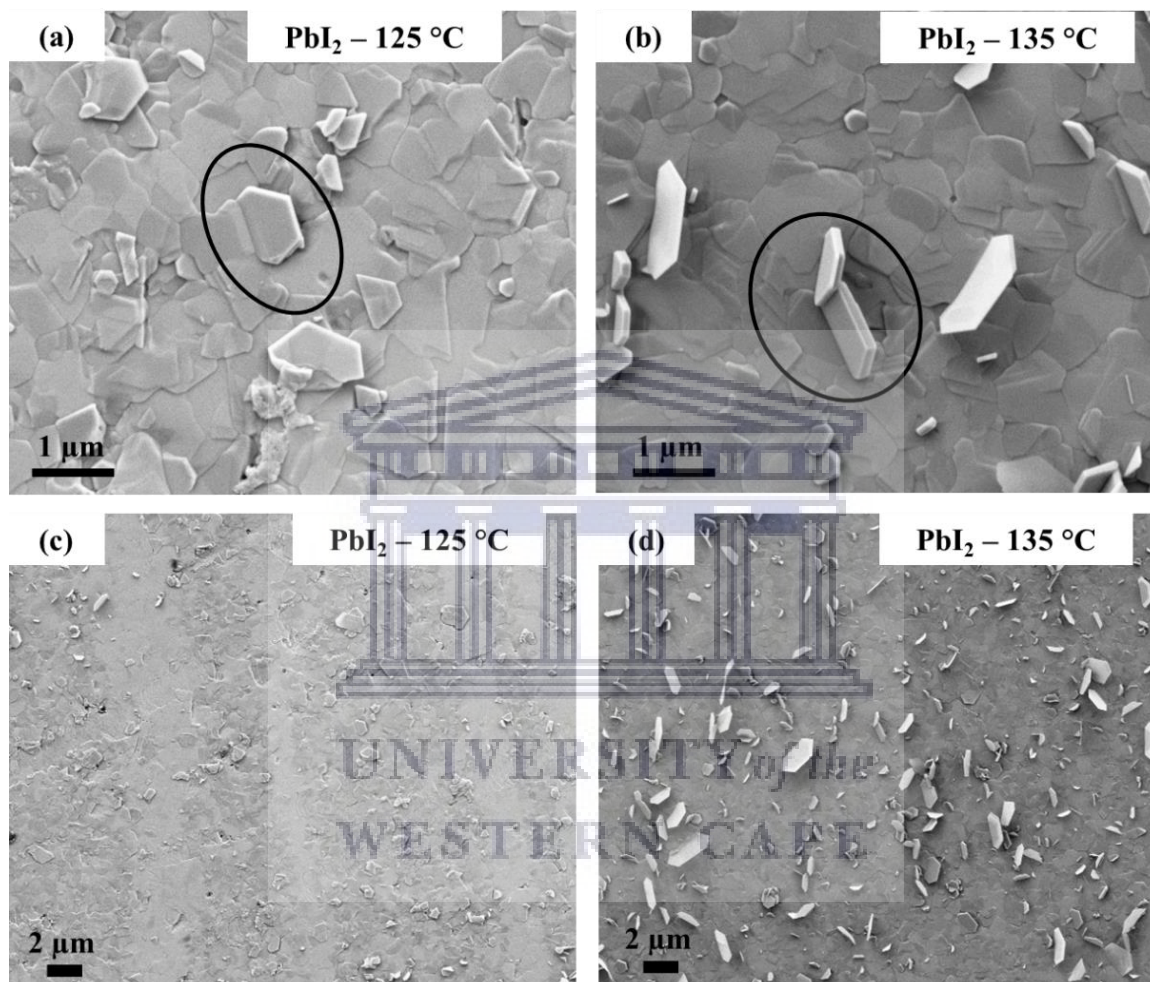


Figure 3.3: Planar SEM micrographs (high magnification) of PbI_2 thin films deposited at different substrate temperatures: (a) 125 °C, and (b) 135 °C; (c) and (d) Corresponding lower SEM magnification micrographs.

These films show a homogeneous film thickness with minimal roughness that are attributed to the surface platelets observed in the planar view SEM micrographs in Figure 3.4(c) and (d).

The thickness of the PbI_2 film deposited at $125\text{ }^\circ\text{C}$ was measured to be about 150 nm from the SEM micrograph (Figure 3.4(c)), which is thinner than the sample deposited at a substrate temperature of $135\text{ }^\circ\text{C}$ that has a thickness of about 290 nm (Figure 3.4(d)). These thickness values agree with that measured by profilometry. The thicker film produced at higher substrate temperature ($135\text{ }^\circ\text{C}$) is due to the faster deposition rate and the fact that the substrates were closer to the source than the lower substrate temperature ($125\text{ }^\circ\text{C}$) position. This observation confirms that the film thickness can be controlled by varying the substrate temperature and distance between source and substrate.

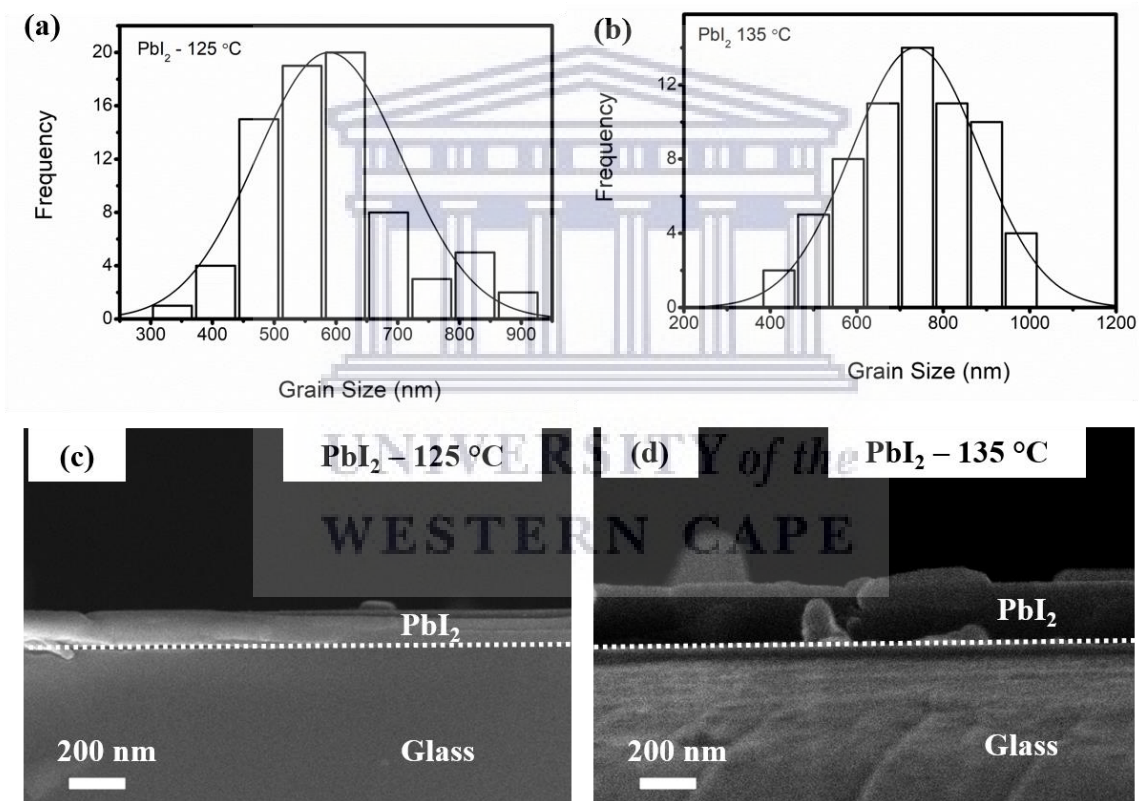


Figure 3.4: (a) and (b) Histograms showing measured lateral grain size distribution of the two PbI_2 thin film samples. Cross-sectional SEM micrographs of the PbI_2 samples for different substrate temperatures: (c) $125\text{ }^\circ\text{C}$, and (d) $135\text{ }^\circ\text{C}$.

These films grow flat on the surface of the glass with no clear grain boundaries across the film thickness. This again agrees with the compact grain nature observed in the planar SEM micrographs. The film thickness is slightly less than the average grain size for both deposition conditions, suggesting a faster lateral grain growth than vertical growth, which is ascribed to the minimized surface energy of the crystalline facets [3.24].

This faster lateral grain growth is clearly shown in the longer lateral dimension of the surface platelets in Figure 3.3(a) and (b) where a platelet grows longer than a micron (1 μm) size compared to the film thickness. This is attributed to the growth mechanism of PbI_2 platelet grains. The growth follows a layer-by-layer pattern of repeating I–Pb–I monolayers that are covalently bonded and separated by a weak Van der Waals bonding [3.20, 3.21, 3.24]. During growth, these monolayers layers are stacked perpendicular to the c-axis and parallel to the surface leading to a flat film surface. This flatness of the PbI_2 film was also realized due to the flat surface of the glass substrate as a rough surface may lead to tilted grains of PbI_2 [3.24]. This implies that the choice of the substrate determines the resulting morphology of the PbI_2 film.

Transmission electron microscopy (TEM) was used to probe the morphology and crystal structure of these platelet grains. The TEM samples were prepared by scraping off the surface of the films to increase the possibility of getting platelets. A low-resolution TEM micrograph of the platelets is shown in Figure 3.5(a) where a bundle of platelets is clearly visible. The high-resolution TEM micrograph in Figure 3.5(b) shows that the platelets are highly crystalline, with the measured inter planar spacing of 0.339 nm averaged over six atomic planes (Figure 3.5(b)) that belongs to the (101) family of plane of the hexagonal PbI_2 structure [3.14, 3.25]. The selected area electron diffraction (SAED) pattern in Figure 3.5(c) further proves that these platelet grains are highly crystalline with diffraction spots that form hexagons, in which the

spots forming the first hexagon are indexed to the (100) planes [3.14, 3.25]. The diffraction spot patterns that lie on the second hexagon with respect to the centre are indexed to the (110) planes. The hexagonal spot pattern of the SAED proves the crystalline nature of the PbI_2 films, in agreement with the XRD data.

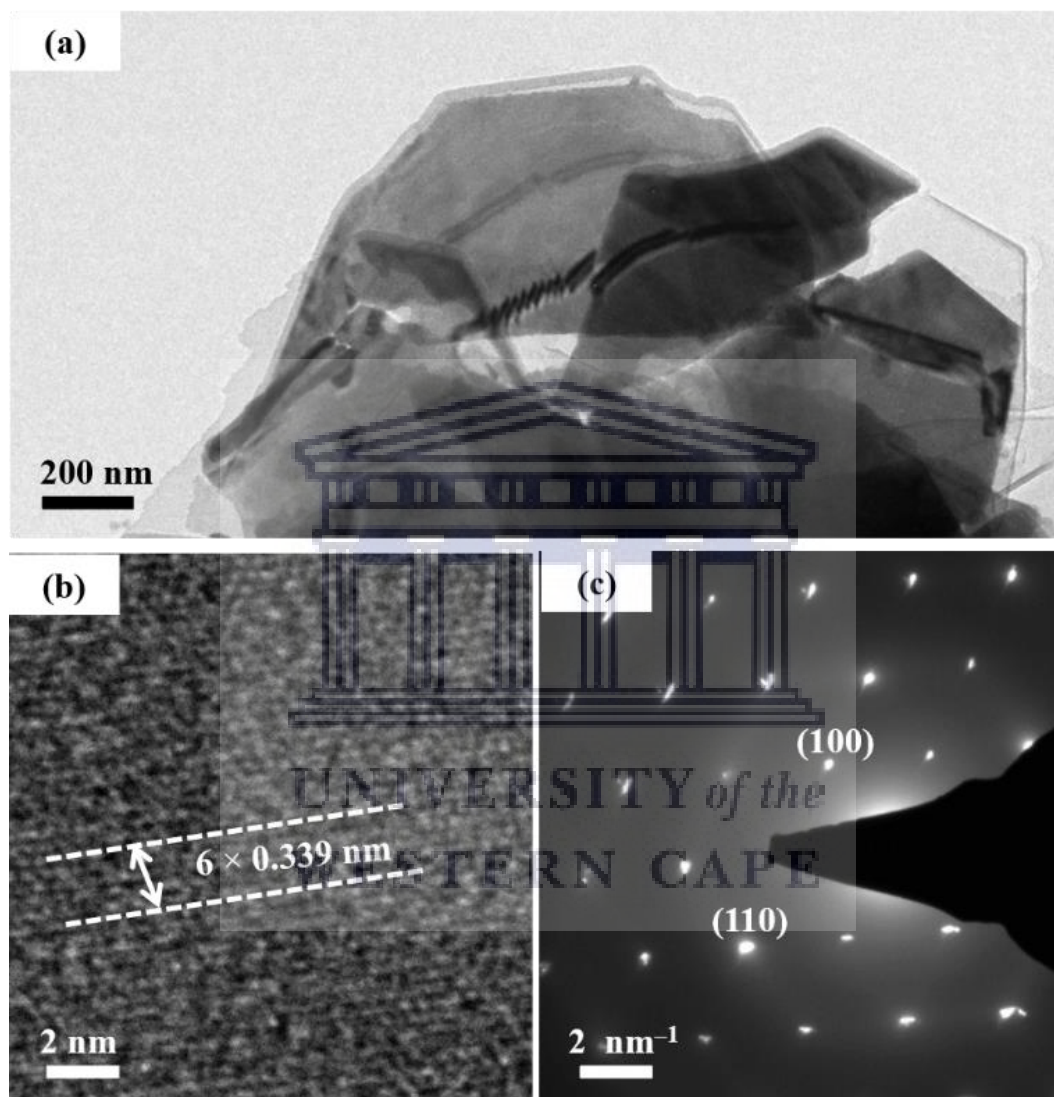


Figure 3.5: (a) Low resolution TEM micrograph of PbI_2 platelets scratched from the film surface; (b) high resolution TEM micrograph of the platelet in (a) showing atomic planes of PbI_2 ; (c) selected area electron diffraction pattern of the PbI_2 platelet showing single crystalline nature.

Elemental composition was verified by energy dispersive X-ray spectroscopy (EDS) taken at various positions of the two samples, with the spectra shown in Figure 3.6(a) and (b). The Pb/I atomic concentration for the 125 °C deposited sample was about 0.681 and for the 135 °C sample was 0.651, both higher than the stoichiometric PbI_2 which has Pb/I value of 0.5. These results show that there is an excess of lead in these films, which suggest the presence of metallic lead (Pb^0) in these films, i.e., un-bonded lead atoms. These results demonstrate the successful deposition of high quality and compact PbI_2 films with controllable morphology and thickness, which is beneficial for perovskite preparation, as the starting Pb halide layer determines the final properties of the resulting perovskite film during the two-step perovskite deposition.

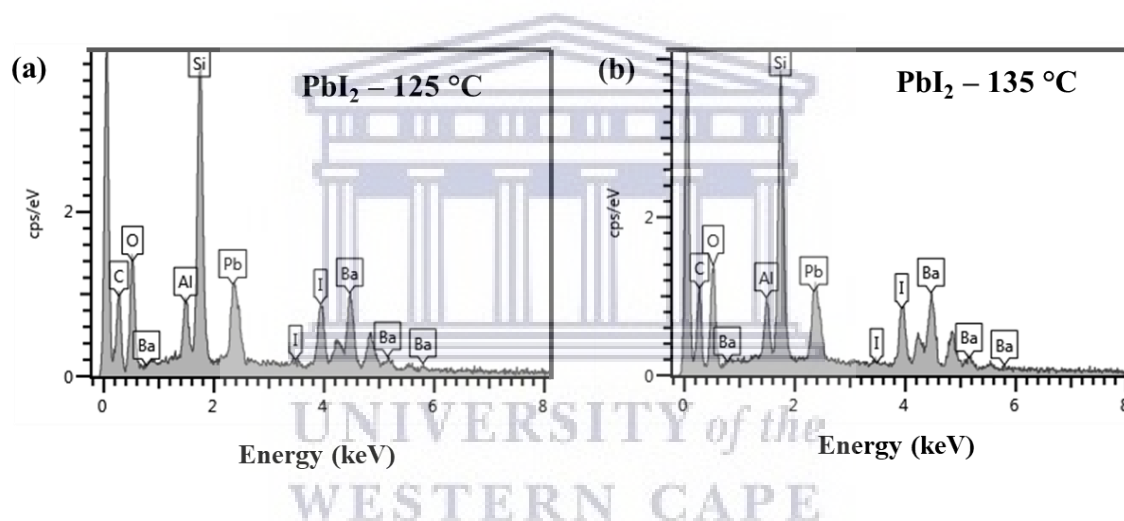


Figure 3.6: EDS spectrums of the PbI_2 film on glass substrates deposited at different substrate temperatures: (a) 125 °C, and (b) 135 °C.

3.3.3 Structural Properties of Lead Chloride Films

Two different substrate temperatures were also investigated for the deposition of lead chloride (PbCl_2) films and were 150 °C and 165 °C. These substrate temperatures are higher than those used during PbI_2 deposition mainly because the sublimation temperature of PbCl_2 was higher (450 °C) compared to that of PbI_2 (380 °C). XRD patterns of the PbCl_2 reveal crystalline films with intense peaks for both samples, as shown in Figure 3.7(a). The observed

peak at 22.25°, 24.67°, 25.21°, 32.55°, 40.05°, and 46.63° 2θ angle are assigned to the (101), (020), (111), (121), (004) and (033) diffracting planes, respectively, based on the the International Centre for Diffraction Data (ICDD), Data No. 00-001-0536 [3.26]. These patterns are indexed to the orthorhombic crystal system, space group *Pnma* of polycrystalline PbCl₂ films [3.27, 3.28].

Table 3.2: Summary of XRD data including lattice parameters (*a*, *b*, and *c*), crystallite sizes and strain of the two orthorhombic PbCl₂ thin films deposited at different substrate temperatures.

| Sample Condition | <i>a</i> (nm) | <i>b</i> (nm) | <i>c</i> (nm) | Crystallite Size (nm) | Strain (×10 ⁻³) |
|------------------|------------------|------------------|------------------|-----------------------|-----------------------------|
| 150 °C | 0.4459 | 0.7575 | 0.9002 | 84.7 | 1.11 |
| 165 °C | 0.4458 | 0.7575 | 0.9001 | 94.7 | 0.839 |

The (111) planes show high peak intensity for both samples (Figure 3.7(a)), but in general these PbCl₂ films show poor texture compared to PbI₂ films. Comparing the two PbCl₂ deposition conditions in Figure 3.7(b), the samples show no significant peak shift where the sample deposited at higher substrate temperature of 165 °C has a higher peak intensity that suggests superior crystallinity. The summary of the lattice parameters is given in Table 3.2, as calculated for the orthorhombic crystal phase. There is a slight lattice compression for the sample deposited at the higher substrate temperature (165 °C) compared to the sample deposited at 150 °C.

The crystallite sizes of these films were also estimated via the W–H method as discussed for the PbI₂ structure. The estimated crystallite sizes for the two samples are also provided in Table 3.2 and the plots are shown in Figure 3.7(c) and (d). The PbCl₂ film deposited at 150 °C

showed smaller crystallites with an average value of about 84.7 nm compared to the sample deposited at 165 °C, with an average crystallite size of 94.7 nm.

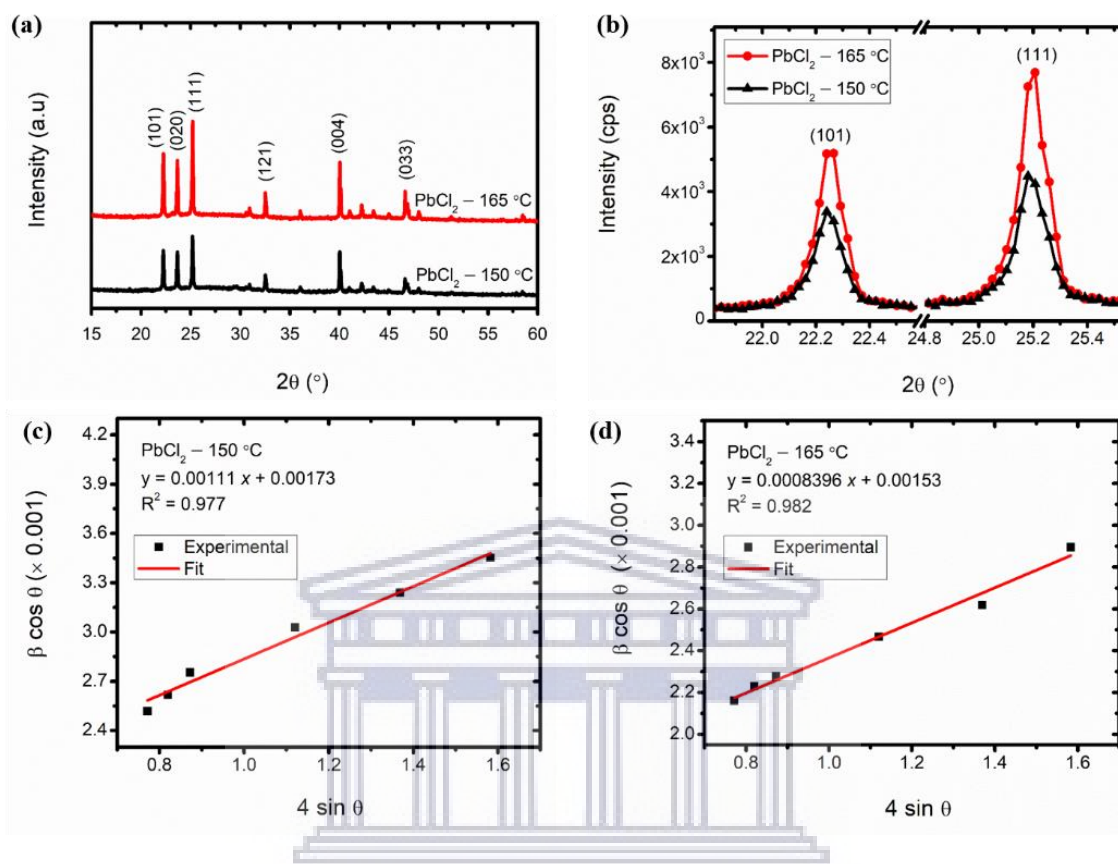


Figure 3.7: (a) Full XRD patterns of PbCl₂ thin films on glass, deposited at different substrate temperatures; (b) Zoomed XRD patterns showing the two intense (101) and (111) peaks of the PbCl₂ films; (c, d) Williamson-Hall plots for crystallite size and strain estimation of the two PbCl₂ films.

The trend in these results is similar to those observed for PbI₂ films with low substrate temperature deposition (150 °C) resulting in a smaller crystallite size. This is related to crystallite growth that is limited by the size of lateral grains and the film thickness, as it is the case for PbCl₂ films where higher substrate temperature (165 °C) deposition resulted in thicker films with larger lateral grains than low substrate temperature (150 °C) deposited films. The sample deposited at 165 °C also show a low strain from the W-H estimation. These XRD results

confirm that highly crystalline PbCl_2 thin films can be achieved by the low-pressure CVD method with control of crystallinity by tuning the substrate temperature. The success of depositing high quality PbCl_2 films provides options for the preparation of Cl-doped hybrid perovskite films.

3.3.4 Morphology of Lead Chloride Films

High magnification planar SEM micrographs of the PbCl_2 thin films deposited at substrate temperatures of 150 °C and 165 °C are shown in Figure 3.8(a) and (b), respectively. The morphology of these films is very distinct to that of the lead iodide films. These PbCl_2 films have well defined semi-spherical grains forming a continuous compact film. Some of the grains grew into scattered nanowires (selected regions in Figure 3.8(a) and (b)), with the nanowire density dependent on the substrate temperature. The film morphology is uniform over large areas, as shown on the lower magnification micrographs in Figure 3.8(c) and (d). The lateral average grain size was estimated from the SEM micrographs and the respective grain size distribution histograms are provided in Figure 3.9(a) and (b). The average grain size of the PbCl_2 thin film deposited at a lower substrate temperature (150 °C) is about 344.8 ± 111.4 nm (Figure 3.9(a)), which is smaller than that of the PbCl_2 film deposited at 165 °C with an average grain size of 386.7 ± 119.5 nm (Figure 3.9(b)). These results are similar to the trend observed for the PbI_2 films.

This enlarged average grain size at a higher substrate temperature (165 °C) is consistent with the increase in PbCl_2 nanowire density as shown in Figure 3.8(c) and (d). The high substrate temperature could be providing sufficient energy to enlarge the grain sizes, which in turn results in the growth of nanowires on the surface of the film. The reliance of the nanowire growth on the substrate temperature has been reported before where catalysts were employed [3.29 – 3.31].

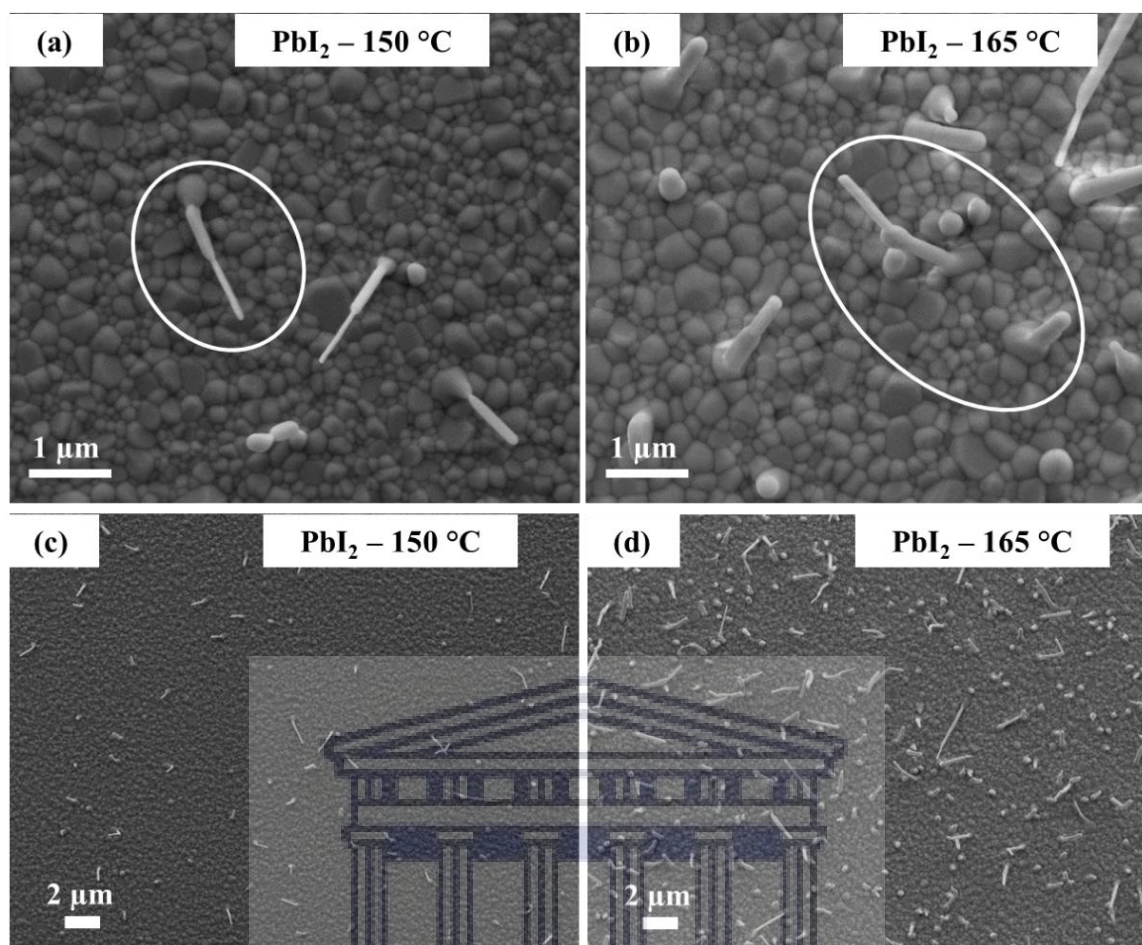


Figure 3.8: Planar SEM micrographs (high magnification) of PbI_2 thin films deposited at different substrate temperatures: (a) 150 °C, and (b) 165 °C; (c) and (d) Corresponding lower SEM magnification micrographs.

It is clearly visible in Figure 3.8(b) that these nanowires nucleate from larger PbCl_2 grains, hence their higher density for the sample with larger average grain size. The formation mechanism of these nanowire growths is unclear, but it can be supposed that the PbCl_2 grain growth has a saturation stage in the lateral direction. At this saturation stage the PbCl_2 protrude outwards where there may be free energy and hence forming the nanowires [3.29 – 3.32]. These results confirm that with low-pressure CVD, different structures of lead halide can be formed by tuning the substrate temperature.

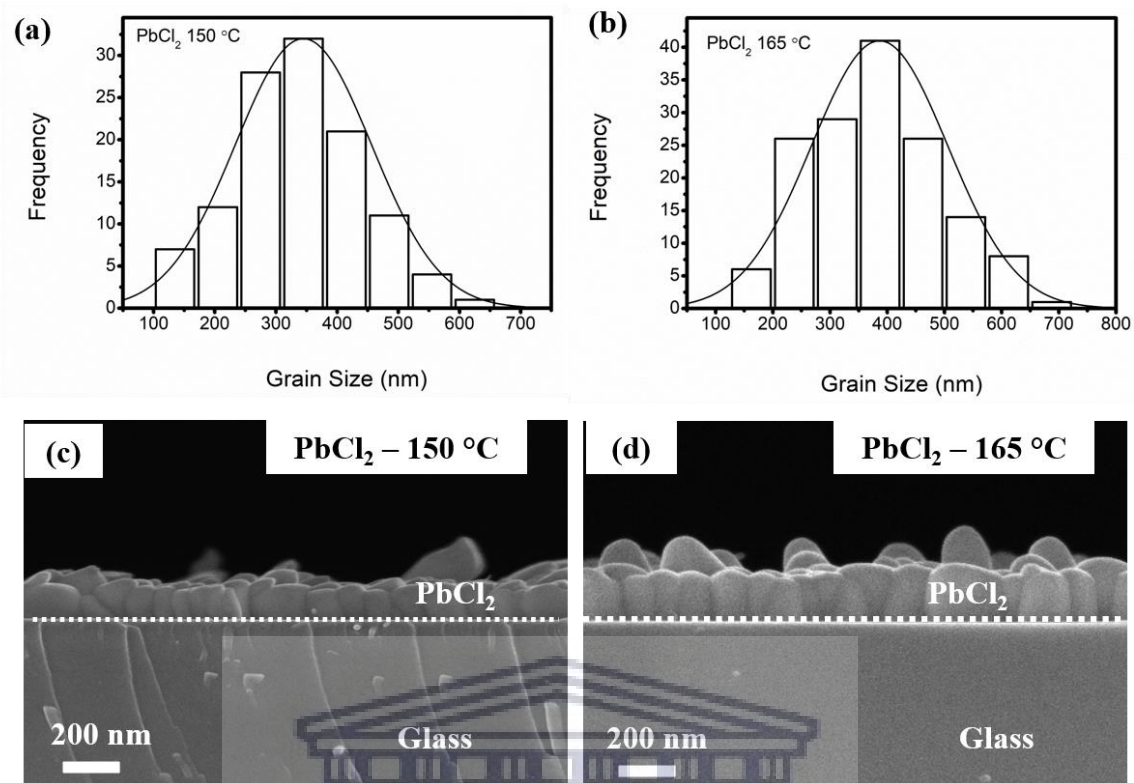


Figure 3.9: (a) and (b) Histograms showing measured lateral grain size distribution of the two PbCl₂ thin film samples as measured from the planar SEM micrographs. Cross-sectional SEM micrographs of the PbCl₂ samples for different substrate temperatures: (c) 150 °C, and (d) 165 °C.

The cross-sectional SEM micrographs of the PbCl₂ films are given in Figure 3.9(c) and (d), where a homogeneous film thickness is observed for both samples. The PbCl₂ grains are more columnar in shape and there are grains protruding out on the film surface, especially for the film deposited at 165 °C (Figure 3.9(d)). These protruding grains are an indication of the nanowire nucleation on the grains. The thickness of the PbCl₂ film deposited at 150 °C amounts to approximately 160 nm (Figure 3.9(c)) and that of the film deposited at 165 °C was measured to be about 210 nm (Figure 3.9(d)).

EDS measurements taken on these two PbCl_2 samples for chemical composition confirmed the presence of lead and chlorine in the films (Figure 3.10(a) and (b)). The EDS spectra were acquired on large surface areas of the films for better statistics. The Pb/Cl atomic concentration for the film deposited at a substrate temperature of $150\text{ }^\circ\text{C}$ was found to be 0.579 and for the film deposited at $165\text{ }^\circ\text{C}$ was found to be 0.519. These values are closer to the stoichiometric value of 0.5 for PbCl_2 compounds that is better than that obtained for PbI_2 films, suggesting less metallic lead in the PbCl_2 films. The EDS results further confirm the successful deposition of high-quality lead chloride films by the low-pressure CVD method.

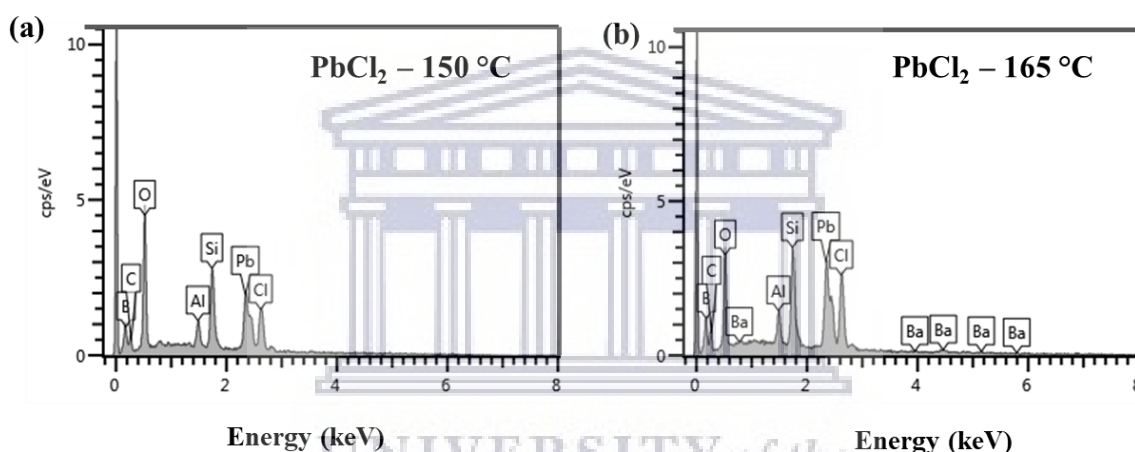


Figure 3.10: EDS spectrums of the PbCl_2 film on glass substrates deposited at different substrate temperatures: (a) $150\text{ }^\circ\text{C}$, and (b) $165\text{ }^\circ\text{C}$.

3.3.5 Optical Properties of the Lead Halide Films

The optical behaviour of the Pb halide thin films was evaluated from UV-Vis spectroscopy in the region $250 - 900\text{ nm}$. The transmittance spectra of the PbI_2 and PbCl_2 films are shown in Figure 3.11(a) and (b), respectively. The PbI_2 films have high light transmittance at wavelengths longer than 500 nm , Figure 3.11(a), whereas the PbCl_2 films transmit over the entire visible range, i.e., wavelengths longer than 350 nm as shown in Figure 3.11(b). For both compounds, the expected increased transmittance for the thinner films are evident.

Furthermore, the increased film thickness is also accompanied with the observed increase in the number of interference fringes for both compounds.

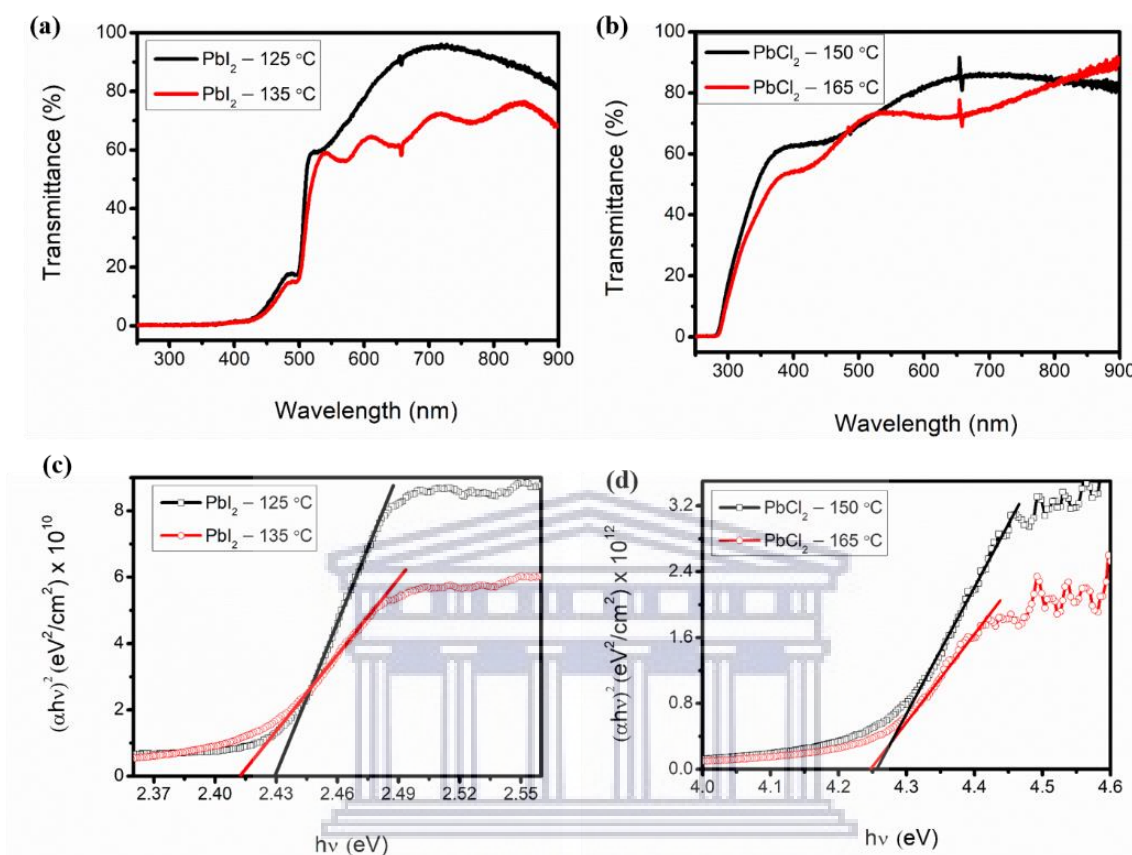


Figure 3.11: (a) UV-Vis transmittance spectrums of PbI₂ thin films on glass; (b) UV-Vis transmittance spectrums of PbCl₂ thin films on glass; (c) Tauc plots of PbI₂ films; and (d) Tauc plots of PbCl₂ films.

The optical band gap (E_g) of the Pb-halide films was estimated from the Tauc relation: $(\alpha h\nu)^2 = A(h\nu - E_g)$, assuming a direct band gap, where α is the absorption coefficient, $h\nu$ is the incident photon energy in eV, and A is a constant [3.7]. The band gap is extracted from the linear part of the plot of $(\alpha h\nu)^2$ vs. $h\nu$, where it intercepts the x-axis ($h\nu$), in which $(\alpha h\nu)^2 = 0$ as shown in Figure 3.11(c) and (d). The extracted optical band gaps were found to be similar at 2.43 eV and 2.41 eV for the PbI₂ films deposited at 125 °C and 135 °C (Figure 3.11(c)), respectively, which

is in the range of previously reported values for PbI₂ thin films [3.1, 3.7]. The PbCl₂ films has a wide optical band gap with similar values of 4.26 eV and 4.25 eV for films deposited at 150 °C and 165 °C (Figure 3.11(d)), respectively. These results show that PbI₂ films are wide band gap semiconductors and PbCl₂ films are insulators.

3.4 Conclusion

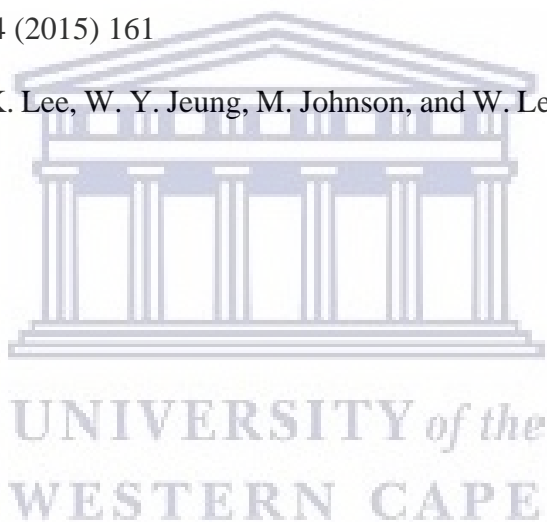
In conclusion, the successful deposition of high-quality crystalline films of lead iodide and lead chloride was realized through a low-pressure chemical vapor deposition method, offering a low-cost alternative for the preparation of precursor films for hybrid perovskite thin films. Highly textured PbI₂ films with large crystallites size of 154.3 nm and 172.4 nm were achieved for films deposited at substrate temperatures of 125 °C and 135 °C, respectively. Large lateral grain sizes were also observed for these PbI₂ films as measured from the SEM micrographs with an average grain size of 588.7 ± 117.6 nm for film deposited at 125 °C and 734.2 ± 144.8 nm for a sample deposited at 125 °C. PbCl₂ showed a reduced texture in the XRD patterns with smaller crystallite sizes than that of the PbI₂ films, with values of 84.7 nm and 94.7 nm for the films deposited at 150 °C and 165 °C, respectively. The PbCl₂ films have a columnar grain shape, compared to flat platelet grains of the PbI₂ films, with an average grain size of 344.8 ± 111.4 nm and 386.7 ± 119.5 nm for the films deposited at 150 °C and 165 °C, respectively. These large grain sizes for these lead halides films are beneficial for the conversion to large-grain perovskite films, which will be beneficial to the performance and stability of the perovskite solar cells. Optically, the PbI₂ films showed a band gap of about 2.4 eV, confirming its semiconducting nature. The PbCl₂ has a wide band gap of 4.3 eV, which shows the insulating properties of this material.

3.5 References

- [3.1] S. Ha, X. Liu, Q. Zhang, D. Giovanni, T. Sum, Q. Xiong, *Advanced Optical Material* 2 (2014) 838
- [3.2] A. Kojima, K. Teshima, Y. Shirai, T. Miyasaka, *Journal of American Chemical Society* 131 (2009) 6050
- [3.3] Z. Tang, S. Tanaka, S. Ito, S. Ikeda, K. Taguchi, and T. Minemoto, *Nano Energy* 21 (2016) 51
- [3.4] Q. Chen, H. Zhou, S. Luo, Y. Liu, G. Li, Y. Yang, *Journal of American Chemical Society* 136 (2014) 622
- [3.5] P. Luo, Z. Liu, W. Xia, C. Yuan, J. Cheng, and Y. Lu, *ACS Applied Materials Interfaces* 7 (2015) 2708
- [3.6] M. Leyden, L. Ono, S. Raga, Y. Kato, S. Wang, and Y. Qi, *Journal of Materials Chemistry A* 2 (2014) 18742
- [3.7] H. Sun, X. Zhu, D. Yang, J. Yang, X. Gao, and X. Li, *Journal of Crystal Growth* 405 (2014) 29
- [3.8] M. Schieber, N. Zamoshchik, O. Khakhan, and A. Zuck, *Journal of Crystal Growth* 310 (2008) 3168
- [3.9] Q. Wei, B. Shen, Y. Chen, B. Xu, Y. Xia, J. Yin, and Z. Liu, *Materials Letters* 193 (2017) 101
- [3.10] J. Xing, X.F. Liu, Q. Zhang, S.T. Ha, Y.W. Yuan, C. Shen, T.C. Sum, and Q. Xiong, *Nano Letters* 15 (2015) 4571
- [3.11] J. Costa, J. Azevedo, L. Santos, and A. Mendes, *Journal of Physical Chemistry C* 121 (2017) 2080
- [3.12] J. Condeles, T. Martins, T. dos Santos, C. Brunello, M. Mulato, and J. Rosolen, *Journal of Non-Crystalline Solids* 338–340 (2004) 81

- [3.13] W. Kong, G. Li, Q. Liang, X. Ji, G. Li, T. Ji, T. Che, Y. Hao, and Y. Cui, *Physica E: Low-dimensional Systems and Nanostructures* 97 (2018) 130
- [3.14] Y. Wang, L. Gan, J. Chen, R. Yang, and T. Zhai, *Science Bulletin* 62 (2017) 1654
- [3.15] Q. Zhang, S.T. Ha, X. Liu, T.C. Sum, and Q. Xiong, *Nano Letters* 14 (2014) 5995
- [3.16] J. Li, H. Wang, X.Y. Chin, H.A. Dewi, K. Vergeer, T.W. Goh, J.W.M. Lim, J.H. Lew, K.P. Loh, C. Soci, T. C. Sum, H.J. Bolink, N. Mathews, S. Mhaisalkar, and A. Bruno, *Joule* 4 (2020) 1035.
- [3.17] K.B. Lohmann, J.B. Patel, M.U. Rothmann, C.Q. Xia, R.D.J. Oliver, L.M. Herz, H.J. Snaith, and M.B. Johnston, *ACS Energy Letters* 5 (2020) 710.
- [3.18] M. Liu, M. Johnston, and H. Snaith, *Nature* 501 (2013) 395
- [3.19] O. Malinkiewicz, A. Yella, Y. Lee, G. Espallargas, M. Graetzel, M. Nazeeruddin, and H. Bolink, *Nature Photon.* 8 (2014) 128
- [3.20] S. Ngqoloda, C.J. Arendse, T.F. Muller, P.F. Miceli, S. Guha, L. Mostert, and C.J. Oliphant, *ACS Applied Energy Materials* 3 (2020) 2350
- [3.21] S. Ngqoloda, C.J. Arendse, T.F. Muller, F.R. Cummings, and C.J. Oliphant, *Materials Today Proceeding* (2020).
- [3.22] E.S.M. Mouele, S. Ngqoloda, S. Pescetelli, A. Di Carlo, M. Dinu, A. Vladescu, A.C. Parau, A. Agresti, M. Braic, C.J. Arendse, M. Braic, and L.F. Petrik, *Coatings* 10 (2020) 1–24
- [3.23] A.K. Zak, W.H.A. Majid, M.E. Abrishami, and R. Yousefi, *Solid State Sciences* 13 (2011) 251
- [3.24] F. Fu, L. Kranz, S. Yoon, J. Lockinger, T. Jager, J. Perrenoud, T. Feurer, C. Gretener, S. Buecheler, and A.N. Tiwari, *Physics Status Solidi A* 212 (2015) 2708
- [3.25] E. Klein, R. Lesyuka, and C. Klinker, *Nanoscale* 10 (2018) 4442

- [3.26] J.D. Hanawalt, H.W. Rinn, and L.K. Frevel, *Industrial & Engineering Chemistry Analytical Edition* 10 (1938) 457.
- [3.27] R. Sass, E. Brackett, and T. Brackett, *Notes* 67 (1963) 864.
- [3.28] L. Fan, Y. Ding, J. Luo, B. Shi, X. Yao, C. Wei, D. Zhang, G. Wang, Y. Sheng, Y. Chen, A. Hagfeldt, Y. Zhao, and X. Zhang, *Journal of Materials Chemistry A*, 5 (2017) 7423
- [3.29] V. Schmidt, J.V. Wittemann, and U. Gosele, *Chemical Reviews* 110 (2010) 361
- [3.30] X. Li, J. Ni, and R. Zhang, *Scientific Reports* 7 (2017) 15029
- [3.31] T. Ogino, M. Yamauchi, Y. Yamamoto, K. Shimomura, and T. Waho, *Journal of Crystal Growth* 414 (2015) 161
- [3.32] W. Shim, J. Ham, K. Lee, W. Y. Jeung, M. Johnson, and W. Lee, *Nano Letters* 9 (2009) 18



CHAPTER FOUR

Air-stable Hybrid Perovskite Solar Cell by Sequential Vapor Deposition in a Single Reactor

ABSTRACT:

Here we demonstrate a facile two-step low-pressure vapour deposition of methyl-ammonium lead iodide (MAPbI₃) perovskite films in a single reactor. Continuous, poly-crystalline lead iodide (PbI₂) films were deposited in the first step and successfully converted to high quality perovskite films in the second step during exposure of PbI₂ films to methyl-ammonium iodide (MAI) vapour. A complete conversion was realized after 90 minutes of exposure with an average grain size of $3.70 \pm 1.80 \mu\text{m}$. The perovskite conversion starts at the PbI₂ surface through the intercalation reaction of PbI₂ and MAI vapour molecules and progresses towards the PbI₂/substrate interface. The coverage and quality of the perovskite thin film is controlled by that of the pre-deposited PbI₂ film. The absorbance measurements confirmed air stability of the fully converted perovskite for 21 days, ascribed to its superior morphology and grain size. Finally, a planar perovskite solar cell, with no additives or additional interfacial engineering, was fabricated and tested under open-air conditions, yielding a best power conversion efficiency of 11.7%. The solar cell device maintains 85% of its performance up to 13 days in open-air with relative humidity up to 80%.

The contents of this chapter were published in: ACS Appl. Energy Mater. 2020, 3, 2350–2359. Modifications were made in this chapter to suit thesis presentation and published supporting information has been included here with discussion.

4.1 Introduction

The organic-inorganic hybrid perovskites have emerged as an interesting class of semiconductor materials for their application in photovoltaic (PV) and other semiconducting devices [4.1 – 4.3]. The first application of perovskites in PV technology was in 2009 by Kojima and co-workers [4.4], with measured power conversion efficiency (PCE) of about 3.8%, and in 2012 by Lee *et al.* [4.5] with improved PCE of about 10.9%. A fast rise in PCE of this material observed in just under a decade from 3.8% to over 25.2% is highly unique compared to other established PV technologies such as c-Si, GaAs, CdTe, and organic based solar cells [4.6]. The high efficiency of these organic metal halides perovskites has been attributed to its excellent optical and electronic properties. These include high optical absorption coefficient (ca. 10^4 cm^{-1}) and wide range of visible absorption with tunable direct band gap (1.5 – 2.3 eV), long carrier diffusion lengths, ambipolar charge transport, low intrinsic recombination rates due to weakly bounded excitons, high crystallinity, and low temperature processing [4.3, 4.7]. However, hybrid perovskite absorbers still face the issue of chemical instability as they degrade under continued exposure to moisture and UV light and are unstable at high temperatures [4.1, 4.3, 4.7].

Perovskite thin films are usually deposited via three main routes: solution spin coating, physical vapour deposition (vacuum thermal evaporation), and chemical vapour deposition (CVD). All these methods are either single step, where the organic cation is deposited simultaneously with the metal halide, or two-step sequential deposition, with the metal halide pre-deposited and organic halide material introduced in the second step [4.8 – 4.14]. The spin-coating methods have several challenges, which include incomplete surface coverage, use of solvents that may promote high instability, processing in inert environments, and lack of reproducibility. Thermal evaporation on the other hand requires the use of dedicated ultrahigh

vacuum systems. In addition, these techniques are not easily scalable and are in most cases incompatible with traditional deposition methods used in the semiconductor industry.

CVD has the advantage of being a well-established technique in the silicon processing industry [4.15]. It allows for the deposition of uniform thin films onto large substrate sizes, which aids in the scalability of the perovskite deposition process. CVD has been employed for the deposition of hybrid perovskite thin films by various groups based on the one-step [4.16] and two-step processes [4.14, 4.15, 4.17 – 4.26]. Although simpler, during one-step CVD it may be difficult to control the co-evaporation of the sources resulting in poor conversion and film quality. The two-step CVD method, referred to as hybrid CVD (HCVD), requires the pre-deposition of the Pb halide on substrates typically by spin coating or thermal evaporation [4.15, 4.17 – 4.26]. The pre-deposited Pb halide thin films are then placed inside the CVD furnace a distance away from the methyl ammonium iodide (MAI) source that is vaporized by thermal heating. The resultant MAI vapours are transported by the inert gas that diffuse through the layered Pb halide structure forming a solid perovskite during a chemical reaction of the MAI molecules with the layered Pb halide [4.15, 4.17].

HCVD still poses a challenge to scalability of the CVD technique, since the pre-deposited Pb halide layers are dependent on the inherent constraints of the spin-coating or thermal evaporation techniques. The highest PCE of perovskite fabricated by CVD method is 18.9% but the PbI_2 was also fabricated by spin coated method and converted to perovskite through CVD [4.27]. Comparative studies of different CVD methods for perovskite deposition and device performances have been given in review papers by Swartwout *et al.* [4.28] and Luo *et al.* [4.29] with PCE ranging between 7.9 and 18.9%.

The major drawback of perovskites is its instability when exposed to humidity, particularly for those grown by spin coating which requires the devices to be processed in a glove box.

There is thus a need to improve the stability of perovskites by producing thin films with large grain sizes, full surface coverage and improved morphology, while maintaining a high throughput on large-area substrates. Several strategies such as interface engineering, addition of interfacial coating layers to protect against moisture permeation, encapsulating layers to shield against moisture, and doping of the perovskite absorber layer have been employed. Amongst solution processed films, the use of ionic additives degrades the performance of encapsulated perovskite solar cells by only 5 % under continuous simulated full spectrum sunlight for more than 75 days at elevated temperatures [4.30].

Air stability remains an issue and there are not many reports of stability tests found in the literature from un-encapsulated CVD grown perovskite solar cells. Wang *et al.* [4.20] investigated the stability of CVD perovskite devices, which remained stable for 100 days stored in air at relative humidity of 40%. However, the group used a fresh hole transport layer and metal contact for each measurement. Peng *et al.* [4.21] also reported on the stability of their perovskite solar cell, which maintained 80% of initial performance after 31 days stored at ambient environment with 30% relative humidity. Another study on CVD grown perovskite device stability was reported by Tran *et al.* [4.26] where they employed single wall carbon nanotubes as a counter electrode and their device maintained 80% of initial 7.9%-efficiency for 500 hours of test under ambient atmosphere. Furthermore, Pammi *et al.* [4.31] investigated long term stability of CVD grown perovskite films on glass but these investigations were not conducted on a functioning device. Another recent study by Hoerantner *et al.* [4.32] demonstrated a fast CVD technique for perovskite preparation achieving 6.9% efficiency but did not discuss any long-term stability measurements. To reduce the production and installation cost of MAPbI₃ perovskite solar panels, the emphasis should be on addressing and improving the chemical stability of the MAPbI₃ perovskite absorber layer, as this will remove the costly and stringent encapsulation process required to protect the perovskite solar cell from humidity.

In this contribution, we report on the vapour deposition of a PbI_2 thin film in a CVD reactor, followed by its conversion to a uniform, poly-crystalline MAPbI_3 perovskite thin film, using the same CVD reactor. The novelty of this approach stems from the deposition of a uniform, compact and crystalline PbI_2 layer in the same CVD reactor at low pressure, as opposed to other hybrid CVD methods where the PbI_2 layer is deposited by either spin-coating or high vacuum thermal evaporation in a different reactor. As the CVD reactor allows for independent control of deposition parameters, this technique aids in improving the reproducibility of the perovskite thin films with enhanced morphology and stability. Moreover, since the deposition of the uniform PbI_2 layer is performed in the same CVD reactor in the first step, a scale-up synthesis is facilitated.

We further investigate the perovskite conversion process by exposing PbI_2 films to the MAI vapours in the second conversion step. The structural, morphological, and compositional properties are probed by powder and grazing incidence X-ray diffraction (XRD), scanning electron microscopy (SEM), and X-ray photoelectron spectroscopy (XPS), respectively. Furthermore, the air stability of a fully converted perovskite thin film is investigated through absorbance measurements for 21 days. The optimum converted perovskite film is applied in planar solar cell architecture with the best PCE of 11.7%, measured in air. The solar cell maintained 85% of its performance for 13 days of measurements under ambient conditions with the temperature ranging from 15 – 22°C and the relative humidity ranging from 60 – 80%.

4.2 Experimental Methods

4.2.1 Perovskite Film Fabrication

Corning glass substrates were cut into 1 cm × 1 cm sizes and subsequently cleaned in acetone and isopropanol for 10 minutes each in an ultrasonic bath and repeatedly rinsed with

deionized water. The CVD system used in this study is composed of a horizontal ceramic-tube, enclosed by a 3-zone ceramic tube furnace (Brother XD 1600MT manufactured by Zhengzhou Brother Furnace Co., LTD), where each zone is 20 cm in length. The base pressure in the system amounts to 10^{-2} mbar and the deposition pressure is maintained by an automated pressure regulating system. A schematic of the CVD system is shown in Figure 4.1(a).

For the deposition of the lead iodide (PbI_2) thin films (Step 1), about 150 mg of lead (II) iodide powder (99%, Sigma–Aldrich) in a ceramic boat was placed in the centre of the first zone and the Corning glass substrates were placed downstream, 15 cm away from PbI_2 source mounted on a ceramic substrate holder. The first zone was subsequently ramped at $10\text{ }^\circ\text{C}/\text{min}$ up to a nominal temperature of $380\text{ }^\circ\text{C}$, which is above the known sublimation temperature of PbI_2 . The temperature of the Corning glass substrate (15 cm downstream from the source) amounted to $145\text{ }^\circ\text{C}$. To transport the PbI_2 vapours towards the substrates, a nitrogen gas (N_2) flow rate of 100 sccm was maintained at a deposition pressure of 300 mbar. The deposition time amounted to 40 minutes for the complete consumption of the PbI_2 powder. Thereafter the N_2 flow was interrupted and the samples were allowed to cool to room temperature. A yellowish, compact PbI_2 thin film was produced, and no post treatment was performed on the PbI_2 thin films (Figure 4.1(b)).

The perovskite conversion of the PbI_2 thin films (Step 2) was performed in the aforementioned CVD system. About 200 mg of methyl ammonium iodide (MAI) (Dyesol) salt was placed in a fresh ceramic boat at also at the centre of the first zone and PbI_2 thin films placed 8 cm downstream from the MAI. The temperature of the MAI boat was subsequently ramped at $10\text{ }^\circ\text{C}/\text{min}$ up to a nominal temperature of $180\text{ }^\circ\text{C}$. The temperature of the PbI_2 /glass substrate (8 cm downstream from the source) amounted to $130\text{ }^\circ\text{C}$. The MAI vapours were transported towards the PbI_2 thin films by a N_2 flow of 100 sccm at a constant pressure of 50 mbar. To

investigate the perovskite conversion process, the conversion times for the MAPbI₃ samples were fixed to 15, 30, 60, 90 and 120 minutes. Figure 4.1(b) displays photographs of the PbI₂ thin film and the converted MAPbI₃ samples after various conversion times.

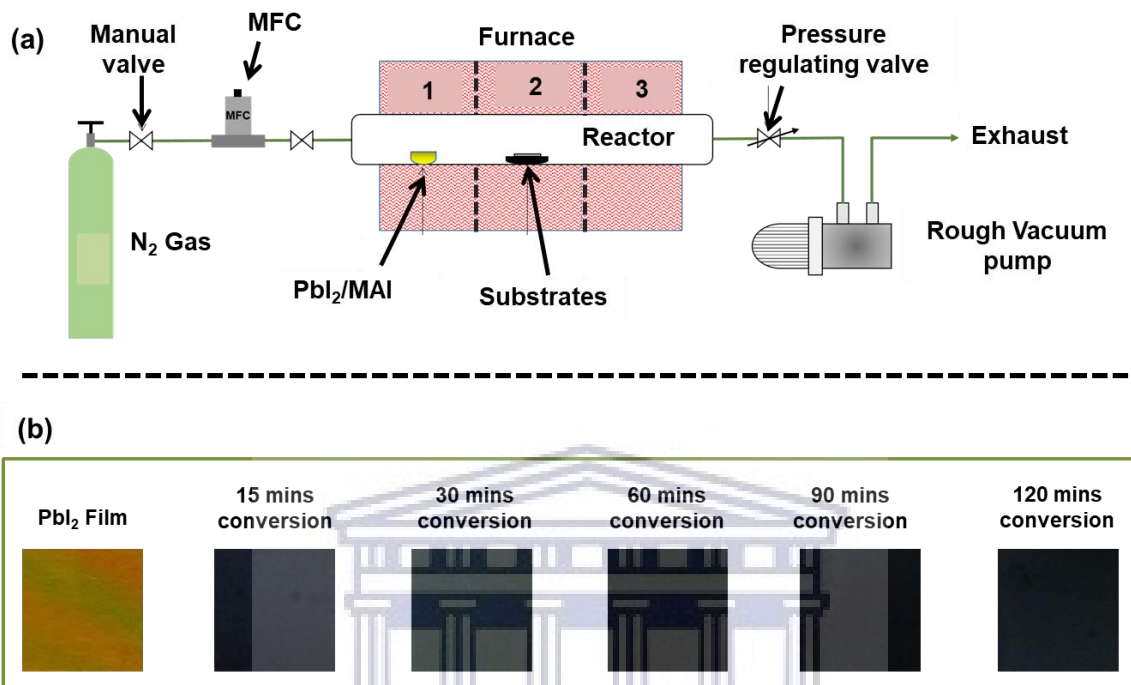


Figure 4.1: (a) Schematic illustration of the home-built chemical vapour deposition system, (b) photographs of the deposited films with a yellow PbI₂ and the dark perovskites after different conversion times as labelled.

4.2.2 Perovskite Solar Cell Fabrication

The device fabrication was done under ambient conditions (temperature and humidity) in air. All chemicals used here were purchased from Sigma-Aldrich and used as bought. Fluorine-doped tin oxide (FTO) coated glass substrates (10 Ohms/sq.) were cut into 1.5 cm × 2 cm sections and etched with Zn powder and 2 M hydrochloric acid (HCl). These samples were sequentially cleaned with hellmanex detergent (2%) and isopropanol in an ultrasonic bath followed by a thorough rinsing in hot deionized water and finally cleaned with UV ozone for 10 minutes. A 365 μL of titanium isopropoxide was added into 2.5 mL of ethanol, and 35 μL

of HCl (2 M) also added into 2.5 mL of ethanol, mixed to form 5 ml solution and stirred for an hour. The prepared solution was spin coated on the etched FTO substrates at 2000 rpm for 30 seconds to obtain a titanium containing film followed by 4000 rpm spin coating as a second coat, also for 30 sec, to fill any voids left during the first spin coating step.

The samples were dried on a hot plate at 150 °C for 5 min and then annealed at 500 °C for 30 minutes using a tube furnace at atmosphere to form a compact (c-)TiO₂ film. The fully converted (90-minute) perovskite film was employed as the absorber layer onto the c-TiO₂ layer. To finalize the device a hole transport layer (HTL) was spin coated on top of the perovskite film at spin speed of 2000 rpm for 30 s. The HTL solution was prepared by dissolving 80 mg of Spiro-MeOTAD in 1 mL of chlorobenzene, to which 40 μL of 4-tert-butylpyridine (tBP) and 25 μL of lithium bis- (trifluoromethanesulfonyl) imide (LITSFI) solution (52 mg of LITSFI in 100 μL of acetonitrile) were added and stirred for 30 minutes. Finally, 100 nm of silver electrode was deposited by thermal evaporation at a deposition pressure of 10⁻⁵ mbar through a shadow mask with device active area of 0.05 cm².

4.2.3 Characterization

The phase composition and the crystal structure were identified by X-ray diffraction (XRD) using a PANalytical Empyrean X-ray diffractometer with Cu Kα1 radiation (1.54 Å) at an acceleration voltage of 45 kV and current of 40 mA over the 2θ-range of 5–50° with a scan step of 0.02°. The morphology of the thin films were investigated using a Zeiss Cross Beam 540 Focused Ion Beam Scanning Electron Microscope (FIB-SEM) operated at an acceleration voltages of 1–3 kV and equipped with energy dispersive X-ray spectroscopy (EDS) for elemental composition.

X-ray photoelectron spectroscopy (XPS) was carried out on a Thermo Scientific ESCALAB 250 surface and depth analysis system equipped with a monochromatic Al K α X-ray (1486.7 eV) source. Optical transmission spectra were measured from 250–1000 nm with a spectral resolution of 0.5 nm, using an Ocean Optics UV-visible spectrophotometer. Current density (J)–voltage (V) characteristics were recorded with a Keithley 2420 source meter under illumination of 100 mW/cm², AM1.5, by a solar simulator (Sciencetech Inc.) in air. The cells were illuminated for 15 seconds before measurements with J–V curves recorded in forward scan (-0.2 to 1 V) and reverse scan (1 to -0.2 V) with a step voltage of 12 mV.

4.3 Results and Discussion

4.3.1 Thin Film Deposition

Crystalline PbI₂ thin films were successfully deposited in the first step of the sequential low pressure chemical vapour deposition (LPCVD method). Figure 4.2(a) shows the XRD pattern of a pure, high quality PbI₂ thin film on glass substrate, depicting its poly-crystalline nature. The observed peaks at ~12.74°, 25.59°, 38.76°, and 52.51° belongs to the (001), (002), (003), and (004) diffracting planes, respectively, based on the Joint Committee on Powder Diffraction Standards (JCPDS, data no. 07-0235). This XRD pattern is indexed to the hexagonal (P $\bar{3}$ m1) structure [4.33, 4.34] of a highly crystalline PbI₂ film.

A slight shift in 2 θ -peak positions was observed as compared to the standard pattern, which suggest a slight compression of the d-spacing (less than 1%) and hence compression of the c-axis lattice constant that can be ascribed to the higher growth temperature (ca. 380° C) of the PbI₂ films. The (001) peak is the most intense, indicating a preferred growth orientation along the [001] direction, which is parallel to the c-axis of the hexagonal crystal structure. This preferred growth direction is linked to the growth mechanism of PbI₂ thin films, which follows

a layer-by-layer growth of repeating I-Pb-I monolayers along the c-axis and separated by a van der Waals gap [4.33 – 4.35]. This van der Waals gap allows an easy intercalation of foreign molecules, such as MAI, during the conversion to perovskite.

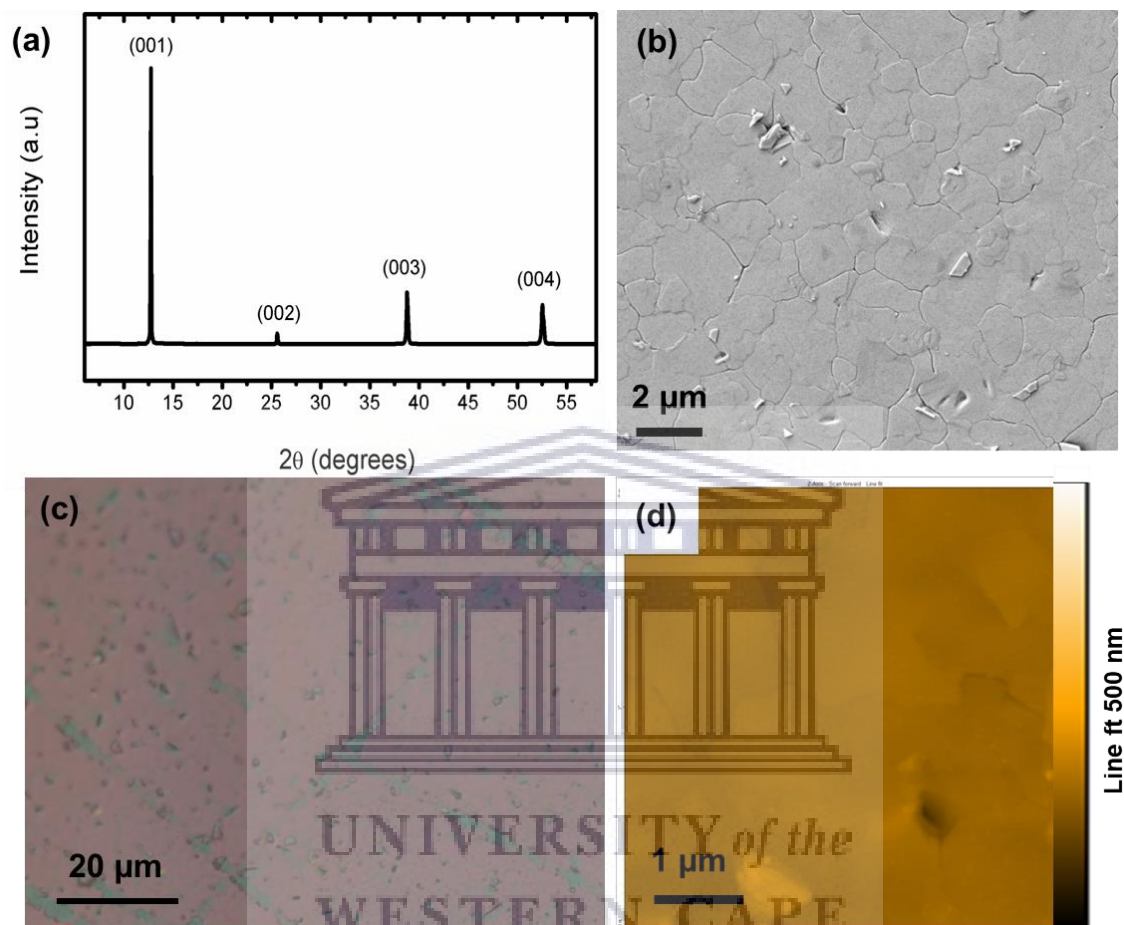


Figure 4.2: (a) XRD pattern, (b) planar SEM micrographs, (c) optical micrograph, and (d) an AFM micrograph of the as-deposited PbI_2 film during the first step of the sequential low pressure CVD method.

A uniform, smooth PbI_2 film is shown in the scanning electron microscopy (SEM) micrograph in Figure 4.2(b) with large and compact visible grains and well-defined grain boundaries. This successful growth of a PbI_2 film is achieved through evaporation of PbI_2 source that moves towards the substrate due to temperature gradient in the CVD tube assisted

by N₂ flow. The growth begins with this layer-by-layer deposition on the substrate forming a continuous film under the optimum conditions of temperature and pressure. The smooth surface is related to the grain formation during deposition (layer-by-layer growth) and these flat grains of PbI₂ are often referred to as platelets grains [4.14, 4.33 – 4.35]. The SEM micrograph also confirms a full surface coverage with no pinholes present in the film.

Optical micrograph of this PbI₂ film is also shown in Figure 4.2(c) depicting a larger area of the film surface with few scratches due to sample handling. The root mean square (RMS) roughness of about 8.5 nm was extracted from the PbI₂ atomic force microscopy (AFM) micrograph in Figure 4.2(d). The smooth surface of the PbI₂ film is related to the platelet grain formation during deposition as discussed earlier, i.e., layer-by-layer growth. The lateral grain size amounts to $1.60 \pm 0.62 \mu\text{m}$ (as measured from the SEM micrograph in Figure 4.2(b)). There are, however, grains larger than 1.6 μm measured along their length. The PbI₂ large grain sizes are due to a fast-preferred grain growth along the lateral direction where there is a minimized facet surface energy as opposed to along the c-axis (vertical direction) [4.35]. Hence, the grains are larger than the film thickness of $230 \pm 15 \text{ nm}$ [4.35]. These larger grains are favourable for conversion to perovskite phase and are expected to grow larger in size during the perovskite conversion through the diffusion of methyl ammonium iodide (MAI) molecules through the layered PbI₂ structure.

The PbI₂ thin films were successfully converted into the MAPbI₃ perovskite films during their exposure to the MAI vapour in the second step. During conversion, the MAI vapour diffuses towards the heated PbI₂ films on glass substrates, which upon contact with the PbI₂ film surface, it diffuses through PbI₂ layered framework. The proposed reaction mechanism is an intercalation of the MAI into the layered PbI₂, beginning at the surface (top) [4.10] or at the

substrate interface (bottom) [4.17]. Here the deposition mechanism and conversion process are investigated at different conversion times.

Figure 4.3(a) shows the XRD patterns of MAPbI₃ perovskites converted after 15, 30, 60, 90 and 120 minute exposure times. The MAPbI₃ patterns show major diffraction peaks at 14.05°, 19.94°, 28.39°, 31.81°, and 40.61° 2θ, assigned to the (110), (112), (220), (310), and (224) planes, respectively, of the tetragonal (I4/mcm) MAPbI₃ phase known to be stable at room temperature [4.36, 4.37]. There are other smaller peaks at 23.44° (211), 24.42° (202), 34.91° (204), and 43.09° (330); also indexed to tetragonal MAPbI₃ perovskite [4.36, 4.37]. The small peak at 23.44° is inconsistent with the cubic symmetry of MAPbI₃, hence confirming a pure tetragonal phase perovskite [4.36, 4.37].

The XRD pattern of the 15 minutes converted film shows sharp peaks belonging to the hexagonal PbI₂ phase (shown by solid diamond) that is more intense than the MAPbI₃ perovskite peaks, which confirms the coexistence of the two phases. This demonstrates that the conversion process is incomplete after 15 minutes exposure. A very small peak at 12.74° that belongs to a low level PbI₂ impurity appears for the 30 and 60 minute converted perovskites (as seen in Figure 4.3(a)), suggesting that the majority of the PbI₂ is converted to perovskite with a small fraction of PbI₂ still present. The PbI₂ impurity peak disappears after 90 minutes conversion time, confirming complete conversion of the PbI₂ film into MAPbI₃ perovskite after this exposure time. Further exposure after 120 minutes does not induce an appreciable change in the XRD pattern. These results show that the intercalating reaction begins the instant that the PbI₂ coated substrate is exposed to the MAI vapour.

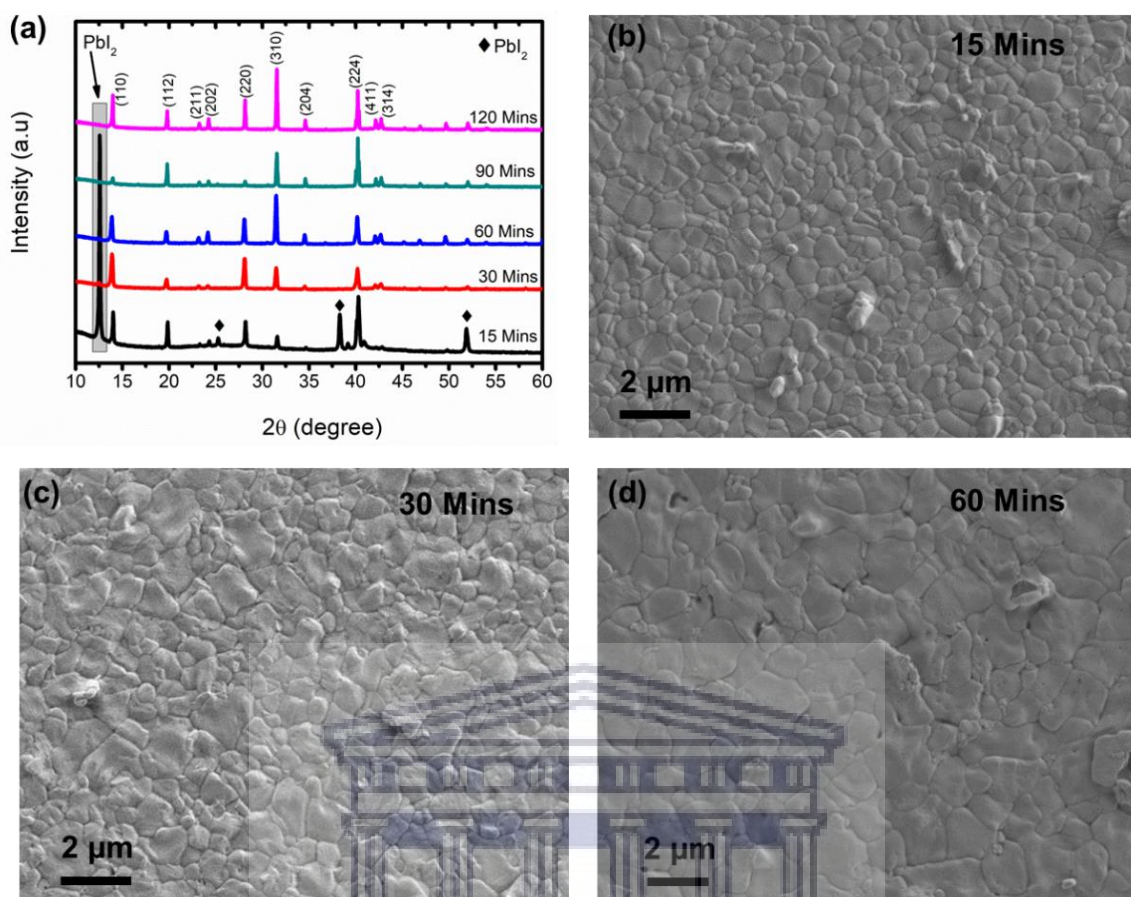


Figure 4.3: (a) XRD pattern of perovskite films, (b–d) top view SEM micrographs of the converted perovskite films after (b) 15 minutes, (c) 30 minutes, and (d) 60 minutes exposure of PbI_2 films to MAI vapour during the second step of the sequential low pressure CVD method.

The morphology of the poly-crystalline perovskite thin films was investigated by means of SEM as shown in Figure 4.3(b–d) and Figure 4.4(a) and (b) for different conversion times. Low surface coverage, pinholes and inhomogeneity of the perovskite thin film often results in poor solar cell performance [4.13]. An advantage of a two-step deposition process, especially in this instance, is that the pre-deposited PbI_2 morphology can be controlled carefully, resulting in high quality perovskite thin films.

The yellow PbI_2 film was converted into a dark brown/black perovskite upon exposure to the MAI vapour during the second step of the sequential deposition where even the partially converted 15 minutes sample appears dark (Figure 4.1(b)). The optical micrographs of the converted perovskite films show uniform and continuous films with full surface coverage for all conversion times, Figure 4.5(a)–(e). The perovskite film obtained after 90 minutes, which is the fully converted sample, shows visible grains of sizes up to $6\ \mu\text{m}$ in the SEM micrograph (Figure 4.4(a)) and in the optical micrograph (Figure 4.5(d)).

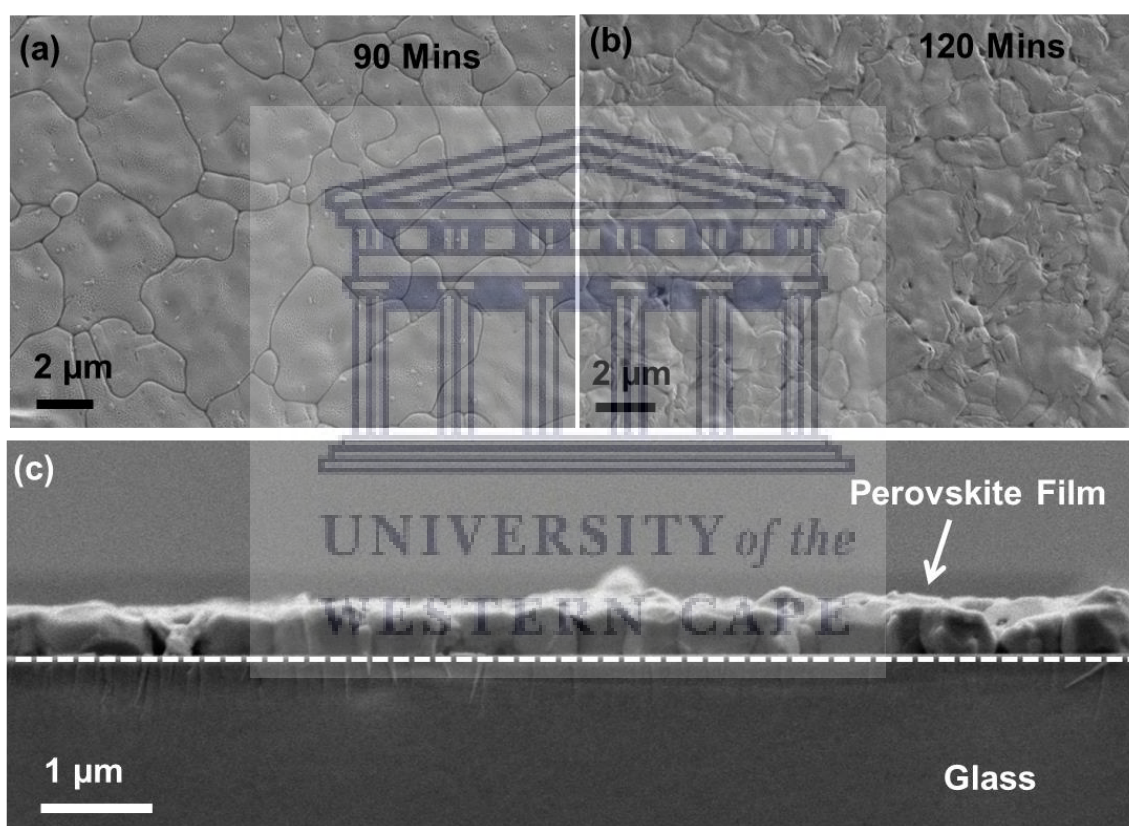


Figure 4.4: (a) Top view SEM micrographs of the converted perovskite films after 90 minutes, and (b) after 120 minutes conversion; (c) a typical cross-sectional micrograph of a perovskite film on glass showing continuous grains across film thickness.

It is known that the grain sizes and shapes of PbI_2 change after conversion to perovskites due to the insertion of the MAI molecule within its layered structure [4.10, 4.15, 4.17]. The lattice parameter along the c-axis expands upon conversion of the hexagonal PbI_2 ($c = 6.95 \text{ \AA}$) to tetragonal MAPbI_3 ($c = 12.44 \text{ \AA}$); and hence the volume of the converted perovskite increases as compared to that of PbI_2 [4.14]. After 15 minutes conversion time, the grains observed from the SEM micrograph (Figure 4.3(b)) are well defined with clear grain boundaries, average grain size of $0.73 \pm 0.24 \text{ \mu m}$, and smaller in size compared to that observed for the PbI_2 film. With prolonged conversion time up to 30 and 60 minutes, the grain size increases to average values of $1.02 \pm 0.58 \text{ \mu m}$ and $1.61 \pm 0.77 \text{ \mu m}$, as shown in Figure 4.3(c) and (d), respectively, and comparable to those measured for the PbI_2 film. However, the grains appear rougher and irregular. Larger and flatter grains are observed after 90 minutes conversion with average size of $3.70 \pm 1.80 \text{ \mu m}$ (Figure 4.4(a)), followed by grain-coarsening and size reduction after 120 minutes conversion to $2.36 \pm 1.03 \text{ \mu m}$ (Figure 4.4(b)). The grain size evolution of these perovskite films is summarized in Table 4.1.

Table 4.1: Grain size, RMS roughness, thickness, and Pb/I ratio from EDS for different conversion times.

| Conversion time (min) | Grain size (μm) | RMS roughness (nm) | Thickness (nm) | Pb/I ratio |
|------------------------------|--|---------------------------|-----------------------|-------------------|
| 0 (PbI_2 layer) | 1.60 ± 0.62 | 8.5 | 230 | 0.58 |
| 15 | 0.73 ± 0.24 | 45.7 | 405 | 0.43 |
| 30 | 1.02 ± 0.58 | 39.8 | 409 | 0.36 |
| 60 | 1.61 ± 0.77 | 33.5 | 415 | 0.37 |
| 90 | 3.70 ± 1.80 | 32.7 | 450 | 0.36 |
| 120 | 2.36 ± 1.03 | 51.9 | 444 | 0.37 |

The RMS roughness extracted from the AFM micrographs of the perovskite thin film reduces from 45.7 nm after 15 minutes conversion to 32.7 nm after 90 minutes conversion, followed by an increase to 51.9 nm after 120 minutes conversion (see Table 4.1 and Figure 4.5(f)–(j)). There is an inverse relationship between the grain size and roughness, which suggest that the grain growth results in a continuous and smooth film. The increase in RMS roughness from pre-deposited PbI_2 thin films to the perovskite films is due to the insertion of the MAI molecule within the layered network of PbI_2 where the perovskite grain formation induces surface roughness. The difference in morphology was also observed in the SEM micrographs with perovskites films depicting defined grains (Figure 4.3 and Figure 4.4) as compared to the flat grains of PbI_2 (Figure 4.2(b)).

The 90 minutes sample had a relatively lower roughness (32.7 nm) than the other perovskite samples, which confirms the smoother and larger grains observed in the SEM micrographs (Figure 4.4(a)). The larger grain size and smoother surface of the 90 minutes sample is attributed to the complete conversion, presenting the saturation stage of this sequential deposition process. It should be noted that the large grain size and low RMS roughness observed after 90 minutes conversion was not observed for any CVD prepared perovskite and without any post-deposition annealing. Pinholes and grain boundaries are defect centres that impede the electron-hole transport, inducing carrier recombination sites and deteriorating device performance [4.38, 4.39]. A typical cross-sectional SEM of our CVD grown perovskite film shows continuous grains across the film thickness with no grain boundaries parallel to the substrate (Figure 4.4(c)), advantageous for efficient charge transport. The superior grain sizes reported here suggests a reduced defect density, which as we see later contribute towards the improved stability and performance of the devices.

The changes in the grain shapes and sizes are related to the deposition kinetics. The unit cell volume of hexagonal PbI_2 is about 0.1255 nm^3 at room temperature and that of cubic MAPbI_3 is about 0.2475 nm^3 at $85 \text{ }^\circ\text{C}$ [4.37], almost double that of PbI_2 (MAPbI_3 were deposited at $180 \text{ }^\circ\text{C}$). This grain morphology evolution suggests that during the initial stages (15 minutes) of the conversion process, the larger grains of PbI_2 shrink and separate during the MAI intercalation into the layered PbI_2 , resulting in smaller, partially converted perovskite grains. With further MAI exposure and subsequent intercalation, the grain size increases due to volume expansion as more PbI_2 is converted to perovskite. The maximum grain size observed after 90 minutes of conversion and the subsequent reduction thereof after 120 minutes suggest that the intercalation stops, and that the saturation stage of the perovskite conversion is achieved after 90 minutes.

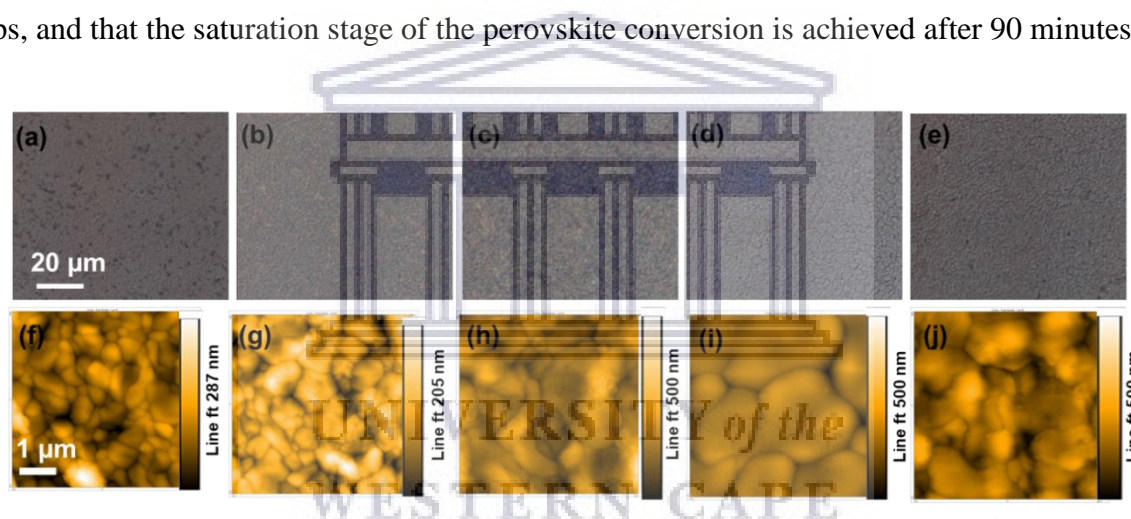


Figure 4.5: (a–e) Optical microscopy micrographs (scale size is same in all) for different conversion times 15–120 minutes, respectively, and (f–j) are the AFM micrographs (scale size is same in all) of the converted perovskites films after different exposure times 15–120 minutes, respectively.

With all the PbI_2 converted to perovskite, the grain growth stops, and the films appear to oversaturate after 120 minutes conversion, resulting in grain size reduction and coarsening. The 120 minutes sample remained exposed to MAI vapour after the saturation stage, but no

signature of MAI residue was observed in the XRD pattern (Figure 4.3(a)) in which MAI diffraction peaks normally appears at 9.84° , 19.74° , and 29.79° [4.40]. The absence of excess MAI and the fact that the 120-minute sample was not subjected to any post-deposition treatment confirm that MAI absorption terminates upon complete conversion during vapour deposition. Therefore, the reduction in the grain size may be attributed to the coarsening of the grains due to unstable crystallization after full conversion. A similar effect was also observed by first Chen *et al.* [4.10] and then by Shen *et al.* [4.19] attributed to thermodynamically stable film formation with prolonged heat supply. The thickness of the PbI_2 layer and the converted perovskite samples are summarized in Table 4.1. The thickness of the fully converted sample (90 minutes with 450 nm) is approximately double that of the PbI_2 layer (230 nm), which agrees with previous reports and accords with the expected volume changes induced during the conversion process [4.37, 4.41].

The XRD pattern of the 15-minutes sample (Figure 4.3(a)) showed strong diffraction of the (110), (220), and (224) peaks, as inferred from the peak intensities, suggesting a mixed preferred orientation, which apparently arises from the volume expansion and the competing steric constraints in the reacted film. Extending the conversion time to 30 minutes resulted in the (110) and (220) being the preferred orientation with larger average grain size than the 15 minutes sample. The 60- and 120-minutes samples are highly orientated along the (310) planes with even larger grain sizes and a similar morphology as seen from their SEM micrographs (Figure 4.3(d) and Figure 4.4(b)). Lastly, the 90 minutes exposed sample has the largest grain size and different orientation along the (224) planes with well suppressed (110) and (220) orientations shown in Figure 4.3(a). These results suggest that larger grains of perovskites, obtained after 90 minutes conversion, do not grow along the (110) and (220), which is preferred orientation for grains $< 1 \mu\text{m}$ [4.10, 4.13, 4.17].

During the conversion process, the MAI intercalates slowly through the layered PbI_2 framework, chemically react with the PbI_2 that subsequently transforms to solid MAPbI_3 . However, this process is time dependent, as the reaction does not happen simultaneously throughout the film thickness. As the exposure time is prolonged, more of the PbI_2 is converted to perovskite (30 and 60 minutes) until the entire film is completely converted (90 minutes). In order to study the presence of PbI_2 through the thickness of the film, grazing incident XRD (GIXRD) was performed on the 30 minutes sample, which had a small PbI_2 peak during normal XRD. GIXRD was probed at different grazing incident angles (0.2° , 0.3° , 0.4° , and 0.5°) as shown in Figure 4.6(a) to investigate the conversion process.

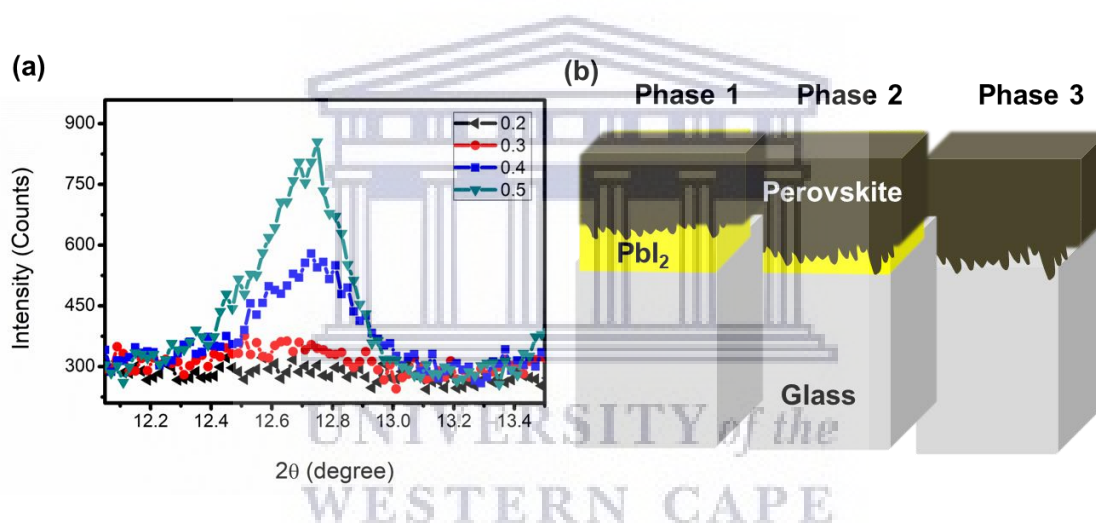


Figure 4.6: (a) Grazing incident XRD pattern of the 30 minutes converted sample at different angles for the PbI_2 peak position and (b) Schematic illustration of the perovskite conversion mechanism.

As a note, low grazing incident angles probe the top surface and higher angles penetrate deeper in the film. The low grazing angle (0.2°) shows no PbI_2 peak, suggesting an absence of PbI_2 on the film surface compared to high grazing angles (0.4° and 0.5°) where the PbI_2 peak appears suggesting a presence of PbI_2 towards the bottom of the perovskite film. These results confirm that the perovskite conversion reaction starts at the PbI_2 surface and continue

downwards towards the substrate. This is in agreement with the proposed perovskite conversion mechanism by Chen *et al.* [4.10]. The schematic illustration in Figure 4.6(b) shows the different phases of conversion: phase one with a high concentration of PbI_2 (15 min conversion), phase two with a small amount of PbI_2 at the bottom (30- and 60-minutes conversion), and finally phase three with a full consumption of PbI_2 (90 minutes).

X-ray photoelectron spectroscopy (XPS) measurements were conducted on the 90 minutes sample to investigate the bonding information and atomic concentration depth-profile. Figure 4.7(a) presents the full XPS survey spectrum taken at the surface of the film showing pronounced peaks of lead and iodide originating from MAPbI_3 . Figure 4.7(b) shows the high resolution XPS spectrums of Pb(II) $4f_{7/2}$ and $4f_{5/2}$ transitions (left hand side two peaks) with binding energies of 138.3 eV and 143.2 eV, respectively. No metallic Pb (Pb^0) was observed on this film surface which is usually associated with small humps at 136.3 eV and 141.2 eV [4.39]. This confirms the high phase lead (II). Also shown in Figure 4.7(b) (right hand side peaks) are high-resolution peaks of Iodine $3d_{5/2}$ and $3d_{3/2}$ transitions with binding energies at 619.2 eV and 631.4 eV, respectively, which further confirms the presence of high phase MAPbI_3 perovskite.

The atomic concentration depth-profile was acquired during the sputtering of the 90 minutes perovskite film with energetic argon ions and the profiles are shown in Figure 4.8(a). The Pb and iodine concentrations are higher on the surface (as expected) and are relatively constant throughout the film thickness. Pb and iodine concentrations decreased towards the glass substrate-film interface, signified by the increased silicon and oxygen atomic concentrations. This substrate-film interface is highlighted in Figure 4.8(a) and found between 200 and 300 seconds of sputtering based on the abrupt reduction of Pb and iodide, accompanied by an increase in silicon and oxygen concentrations (from the substrate). The presence of oxygen and

silicon on the surface is due to sample oxidation and contamination during handling and storage.

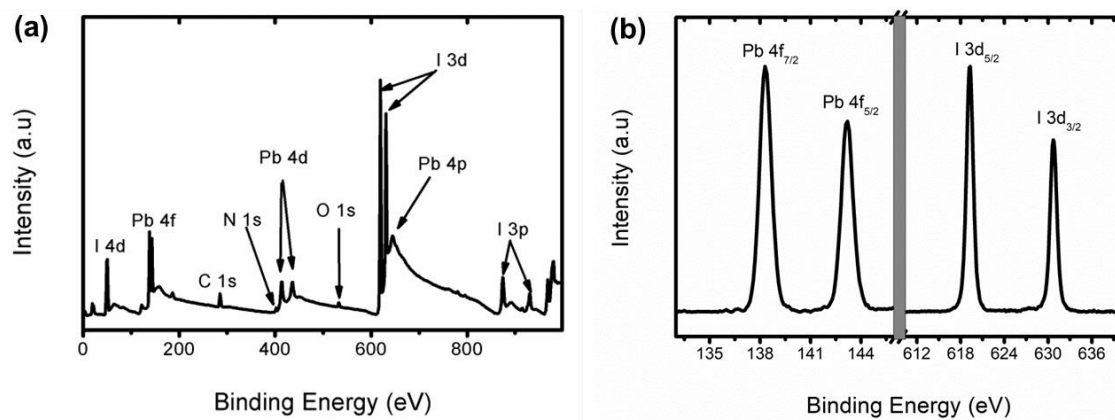


Figure 4.7: (a) XPS full survey spectrum taken at the surface of the 90 minutes converted perovskite sample, (b) is the high-resolution spectrum with Pb and iodine peaks as shown.

The Pb:I ratio-depth profile (Figure 4.8(b)) confirms a perovskite rich film throughout its thickness (up to 300 s sputtering time), with ratio between 0.3 and 0.45, which is close to a theoretical value of 0.333 for MAPbI_3 . The slight increase on the Pb:I ratio in Figure 4.8(b) after longer sputtering time (40 sec) might be due to an iodine deficiency caused by perovskite exposure to energetic Ar ions. This deficiency of iodine was also confirmed by an increase in metallic Pb (Pb^0) after longer sputtering time (255 sec) where the Pb^0 peak intensity increases as shown in Figure 4.8(c) with Pb XPS spectrums taken after different sputtering times [4.39]. This increase in Pb^0 peak intensity was accompanied by a shift in Pb(II) 4f_{7/2} and 4f_{5/2} peak positions towards higher binding energies, Figure 4.8(c). The Pb:I ratio obtained from energy dispersive X-ray spectroscopy (EDS) of different samples including PbI_2 is summarized in Table 4.1. All conversion times, except for the 15 minutes sample, confirmed rich perovskite

thin films. The 15 minutes sample had a higher Pb:I ratio of 0.46 closer to that of PbI_2 (0.58), confirming the mixed phase of this sample.

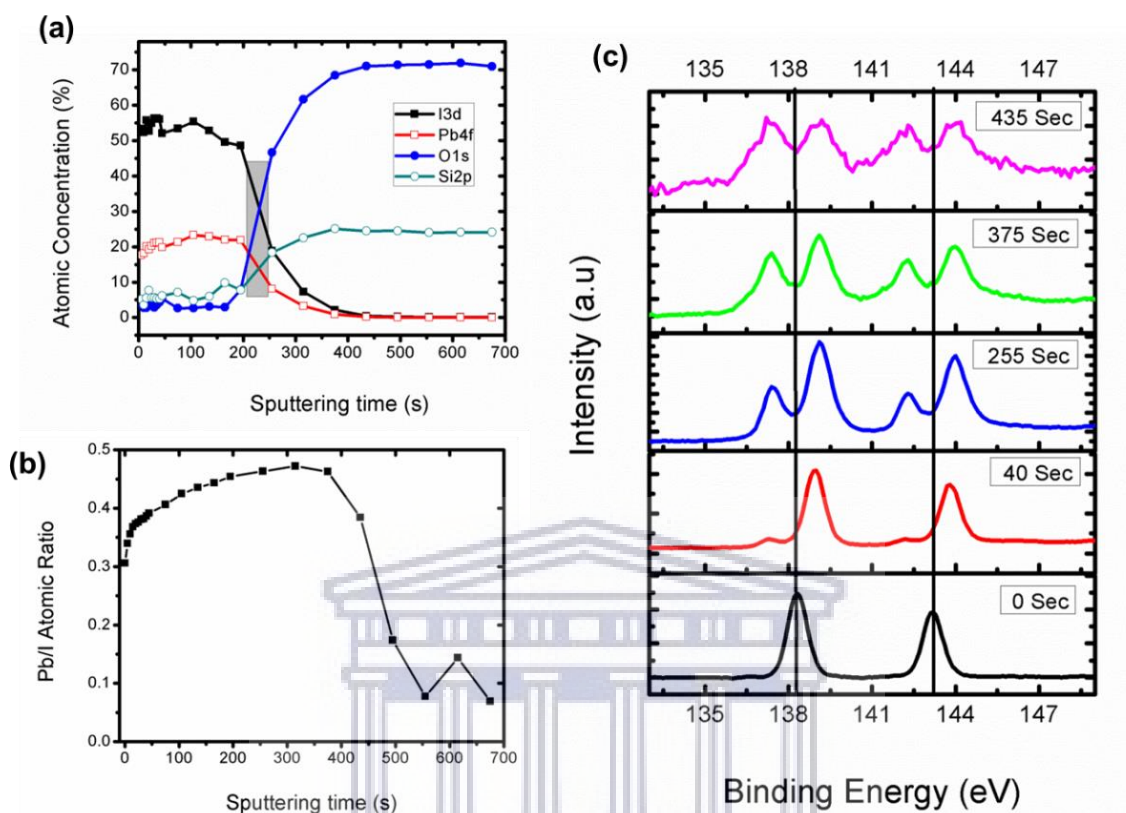


Figure 4.8: (a) Atomic concentration profiles obtained from sputtering the 90 minutes sample, (b) Pb/I atomic ratio profile at different sputtering times of the 90 min sample, XPS high resolution profile of lead in the 90 min sample at different sputtering times.

4.3.2 Film Optical Properties and Stability

The optical properties of these perovskite films were measured by a UV-Vis spectroscopy in transmittance mode, converted into absorbance and simulated to extract absorption coefficient, refractive index and the band gap as was discussed in Chapter 3.7, the results are shown in Figure 4.9. The perovskite films absorb throughout the visible range with a quick drop at about 750 nm as shown in Figure 4.9(a). This wide absorption also confirms the high quality of sequential vapour grown perovskite films. The 15 minutes converted sample showed

a reduced absorbance due to its partial conversion nature, Figure 4.9(a). A true representation of the absorbance of these films is illustrated in its calculated absorption coefficient spectra, shown in Figure 4.9(b). The PbI_2 thin film starts absorbing at energies above 2.4 eV as compared to the converted perovskite films. The perovskite films in comparison start absorbing just above 1.6 eV with absorption coefficients above $1.8 \times 10^4 \text{ cm}^{-1}$ for the 15 mins sample and above $3 \times 10^4 \text{ cm}^{-1}$ for the 30–120 minutes samples at energy of 1.7 eV, as shown in the inset of Figure 4.9(b).

The 15-minute converted sample shows similar absorption coefficient spectra to the PbI_2 with similar humps at about 2.5 and at 3.0 eV, confirming the mixed phase of this sample, Figure 4.9(b). These features were not observed for the other perovskite films confirming the low level PbI_2 impurity existing on these samples (especially the 30 mins and 60 mins samples). The refractive index spectra of the PbI_2 and the perovskite films are presented in Figure 4.9(c); showing a peak at about 1.6 eV for the perovskite films and a sharp peak at 2.4 eV for PbI_2 and the 15 minutes converted perovskite film. The peaks at 1.6 eV and 2.4 eV are attributed to the perovskite absorption edge and the PbI_2 absorption edge, respectively [4.42, 4.43].

The presence of PbI_2 in perovskite films increases the refractive index due to its high crystallinity thus the enhanced refractive index of the 15 minutes sample compared to the other perovskite samples [4.42, 4.43]. There are no refractive index peaks below the direct band gap transition from both these respective films (PbI_2 , 2.4 eV and perovskites, 1.6 eV), which suggests the absence of any in-gap defect trap states [4.42, 4.43]. The calculated band gaps of the perovskite samples employing the Tauc function are provided in Figure 4.9(d). The calculated band gaps agree with the known MAPbI_3 perovskite optical band gap of 1.5–1.6 eV [4.42, 4.43]. The steady state photoluminescence spectrum of the 90 mins sample shows an

intense peak at about 775 nm (1.59 eV) as shown in Figure 4.10(a) and it agrees with the estimated Tauc band gap in Figure 4.9(d).

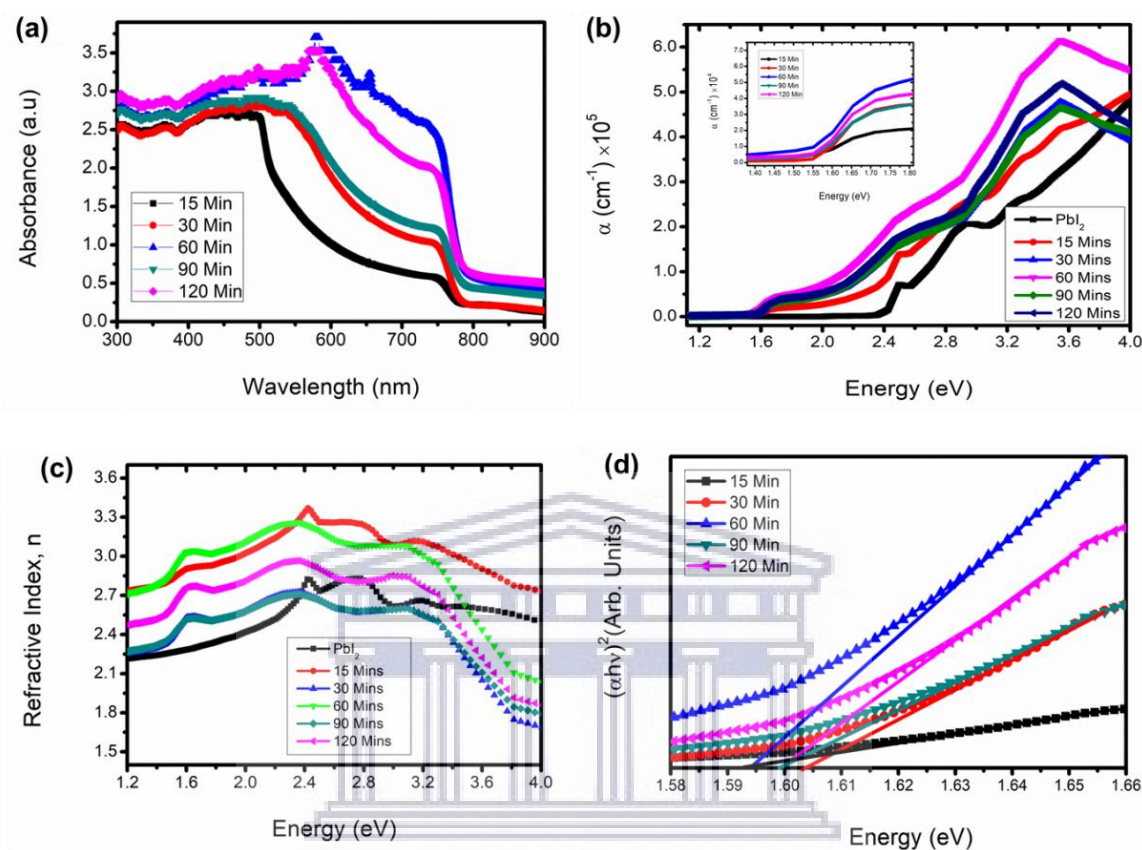


Figure 4.9: (a) Absorbance spectra of the converted perovskite films, (b) calculated absorption coefficient spectra, (c) extracted refractive index, and (d) the calculated optical band gap of the films.

After initial characterization (Figure 4.10(a)), the absorbance spectra were measured daily on the fully converted perovskite sample (90 minutes) to investigate the air stability of the films. Samples were placed in the dark with uncontrolled ambient conditions (temperature and humidity). Temperatures during the measured days ranged from 15–22 °C and relative humidity from 60–80%. Figure 4.10(b) shows the evolution of the absorbance spectra of the 90 minutes perovskite sample. The film remained stable for 21 days of measurements, with

slight changes in absorbance associated with the inhomogeneity of the sample thickness. The stability of the fully converted sample is due to its superior grain size and crystalline quality that is concomitant with a reduced defect density. Furthermore, the purity and compactness of these CVD deposited films with no pin holes to trap moisture and the absence of solvents in both deposition steps also contribute to its prolonged stability.

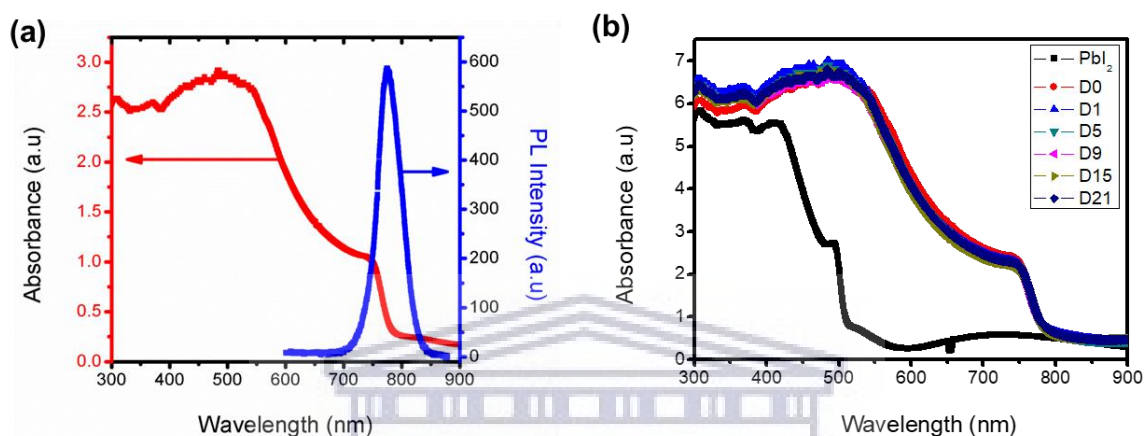


Figure 4.10: (a) Absorbance and photoluminescence spectra of the 90-minute converted perovskite and (b) evolution of the absorbance spectra of the same sample measured for 21 days at ambient room conditions to probe film air stability.

4.3.3 Device Performance and Stability

The 90 minutes converted sample with larger grain size was subsequently used as the absorber layer in a planar perovskite solar cell. The corresponding cross section of the planar perovskite solar cell device is shown in Figure 4.11(a) with FTO coated on glass followed by a double spin coated c-TiO₂ film as an electron transport layer (ETL), then the MAPbI₃ perovskite, and finally a layer of Spiro-MeOTAD as hole transport material (HTL). The device was prepared in open air (without the use of a glove box) and finalized by depositing a 100 nm Ag layer as back metal contact.

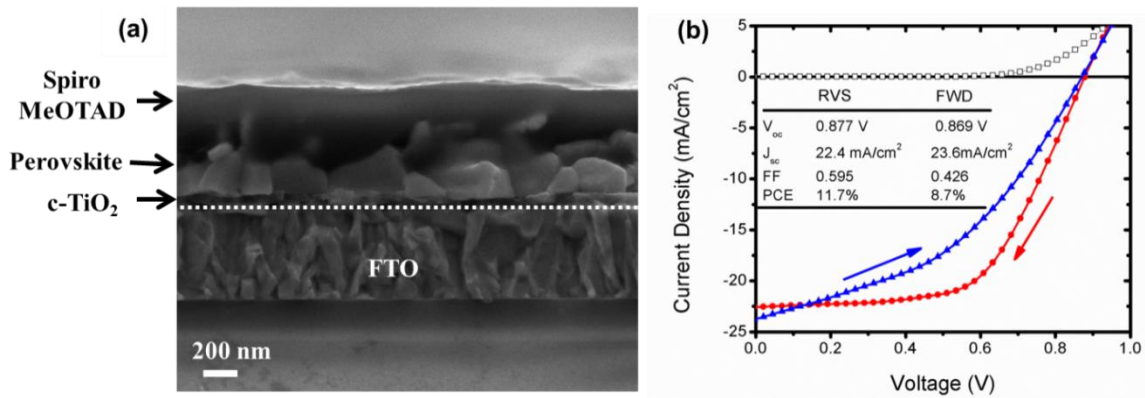


Figure 4.11: (a) SEM cross sectional view of the 90-minute perovskite solar cell showing all the layers except the metal contact. (b) J–V characteristic scanned in forward and reverse also showing the respective device parameters and performance.

The solar cells were characterized by current and voltage measurements under simulated AM 1.5G (100 mW/cm²) solar irradiation in air, scanning in both forward and reverse. The current density (J)–voltage (V) curve is shown in Figure 4.11(b) for both forward and reverse scans, indicated with arrows. As shown, the device had an open circuit voltage (V_{oc}) of 0.869 V, short circuit current density (J_{sc}) of 23.6 mA/cm², fill factor (FF) of 0.426, and power conversion efficiency (PCE) of 8.7% under forward scan. There is a hysteresis between forward and reverse sweeps. The reverse scan showed a better performance: $V_{oc} = 0.877$ V, $J_{sc} = 22.4$ mA/cm², FF = 0.595, and PCE = 11.7%.

The most probable cause for hysteresis in our devices is due to ion migration, ferroelectric polarization, and charge accumulation at the c-TiO₂/perovskite interface [4.44 – 4.46]. Charge trapping at this interface lowers both FF and V_{oc} . Doping of the c-TiO₂ layer [4.47, 4.48] and interface engineering [4.49] are normally employed as a means to increase the TiO₂ conductivity, improving the performance, and reducing the hysteresis of the device. Here we did not perform any c-TiO₂ doping, as the objective was to determine the applicability of a two-step CVD grown perovskite film for solar cell application. Future studies will entail the

optimization of the individual non-perovskite layers and detailed quantum efficiency measurements.

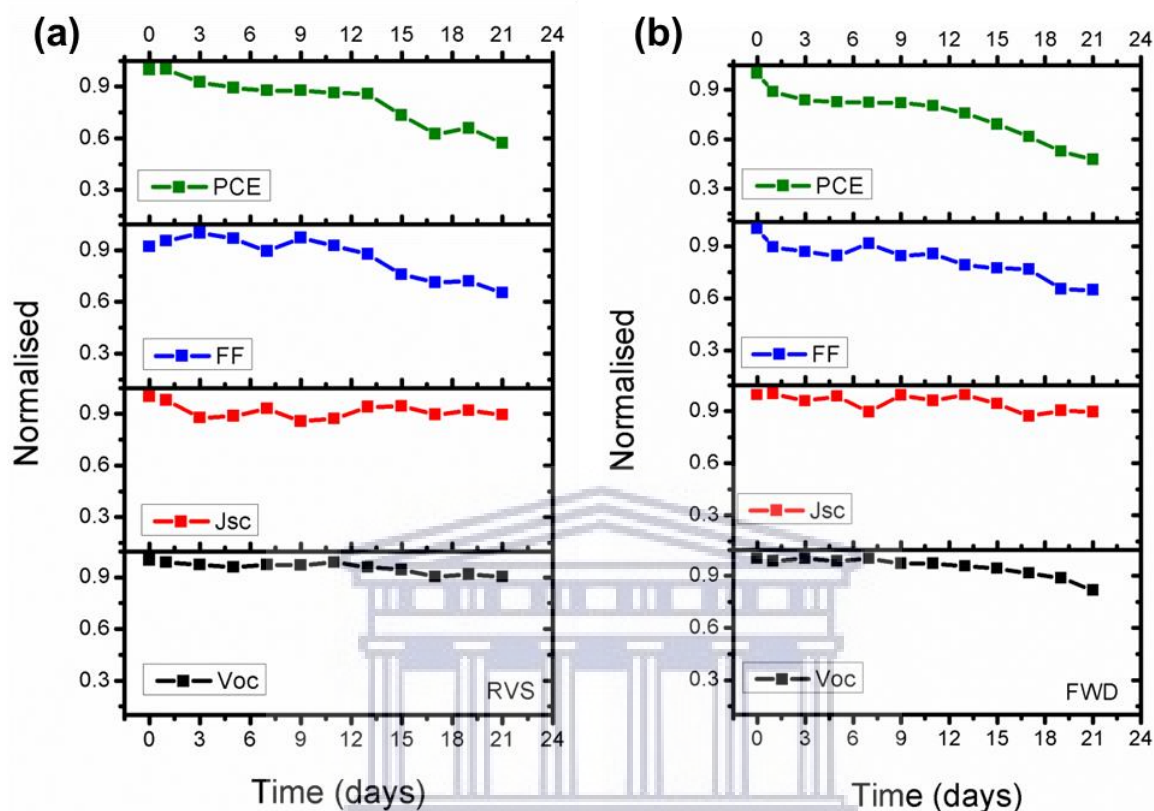


Figure 4.12: Evolution of the normalized open circuit voltage (V_{oc}), short circuit current density (J_{sc}), fill factor (FF) and the power conversion efficiency (PCE) of the device measured for 21 days in (a) reverse and (b) forward scan.

Although the device showed hysteresis, we tested its performance stability since the film was stable under ambient room conditions. The devices were kept in the dark under ambient room conditions with temperature ranging between 15–22 °C and relative humidity ranged between 60–80%. Figure 4.12(a) and (b) shows the evolution of the V_{oc} , J_{sc} , FF, and PCE in reverse and forward scans as a function of time. These values were divided by the values obtained on day 1, i.e., normalised to day 1 device characteristics. V_{oc} remain above 90% throughout the measured period under reverse scan and the minimum J_{sc} was 87%, fluctuating

between this value and 99% (both in Figure 4.12(a)). A similar trend was observed at forward scan, except for a fast drop in V_{oc} during the final two days of measurements to about 80% (Figure 4.12(b)). The FF and the corresponding PCE were maintained at above 85% of their highest values for the first 13 days in the reverse sweep and then dropped significantly (Figure 4.12(a)). A steady drop in FF and PCE was observed for the forward sweep as shown in Figure 4.12(b). The corresponding J–V curves measured on consecutive days where the above values were extracted are shown in Figure 4.13(a) and (b) for both reverse and forward scans.

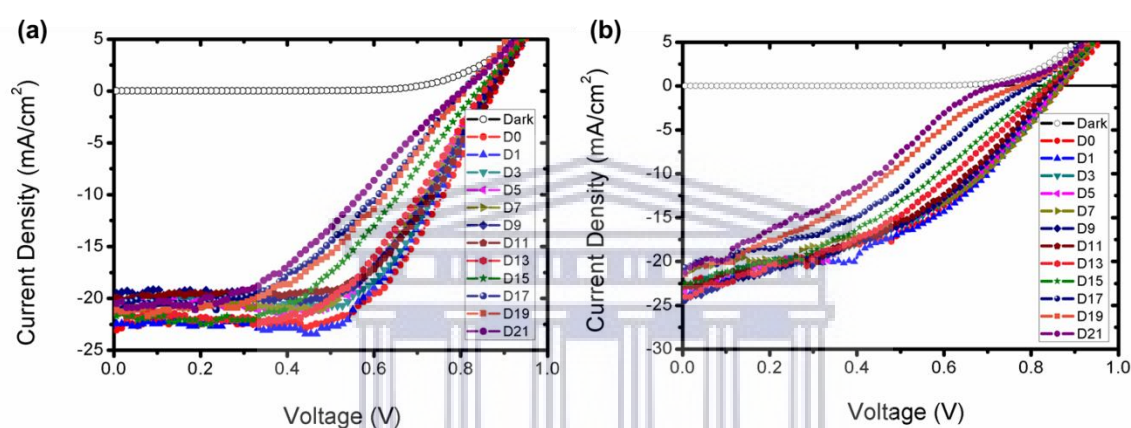


Figure 4.13: J–V characteristics curves of the perovskite solar cell measured at different days for (a) reverse and (b) forward scan.

The drop in device performance is attributed to the possibility of ion migration, which inhibits charge transport at the layer interfaces (electron and hole transport layers). Another possible reason could be the corrosion of the Ag contacts, which appeared as early as day 9 of measurements with a brownish colour around its edges and regions in contact with the FTO. The corrosion of Ag metal reduces its conductivity and creates a high series resistance in the device [4.9]. Even though the efficiency our device is poor it is comparable to some of the CVD processed perovskite [4.28, 4.29].

4.4 Conclusion

We have demonstrated the deposition of pure, highly crystalline, smooth, and compact MAPbI₃ perovskite films on glass substrates using a sequential vapour deposition method at low pressures in a single reactor. The as-deposited PbI₂ films, grown in the first step were successfully converted to MAPbI₃ perovskite during their exposure to MAI vapour in the second step using the same CVD reactor. The conversion begins at the surface and progresses towards the glass substrate, resulting in tetragonal MAPbI₃ perovskites. A growth in grain size was realized as the conversion time increases up to 90 minutes, where conversion saturation was observed with a grain size of $3.70 \pm 1.80 \mu\text{m}$. A perovskite rich film was confirmed from the XPS depth profile. The fully converted perovskite film (90 minutes) was found to be optically stable in air with high relative humidity up to 80% for more than 21 days. This stability is ascribed to its superior grain size, crystalline quality, high purity, and compactness of the film. Air-processed planar perovskite solar cell devices under similar ambient room conditions were achieved. The best device performance achieved was 11.7% achieved, albeit with a hysteresis. After 13 days of exposure to high relative humidity, 85% of its initial PCE was maintained. This work opens a path towards a low-cost, scalable deposition technique for the manufacturing of air-stable hybrid alkali-halide perovskite solar panels.

4.5 References

- [4.1] A.B. Djurisić, F.Z. Liu, H.W. Tam, M.K. Wong, A. Ng, C. Surya, W. Chen, and Z.B. He, *Progress in Quantum Electronics* 53 (2017) 1
- [4.2] S. Senanayak, B. Yang, T. Thomas, N. Giesbrecht, W. Huang, E. Gann, B. Nair, K. Goedel, S. Guha, X. Moya, C. R. McNeill, P. Docampo, A. Sadhanala, R.H. Friend, and H. Sirringhaus, *Science Advances* 3 (2017) 1601935.
- [4.3] R. Wang, M. Mujahid, Y. Duan, Z-K. Wang, J. Xue, and Y. Yang, *Advanced Functional Materials* 2019, 1808843.
- [4.4] A. Kojima, K. Teshima, Y. Shirai, and T. Miyasaka, *Journal of American Chemical Society* 131 (2009) 6050.
- [4.5] M. Lee, J. Teuscher, T. Miyasaka, T. Murakami, and H. Snaith, *Science* 338 (2012) 643.
- [4.6] National Renewable Energy Laboratory (NREL) Best Research-Cell Efficiencies. (<https://www.nrel.gov/pv/assets/images/efficiency-chart.png>), Accessed on 9 June 2019.
- [4.7] L. Ono, M. Leyden, S. Wang, and Y. Qi, *Journal of Materials Chemistry A* 4 (2016) 6693.
- [4.8] H. Xi, S. Tang, X. Ma, J. Chang, D. Chen, Z. Lin, P. Zhong, H. Wang, and C. Zhang, *ACS Omega* 2 (2017) 326.
- [4.9] Y. Kato, L. K. Ono, M. V. Lee, S. Wang, S. R. Raga, and Y. Qi, *Advanced Materials Interfaces* 2 (2015) 1500195.
- [4.10] Q. Chen, H. Zhou, S. Luo, Y. Liu, G. Li, and Y. Yang, *Journal of American Chemical Society* 136 (2014) 622.
- [4.11] R. Sheng, A. Ho-Baillie, S. Huang, S. Chen, X. Wen, X. Hao, and M. A. Green, *Journal of Physical Chemistry C* 1197 (2015) 3545.

- [4.12] C.W. Chen, H.W. Kang, K.M. Chiang, and H.W. Lin, *Advanced Materials* 26 (2014) 6647.
- [4.13] M. Liu, M. Johnston, and H. Snaith, *Nature* 501 (2013) 395.
- [4.14] S. Ha, X. Liu, Q. Zhang, D. Giovanni, T. Sum, and Q, *Advanced Optical Materials* 2 (2014) 838.
- [4.15] P. Luo, Z. Liu, W. Xia, C. Yuan, J. Cheng, and Y. Lu, *ACS Applied Materials Interfaces* 7 (2015) 2708.
- [4.16] M. Tavakoli, L. Gu, Y. Gao, J. He, A. Rogach, Y. Yao, and Z. Fan, *Scientific Reports* 5 (2015) 14083.
- [4.17] M.R. Leyden, L. Ono, S. Raga, Y. Kato, S. Wang, and Y. Qi, *Journal of Materials Chemistry A* 2 (2014)18742.
- [4.18] M.R. Leyden, Y. Jiang, and Y. Qi, *Journal of Materials Chemistry A* 4 (2016) 13125.
- [4.19] P.S. Shen, J.S. Chen, Y.H. Chiang, M. Li, T. Guo, and P. Chen, *Advanced Materials Interfaces* 3 (2016) 1500849.
- [4.20] B. Wang and T. Chen, *Advanced Science* 3 (2016) 1500262.
- [4.21] Y. Peng, G. Jing, and T. Cui, *Journal of Materials Chemistry A* 3 (2015) 12436.
- [4.22] A. Ioakeimidis, C. Christodoulou, M. Lux-Steiner, and K. Fostiropoulos, *Journal of Solid State Chemistry* 244 (2016) 20.
- [4.23] P.S. Shen, Y.H. Chiang, M.H. Li, T. Guo, and P. Chen, *Applied Materials* 4 (2016) 091509.
- [4.24] Y. Jiang, M.R. Leyden, L. Qiu, S. Wang, L.K. Ono, Z. Wu, E.J. Juarez-Perez, and Y. Qi, *Advanced Functional Materials* 28 (2018) 1703835.
- [4.25] X. Wei, Y. Peng, G. Jing, and T. Cui, *Japanese Journal of Applied Physics* 57 (2018) 052301.

- [4.26] V-D. Tran, S.V. Pammi, V-D. Dao, H-S. Choi, and S-G. Yoon, *Journal of Alloys and Compounds* 747 (2018) 703.
- [4.27] J. Yin, H. Qu, J. Cao, H. Tai, J. Li, and N. Zheng, *Journal of Materials Chemistry A* 4 (2016) 13203.
- [4.28] R. Swartwout, M.T. Hoerantner, and V. Bulovic, *Energy Environmental Materials* 2 (2019) 119.
- [4.29] P. Luo, S. Zhou, W. Xia, J. Cheng, C. Xu, and Y. Lu, *Advanced Materials Interfaces* (2017) 1600970.
- [4.30] S. Bai, P. Da, C. Li, Z. Wang, Z. Yuan, F. Fu, M. Kawecki, X. Liu, N. Sakai, J.T-W. Wang, S. Huettner, S. Buecheler, M. Fahlman, F. Gao, and H.J. Snaith, *Nature* 571 (2019) 245.
- [4.31] S.V.N. Pammi, H-W. Lee, J-H. Eom, and S-G. Yoon, *ACS Applied Energy Materials* 1 (2018) 3301.
- [4.32] M.T. Hoerantner, , E.L. Wassweiler, H. Zhang, A. Panda, M. Nasilowski, A. Osherov, R. Swartwout, R.A. Driscoll, N.S. Moody, M.G. Bawendi, K.F. Jensen, and V. Bulovic, *ACS Applied Materials Interfaces* 11 (2019) 32928.
- [4.33] H. Sun, X. Zhu, D. Yang, J. Yang, X. Gao, and X. Li, *Journal of Crystal Growth* 405 (2014) 29.
- [4.34] M. Schieber, N. Zamoshchik, O. Khakhan, and A. Zuck, *J Journal of Crystal Growth* 310 (2008) 3168.
- [4.35] F. Fu, L. Kranz, S. Yoon, J. Lockinger, T. Jager, J. Perrenoud, T. Feurer, C. Gretener, S. Buecheler, and A. N. Tiwari, *Physics Status Solidi A* 212 (2015) 2708.
- [4.36] H.S. Kim, S. Im, and N.G. Park, *Journal of Physical Chemistry C* 118 (2014) 5615.
- [4.37] T. Baikie, Y. Fang, J. Kadro, M. Schreyer, F. Wei, S. Mhaisalkar, M. Graetzel, and T. White, *Journal of Materials Chemistry A* 1 (2013) 5628.

- [4.38] X. Liu, X. Xia, Q. Cai, F. Cai, L. Yang, Y. Yan, and T. Wang, *Solar Energy Materials and Solar Cells* 159 (2017) 412.
- [4.39] W. Zhang, S. Pathak, N. Sakai, T. Stergiopoulos, P.K. Nayak, N.K. Noel, A.A. Haghghirad, V.M. Burlakov, D.W. de Quilettes, A. Sadhanala, W. Li, L. Wang, D.S. Ginger, R.H. Friend, H.J. Snaith, *Nature Communication* 6 (2015) 10030.
- [4.40] Z. Song, S. Waththage, A. Phillips, B. Tompkins, R. Ellingson, and M. Heben, *Chemistry of Materials* 27 (2015) 4612.
- [4.41] D. Liu, M.K. Gangishetty, and T.L. Kelly, *Journal of Materials Chemistry A* 2 (2014) 19873.
- [4.42] M. Green, Y. Jiang, A. Soufiani, and A. Ho-Baillie, *Journal of Physical Chemistry Letters* 6 (2015) 4774.
- [4.43] Q. Lin, A. Armin, R. Nagiri, P. Burn, and P. Meredith, *Nature Photonics* 9 (2015) 106.
- [4.44] S. Tombe, G. Adam, H. Heilbrunner, D. Hazar Apaydin, C. Ulbricht, N. Serdar Sariciftci, C.J. Arendse, E. Iwuoha, and M. C. Scharber, *Journal of Materials Chemistry C* 5 (2017) 1714.
- [4.45] N. Ahn, K. Kwak, M.S. Jang, H. Yoon, B.Y. Lee, J-K. Lee, P.V. Pikhitsa, J. Byun, and M. Choi, *Nature Communications* 7 (2016) 13422.
- [4.46] A.K. Jena, H-W. Chen, A. Kogo, Y. Sanehira, M. Ikegami, and T. Miyasaka, *ACS Applied Materials Interfaces* 7 (2015) 9817.
- [4.47] G. Yin, J. Ma, H. Jiang, J. Li, D. Yang, F. Gao, J. Zeng, Z. Liu, and S.F. Liu, *ACS Applied Materials Interfaces* 9 (2017) 10752.
- [4.48] D. Liu, S. Li, P. Zhang, Y. Wang, R. Zhang, H. Sarvari, F. Wang, J. Wu, Z. Wang, and Z.D. Chen, *Nano Energy* 31 (2017) 462.
- [4.49] X. Guo, B. Zhang, Z. Lin, J. Ma, J. Su, W. Zhu, C. Zhang, J. Zhang, J. Chang, and Y. Hao, *Organic Electronics* 62 (2018) 459.

CHAPTER FIVE

Mixed-Halide Perovskites Solar Cells Through PbI₂ and PbCl₂ Precursor Films by Sequential Chemical Vapor Deposition

ABSTRACT:

Mixed halide perovskites with chlorine (Cl) content have received significant interest due to better charge transport properties and longer diffusion length compared to pure iodine-based perovskites. The superior properties of Cl-doped perovskites improve solar cell device performance, although the quantification of Cl composition in the perovskite films remain difficult to achieve. Hence, it is difficult to correlate the Cl-quantity with the improved device performance. In this work, we deposited Cl-doped perovskite films through a facile three- and two-step sequential chemical vapor deposition (CVD) where lead halide films were deposited in the first steps of the process and subsequently converted to perovskites. No Cl substitution by iodine was observed during a sequential deposition of lead chloride and lead iodide films which reacted to form a lead chloride iodide phase (PbI₂Cl). The substitution of Cl by iodine ions only occurred during the conversion to perovskite phase. Large perovskite grains (greater than 2 μm) were realized when converting a PbI₂ film to perovskite compared to chlorine containing lead halide films, contradicting literature. However, Cl doped perovskite solar cells showed improved device efficiencies as high as 10.87% compared to an un-doped perovskite solar cell (8.76%).

The contents of this chapter were published in: Solar Energy 215 (2021) 179–188. Modifications were made in this chapter to suit thesis presentation and published supporting information has been included here with discussion.

5.1 Introduction

Organic-inorganic hybrid perovskites are considered one of the most attractive semiconductors owing to their excellent optical and electrical properties, such as suitable optical bandgap, high absorption coefficient, low exciton binding energy, high charge mobility of electrons and holes, long charge carrier diffusion lengths and facile deposition methods [5.1 – 5.3]. Since their first application as light absorbing materials in photovoltaic technology [5.4], perovskites based solar cells have achieved remarkable progress with certified record power conversion efficiency (PCE) of over 25.2% in just a few years [5.5].

Hybrid perovskites are composed of an organic cation such as methyl ammonium (MA^+), inorganic lead (Pb^{2+}), and lastly halide anions (iodine (I^-), bromide (Br^-), chlorine (Cl^-), or mixed halides) [5.1 – 5.3]. There are other combinations that have been used such as replacement of the MA cation with formamidinium, but the methyl ammonium lead iodide (MAPbI_3) or mixed halide $\text{MAPbI}_{3-x}\text{Cl}_x$ perovskites have received wider attention [5.6]. Mixed halide perovskites have longer charge carrier diffusion lengths of up to 3 μm compared to its pure iodide-based counterparts with diffusion lengths ranging between 0.1 and 1 μm [5.7].

Even though doping hybrid perovskites with chlorine (Cl^-) ions improves device performance, its role has been largely debated and its incorporation within the perovskite structure has also been doubted [5.6, 5.8]. It is known that enhanced crystallization of perovskite films with improved grain size occurs when Cl is included in one of the perovskite deposition precursors, such as lead chloride (PbCl_2) or MA chloride (MACl) [5.8 – 5.12]. The improved crystallization of Cl-doped perovskites is achieved through slow crystal growth compared to the pure iodine-based counterparts; this in return suppresses the defect density at the grain boundaries [5.13 – 5.16]. These general conclusions mainly relate to perovskite films where the solution method is used at either during single or two step synthesis [5.8 – 5.16].

The uncertainty about the presence of Cl in perovskite films stems from the difficulty in detecting it through elemental composition characterization techniques such as X-ray photoelectron spectroscopy (XPS) and energy dispersive X-ray spectroscopy (EDS) [5.17, 5.18]. This difficulty arises because the Cl composition in the films is usually very low and below the detection limit (0.1 at.%) of these characterization techniques [5.6]. This low Cl concentration in the films is due to an easy replacement of a smaller Cl⁻ ionic radius (1.67 Å) by a larger I⁻ ionic radius (2.07 Å) during the perovskite intercalation reaction [5.9].

There are two main routes for perovskite deposition, namely solution methods where perovskite precursors are dissolved in appropriate solvents, whereas the other method entails vapour deposition from perovskite solid precursors (powders) [5.19 – 5.28]. During spin coating of mixed halide perovskites it is usually required to have a molar ratio of 1:3 for PbCl₂:MAI in order to achieve better device performance [5.6, 5.8, 5.22]. Another challenge with spin coating is the difficulty in dissolving PbCl₂ in DMF (common solvent) making it difficult to study the as-deposited PbCl₂ before conversion to perovskites [5.6, 5.12], as investigated in a series of PbCl₂:PbI₂ molar ratios dissolved in a blend of DMF and dimethyl sulfoxide (DMSO) during a two-step spin coating. The devices prepared from precursor solution containing more PbCl₂ performed poorly due to poor conversion of thin films to perovskites.

There have been a number of studies on the deposition of PbCl₂ films through high vacuum thermal evaporation [5.17, 5.23 – 5.26], with few using low pressure (around 1 mbar) chemical vapour deposition (CVD) [5.27, 5.28]. Furthermore, low pressure CVD has been used to prepare perovskite films, but mainly during the conversion step from either solution deposited PbI₂ [5.29 – 5.33] or vacuum deposited (thermal evaporation) Pb halide films [5.26, 5.34, 5.35]. Preparation of perovskite films for solar cell devices using two step depositions where Pb

halides and the conversion to perovskites are both done in the CVD chamber are very rare [5.36, 5.37]. In essence, the two-step low pressure CVD method offers a simplified scalable route for perovskite deposition through the use of a single CVD chamber.

Therefore, we explore a three-step deposition of mixed halide perovskites through the deposition of PbCl_2 and PbI_2 layers sequentially, using a low-pressure CVD method such that a stable lead chloride iodide (PbICl) phase is formed. This route is compared to a two-step deposition of perovskite films where separate layers of PbCl_2 and PbI_2 are deposited individually on separate substrates. These Pb halide films are exposed to MAI vapour as the last step of the three- and two-step deposition for the conversion to perovskite phase where the intercalation reaction takes place between the pre-deposited Pb halides and the MAI molecules. According to available literature, this is a first study where perovskite solar cells are prepared by exposing CVD grown PbICl and PbCl_2 films into MAI vapour for conversion to perovskites using the same CVD furnace. It is observed here that during the Pb halide double layer deposition at high substrate temperatures and relatively low pressure there was no substitution of Cl by iodine; instead, a stable PbICl phase was formed. However, during the step whereby the chlorine containing films were exposed to the MAI vapour, chlorine was completely replaced by iodine according to our EDS and XPS results, similar to what has been reported before [5.17, 5.18].

We observe that converting a PbI_2 film yields large perovskite grains (average grain size of 1048 nm) compared to converting the PbCl_2 film, which produced perovskites with average grain size of 937 nm. These results contradict the notion that Cl-doping in perovskite leads to improved crystallization and larger grain size [5.13 – 5.16]. Our results suggest that the grain size is not the only factor for improving the solar cell efficiency. Planar perovskite solar cell

device performance was improved for Cl-doped perovskites with PCE as high as 10.87% compared to its pure iodine-based counterparts with PCE = 8.76%.

5.2 Experimental Section

5.2.1 Fabrication of Perovskite Solar Cells

The perovskite solar cells fabrications were all done under fully open air and at ambient room conditions (temperature and relative humidity). A similar fabrication procedure was adopted from our previous report [5.37]. Chemicals employed here were purchased from Sigma–Aldrich (unless stated) and used as bought. Fluorine-doped tin oxide (FTO) coated on glass substrates (10 Ohms/sq.) were cut into 1.5 cm by 2 cm pieces and etched with Zn powder and 2 M hydrochloric acid (HCl). Samples were cleaned with hellmanex detergent (2%) and then isopropanol in an ultrasonic bath sequentially and followed by a thorough rinsing in hot deionized water then treated under UV Ozone for 15 min. Then, 365 μL of titanium isopropoxide was added into 2.5 ml of ethanol, and 35 μL of HCl (2 M) was added into 2.5 ml of ethanol, mixed and stirred for an hour. The solution was spin coated on etched FTO substrates at 2000 rpm for 30 s; the spin coating was repeated with a 4000 rpm spin speed for 30 s and dried on a hot plate for 5 min. The films were then annealed at 500 $^{\circ}\text{C}$ for 30 min to form a compact titanium dioxide (c-TiO₂) film [5.37].

Lead halide films were prepared by two-step sequential CVD to deposit double halide layers of PbCl₂ and PbI₂ for the formation of lead chloride iodide (PbICl), and one-step CVD to deposit single halide layers (PbI₂ and PbCl₂), respectively. For the deposition of these mixed halides films, first PbCl₂ was deposited (~75 nm thickness) followed by PbI₂ (also ~75 nm) and the sample named PbCl₂/PbI₂. For single halide layers, film thicknesses were about 150

nm for both PbI_2 and PbCl_2 . These deposition steps are shown schematically in Figure 5.1 together with the conversion to perovskites.

For the Pb halides (PbI_2 or PbCl_2) deposition about 150 mg of lead (II) iodide powder (99%) or lead (II) chloride powder (98%) was placed at the centre of the first zone inside a three-zone tube furnace (Brother XD 1600MT) using ceramic boats [5.37]. Glass/FTO/c- TiO_2 substrates were placed down-stream at optimized temperature dependent positions. The furnace was pumped down to a base pressure of 0.08 mbar followed by ramping of the source (PbI_2 or PbCl_2) zones to their respective sublimation temperatures, 380 °C for PbI_2 and 450 °C for PbCl_2 . To prepare the PbICl film, about 75 nm thick PbCl_2 was deposited with a substrate temperature of 150 °C, placed downstream at 18 cm away from the source. The thin PbCl_2 sample was exposed to PbI_2 vapour employing substrates temperature of 125 °C (at 17 cm downstream) which would give 75 nm of PbI_2 film; the two compounds reacted to form PbICl .

To achieve a 150 nm thick PbI_2 layer a 135 °C nominal substrate temperature was employed with substrates placed at about 16 cm downstream. And finally, for 150 nm thick PbCl_2 film the samples were placed at about 17 cm away from the source at a substrate temperature of 160 °C. Pb halide vapours were transported towards the substrates by using nitrogen gas (N_2) at a flow rate of 100 standard cubic centimetres per minute (sccm) with deposition maintained at a deposition pressure of 300 mbar controlled through an automated pressure regulating system. Deposition was allowed to dwell for 40 minutes before the furnace was allowed to cool down to room temperature.

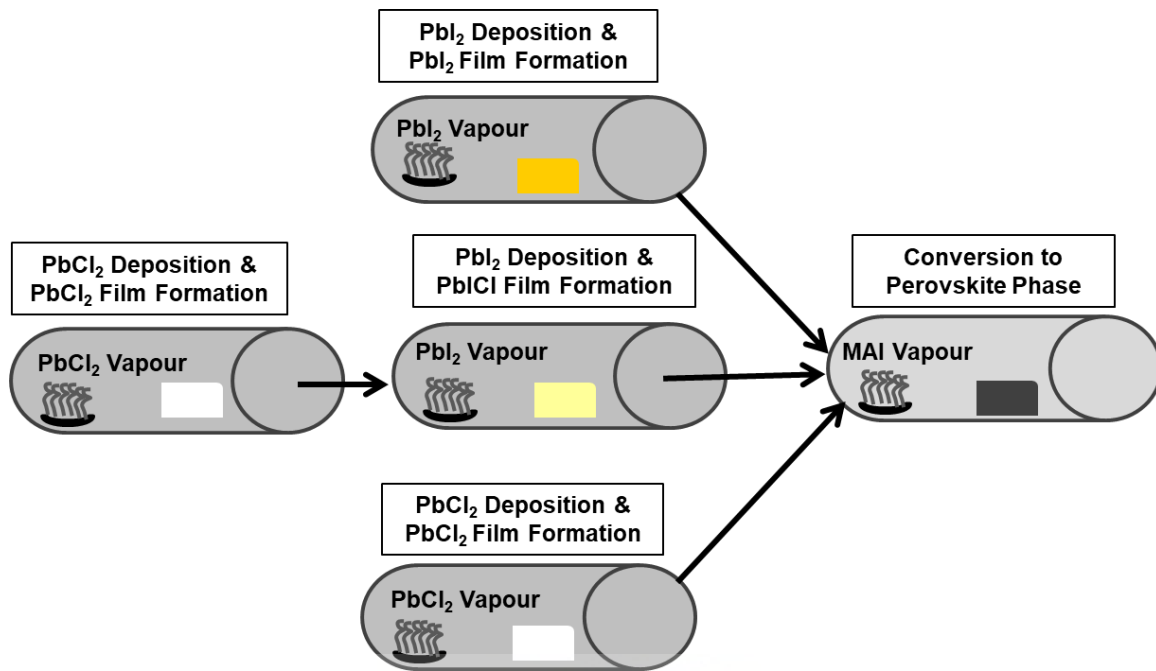


Figure 5.1: Schematic representation of the perovskite film deposition process during the two- and three step sequential low pressure CVD method.

The perovskite conversion from the Pb halide thin films (last step) was performed in the same CVD furnace with a fresh ceramic tube employing a modified method compared to our previous publication [5.37]. Briefly, about 150 mg of methyl ammonium iodide (MAI) (Dyesol) salt was placed on a fresh ceramic boat also at the centre of the first zone and Pb halide films on Glass/FTO/c-TiO₂ substrates placed also downstream at a distance of 8 cm away from the MAI source. The temperature of the MAI was subsequently ramped up to a nominal temperature of 180 °C, and the substrate positioned at a nominal temperature of 130 °C. The conversion of Pb halides to perovskites was carried out at a controlled pressure of 10 mbar under a constant 100 sccm flow of N₂ gas. The exposure was allowed for 60 minutes which is our optimized conversion time where Pb halides fully convert to MAPbI₃ or mixed halide perovskites films. The low pressure (10 mbar) and shorter time (60 minutes) used in this

work compared to our previous publication were based on the new optimum conditions for Cl containing perovskites. The deposition steps schematic is shown in Figure 5.1.

To finalize the device a hole transport layer (HTL) was spin coated on top of the perovskite film at different spin speeds of 2000 rpm 20 s. The HTL solution was prepared by dissolving 80 mg of 2,2'',7,7''-tetrakis(N,N-di-p-methoxyphenylamine)-9,9-spirobifluorene (Spiro-MeOTAD) in 1 mL of chlorobenzene, to which 40 μ L of 4-tert-butylpyridine (tBP) and 25 μ L of lithium bis- (trifluoromethanesulfonyl)imide (LITSEFI) solution (52 mg of LITSEFI in 100 μ L of acetonitrile) were added and stirred for 30 minutes. Finally, a 100 nm silver electrode was deposited by vacuum thermal evaporation under a pressure of 1×10^{-5} mbar through a shadow mask made of ultrathin stainless steel, with device active area of 0.0512 cm².

5.2.2 Characterization

The Panalytical Empyrean X-ray diffractometer with Cu K α (1.54 Å) was used to study the phase composition and crystal structure of the films and was operated at an acceleration voltage of 45 kV and a current of 40 mA, scanning over 2 θ range of 10–100° with a scan step of 0.02°. A Zeiss Auriga field-emission gun Scanning Electron Microscope (FEGSEM) and a Zeiss Cross Beam 540 focused ion beam scanning electron microscope (FIBSEM) operated at acceleration voltages of 1–5 kV were used to investigate the morphology of the films. The FIBSEM is equipped with energy dispersive X-ray spectroscopy (EDS) facilities to identify the elemental composition of the samples. To investigate chemical composition of the converted perovskites films, X-ray photoelectron spectroscopy (XPS) was employed, using a Thermo Scientific ESCALAB 250Xi surface analysis instrument, equipped with a monochromatic Al K α Xray (1486.7 eV) source. Optical transmission measurements were performed using an Ocean Optics UV–visible spectrophotometer and the spectra were measured from 250 to 1000 nm with spectral resolution of 0.5 nm. Photoluminescence (PL)

measurements were performed in reflection geometry using the 457 nm line of an Argon ion laser as the excitation source with the laser power on the sample being <10 mW. The PL spectra were collected with an Ocean Optics USB Flame Spectrometer. Current density–voltage (J–V) curves were recorded using a Keithley 2420 source meter with an illumination of 100 mW/cm², AM1.5, employing a solar simulator (Sciencetech Inc.) in air. The solar cells were illuminated for 15 s before measurements and were scanned in reverse (from 1 V to –0.2 V) and forward (–0.2 V to 1 V) with a step voltage of 12 mV.

5.3 Results and Discussion

5.3.1 Structural and Morphological Properties

The sequential CVD of perovskite films during the three-step and two-step processes is shown schematically in Figure 5.1. Pb halide films were formed in the first steps of the deposition process and these films were subsequently converted to perovskites in the final step. Briefly, during the three-step sequential deposition about 75 nm PbCl₂ film was deposited first followed by another 75 nm PbI₂ layer (second step) for the sample named PbCl₂/PbI₂. During this route a stable lead chloride iodide film (PbICl) was formed with a total thickness of about 143 nm (measured with a thickness profilometer). For the two-step deposition, in the first step single layers of PbI₂ (sample PbI₂) and PbCl₂ (sample PbCl₂) were separately deposited with a thickness of about 150 nm each. The successful deposition of these layers is validated by the X-ray diffraction (XRD) patterns in Figure 5.2(a) deposited on fluorine doped tin oxide (FTO) coated with a thin layer of compact titanium dioxide (c-TiO₂) layer as described in the experimental section.

Figure 5.2(a) shows a crystalline PbI₂ indexed to a hexagonal ($P\bar{3}m1$) structure [5.38, 5.39] with peaks at ~12.74°, 25.59°, and 38.75°, assigned to the (001), (002), and (003) diffracting

planes, respectively, based on the Joint Committee on Powder Diffraction Standards (JCPDS, data no. 07-0235). The PbCl_2 film shows XRD peaks (Figure 5.2(a)) at 22.01° , 22.92° , 23.44° , 24.99° , 32.33° , and 40.0° indexed to the (101), (020), (210), (111), (121), and (004) diffracting planes, respectively, (JCPDS, data no. 01-0536) and all belong to the orthorhombic (Pnma) PbCl_2 structure [5.40].

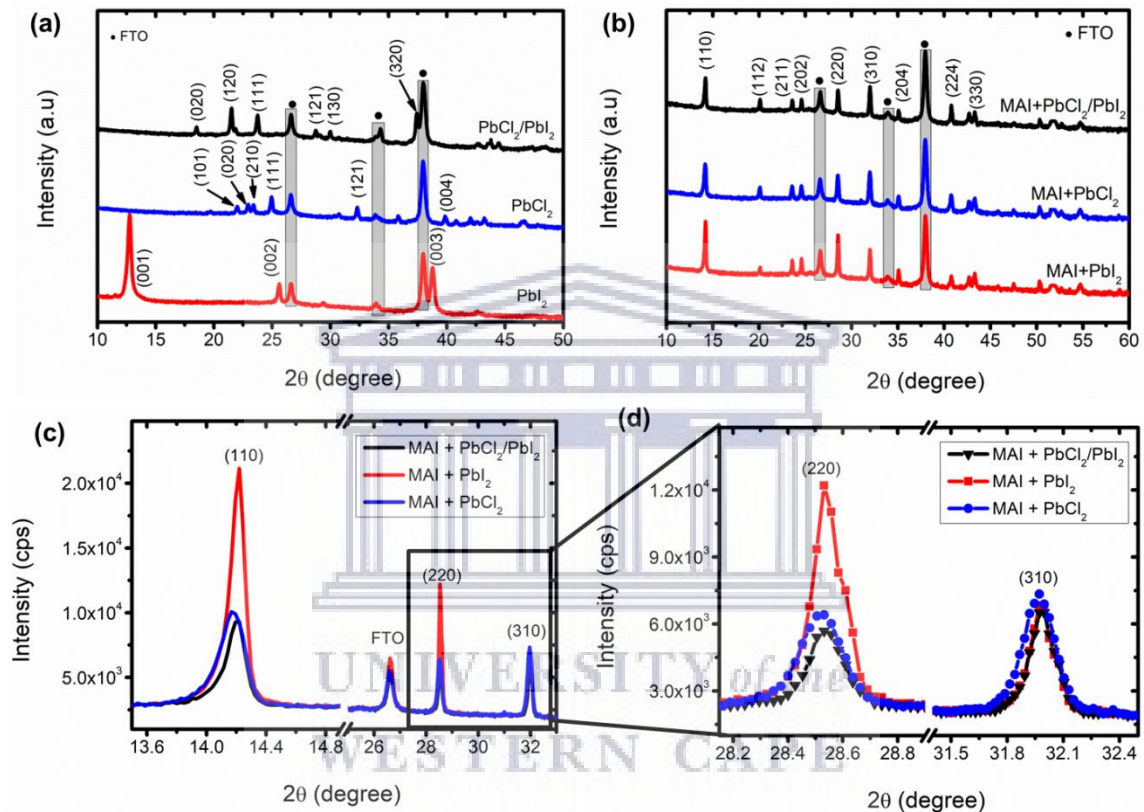


Figure 5.2: (a) XRD patterns of Pb halide films on FTO, (b) XRD patterns of converted perovskite films; (c) selected XRD peaks of the converted perovskites (110), (220), and (310) planes; (d) magnified (220) and (310) perovskite XRD peaks.

The double layered Pb halide film ($\text{PbCl}_2/\text{PbI}_2$ sample) on the other hand showed a mixed halide phase of PbICl through the reaction of PbCl_2 and PbI_2 . This phase is shown by diffraction peaks at 18.47° , 21.51° , 23.68° , 28.70° , 30.02° , and 37.41° indexed to the (020), (120), (111),

(121), (130), and (320) diffracting planes, Figure 5.2(a) top XRD pattern. These diffraction peaks belong to the orthorhombic (Pnam) PbICl structure (JCPDS, data no. 73-0361) [5.12, 5.41, 5.42]. These XRD patterns show a successful deposition of PbI_2 , PbCl_2 , and PbICl phases with the low-pressure CVD method, providing a viable way of synthesizing Cl doped perovskite films. The absence of peaks belonging to PbI_2 or PbCl_2 on the XRD patterns of the $\text{PbCl}_2/\text{PbI}_2$ sample proves the existence of a pure PbICl phase during an in-situ reaction of PbCl_2 and PbI_2 compounds.

These films were subsequently exposed to MAI vapour for the conversion to perovskite films as the last step of the procedure, depicted in Figure 5.1 schematic. XRD patterns of the converted perovskite are shown in Figure 5.2(b) for all the samples; the perovskite sample naming is extended by adding MAI in front of the sample name used for Pb halides. The patterns show the known peaks of the tetragonal hybrid perovskite structure with major peaks at 14.05° , 28.54° , and 31.98° assigned to the (110), (220), and (310) planes, respectively [5.43]. Interestingly, the perovskite film converted from a PbI_2 layer (sample MAI+ PbI_2) has intense (110) and (220) peaks compared to the Cl-doped perovskite samples (sample MAI+ PbCl_2 and MAI+ $\text{PbCl}_2/\text{PbI}_2$) as shown in Figure 5.2(b), and more clearly in Figure 5.2(c) and (d).

The higher intensity of these peaks is due to the preference of crystals along these planes for the PbI_2 -based perovskite sample. The intensity ratio of the (310) to the (220) peak is enhanced for the Cl-doped perovskite samples, suggesting a reduced texture compared to the pure iodine sample which showed more pronounced texture i.e. low (310)/(220) peak ratio (Figure 5.2(d)). This reduced texture on the Cl-doped perovskite films is a first proof of a chlorine inclusion in these samples (sample MAI+ PbCl_2 and MAI+ $\text{PbCl}_2/\text{PbI}_2$) as has been previously reported [5.41]. There were no impurities detected in these samples such as the PbI_2 impurity at 12.70° , while MAPbCl_3 normally appears at 15.80° for chlorine containing

perovskites [5.10 – 5.12]. The absence of these unwanted impurities confirms a successful conversion of the pre-deposited Pb halide films to a high-quality perovskite phase through the low-pressure CVD technique. This also indicates that there is no phase segregation in these samples. There was no significant lattice reduction for the chlorine doped samples compared to the PbI_2 -based sample which indicates a negligible Cl content for these films [5.44, 5.45]. Calculated lattice parameters of a tetragonal perovskite phase are shown in Table 5.1.

Table 5.1: Calculated lattice parameters of the converted perovskite samples based on a tetragonal phase using the XRD patterns.

| Sample | Lattice parameter 'a' (Å) | Lattice parameter 'c' (Å) |
|------------------------------------|---------------------------|---------------------------|
| MAI + $\text{PbCl}_2/\text{PbI}_2$ | 8.831 | 12.50 |
| MAI + PbI_2 | 8.829 | 12.50 |
| MAI + PbCl_2 | 8.834 | 12.51 |

Figure 5.3(a)–(c) shows the planar scanning electron microscopy (SEM) micrographs of the Pb halide films on FTO/c- TiO_2 substrates obtained during the low-pressure CVD process. There is a clear difference in morphologies of the Pb halides films based on the different deposition conditions. Sample $\text{PbCl}_2/\text{PbI}_2$ where the PbCl_2 film was deposited first followed by PbI_2 showed rough columnar-like grains mixed with flatter grains and spaces in-between (Figure 5.3(a)); the average grain size was calculated to be about 93 ± 22 nm as given in Table 5.2.

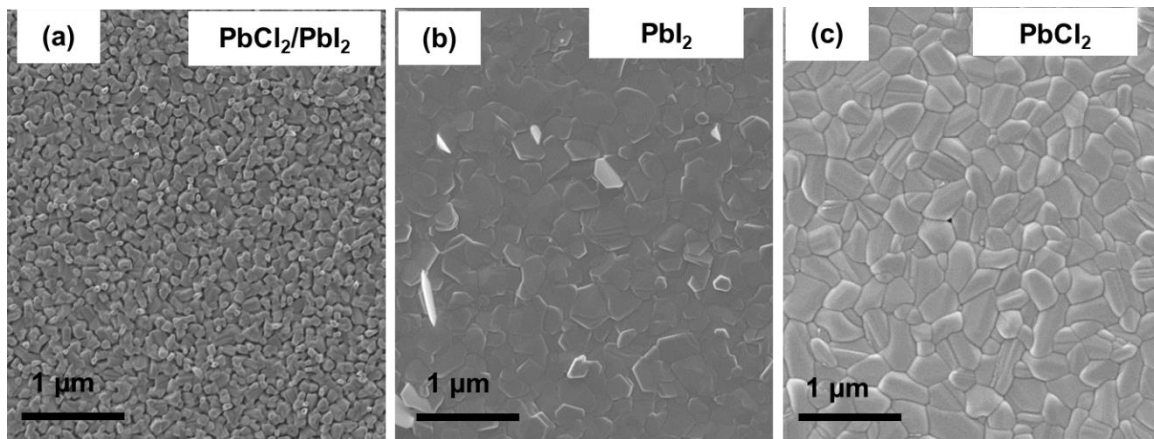


Figure 5.3: (a)–(c) Planar/surface SEM micrograph of pre-deposited Pb halide thin films with sample numbering shown on the micrographs.

This difference in grain shape of the PbI₂ film is related to the distinct grain formation of the PbI₂ and PbCl₂ as also shown by these individual layers in Figure 5.3(b) and (c), respectively. PbI₂ grains form in a layer-by-layer pattern of hexagonal platelets (grains), evidenced by their flat morphology in Figure 5.3(b) compared to the PbCl₂ film which forms more spherical, well defined grains as shown in Figure 5.3(c). Starting with a film that has spherical grains (PbCl₂), the subsequent second step resulted into PbI₂ platelets forming at different angles and interconnecting with the PbCl₂ grains, and finally after reacting, columnar PbI₂ grains were formed. This rough morphology of the PbI₂ phase was also identified by L. Fan and co-workers [5.12] and suggested that it is beneficial for an easy conversion to perovskite. The PbI₂ film in Figure 5.3(b) had smooth and flat grains with an average grain size of 288 ± 86 nm compared to the PbCl₂ counterpart which has larger and more spherical grains of about 366 ± 89 nm in average as seen in Figure 5.3(c). The smaller average grain size of the PbI₂ film is due to grain coarsening during the reaction of PbCl₂ and PbI₂ compounds. Grain size distribution of these Pb halides films is shown in Figure 5.3(a)–(c).

Table 5.2: Summary of Pb halides and perovskites film thicknesses, grain size, and Pb:I:Cl ratios obtained from EDS.

| Sample | Thickness (nm) | Grain Size (nm) | Pb:I:Cl ratio (EDS) |
|---|----------------|-----------------|---------------------|
| PbCl ₂ /PbI ₂ | 143 ± 6 | 93 ± 22 | 1 : 1.4 : 1.1 |
| PbI ₂ | 150 ± 8 | 288 ± 86 | 1 : 2.6 : 0 |
| PbCl ₂ | 150 ± 7 | 366 ± 89 | 1 : 0 : 2 |
| MAI + PbCl ₂ /PbI ₂ | 355 ± 5 | 578 ± 167 | 1 : 3.8 : 0 |
| MAI + PbI ₂ | 295 ± 4 | 1048 ± 321 | 1 : 3.9 : 0 |
| MAI + PbCl ₂ | 490 ± 6 | 937 ± 282 | 1 : 3.7 : 0 |

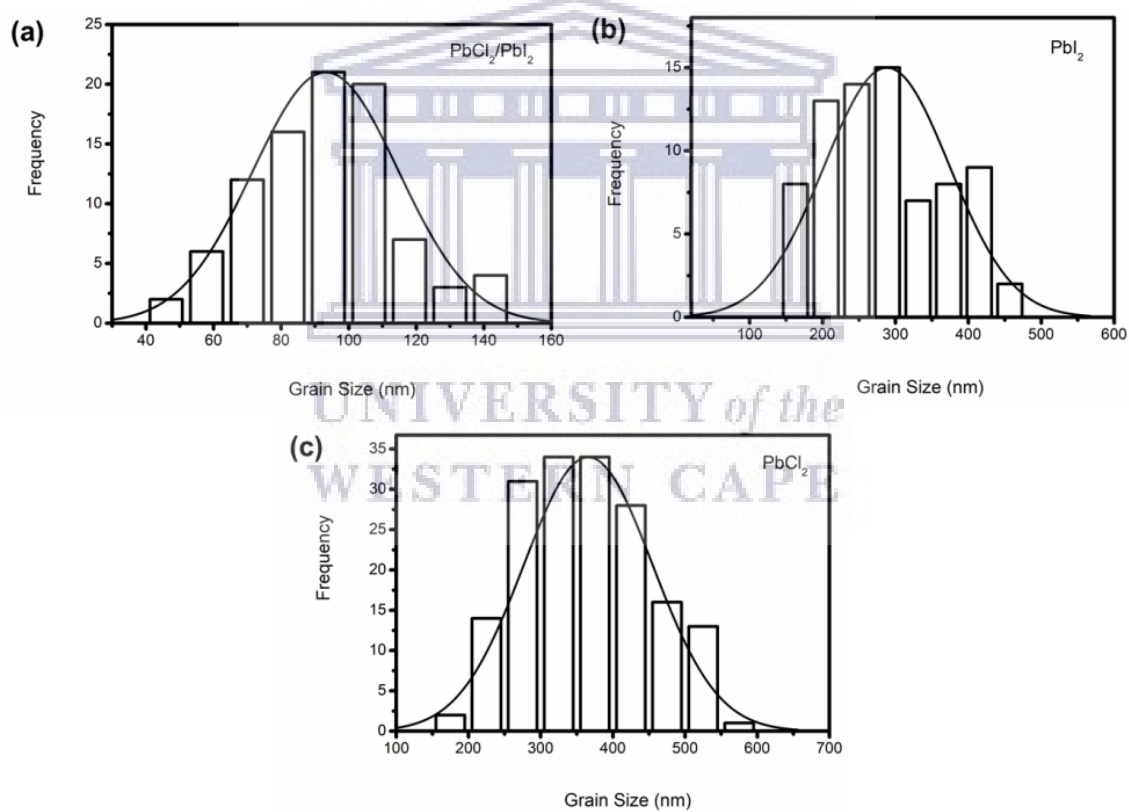


Figure 5.4: (a)–(c) Pb halides grain size distribution plots with sample number shown accordingly.

The planar SEM micrographs of the converted perovskite films are shown in Figure 5.5(a)–(c) depicting well-defined and compact grains, larger than those of the pre-deposited Pb halide counterparts. The perovskite film converted from the PbI₂ film (sample MAI+PbCl₂/PbI₂) shows smaller grains than the pure halide counterparts, but with larger than the grains of the starting PbI₂ layer as shown Figure 5.5(a). The average lateral grain size of this sample was estimated to be about 578 ± 167 nm, shown in Table 5.2. In contrast, sample MAI+PbI₂ showed very large, compact, and flat grains with an average grain size of 1048 ± 321 nm even though there were grains larger than $2 \mu\text{m}$ as shown in Figure 5.5(b).

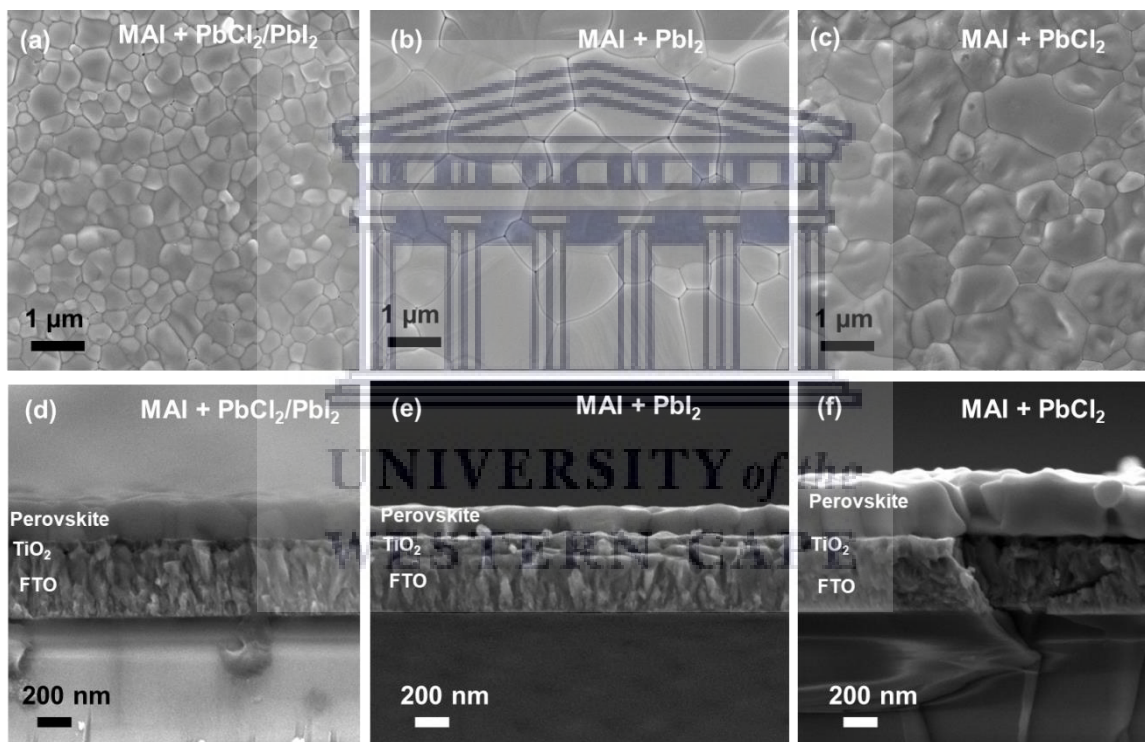


Figure 5.5: (a)–(c) Planar/surface SEM micrographs of the converted perovskite thin films during the last step of the sequential CVD process; (d)–(f) cross sectional view SEM of the respective perovskite samples.

On the other hand, sample MAI+PbCl₂ also showed well-defined, compact, and rougher grains with an average size of 937 ± 282 nm as illustrated in Figure 5.5(c). Another sample that

was compared in this study was under conditions where a film of PbI_2 was deposited first followed by a PbCl_2 film, forming a PbICl phase that was eventually converted to a perovskite, yielding a similar morphology to the $\text{MAI}+\text{PbCl}_2/\text{PbI}_2$ film (Figure 5.6). The perovskite grain size distributions are also included in the Figure 5.7(a)–(c).

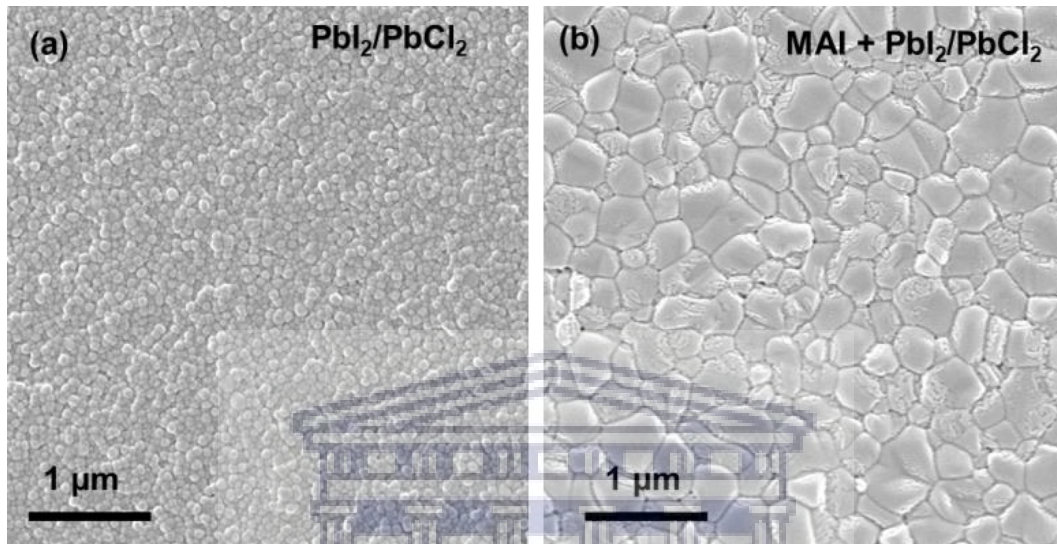


Figure 5.6: Planar SEM micrographs of the samples of: (a) the lead halide, and (b) the converted perovskite film. The Pb halide sample was deposited by starting with a PbI_2 film and followed by a deposition of PbCl_2 hence forming a PbICl phase.

The difference in grain sizes between these samples can be attributed to the morphology of the starting Pb halides layers. The PbICl films had very small and rough grains and this might have contributed to poor crystallization of the final perovskite film, with small grains of the starting Pb halide yielding smaller perovskite grains after conversion. The porosity of the starting PbICl film was shown to result into larger perovskite grains during solution method [5.12] but our results prove otherwise for low pressure CVD. Instead, the porous nature of the PbICl phase might have improved the conversion rate to perovskite but all these samples in this study were converted for 60 minutes as it was an optimum conversion time for PbI_2 and PbCl_2 films.

In comparison, the perovskite prepared from a PbCl_2 film had relatively larger grains compared to the sample $\text{MAI}+\text{PbCl}_2/\text{PbI}_2$ due to larger grains of the starting PbCl_2 . The sample converted from a flat PbI_2 film had very large grains and this is due to easy intercalation of the MAI molecule into the layered structure of the PbI_2 [5.37]. These results contradict what have been previously reported that Cl incorporation into the perovskite structure improves crystallization leading to larger grains reported for perovskite films prepared by solution methods [5.10 – 5.12, 5.28]. Our results further shows that low pressure CVD grown PbI_2 film leads to larger and smooth perovskite grains compared to starting with a Cl-containing compound.

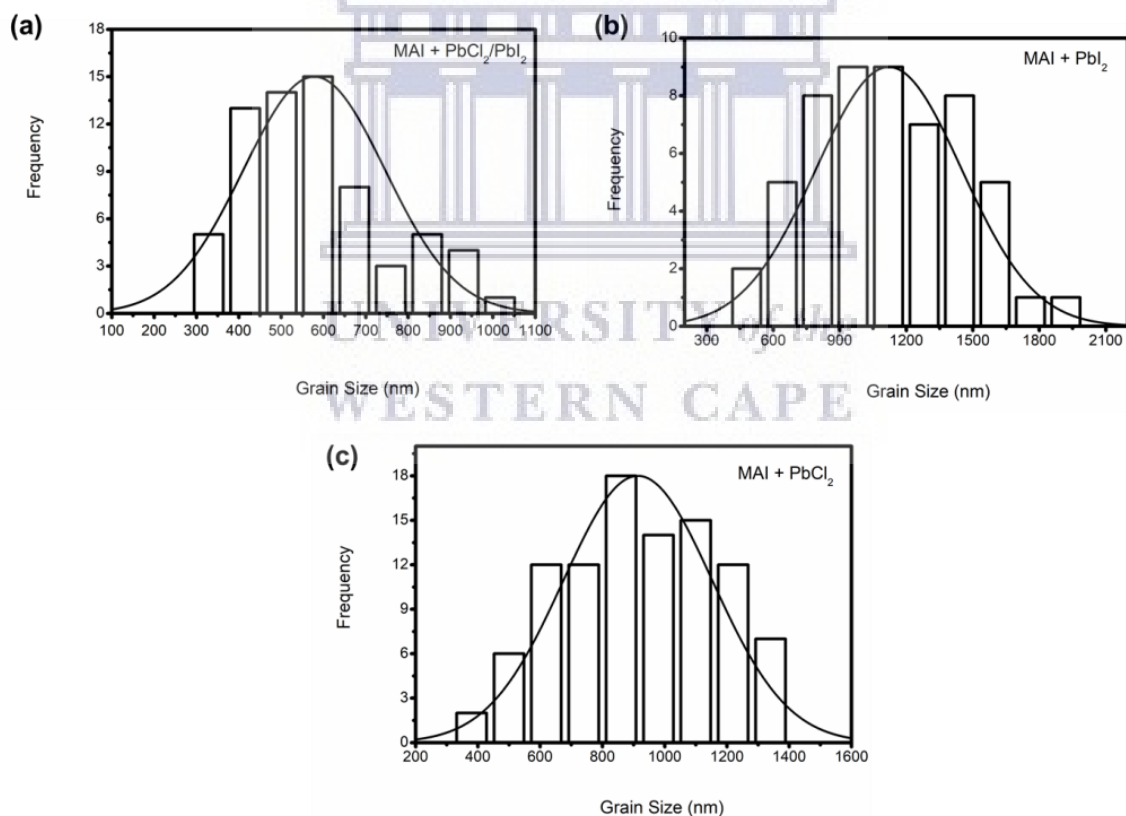


Figure 5.7: (a)–(c) Converted perovskite film grain size distribution plots with sample number shown on each plot.

The respective cross-sectional SEM in Figure 5.5(d)–(f) shows continuous grains across the film thickness, which is an advantage for efficient charge transport as there are less grain boundaries and hence suppressed charge recombination in the device [5.9]. Further, these cross-sectional SEM micrographs also illustrate an intimate contact between the perovskite films and the underlying *c*-TiO₂ layer. These perovskite films have a uniform thickness over large areas (Figure 5.8(a)–(c)), demonstrating the scalable advantage of employing the sequential CVD method.

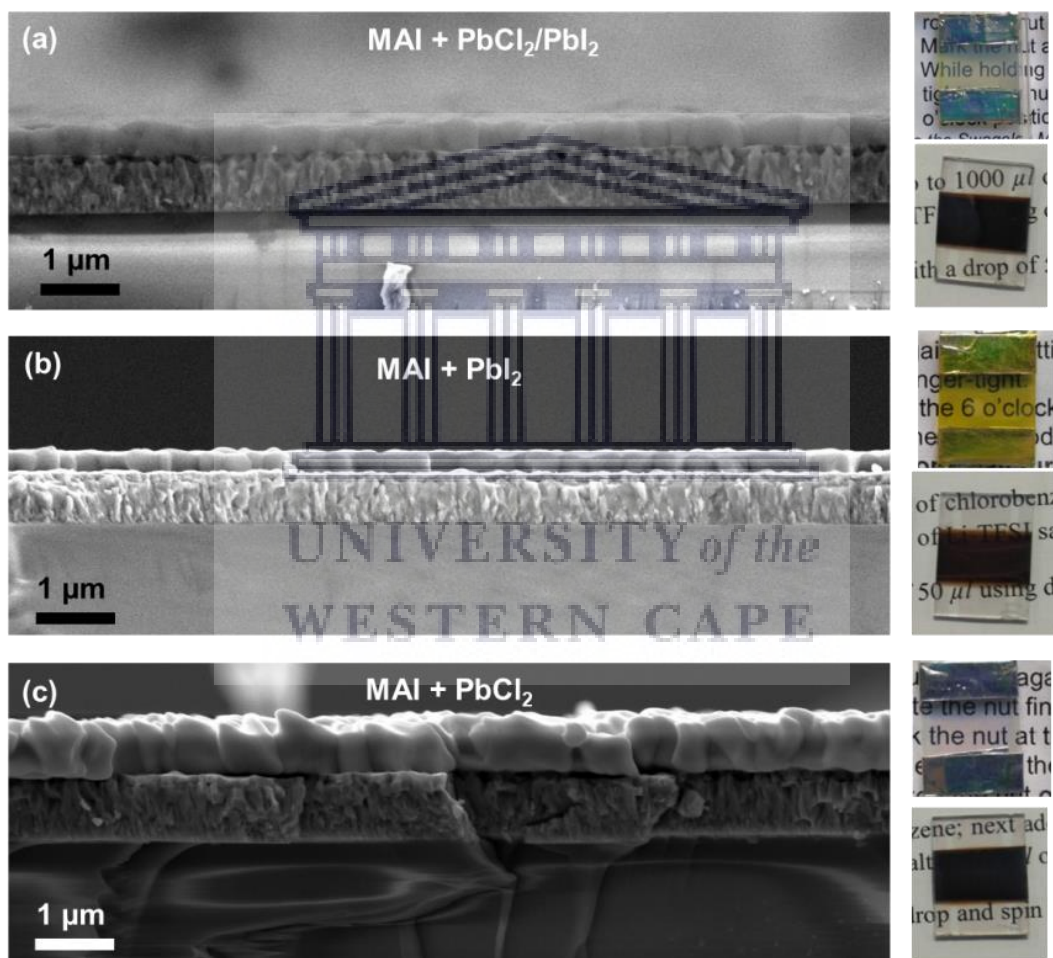


Figure 5.8: (a)–(c) Low magnification cross sectional view SEM micrographs of the perovskite films showing a uniform thickness; next to each cross section are the photographs of the respective samples before and after conversion.

The perovskite film converted from the PbI_2 film had thickness of about 295 ± 4 nm, almost double that of the starting PbI_2 and thinner than the other two samples. Perovskite sample MAI+ PbCl_2 / PbI_2 resulted in a thickness of 355 ± 5 nm from a thickness about 143 nm starting PbI_2 film, and finally sample MAI+ PbCl_2 had a thickness of 490 ± 6 nm that is more than 3 times the starting PbCl_2 film. The film thickness increase for these converted perovskites is consistent with the known volume expansion of Pb halide films when converted to perovskite phase [5.23, 5.26, 5.27, 5.46]. Furthermore, the lateral grain sizes of these films are larger than the film thickness especially for sample MAI+ PbI_2 and MAI+ PbCl_2 , and this is also beneficial for better device performance compared to solution processed perovskites [5.9, 5.28, 5.41, 5.46]. The summary of film thicknesses and grain sizes are provided in Table 5.2.

Energy dispersive X-ray spectroscopy (EDS) was used to assess the elemental composition of both Pb halide films and the converted perovskite films. The summary of the atomic ratio of Pb/I/Cl is given in Table 5.2 for all the samples studied here. Firstly, there was more iodine detected in all the samples with Pb:I ratio of 1:2.6 for the PbI_2 which theoretically should be 1:2. The PbI_2 film had a Pb:I:Cl ratio of 1:1.7:1 and the PbCl_2 film had a Pb:Cl ratio of 1:2 agreeing well with the theoretical value of 1:2. These results were important in this study to show that Cl ions remained in the PbI_2 films even though these films were formed under high temperatures and low pressures.

The converted perovskites on the other hand showed no Cl composition in the EDS analysis, which also confirms the limitation of EDS for detecting low atomic composition (detection limit of 0.1–1 atomic %) [5.6]. The conversion to perovskites here was achieved at nominal substrate temperatures of 130 °C comparable to that of PbI_2 phase formation (125 °C). The Cl was not replaced by the iodine during PbI_2 phase formation, but this did occur during conversion to perovskite where no Cl could be detected. Comparing the two conditions it shows

that the smaller ionic radii of Cl cause it to be easily replaced by larger ionic radii of iodine only during perovskite phase formation in the presence of methyl ammonium. This means the Cl ions on the perovskite structure are weakly bonded to the Pb whereas they are tightly bonded on the PbCl structure.

The formation of a perovskite phase with the presence of the MA molecule further facilitates the replacement of Cl ions by the iodine. The EDS results also show that the chlorine was completely replaced by iodine during conversion to perovskites, even when we started with the pure PbCl₂ film (sample MAI+PbCl₂). To study the elemental composition in detail, X-ray photoelectron spectroscopy (XPS) was employed on the converted perovskite films. The XPS full survey spectra of the surface of the perovskites films are shown in Figure 5.9(a), showing the elements in the films [5.19]. The absence of the Cl 2p peak between 196 eV and 202 eV [5.12, 5.19] in the XPS spectra (Figure 5.9(b)) confirms that Cl is not present in these perovskite films, which is in agreement with the EDS data. The possible scenario is that during the conversion of PbCl₂ or PbICl to the perovskite phase, these compounds dissociates and Cl⁻ escapes in gaseous phase as MACl with Pb or iodine remaining in the perovskites [5.9].

Also shown in Figure 5.9(c) and (d) are the high resolution XPS core level spectra of I 3d and Pb 4f, respectively, of the perovskite films. There are no observable shifts in peak positions for the I 3d and Pb 4f binding energies with respect to different samples, suggesting a similar chemical environment on all three perovskite samples. The similar binding energies for I 3d and Pb 4f in all these perovskites films is consistent with the absence of Cl in the films. Further, there is no indication of metallic lead (Pb⁰) in these perovskite samples (Figure 5.9(d)), which usually has a small hump at about 137 eV and 141 eV binding energies that are associated with unbonded Pb [5.47, 5.48]. The presence of Pb⁰ in the perovskites act as a defect site and therefore undesirable. Lastly, the calculated atomic composition from the high resolution XPS

spectra of iodine and lead showed similar results to that of the EDS results. The Pb:I:Cl ratio from XPS were: 1:4.0:0 (sample MAI+PbI₂), 1:3.9:0 (sample MAI+PbCl₂), and 1:3.9:0 (sample MAI+PbCl₂/PbI₂). Again, this excessive iodine content is consistent with the absence of unbonded metallic lead, which confirms the high-quality perovskite films.

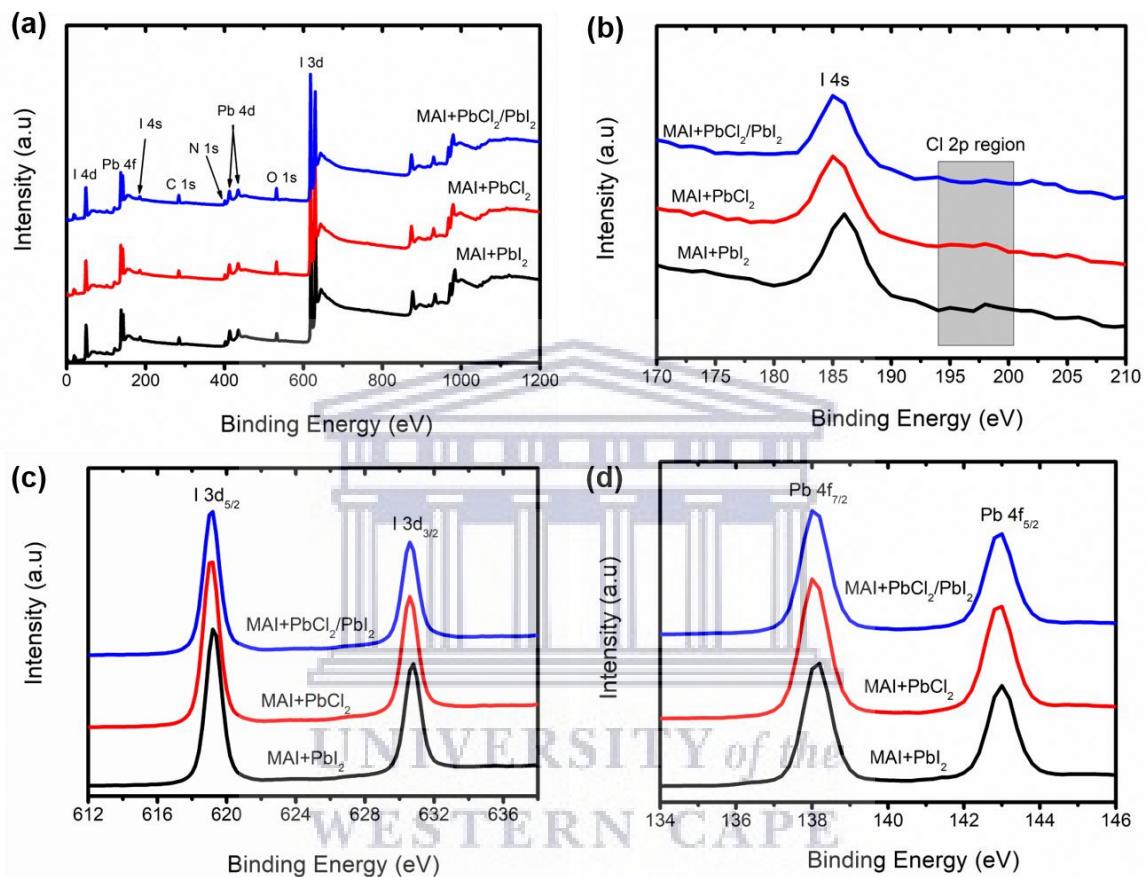


Figure 5.9: (a) XPS full survey spectra of the top surface of converted perovskites films; (b) Zoomed XPS spectra from (a) showing the region of Cl 2p peak. (c) and (d) High resolution XPS core level spectra of I 3d, and Pb 4f, respectively.

5.3.2 Optical Properties and Device Characterization

The absorbance spectra of the converted perovskite films are all identical with high absorption over the visible range as shown in Figure 5.10(a). Sample MAI+PbCl₂ showed a slightly higher absorbance in this region (visible) and this is attributed to the higher film

thickness of this sample compared to the other two samples. Similar optical band gaps of 1.59 eV for all the samples was estimated by analysing Tauc plots for a direct band gap perovskite as shown in Figure 5.10(b) [5.41]. The estimated band gaps also lie within reported values of tetragonal MAPbI₃ perovskites [5.49, 5.50] with no indication of a band gap shift for Cl doped perovskites compared to the pure iodine-based counterparts [5.8, 5.44, 5.45].

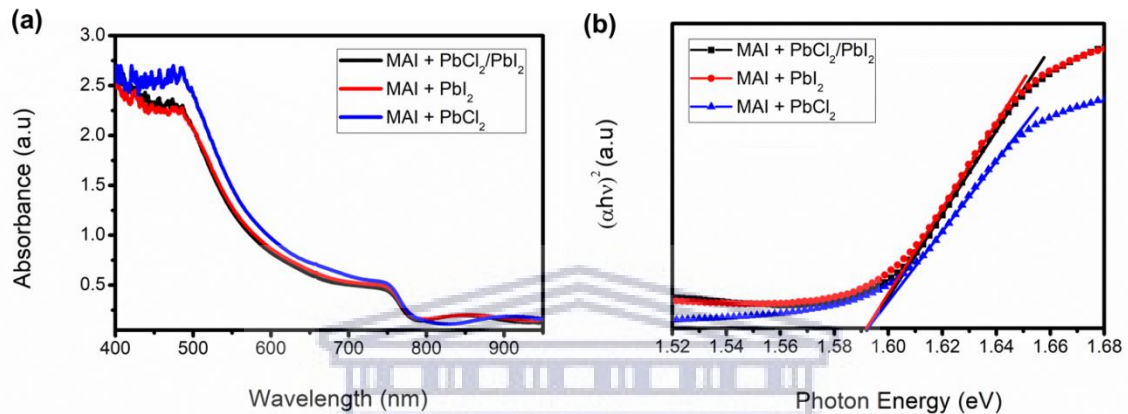


Figure 5.10: (a) Absorbance spectrums of the converted perovskite films on FTO/c-TiO₂, and (b) Tauc plots of the perovskite films showing their estimated optical direct band gaps.

The absorbance spectra of the perovskites were also simulated near the band-edge using the Elliott model to extract the band gap and exciton binding energies, shown in Figure 5.11(a)–(c). The fitting details using the Elliott model are provided in Appendix A. The band gap energies are almost the same for all three samples ranging between 1.70 eV and 1.72 eV; larger than the Tauc based band gaps as expected [5.49]. The excitonic binding energies of the three samples lie between 45 and 54 meV, further suggesting low trap densities for these perovskite samples.

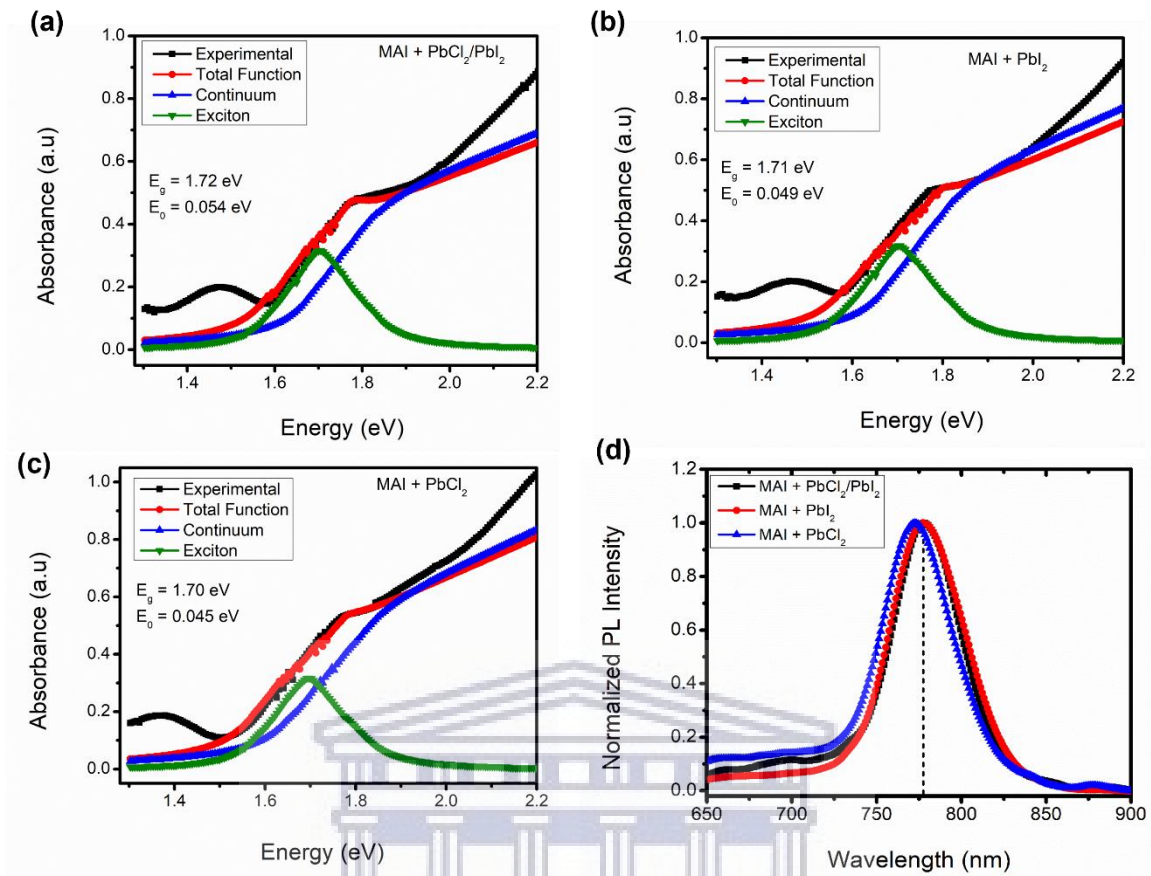


Figure 5.11: (a)–(c) Simulated and experimental optical absorption spectra. (d) Normalized steady state PL spectra of the perovskites thin films on glass substrates (Glass/Perovskites).

The photoluminescence (PL) spectra of the perovskites films are shown in Figure 5.11(d), where an emission peak centered at about 777 nm (1.596 eV) is observed for the MAI+PbCl₂/PbI₂ and MAI+PbI₂ samples. The emission peak for the MAI+PbCl₂ perovskites sample is centered at 773 (1.604 eV) nm displaying a slight blue shift (4 nm) compared to the other perovskite samples. These PL emission peaks are consistent with the Tauc plots for the band gap (~1.60 eV) and agrees with literature [5.9, 5.22, 5.41]. The slight blue shift of the MAI+PbCl₂ sample may be due to the minute presence of the Cl, although it was not detected by XPS and EDS [5.9, 5.22].

The planar perovskite solar cell devices were completed by a deposition of a Spiro–MeOTAD layer which acts as a hole transport material (HTM), and finally a thin layer (100 nm) of silver metal (Ag) as a back contact was deposited. The complete device had Glass/FTO/c-TiO₂/perovskite/Spiro–MeOTAD/Ag sequence. The deposition of the HTM and the device characterization was done in ambient air (20 °C and 55% relative humidity) without any use of a glove box. The device performance was then characterized by current and voltage measurements under simulated AM 1.5G (100 mW/cm²) solar irradiation in air. The best current density (J)–voltage (V) curves of all the samples are shown in Figure 5.12(a) for reverse scan and in Figure 5.12(b) for forward scan. Device parameters (best and average) are summarized in Table 5.3 with open circuit voltage (V_{oc}), short circuit current density (J_{sc}), fill factor (FF), and power conversion efficiency (PCE) provided for reverse scans. The device parameters for the forward scan are summarised in Table 5.4 only showing the best parameters.

Interestingly, the chlorine doped perovskite devices showed well-improved V_{oc} of 0.907 V for sample MAI+PbCl₂/PbI₂ and 0.938 V for sample MAI+PbCl₂ compared to the pure iodine-based device (MAI+PbI₂) with $V_{oc} = 0.862$ V (Figure 5.12(a)). The Cl doped perovskite samples also showed improved fill factor with 0.545 for sample MAI+PbCl₂/PbI₂ and 0.562 for sample MAI+PbCl₂ when compared to MAI+PbI₂ sample which has a fill factor of 0.517. The measured current density of these samples was 20.55 mA/cm² for sample MAI+PbCl₂/PbI₂, 20.64 mA/cm² for sample MAI+PbCl₂ and 19.65 mA/cm² for sample MAI+PbI₂ (Figure 5.12(a)). The highest PCE of 10.87% was from the sample MAI+PbCl₂ followed by 10.14% for sample MAI+PbCl₂/PbI₂, and lastly 8.76% for sample MAI+PbI₂. These devices had lower PCE compared to our previous publication [5.37] and even worse for the MAI+PbI₂ sample. This was because the deposition conditions were altered for best optimum film conditions of the Cl-doped samples.

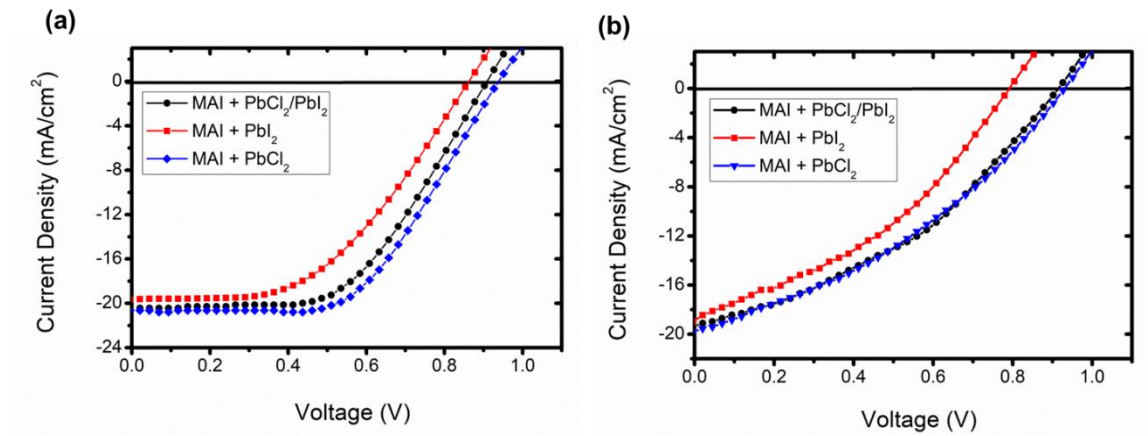


Figure 5.12: (a) J–V characteristic curves of the best perovskite solar cell devices under 100 mW/cm² illumination at reverse scan, (b) forward scan J–V curves of the same solar cell devices.

Table 5.3: Solar cell device performances of different samples (4 devices each) extracted from the J–V curves; Voc (open circuit voltage), Jsc (short circuit current density), FF (fill factor), and PCE (power conversion efficiency).

| Sample | | V _{oc} (V) | J _{sc} (mA/cm ²) | FF | PCE (%) |
|---|---------|---------------------|---------------------------------------|---------------|-------------|
| MAI + PbCl ₂ /PbI ₂ | Best | 0.907 | 20.55 | 0.545 | 10.14 |
| | Average | 0.903 ± 0.012 | 19.52 ± 0.37 | 0.528 ± 0.009 | 9.57 ± 0.11 |
| MAI + PbI ₂ | Best | 0.862 | 19.65 | 0.517 | 8.76 |
| | Average | 0.830 ± 0.02 | 18.45 ± 0.66 | 0.485 ± 0.016 | 7.43 ± 0.50 |
| MAI + PbCl ₂ | Best | 0.938 | 20.64 | 0.562 | 10.87 |
| | Average | 0.936 ± 0.008 | 19.73 ± 0.46 | 0.536 ± 0.014 | 9.86 ± 0.42 |

Since the MAI+PbI₂ sample had larger grains it is expected to have a reduced density of trap states at the grain boundaries compared to smaller grain size Cl-doped samples [5.51, 5.52], which should ideally improve the device performance. However, this is contradictory to our observed results, which shows that the device performance is not solely dependent on the

perovskite grain size. The low concentration of Cl present in the doped samples demonstrates that Cl passivates the dangling bond defects at grain boundaries and on the film surface, resulting in reduced charge trap states and the suppression of charge recombination [5.12, 5.51, 5.52]. This leads to an improved charge injection towards the transport layers, leading to an increased V_{oc} , FF and ultimately their performance [5.10, 5.12, 5.44, 5.53, 5.54]. In addition to this, the expected longer carrier diffusion length in the Cl-doped perovskite thin films plays a crucial role in improving the solar cell performance [5.55]. In general, these perovskite devices suffer from relatively poor fill factor and V_{oc} mainly due to poor charge transport at the perovskite/c-TiO₂ interface resulting in poor device performances [5.56, 5.57].

Table 5.4: Solar cell device performances of different samples extracted from the J–V curves during forward scan (-0.2 to 1 V).

| Sample | V_{oc} (V) | J_{sc} (mA/cm ²) | FF | PCE (%) |
|---|--------------|--------------------------------|-------|---------|
| MAI + PbCl ₂ /PbI ₂ | 0.914 | 19.33 | 0.385 | 6.80 |
| MAI + PbI ₂ | 0.791 | 18.86 | 0.376 | 5.61 |
| MAI + PbCl ₂ | 0.928 | 19.75 | 0.359 | 6.57 |

The forward scan J–V curves are shown in Figure 5.12(b) and all showed poor FF compared to the reverse scans, which demonstrates high device hysteresis. Hysteresis is a norm in planar heterojunction perovskite devices that result from poor charge transport at the electron transport layer, i.e., compact TiO₂ [5.11, 5.56, 5.57]. A similar trend was observed during the forward scans with higher V_{oc} for Cl doped perovskite films (V_{oc} higher than 0.9 V) compared to the PbI₂-based perovskite device with $V_{oc} = 0.791$ V shown in Table 5.4. These device performances prove that the incorporation of chlorine in the perovskite structure improves the performance of organic-inorganic perovskite solar cells. It is shown here (based on the reverse

scan) that by starting with a pure PbCl_2 layer and its exposure to MAI vapour improves V_{oc} by 76 mV compared to the pure iodine-based counterparts.

5.4 Conclusion

A low-pressure CVD method was used to successfully deposit Cl-doped perovskite solar cell devices via three- and two-step routes from chlorine-containing Pb halide films and compared to pure iodine-based perovskite. It is demonstrated here for the first time that Cl is not substituted by iodine during the high temperature sequential CVD of PbCl_2 and PbI_2 layers; instead, the compounds reacted to form a stable lead chloride iodide phase. It is further shown that Cl is easily substituted by iodine during the perovskite formation under similar substrate temperatures as the Pb halide deposition, though different deposition pressures were used. We also showed that the presence of Cl in the Pb halide films does not necessarily improve the grain size of the final perovskite films compared to its pure iodine counterparts, but its presence is still beneficial to the device performance. Lastly, the open circuit voltage (V_{oc}) was improved significantly for perovskites prepared from Cl-containing Pb halides, thereby increasing the device efficiencies. The highest device performance of 10.87% ($V_{oc} = 0.938$ V) was achieved for the perovskite converted from PbCl_2 compared to just 8.76% ($V_{oc} = 0.862$ V) for PbI_2 -based perovskite. This improved V_{oc} and efficiency were attributed to the low trap density at grain boundaries and at film surface for Cl-doped perovskites allowing easy injection of charge carriers to the respective charge transport layers. This work will aid in the development of a scalable, low-cost synthesis technique for the manufacturing of mixed-halide hybrid perovskite solar panels.

5.5 References

- [5.1] A. Jena, A. Kulkarni, and T. Miyasaka, *Chemical Reviews* 119 (2019) 3036.

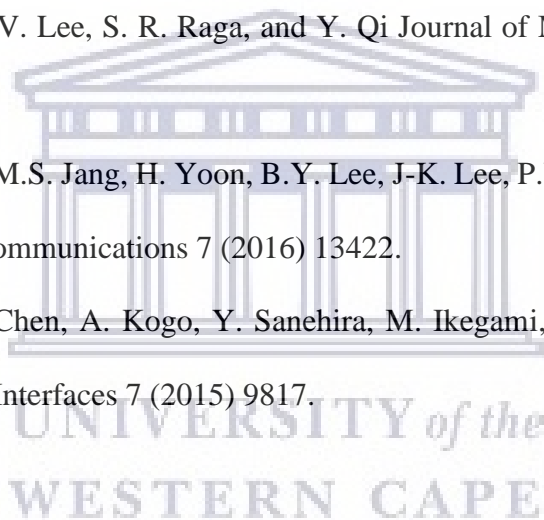
- [5.2] R. Wang, M. Mujahid, Y. Duan, Z-K. Wang, J. Xue, and Y. Yang, *Advanced Functional Materials* (2019) 1808843.
- [5.3] R. Swartwout, M.T. Hoerantner, and V. Bulovic, *Energy & Environmental Materials* 2 (2019) 119.
- [5.4] A. Kojima, K. Teshima, Y. Shirai, and T. Miyasaka, *Journal of American Chemical Society* 131 (2009) 6050.
- [5.5] National Renewable Energy Laboratory (NREL). Research Cell Efficiency Records. http://www.nrel.gov/ncpv/images/efficiency_chart.jpg (accessed 7 July 2020).
- [5.6] L.K. Ono, E.J. Juarez-Perez, and Y. Qi, *ACS Applied Materials Interfaces* 9 (2017) 30197.
- [5.7] L. Ono, M. Leyden, S. Wang, and Y. Qi, *Journal of Materials Chemistry A* 4 (2016) 6693.
- [5.8] J. Chae, Q. Dong, J. Huang, and A. Centrone, *Nano Letters* 15 (2015) 8114.
- [5.9] H. Zhang, Y. Lv, J. Wang, H. Ma, Z. Sun, W. Huang, *ACS Applied Materials Interfaces* 11 (2019) 6022.
- [5.10] C. Wittich, E. Mankel, O. Clemens, K. Lakus-Wollny, T. Mayer, W. Jaegermann, and H-J. KleeB, *Thin Solid Films* 650 (2018) 51.
- [5.11] P. Luo, Z. Liu, W. Xia, C. Yuan, J. Cheng, C. Xu, Y. Lu, *Journal of Materials Chemistry A* 3 (2015) 22949.
- [5.12] L. Fan, Y. Ding, J. Luo, B. Shi, X. Yao, C. Wei, D. Zhang, G. Wang, Y. Sheng, Y. Chen, A. Hagfeldt, Y. Zhao, and X. Zhang, *Journal of Materials Chemistry A* 5 (2017) 7423.
- [5.13] Q. Dong, Y. Yuan, Y. Shao, Y. Fang, Q. Wang, and J. Huang, *Energy & Environmental Science* 8 (2015) 2464.

- [5.14] J. Richter, M. Abdi-Jalebi, A. Sadhanala, M. Tabachnyk, J.P.H. Rivett, L.M. Pazos-Outón, K.C. Gödel, M. Price, F. Deschler, and R.H. Friend, *Nature Communications* 7 (2016) 13941.
- [5.15] B. Yang, J. Keum, O. S. Ovchinnikova, A. Belianinov, S. Chen, M.H. Du, I.N. Ivanov, C.M. Rouleau, D.B. Geohegan, and K. Xiao, *Journal of American Chemical Society* 138 (2016) 5028.
- [5.16] B. Yang, C.C. Brown, J. Huang, L. Collins, X. Sang, R.R. Unocic, S. Jesse, S.V. Kalinin, A. Belianinov, and J. Jakowski, *Advanced Functional Materials* 27 (2017) 1700749.
- [5.17] T.-W. Ng, C.-Y. Chan, M.-F. Lo, Z.Q. Guan, and C.-S. Lee, *Journal of Materials Chemistry A* 3 (2015) 9081.
- [5.18] S.T. Williams, F. Zuo, C.-C. Chueh, C.-Y. Liao, P.-W. Liang, and A. K. Jen, *ACS Nano* 8 (2014) 10640.
- [5.19] H. Yu, F. Wang, F. Xie, W. Li, J. Chen, and N. Zhao, *Advanced Functional Materials* 24 (2014) 7102.
- [5.20] S. Luo, P. You, G. Cai, H. Zhou, F. Yan, and W.A. Daoud, *Materials Letters* 169 (2016) 236.
- [5.21] S. Tombe, G. Adam, H. Heilbrunner, D. Hazar Apaydin, C. Ulbricht, N. Serdar Sariciftci, C.J. Arendse, E. Iwuoha, and M. C. Scharber, *Journal of Materials Chemistry C* 5 (2017) 171.
- [5.22] X. Cao, L. Zhi, Y. Jia, Y. Li, K. Zhao, X. Cui, L. Ci, K. Ding, and J. Wei, *Electrochimica Acta* 275 (2018) 1.
- [5.23] C.W. Chen, H.W. Kang, K.M. Chiang, and H.W. Lin, *Advanced Materials* 26 (2014) 6647.
- [5.24] M. Liu, M. Johnston, and H. Snaith, *Nature* 501 (2013) 395.

- [5.25] D. Yang, Z. Yang, W. Qin, Y. Zhang, S. Liu, and C. Li, *Journal of Materials Chemistry A* 3 (2015) 9401.
- [5.26] M. Leyden, L. Ono, S. Raga, Y. Kato, S. Wang, and Y. Qi, *Journal of Materials Chemistry A* 2 (2014) 18742.
- [5.27] S. Ha, X. Liu, Q. Zhang, D. Giovanni, T. Sum, and Q. Xiong, *Advanced Optical Materials* 2 (2014) 838.
- [5.28] M. Tavakoli, L. Gu, Y. Gao, J. He, A. Rogach, Y. Yao, and Z. Fan, *Scientific Reports* 5 (2015) 14083.
- [5.29] P. Luo, Z. Liu, W. Xia, C. Yuan, J. Cheng, and Y. Lu, *ACS Applied Materials Interfaces* 7 (2015) 2708.
- [5.30] P.S. Shen, J.S. Chen, Y.H. Chiang, M. Li, T. Guo, and P. Chen, *Advanced Mater Interfaces* 3 (2016) 1500849.
- [5.31] B. Wang, and T. Chen, *Advanced Science* 3 (2016) 1500262.
- [5.32] Y. Peng, G. Jing, and T. Cui, *Journal of Materials Chemistry A* 3 (2015) 12436.
- [5.33] P.S. Shen, Y.H. Chiang, M.H. Li, T. Guo, and P. Chen, *Applied Materials* 4 (2016) 091509.
- [5.34] M. R. Leyden, Y. Jiang, and Y. Qi, *Journal of Materials Chemistry A* 4 (2016) 13125.
- [5.35] A. Ioakeimidis, C. Christodoulou, M. Lux-Steiner, and K. Fostiropoulos, *Journal of Solid State Chemistry* 244 (2016) 20.
- [5.36] V.-D. Tran, S.V. Pammi, V.-D. Dao, H.-S. Choi, and S.-G. Yoon, *Journal of Alloys and Compounds* 747 (2018) 703.
- [5.37] S. Ngqoloda, C. J. Arendse, T. F. Muller, P. F. Miceli, S. Guha, L. Mostert, C. J. Oliphant, *ACS Applied Energy Materials* 3 (2020) 2350.
- [5.38] H. Sun, X. Zhu, D. Yang, J. Yang, X. Gao, and X. Li, *Journal of Crystal Growth* 405 (2014) 29.

- [5.39] M. Schieber, N. Zamoshchik, O. Khakhan, A. Zuck, *Journal of Crystal Growth* 310 (2008) 3168.
- [5.40] J. Costa, J. Azevedo, L. Santos, and A. Mendes, *Journal of Physical Chemistry C* 121 (2017) 2080.
- [5.41] Y. Li, J.K. Cooper, R. Buonsanti, C. Giannini, Y. Liu, F.M. Toma, and I.D. Sharp, *Journal of Physical Chemistry Letters* 6 (2015) 493.
- [5.42] N. Wu, C. Shi, C. Ying, J. Zhang, and M. Wang, *Applied Surface Science* 357 (2015) 2372.
- [5.43] T. Baikie, Y. Fang, J. Kadro, M. Schreyer, F. Wei, S. Mhaisalkar, M. Graetzel, and T. White, *Journal of Materials Chemistry A* 1 (2013) 5628.
- [5.44] Z. Liu, L. Qiu, E.J. Juarez-Perez, Z. Hawash, T. Kim, Y. Jiang, Z. Wu, S.R. Raga, L.K. Ono, S. Liu, and Y. Qi, *Nature Communications* 9 (2018) 3880.
- [5.45] Y. Li, W. Sun, W. Yan, S. Ye, H. Peng, Z. Liu, Z. Bian, and C. Huang, *Advanced Functional Materials* 25 (2015) 4867.
- [5.46] Q. Chen, H. Zhou, S. Luo, Y. Liu, G. Li, and Y. Yang, *Journal of American Chemical Society* 136 (2014) 622.
- [5.47] T.G. Kim, S. W. Seo, H. Kwon, J. Hahn, and J. W. Kim, *Physical Chemistry Chemical Physics* 17 (2015) 24342.
- [5.48] W. Zhang, S. Pathak, N. Sakai, T. Stergiopoulos, P. K. Nayak, N. K. Noel, A. A. Haghighirad, V. M. Burlakov, D. W. deQuilettes, A. Sadhanala, W. Li, L. Wang, D. S. Ginger, R. H. Friend, and H. J. Snaith, *Nature Communications* 6 (2015) 10030.
- [5.49] M. Green, Y. Jiang, A. Soufiani, and A. Ho-Baillie, *Journal of Physical Chemistry Letters* 6 (2015) 4774.
- [5.50] Q. Lin, A. Armin, R. Nagiri, P. Burn, and P. Meredith, *Nature Photonics* 9 (2015) 106.

- [5.51] T. Zhao, C.-C. Chueh, Q. Chen, A. Rajagopal, and A. K.-Y. Jen, *ACS Energy Letters* 1 (2016) 757.
- [5.52] R.J. Stewart, C. Grieco, A. V. Larsen, G. S. Doucette, and J. B. Asbury, *Journal of Physical Chemistry C* 120 (2016) 12392.
- [5.53] Q. Chen, H. Zhou, Y. Fang, A. Stieg, T. Song, H.-H. Wang, X. Xu, Y. Liu, S. Lu, J. You, P. Sun, J. McKay, M. Goorsky, and Y. Yang, *Nature Communications* 6 (2015) 7269.
- [5.54] Y. Wu, X. Li, S. Fu, L. Wan, and J. Fang, *Journal of Materials Chemistry A* 7 (2019) 8078.
- [5.55] M. R. Leyden, M. V. Lee, S. R. Raga, and Y. Qi *Journal of Materials Chemistry A* 3 (2015) 16097.
- [5.56] N. Ahn, K. Kwak, M.S. Jang, H. Yoon, B.Y. Lee, J-K. Lee, P.V. Pikhitsa, J. Byun, and M. Choi, *Nature Communications* 7 (2016) 13422.
- [5.57] A.K. Jena, H.-W. Chen, A. Kogo, Y. Sanehira, M. Ikegami, and T. Miyasaka, *ACS Applied Materials Interfaces* 7 (2015) 9817.



SUMMARY

Organic-inorganic hybrid perovskites are considered one of the most attractive semiconductors owing to their excellent optical and electrical properties, such as suitable optical bandgap, high absorption coefficient, low exciton binding energy, high charge mobility of electrons and holes, long charge carrier diffusion lengths and facile deposition methods. Since their first application as light absorbing materials in photovoltaic technology in 2009, perovskites based solar cells have achieved remarkable progress with certified record power conversion efficiency (PCE) of over 25.2% in just a few years.

This thesis reports on the deposition of perovskite thin films solar cells such as methyl ammonium lead iodide (MAPbI_3) or mixed halide $\text{MAPbI}_{3-x}\text{Cl}_x$ (x is usually very small) through a low pressure sequential chemical vapour deposition (CVD) method. This method involved a deposition of lead halides (lead iodide, lead chloride, or lead chloride iodide) in the step(s) of the process and thereby converting these lead halides films into a perovskite phase during the second/last step. A CVD tube furnace was used for both the deposition of lead halides and their subsequent conversion to perovskite phase.

The first phase of this project was to optimise the deposition of lead halide films i.e., lead iodide (PbI_2) and lead chloride (PbCl_2). A successful deposition of high-quality crystalline films of PbI_2 and PbCl_2 were realised through this low-pressure CVD method. Highly textured PbI_2 films with crystallite sizes of 154.3 nm and 172.4 nm for films deposited at substrate temperatures of 125 °C and 135 °C, respectively, were obtained. Large lateral grain sizes were also observed for these PbI_2 films as measured from the SEM micrographs with average grain size of 588.7 ± 117.6 nm for film deposited at 125 °C and 734.2 ± 144.8 nm for a sample deposited at 125 °C substrate temperature.

PbCl₂ films showed reduced texture on the XRD patterns with smaller crystallite sizes than those of PbI₂ samples with values of 84.7 nm for the sample deposited at 150 °C and 94.7 nm for the sample deposited at 165 °C substrate temperatures. The PbCl₂ films have columnar grain shape compared to flat platelet grains of the PbI₂ films with average grain size of about 344.8 ± 111.4 nm and 386.7 ± 119.5 nm for the 150 °C and 165 °C substrate temperatures, respectively. These large grain sizes for these lead halides films are beneficial for conversion to perovskite films. It is expected that a fully converted perovskite film from a pre-deposited lead halide will have even larger grains than the pre-deposited Pb halides. Optically, the PbI₂ films showed a band gap of about 2.4 eV confirming the material semiconducting properties. The PbCl₂ on the other side had a wide band gap of 4.3 eV which shows insulating properties of this material.

After the successful optimisation of the Pb halides, then the PbI₂ films were converted to perovskite phase at different times (15, 30, 60, 90, 120 minutes) to study the conversion mechanism. The as-deposited PbI₂ films with lateral grain size of about 1.60 ± 0.62 μm, grown in the first step were successfully converted to highly crystalline, smooth, and compact MAPbI₃ perovskite. The conversion was achieved by exposing the pre-deposited PbI₂ to methyl ammonium iodide (MAI) vapour in the second step using the same CVD reactor. It was observed that the conversion begins at the surface of the PbI₂ and progresses towards the glass substrate, resulting in tetragonal MAPbI₃ perovskites.

A growth in grain size was realized as the conversion time increases from 15 minutes up to 90 minutes, where conversion saturation was observed with a grain size of 3.70 ± 1.80 μm for the sample converted for 90 minutes. A perovskite rich film was confirmed from the XPS depth profile. It was observed that the 15 minutes converted sample had mixed phases of PbI₂ and that of MAPbI₃ perovskites as deduced from the XRD results; but after 30 minutes conversion

a small PbI_2 impurity remained suggesting a more perovskite phase. The fully converted perovskite film (90 minutes) was found to be optically stable in air with high relative humidity up to 80% for more than 21 days. This stability is ascribed to its superior grain size, crystalline quality, high purity, and compactness of the film.

Air-processed planar perovskite solar cell devices under similar ambient room conditions as perovskite thin films on glass were achieved. The planar solar cell composed of glass substrate followed by fluorine doped tin oxide, thin compact titanium dioxide as electron transport layer, perovskite absorber layer, doped Spiro-MeOTAD as hole transport layer, and then silver metal contact. The best device performance achieved was 11.7% achieved at 100 mW/cm^2 illumination, albeit with a hysteresis. The device maintained 85% of its initial PCE for 13 days of measurements while stored at high humidity conditions.

The final phase of this project looked into the preparation Cl-doped perovskite solar cell devices via three- and two-step sequential CVD method using chlorine-containing Pb halide films and compared to pure iodine-based perovskite. It was observed that Cl was not substituted by iodine during high temperature sequential CVD of PbCl_2 and PbI_2 layers; instead, the compounds reacted to form a stable lead chloride iodide phase. It was shown that Cl was easily substituted by iodine during the perovskite formation under similar substrate temperatures as the Pb halide deposition, though different deposition pressures were used. It was also observed that the presence of Cl in the Pb halide films does not necessarily improve the grain size of the final perovskite films compared to its pure iodine counterparts, but its presence is still beneficial to device performance.

Lastly, the open circuit voltage (V_{oc}) was improved significantly for planar perovskites solar cells prepared from Cl-containing Pb halides, hence increasing device efficiencies. The highest device performance of 10.87% ($V_{oc} = 0.938 \text{ V}$) was achieved for the perovskite converted from

PbCl₂ compared to just 8.76% ($V_{oc} = 0.862$ V) for PbI₂-based perovskite. This improved V_{oc} and efficiency was attributed to the low trap density at grain boundaries and at film surface for Cl-doped perovskites allowing easy injection of charge carriers to the respective charge transport layers. This work will aid in the development of a scalable, low-cost synthesis technique for the manufacturing of mixed-halide hybrid perovskite solar panels.

This study demonstrated the successful deployment of a sequential CVD method to prepare perovskite thin films with both the deposition of Pb halides and their subsequent conversion to perovskite phase done in the same CVD reactor, thereby simplifying the deposition process. The solar cells performed relatively poor compared to previous studies where CVD method was employed and this stems from poor charge transport layers used such as compact TiO₂ and the Spiro-MeOTAD layer.

As recommendation, an extensive study to improve the device performance is necessary such as further optimisation of the Spiro-MeOTAD layer deposition. Interface engineering between the perovskite absorber layer and the c-TiO₂ has been shown to improve charge transport from the perovskite to the c-TiO₂ such as inserting a thin layer of PCBM fullerene. Replacing the c-TiO₂ layer altogether with tin oxide (SnO_x) layer may also improve the device performances and reduce hysteresis.

APPENDIX A

Simulation of optical absorption near band-edge.

We simulate the absorption spectrums (**Figure 5.11(a)–(c)**, *CH 5.3.2*) near the band-edge using the Elliott formalism [B1]. The absorption coefficient (α) is directly proportional to the imaginary part of the dielectric function (ε'') and is given by:

$$\alpha(\omega) = \frac{\omega}{n(\omega)c} \varepsilon''(\omega). \quad (1)$$

If the refractive index (n) is only weakly dependent on the frequency,

$$\alpha(\omega) = \frac{\omega}{n_b c} \varepsilon''(\omega) = \frac{\omega}{n_b c} \chi''(\omega), \quad (2)$$

where n_b is the background refractive index and χ'' is the imaginary part of the susceptibility.

The resonant part of the optical susceptibility for a 3D semiconductor is given by [B2]

$$\chi(\omega) = -\frac{2|d_{cv}|^2}{\pi E_0 a_0^3} \left[\sum_n \frac{1}{n^3} \frac{E_0}{\hbar(\omega + i\delta) - E_g - E_n} + \frac{1}{2} \int dx \frac{x e^{\pi x}}{\sinh(\pi/x)} \frac{E_0}{\hbar(\omega + i\delta) - E_g - E_0 x^2} \right]. \quad (3)$$

Using Eq. (3) in (2), and using the Dirac identity, one obtains the band-edge absorption as [B2]:

$$\alpha(\omega) = \alpha_0^{3D} \frac{\hbar\omega}{E_0} \left[\sum_{n=1}^{\infty} \frac{4\pi}{n^3} \delta(\Delta + \frac{1}{n^2}) + \Theta(\Delta) \frac{\pi e^{-\pi/\sqrt{\Delta}}}{\sinh(\pi/\sqrt{\Delta})} \right], \quad (4)$$

The first and second term in (4) represent the excitonic state and the continuum, respectively. In Eq.(4), $\Delta = \frac{(\hbar\omega - E_g)}{E_0}$, where E_g is the band gap energy and E_0 is the excitonic binding energy.

References

[B1] R. J. Elliott, *Physics Reviews* 108 (1957) 1384–1389.

[B2] H. Haug, and S. W. Koch, ‘Quantum theory of the optical and electronic properties of semiconductors’, World Scientific (2004).

PUBLICATIONS

1. ***S. Ngqoloda**, C.J. Arendse, S. Guha, T.F. Muller, S.C. Klue, S.S. Magubane, C.J. Oliphant, “*Mixed-halide perovskites solar cells through PbI₂ and PbCl₂ precursor films by sequential chemical vapor deposition*”, *Solar Energy* 215 (2021) 179. <https://doi.org/10.1016/j.solener.2020.12.042>.
2. ***S. Ngqoloda**, C.J. Arendse, T.F. Muller, P.F. Miceli, S. Guha, L. Mostert, and C.J. Oliphant, “*Air-Stable Hybrid Perovskite Solar Cell by Sequential Vapor Deposition in a Single Reactor*”, *ACS Applied Energy Materials* 3 (2020) 2350. <https://dx.doi.org/10.1021/acsaem.9b01925>.
3. ***S. Ngqoloda**, C.J. Arendse, T.F. Muller, S.S. Magubane, and C.J. Oliphant, “*Controlled Deposition of Lead Iodide and Lead Chloride Thin Films by Low-Pressure Chemical Vapor Deposition*”, *Coatings* 10 (2020) 1208. <https://doi.org/10.3390/coatings10121208>.
4. ***S. Ngqoloda**, C.J. Arendse, T.F. Muller, F.R. Cummings, and C. Oliphant, “*Effect of HTL thickness on air processed CVD perovskite solar cells*”, *Materials Today Proceedings*. (2020). <https://doi.org/10.1016/j.matpr.2020.04.074>.
5. U. Nwankwo, **S. Ngqoloda**, A.C. Nkele, C.J. Arendse, K.I. Ozoemena, A.B.C. Ekwealor, R. Jose, M. Maaza, and F.I. Ezema, “*Effects of alkali and transition metal-doped TiO₂ hole blocking layers on the perovskite solar cells obtained by a two-step sequential deposition method in air and under vacuum*”, *RSC Advances*, 2020, 10, 13139. <https://doi.org/10.1039/d0ra01532f>
6. E.S.M. Mouele, **S. Ngqoloda**, S. Pescetelli, A. Di Carlo, M. Dinu, A. Vladescu, A.C. Parau, A. Agresti, M. Braic, C.J. Arendse, and L.F. Petrik, “*Spin Coating Immobilisation of C-N-TiO₂ Co-Doped Nano Catalyst on Glass and Application for*

Photocatalysis or as Electron Transporting Layer for Perovskite Solar Cells”,
Coatings 10 (2020) 1029. <https://doi.org/10.3390/coatings10111029>.

7. T.E. Mazibuko, S. Halindintwali, C.J.Arendse, **S. Ngqoloda**, O. Nemraoui, C. Mtshali, M. Madhuku, “*Spectrometry studies of Ag implanted silicon carbide thin films for application as a diffusion barrier against transition metals*”, *Materials Today Proceedings*. (2020). <https://doi.org/10.1016/j.matpr.2020.03.310>.

* *Indicates publication emanating from this thesis.*

